

University of Windsor

## Scholarship at UWindor

---

Electronic Theses and Dissertations

Theses, Dissertations, and Major Papers

---

8-31-2018

# Synthesizing Efficient Quasi-one-dimension Titanium Dioxide Nanocatalyst for Enhanced Photocatalytic Degradation of Aqueous Organic Pollutants and Hydrogen Production

Tao Peng

*University of Windsor*

Follow this and additional works at: <https://scholar.uwindsor.ca/etd>

---

### Recommended Citation

Peng, Tao, "Synthesizing Efficient Quasi-one-dimension Titanium Dioxide Nanocatalyst for Enhanced Photocatalytic Degradation of Aqueous Organic Pollutants and Hydrogen Production" (2018). *Electronic Theses and Dissertations*. 7557.

<https://scholar.uwindsor.ca/etd/7557>

This online database contains the full-text of PhD dissertations and Masters' theses of University of Windsor students from 1954 forward. These documents are made available for personal study and research purposes only, in accordance with the Canadian Copyright Act and the Creative Commons license—CC BY-NC-ND (Attribution, Non-Commercial, No Derivative Works). Under this license, works must always be attributed to the copyright holder (original author), cannot be used for any commercial purposes, and may not be altered. Any other use would require the permission of the copyright holder. Students may inquire about withdrawing their dissertation and/or thesis from this database. For additional inquiries, please contact the repository administrator via email ([scholarship@uwindsor.ca](mailto:scholarship@uwindsor.ca)) or by telephone at 519-253-3000ext. 3208.

**Synthesizing Efficient Quasi-one-dimension Titanium Dioxide Nanocatalyst for  
Enhanced Photocatalytic Degradation of Aqueous Organic Pollutants and Hydrogen  
Production**

By

**Tao Peng**

A Dissertation  
Submitted to the Faculty of Graduate Studies  
through the Department of Civil and Environmental Engineering and  
Chimie Physique et de Chimie Analytique de Paris Centre (ED 388)  
in Partial Fulfillment of the Requirements for  
the Degree of Doctor of Philosophy  
at the University of Windsor, Windsor, Ontario Canada and Sorbonne University, Paris  
France

Windsor, Ontario, Canada

2018

© 2018 Tao Peng

Synthesizing Efficient Quasi-one-dimension Titanium Dioxide Nanocatalyst for Enhanced Photocatalytic Degradation of Aqueous Organic Pollutants and Hydrogen Production

by

Tao Peng

APPROVED BY:

---

G. Achari, External Examiner  
University of Calgary

---

H. Eichhorn  
Department of Chemistry and Biochemistry

---

R. Seth  
Department of Environmental Engineering

---

J. A. Lalman, Advisor  
Department of Environmental Engineering

---

F. Arefi-Khonsari, Co-Advisor  
Sorbonne University

Additional committee members assigned by Sorbonne University, France:

P. Supiot, External Examiner, Sciences and Technologies, University of Lille, France

C. Jolival, Laboratoire de Reactivity de Surfaces (LRS), Sorbonne University, France

A. Pailleret, Laboratoire Interfaces and Electrochemical Systems (LISE), Sorbonne University, France

July 19<sup>th</sup>, 2018

# **DECLARATION OF CO-AUTHORSHIP / PREVIOUS PUBLICATION**

## **I. Co-Authorship Declaration**

I hereby declare that this thesis incorporates material that is result of joint research, as follows: collaboration with Dr. Jerald A. Lalman and Dr. Farzaneh Arefi-Khonsari as co-advisors. The collaboration is covered in Chapters 5 and Chapter 6. In all cases, the key ideas, primary contributions, experimental designs, data analysis, interpretation and writing were performed by the author, and the contribution of co-authors was primarily through the assisting of the statistical analysis.

I am aware of the University of Windsor Senate Policy on Authorship and I certify that I have properly acknowledged the contribution of other researchers to my thesis, and have obtained written permission from the co-authors to include the above material in my thesis.

I certify that, with the above qualification, this thesis, and the research to which it refers, is the product of my own work.

## **II. Declaration of Previous Publications**

This thesis includes 6 original papers that have been previously published/submitted for publication in a peer reviewed journals, as follows:

Thesis Chapter	Publication title/full citation	Publication status
Chapter 3	The role of hydrothermal conditions in determining TiO <sub>2</sub> nanotube bandgap and crystal phases. <i>Mater. Res. Bull.</i> 105, 104-113 (2018)	Published
Chapter 4	(1). Evaluating the hydrothermal synthesis of 1D TiO <sub>2</sub> nanomaterials for the photocatalysis of selected organic chemicals <i>Desalin. Water Treat.</i> (2017)	Accepted
	(2). Optimizing photocatalytic hydrogen production from water-ethanol mixture using 1D TiO <sub>2</sub> <i>J. Environ. Chem. Eng.</i> (2018)	Submitted
Chapter 5	(1). Enhanced TiO <sub>2</sub> nanorods photocatalysts with partially reduced graphene oxide for degrading aqueous hazardous pollutants <i>Environ Sci Pollut Res Int.</i> (2018)	Published
	(2). Designing a 3D three-dimensional Ag-RGO-TiO <sub>2</sub> nanorods photocatalyst thin-film for degrading model organic pollutants water treatment under visible light conditions	In preparation
Chapter 6	One-step deposition of nano-Ag-TiO <sub>2</sub> coatings by atmospheric pressure plasma jet for water treatment: Application to trace pharmaceutical removal by solar photocatalysis	In preparation

I certify that I have obtained a written permission from the copyright owner(s) to include the above published material(s) in my thesis. I certify that the above material describes work completed during my registration as a graduate student at the University of Windsor and Sorbonne University.

### III. General

I declare that, to the best of my knowledge, my thesis does not infringe upon anyone's copyright nor violate any proprietary rights and that any ideas, techniques

quotations, or any other material from the work of other people included in my thesis, published or otherwise, are fully acknowledged in accordance with the standard referencing practices. Furthermore, to the extent that I have included copyrighted material that surpasses the bounds of fair dealing within the meaning of the Canada Copyright Act, I certify that I have obtained a written permission from the copyright owner(s) to include such material(s) in my thesis.

I declare that this is a true copy of my thesis, including any final revisions, as approved by my thesis committee and the Graduate Studies office, and that this thesis has not been submitted for a higher degree to any other University or Institution.

## ABSTRACT

This dissertation is focused on synthesizing Q1D TiO<sub>2</sub>-based nanocatalysts for degrading aqueous organic pollutants and producing H<sub>2</sub>. A facile alkaline hydrothermal process was used to synthesize Q1D TiO<sub>2</sub> under different hydrothermal synthesis factors (reaction temperature, NaOH concentration and TiO<sub>2</sub> precursor concentration). The hydrothermal synthesis factors significantly affected the Q1D TiO<sub>2</sub> phase structure, crystal size, specific surface area (SSA), bandgap, photocatalytic activities. A Box-Behnken design (BBD) model was used to optimize the hydrothermal factors for synthesizing Q1D TiO<sub>2</sub> with maximum photodegradation rate and H<sub>2</sub> production rate.

The optimized Q1D TiO<sub>2</sub> with maximum photodegradation rate was further enhanced with partially reduced graphene oxide (RGO) (designated as GT) for degrading aqueous hazardous pollutants. The study also examined the impact of the RGO atomic oxygen-to-carbon (O/C) ratio on GT photocatalytic activities. The highest photocatalytic activity was observed when the RGO atomic O/C ratio was 0.130±0.003. Next, the GT photocatalyst was enhanced with Ag NPs (designated as Ag-GT). The highest photocatalytic activity was observed for a silver content of 10 wt% in the photocatalyst film.

Finally, an atmospheric pressure plasma jet (APPJ) was employed to synthesize micrometer thick Ag nanoparticles modified TiO<sub>2</sub> (Ag-TiO<sub>2</sub>) coatings, presenting a core-shell structure for degrading RhB and trace pharmaceutical compounds using a solar light source. The Ag-TiO<sub>2</sub> coatings were characterized having a porous anatase phase, improved charge separation and visible light absorption. The highest photodegradation rate was observed for a silver content of 0.4wt% in the composite.

**Keywords:** TiO<sub>2</sub>, hydrothermal, photodegradation, H<sub>2</sub> production, graphene, atmospheric pressure plasma jet, Ag nanoparticles.



## **DEDICATION**

I dedicate my dissertation to my parents for their sacrifices, sharing equally my entire emotional burdens, offering me all their love and inspiring me to this goal.

I dedicate this dissertation to my wife Zhao Wang.

My sincere gratitude to all my loved ones whose support and encouragement has provided me the strength and perseverance needed to complete this dissertation.

## ACKNOWLEDGEMENTS

I owe thanks to many individuals who deserve credit and appreciation for their role in helping me during my PhD study. This cotutelle thesis is based on research work conducted at the University of Windsor, Windsor, Ontario Canada and Sorbonne University, Paris, France.

I wish to thank my principal advisor, Professor Jerald A. Lalman, for his continuous technical advice, constructive appraisal and on-going feedback throughout the duration of this work. I express my deepest appreciation for his guidance which were invaluable for my PhD study.

I extend my sincere gratitude to my co-advisor, Professor Farzaneh Arefi-Khonsari, who provided me with the opportunity to initiate an international cooperate with Laboratoire Interfaces et Systemes Electrochimiques (LISE), Sorbonne University. Professor Arefi-Khonsari provided many valuable suggestions and inspiring advices.

Besides my advisors, I would like to thank Professor Gopal Achari, Professor Philippe Suptot, Professor Alain Pailleret, Professor Claude Jolival, Professor S. Holger Eichhorn and Professor Rajesh Seth for serving on my dissertation committee, and spending time reading and revising my dissertation.

My sincere thanks to our technical staff Mr. Bill Middleton, lab technician, for unreserved technical cooperation and help in the lab by providing the required material for the research work.

I would like to thank Dr. Lalman's research team members past and present. They include Dr. Wudneh Ayele Shewa, Dr. Srimanta Ray including graduate students Fatemeh Saadat Ghareh Bagh, Guocheng Zhang and Lu Cao.

Dr. Farzaneh Arefi-Khonsari's research team members (past and present) include Dr. Jerome Pulpytel, Dr. Houssam Fakhouri, and graduate students Abdessadk Anagri, Tabibian Shayan and Ben Said Sarab.

My sincere appreciation to Dr. S. H. Eichhorn for providing access to several analytical instruments and invaluable assistance with x-ray diffraction (XRD). My sincere appreciation to Dr. Bulent Mutus for invaluable assistance with photoluminescence spectra using a Varian Cary Eclipse Fluorescence Spectrophotometer (Mississauga, ON). I thank Dr. Jian Zhang from Huazhong University of Technology for permitting use a high-resolution transmission electron microscope (HRTEM), x-ray photoelectron spectroscopy (XPS), XRD, Brunauer-Emmett-Teller (BET), and field emission scanning electron microscope (FESEM). I extend my gratitude to Ms. Sharon Lackie from the Great Lakes Institute of Environmental Research (GLIER) for assisting with the FESEM and Raman spectroscopic studies. Special thanks to members of my comprehensive examination committee which include Dr. Xiaohong Xu, Dr. Paul Henshaw, Dr. Rajesh Seth and Dr. Nihar Biswas, for their participation, perceptive comments and suggestions.

I would like to thank the Natural Sciences and Engineering Research Council (NSERC) of Canada (Grant No. 261797-2009), the University of Windsor (Grant No. 13320), the Canada Research Chair Program, the Ontario Trillium Scholarship, the Mitacs Scholarship and the European project (FP7 NMP NATIONMEM) for funding this work.

# TABLE OF CONTENTS

DECLARATION OF CO-AUTHORSHIP / PREVIOUS PUBLICATION .....	iii
ABSTRACT .....	vi
DEDICATION .....	viii
ACKNOWLEDGEMENTS .....	ix
LIST OF ABBREVIATIONS/SYMBOLS .....	xvii
GENERAL INTRODUCTION.....	1
1. STATE OF THE ART: FABRICATION AND PHOTOCATALYTIC PROPERTIES OF TiO <sub>2</sub> NANOMATERIALS .....	4
1.1. Introduction .....	4
1.2. Principles of photocatalysis.....	5
1.3. TiO <sub>2</sub> nanomaterials morphologies and crystallographic structures.....	7
1.4. TiO <sub>2</sub> nanomaterials synthesis .....	13
1.4.1. <i>Sol-gel method</i> .....	13
1.4.2. <i>Sol method</i> .....	14
1.4.3. <i>Hydrothermal method</i> .....	15
1.4.4. <i>Solvothermal method</i> .....	17
1.4.5. <i>Chemical/physical vapor deposition</i> .....	18
1.4.6. <i>Electrochemical methods</i> .....	20
1.4.7. <i>Direct oxidation method</i> .....	21
1.4.8. <i>Surfactant-controlled method</i> .....	21
1.4.9. <i>Other methods</i> .....	22
1.5. Preparation of quasi-one-dimension TiO <sub>2</sub> nanostructure .....	22
1.5.1. <i>Why quasi-one-dimension TiO<sub>2</sub> nanostructure?</i> .....	22
1.5.2. <i>Growth of quasi-one-dimension TiO<sub>2</sub> nanostructure</i> .....	23
1.5.3. <i>Alkaline hydrothermal method and its parameters</i> .....	24
1.5.4. <i>Quasi-one-dimension TiO<sub>2</sub> nanostructure formation mechanisms for alkaline                 hydrothermal method</i> .....	25
1.6. Plasma thin film and its applications.....	27

1.6.1. Advantages of TiO <sub>2</sub> thin film or coating .....	27
1.6.2. Plasma enhanced chemical vapor deposition (PECVD) .....	29
1.6.3. Magnetron sputter deposition .....	31
1.7. Modifications of TiO <sub>2</sub> nanomaterials .....	32
1.7.1. Modifying TiO <sub>2</sub> crystal structure and morphology .....	32
1.7.2. Metal and nonmetal doping .....	34
1.7.3. Depositing noble metals .....	36
1.7.4. Semiconductor coupling .....	36
1.7.5. Enhancing TiO <sub>2</sub> with carbon materials .....	38
1.8. Summary of the research objectives .....	40
1.9. References .....	42
2. MATERIALS AND EXPERIMENTAL METHODS .....	53
2.1. Introduction .....	53
2.2. Chemicals .....	53
2.3. Characterization instruments and processes .....	54
2.3.1. Electron microscopy .....	54
2.3.2. Raman spectra .....	55
2.3.3. X-ray diffraction (XRD) analysis .....	55
2.3.4. Diffuse reflectance UV-visible spectroscopy (DRS) and dye concentration ...	55
2.3.5. X-ray photoelectron spectroscopy (XPS) .....	56
2.3.6. Brunauer–Emmett–Teller (BET) and specific surface area (SSA) .....	56
2.3.7. High performance liquid chromatograph (HPLC) .....	56
2.3.8. Gas chromatograph (GC) .....	57
2.3.9. Photoelectrochemical measurements .....	57
2.3.10. Photocatalytic reactor .....	58
2.3.11. Optical emission spectroscopy of plasma .....	59
2.3.12. Thin film photocatalytic activity test .....	59
2.4. Graphene oxide (GO) and quasi-one-dimension (Q1D) TiO <sub>2</sub> synthesis .....	61
2.4.1. Synthesis of graphene oxide (GO) .....	61
2.4.2. Hydrothermal synthesis .....	62
2.4.3. Plasma process used for deposition .....	63

2.5. References .....	65
<b>3. THE IMPACT OF HYDROTHERMAL FACTORS ON QUASI-ONE-DIMENSION TiO<sub>2</sub> NANOSTRUCTURE, CRYSTAL SIZE AND BANDGAP .....</b>	<b>68</b>
3.1. Introduction .....	69
3.2. Experimental .....	71
3.2.1. <i>Preparation of the quasi-one-dimension TiO<sub>2</sub> photocatalyst</i> .....	71
3.2.2. <i>Characterization studies</i> .....	71
3.2.3. <i>Experimental design, optimization study and statistical analysis</i> .....	72
3.3. Results and discussion.....	74
3.3.1. <i>Morphology</i> .....	74
3.3.2. <i>Bandgap (eV)</i> .....	77
3.3.3. <i>Analysis of the experimental design</i> .....	78
3.3.3.1. <i>Impacts of factor variables on the bandgap</i> .....	78
3.3.3.2. <i>Model fitting using analysis of variance (ANOVA)</i> .....	79
3.3.3.3. <i>Factor interaction plots</i> .....	81
3.3.4. <i>Response model verification, optimization and validation</i> .....	83
3.3.5. <i>Phase structure analysis</i> .....	87
3.3.6. <i>Crystal size and specific surface area (SSA)</i> .....	90
3.3.7. <i>Effects of crystal size/specific surface area on Q1D TiO<sub>2</sub> bandgap</i> .....	93
3.4. Conclusions .....	94
3.5. References .....	95
<b>4. OPTIMIZING QUASI-ONE-DIMENSION TiO<sub>2</sub> PHOTOCATALYST: PHOTODEGRADING AQUEOUS ORGANIC POLLUTANTS AND PHOTOCATALYTIC HYDROGEN PRODUCTION .....</b>	<b>101</b>
4.1. Introduction .....	102
4.2. Photocatalytic experiments.....	103
4.2.1. <i>Preparation of the Q1D nanometric TiO<sub>2</sub> photocatalyst</i> .....	103
4.2.2. <i>Photocatalysis of selected organic pollutants</i> .....	104
4.2.3. <i>Photocatalytic hydrogen production</i> .....	105
4.3. The impact of hydrothermal factors on the photodegradation of aqueous organic pollutants .....	106

4.3.1. <i>Selecting model chemicals to assess implementing photodegradation as a technology for treating wastewater effluents and drinking water supplies</i> ...	107
4.3.2. <i>Experimental design and statistical analysis</i> .....	108
4.3.3. <i>Rhodamine b photocatalysis</i> .....	109
4.3.4. <i>Impact of hydrothermal conditions on the apparent rhodamine b degradation constant k</i> .....	111
4.3.5. <i>Modeling and optimization of hydrothermal synthesis</i> .....	112
4.3.6. <i>Response surface model development</i> .....	118
4.3.7. <i>Response surface model verification</i> .....	119
4.3.8. <i>Photocatalysis of other pollutants using the optimized Q1D TiO<sub>2</sub></i> .....	122
4.3.9. <i>Photodegradation conclusions</i> .....	124
4.4. <i>The impact of hydrothermal synthesis factors on photocatalytic hydrogen production from water-ethanol mixture</i> .....	125
4.4.1. <i>Introduction: Photocatalytic hydrogen production</i> .....	125
4.4.2. <i>Experimental design and statistical analysis</i> .....	127
4.4.3. <i>Photocatalytic hydrogen production</i> .....	129
4.4.4. <i>Impact of hydrothermal conditions on hydrogen production rate</i> .....	130
4.4.5. <i>Modeling and effects of factors on response variable hydrogen production rate</i> .....	131
4.4.6. <i>Response surface model development</i> .....	135
4.4.7. <i>Response surface model verification</i> .....	136
4.4.8. <i>Phase structure, crystal size and bandgap</i> .....	139
4.4.9. <i>Conclusions: Photocatalytic hydrogen production</i> .....	143
4.5. <i>Conclusions</i> .....	143
4.6. <i>References</i> .....	144
<b>5. ENHANCED TiO<sub>2</sub> NANORODS PHOTOCATALYSTS WITH PARTIALLY REDUCED GRAPHENE OXIDE AND AG NANOPARTICLES FOR DEGRADING AQUEOUS HAZARDOUS POLLUTANTS</b> .....	<b>155</b>
5.1. <i>Introduction</i> .....	156
5.2. <i>Experimental</i> .....	159
5.2.1. <i>Synthesis of reduced graphene oxide-TiO<sub>2</sub> nanorods (designated as GT) photocatalyst with varied RGO atomic oxygen-to-carbon (O/C) ratio</i> .....	159

5.2.2. <i>Ag-RGO-TiO<sub>2</sub> nanorods (designated as Ag-GT) synthesis and Ag-GT film preparation</i> .....	161
5.2.3. <i>Characterization studies</i> .....	162
5.2.4. <i>Photoelectrochemical measurements</i> .....	163
5.2.5. <i>Photocatalytic activity under ultraviolet (UV) light</i> .....	164
5.2.6. <i>Ag-GT film photocatalytic activity under visible irradiation</i> .....	165
5.3. Graphene based TiO <sub>2</sub> nanorods (GT) photocatalyst with optimum RGO atomic oxygen-to-carbon (O/C) ratio .....	166
5.3.1. <i>The graphene based TiO<sub>2</sub> nanorods (GT) morphology and phase structure</i> .....	166
5.3.2. <i>Removing oxygen-containing groups and adjusting the the atomic oxygen-to-carbon (O/C) ratio of reduced graphene oxide (RGO)</i> .....	170
5.3.3. <i>Interaction between reduced graphene oxide (RGO) and TiO<sub>2</sub> nanorods (TNRs)</i> .....	174
5.3.4. <i>Optical response and bandgap</i> .....	176
5.3.5. <i>Charge transportation and separation</i> .....	177
5.3.6. <i>Photocatalytic activity</i> .....	179
5.3.7. <i>The mechanism of reduced graphene oxide (RGO) atomic oxygen-to-carbon (O/C) ratio</i> .....	184
5.4. Ag-reduced graphene oxide-TiO <sub>2</sub> nanorods (Ag-GT) photocatalyst with optimum Ag loading .....	186
5.4.1. <i>Morphology analysis</i> .....	186
5.4.2. <i>Structure analysis</i> .....	187
5.4.3. <i>Diffuse reflectance UV-visible spectroscopy (DRS) and bandgap</i> .....	189
5.4.4. <i>Photoelectrochemical studies</i> .....	191
5.4.5. <i>Photocatalytic activity</i> .....	192
5.4.6. <i>Reaction mechanism</i> .....	194
5.5. Conclusions .....	195
5.6. References .....	196
6. ONE-STEP DEPOSITION OF NANO-AG-TIO <sub>2</sub> COATINGS BY ATMOSPHERIC PRESSURE PLASMA JET FOR DEGRADING TRACE PHARMACEUTICAL USING SOLAR ENERGY .....	208
6.1. Introduction .....	208
6.2. Experimental Methods .....	211



6.2.1. <i>Optical emission spectroscopy of atmospheric pressure plasma jet (APPJ) plasma</i> .....	212
6.2.2. <i>Thin film characterization</i> .....	212
6.3. Results and discussion.....	212
6.3.1. <i>Plasma jet characterization</i> .....	212
6.3.2. <i>Morphology and Ag diffusion in composite Ag-TiO<sub>2</sub> thin films</i> .....	216
6.3.3. <i>Effect of Ag incorporating on the crystal structure</i> .....	218
6.3.4. <i>Photocatalytic activity</i> .....	220
6.3.5. <i>Mechanism of photocatalytic oxidation by Ag-TiO<sub>2</sub></i> .....	226
6.4. Conclusions.....	226
6.5. References.....	227
7. GENERAL CONCLUSIONS AND RECOMMENDATIONS.....	235
RESUME DE LA THESE.....	244
8. ENGINEERING SIGNIFICANCE.....	252
APPENDICES.....	255
Chapter 3: copyright.....	255
Chapter 5: copyright.....	256
LIST OF PUBLICATIONS AND CONFERENCES.....	259
VITA AUCTORIS.....	262

## LIST OF ABBREVIATIONS/SYMBOLS

0D, 1D, 2D and 3D	D represents dimension
AD	Anderson-Darling
Ag-TiO <sub>2</sub>	Ag nanoparticles modified TiO <sub>2</sub>
ANOVA	Analysis of variance
APPJ	Atmospheric pressure plasma jet
BBD	Box-Behnken experimental design
BET	Brunauer-Emmett-Teller
BZF	Bezafibrate
CBZ	carbamazepine
CVD	Chemical vapor deposition
DBD	Dielectric barrier discharges
DF	Degrees of freedom
DRS	Diffuse reflectance UV-visible spectroscopy
e <sup>-</sup> -h <sup>+</sup>	Electron and hole pair
ε	Quantum efficiency
EDX	Energy dispersive X-ray
FESEM	Field emission scanning electron microscope
FTO	F-doped SnO <sub>2</sub> -coated
GC	Gas chromatograph
GO	Graphene oxide
GOT	Graphene oxide and TiO <sub>2</sub> nanorods mixture
GT	Enhanced TiO <sub>2</sub> nanorods with reduced graphene oxide

H <sub>2</sub>	Hydrogen
HPLC	High performance liquid chromatograph
HRTEM	High resolution transmission electron microscopy
MB	Methylene blue
MO	Methyl orange
MS	Mean square
N <sub>2</sub>	Nitrogen
NHE	Standard hydrogen electrode
NPs	Nanoparticles
O <sub>3</sub>	Ozone
OFAT	One-factor-at-a-time
PDA	Photodiode array
PECVD	Plasma enhanced chemical vapor deposition
PVDF	Polyvinylidene difluoride
PVD	Physical vapor deposition
Q1D	Quasi-one-dimensional
RF	Radio frequency
RGO	Reduced graphene oxide
RhB	Rhodamine b
RSM	Response surface methodology
SCE	Saturated calomel electrode
SEM	Scanning electron microscope
SSA	Specific surface area

TCD	Thermal conductivity detector
TiO <sub>2</sub>	Titanium dioxide
TNRs	Titanium dioxide nanorods
TNTs	Titanium dioxide nanotubes
TrPCs	Trace pharmaceutical compounds
TTIP	Titanium isopropoxide
UV	Ultraviolet
VLX	Venlafaxine
XPS	X-ray photoelectron spectroscopy
XRD	X-ray diffraction

### GENERAL INTRODUCTION

Titanium dioxide ( $\text{TiO}_2$ ) is widely considered as a potential solution for photodegradation of hazardous pollutant and production of clean energy.  $\text{TiO}_2$  has been used as photoelectrochemical cell, photovoltaics and photocatalysis, because of its wide bandgap and strong ability to split water for hydrogen production. However, the low efficiency of pure  $\text{TiO}_2$  photocatalyst is a challenge in practical applications. The factors affecting the use of photocatalysts to degrade hazardous pollutants and produce  $\text{H}_2$  include phase structure, crystal size, BET specific surface area (SSA), bandgap, charge transportation, charge separation, doping, cocatalyst and coupling other metal oxide semiconductors.

The methods for improving  $\text{TiO}_2$  overall photocatalytic efficiency include: (1): use of  $\text{TiO}_2$  nanostructure with increasing SSA, (2): modifying the crystal structure and morphology, (3): narrowing bandgap, (4): suppressing charge recombination, and (5): enhancing charge transfer. In this dissertation, we will focus on synthesis, modification and characterization of quasi-one-dimension (Q1D)  $\text{TiO}_2$  nanophotocatalyst for hazardous wastewater treatment and hydrogen production, as well as the deposition of thin films of  $\text{TiO}_2$  using the plasma-enhanced chemical vapor deposition (PECVD) for photodegrading organic pollutants. Eight chapters are present in this dissertation.

In Chapter 1, the fundamental photocatalytic processes and the state of the art will be described for synthesis and modification of  $\text{TiO}_2$ . In Chapter 2, the methodology will be described for the synthesis and characterization of Q1D  $\text{TiO}_2$  nano photocatalysts.

In Chapter 3, the effects of three hydrothermal synthesis factors (reaction temperature, NaOH concentration and  $\text{TiO}_2$  concentration) on Q1D  $\text{TiO}_2$  phase structure, crystal size

## GENERAL INTRODUCTION

and SSA, bandgap will be examined using a 3-factor 3-level Box Behnken design (BBD) statistical model. The hydrothermal factors will be optimized for synthesizing Q1D TiO<sub>2</sub> with maximum and minimum bandgaps. In Chapter 4, the BBD model will be developed to evaluate the effects of hydrothermal synthesis factors on the photocatalytic activities in terms of: photodegrading aqueous organic pollutants and photocatalytic H<sub>2</sub> production using Q1D TiO<sub>2</sub>. The hydrothermal factors will be optimized for synthesizing Q1D TiO<sub>2</sub> with maximum photodegradation rate of pollutants and H<sub>2</sub> production rate. The role of phase structure, crystal size and bandgap will be investigated.

In Chapter 5, the optimized Q1D TiO<sub>2</sub> with maximum photodegradation rate will be modified with partially reduced graphene oxide (RGO) (designated as GT) and partially RGO plus Ag nanoparticles (NPs) (designated as Ag-GT) for further enhancing the photodegradation. The RGO oxidation degree (atomic O/C ratio) will be investigated to maximize the photodegradation rate for degrading rhodamine b (RhB), methyl orange (MO), methylene blue (MB) and phenol by using ultraviolet (UV) light. Next, the GT with optimum oxidation degree will be deposited with Ag nanoparticles. The surface plasmon resonance (SPR) effect of Ag nanoparticles will enable the photodegradation under visible light. In addition, the impact of Ag content (5-15wt%) on the photodegradation rate will be investigated.

The disadvantages of TiO<sub>2</sub> powders include the need for separation or filtration steps, the problematic use in continuous flow systems and the particles agglomeration. Thin film deposition techniques of TiO<sub>2</sub> overcome these disadvantages. That is why in Chapter 6, micrometer thick Ag nanoparticles (NPs) modified TiO<sub>2</sub> (designated as Ag-TiO<sub>2</sub>) thin films will be deposited by using an atmospheric pressure plasma jet (APPJ) technique

## GENERAL INTRODUCTION

which is one of the PECVD methods. The PECVD has advantages of low cost, high deposition rate, low temperature, one step process, easy implementation, and in-line process capabilities. The effects of APPJ parameters (carrier gas flow rate, power rate) and Ag content on the distribution of Ag, the crystallinity of TiO<sub>2</sub>, the TiO<sub>2</sub> particle size and photodegradation rate will be studied in detail. The photodegradation rate will be investigated using RhB and different pharmaceutical compounds under solar irradiation.

Chapter 7 and 8 presents the general conclusions and engineering significance of this research project, respectively.

# STATE OF THE ART: FABRICATION AND PHOTOCATALYTIC PROPERTIES OF TiO<sub>2</sub> NANOMATERIALS

## 1.1. Introduction

Titanium dioxide (TiO<sub>2</sub>) is a widely studied semiconducting metal oxide since the discovery of its photocatalytic splitting of water on TiO<sub>2</sub> electrode under ultraviolet irradiation by Fujishima and Honda in 1972 [1-3]. Because of its high thermal stability, wide bandgap with suitable band-edge, low cost, non-toxic effect and corrosion-resistant properties [1], TiO<sub>2</sub> has been used in many promising applications such as photovoltaics and photocatalysis. The primary applications of photocatalysis include the following two categories: 1. photocatalysis of water into O<sub>2</sub> and H<sub>2</sub>, and 2. photodegradation of aqueous and atmospheric organic pollutant [1-4]. The photocatalytic efficiency is governed by TiO<sub>2</sub> material properties, the irradiance frequency, and irradiance intensity. In particular, the material properties dominating the photocatalytic activity include bandgap, charge transportation, crystal structure, specific surface area (SSA) and particles size [5]. Understanding these properties individually is essential in designing a high performance photocatalyst.

Developing methods to modify TiO<sub>2</sub> by increasing the specific surface area (SSA), decreasing particle size, optimizing crystal structure are effective strategies for enhancing the overall photocatalytic reaction efficiency [1, 6-9]. Nanostructure materials can be classified with sizes less than 100 nm or having low-dimensionality including 0D, 1D and 2D where D represents dimension [10]. Typically, quantum dots with size less than 10 nm is included under the 0D classification. 1D group includes nanotubes, nanowires,



nanofiber, nanorods and nanobelt. 2D group includes nanoplate and nanosheet. When compared to bulk TiO<sub>2</sub>, nanostructured TiO<sub>2</sub> shows novel properties and can be utilized to improve the photocatalytic activities [11]. TiO<sub>2</sub> Q1D nanostructures are particularly interesting due to their high SSA, enhanced charge carrier conductivity, and excellent mechanical strength [1].

The photocatalytic activities of pure TiO<sub>2</sub> is able to attain a limited level of photocatalytic efficiency due to the fast recombination of photo-generated electrons (e<sup>-</sup>) and holes (h<sup>+</sup>) pairs [4] and its wide bandgap of approximately 3.2 eV which absorbs only UV light (2-3% of the solar spectrum) [4, 5]. A wide variety of different methods have been developed to increase the activity of TiO<sub>2</sub> by suppressing charge recombination and extending the wavelength response range in the visible light region [4]. These methods include doping TiO<sub>2</sub> nanomaterials with other elements [5, 12, 13], sensitizing with photosensitizers such as dyes [12], depositing metal nanoparticles [4, 14] or coupling with other semiconductors [15] and incorporating carbon materials [16, 17].

## 1.2. Principles of photocatalysis

A schematic process shows splitting H<sub>2</sub>O into H<sub>2</sub> and O<sub>2</sub> over TiO<sub>2</sub> photocatalysts (Figure 1.1) [18]. The three main steps include the following (Figure 1.1a): 1. photo-generation of e<sup>-</sup> and h<sup>+</sup> in the semiconductor when excited with photons with energy greater than the TiO<sub>2</sub> bandgap, 2. transportation of the charge carriers to the TiO<sub>2</sub> surface and 3. surface charge transfer between carriers with reactants (e.g., H<sub>2</sub>O). In competition, the photo-generated charge carriers may recombine with each other dissipating energy without mediating a reaction with the reactants. Recombination is the major limitation in

semiconductor photocatalysis since, it decreases the overall efficiency. In the case of water splitting (Figure 1.1b), the energy position of the lowest level in the conduction band is more negative than the reduction potential of water (0 V versus NHE at pH = 0) ( $2\text{H}^+ + 2\text{e}^- = \text{H}_2$ ) while the energy of highest level in the valence band is more positive than the oxidation potential of water (+1.23 vs NHE at pH = 0) ( $4\text{OH}^- + 4\text{h}^+ = \text{O}_2 + 2\text{H}_2\text{O}$ ). Photogenerated carriers can also split renewable organic components (e.g. ethanol) to produce  $\text{H}_2$  [19]. The gas evolution rate in  $\mu\text{mol}\cdot\text{h}^{-1}$  units is used to compare the photocatalytic efficiency for different photocatalysts. The efficiency is also based on the quantum yield which is defined as the number of events occurring per photon absorbed [19, 20].

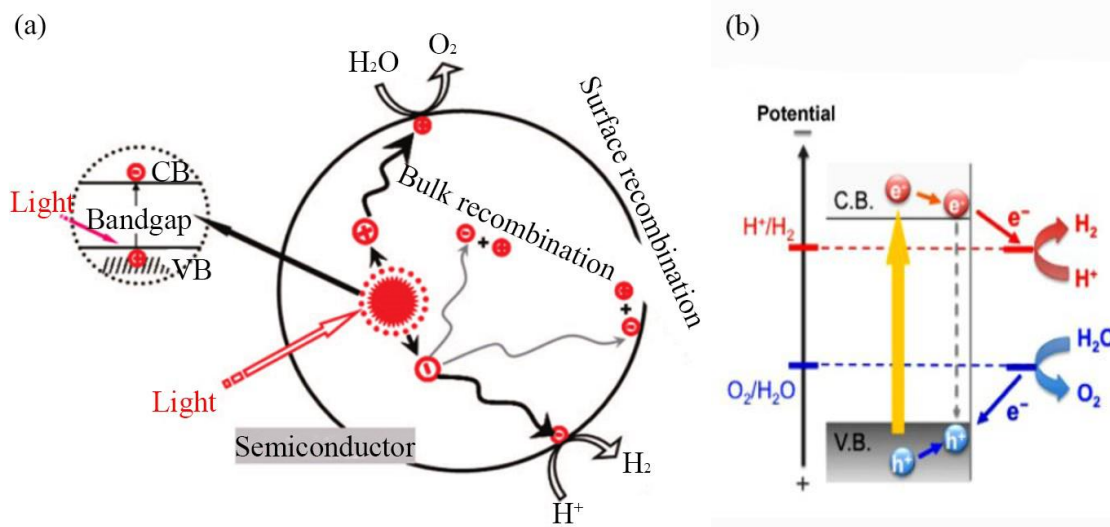


Figure 1.1: Schematic illustrating water splitting using  $\text{TiO}_2$  [18, 21]: (a) Charge transfer and recombination during photocatalytic water splitting, (b) The energy position of the valence and conduction bands.

Notes: <sup>a</sup> Valence band is the energy band occupied by the valence electrons and the highest occupied band [21], <sup>b</sup> conduction band is the lowest unfilled energy band and allows electrons moving freely [21], and <sup>c</sup> CB and VB represent conduction band and valence band, respectively.

In addition to reacting with water and ethanol to produce  $H_2$  and  $O_2$ , the photogenerated carries are able to degrade organic pollutants [22]. As shown in Figure 1.2, holes in valence band oxidize water and subsequently generates extremely powerful oxidants ( $\bullet OH$  radicals) which functions as oxidants to oxidize organic pollutants [22]. Electrons can be transferred to  $O_2$  dissolved in water to subsequently generate a superoxide radical anion ( $O_2^{\bullet -}$ ). This superoxide radical anion is also a powerful oxidant which reacts with organic pollutants to subsequently produce  $CO_2$  [22].

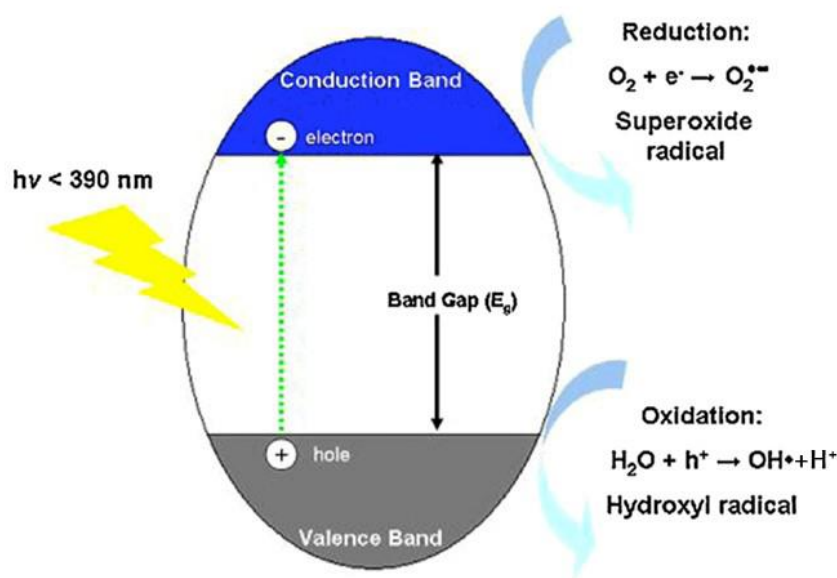


Figure 1.2: Schematic diagram for the reaction steps in photodegradation of aqueous organic pollutants [22].

Note: CB and VB represent conduction band and valence band, respectively.

### 1.3. $TiO_2$ nanomaterials morphologies and crystallographic structures

Thin films, powder, and single crystals are typical forms of bulk  $TiO_2$ . To increase the SSA, decreasing the  $TiO_2$  particle size to the nanometer scale leads to nanomaterials such as nanoparticles, nanorods, nanowires, nanotube, nanofilms, nanosheet and nanoribbons [23]. Nanowires/nanofibers are Q1D structures with diameters less than 100

nm and a specific growth direction while nanorods have a similar structure to nanowires, but the length is shorter. Nanotubes have a hollow interior structure while nanobelt/nanoribbons are similar in structure to nanowires but with well-defined side faces. Models for selected  $\text{TiO}_2$  Q1D nanostructure are shown in Figure 1.3.

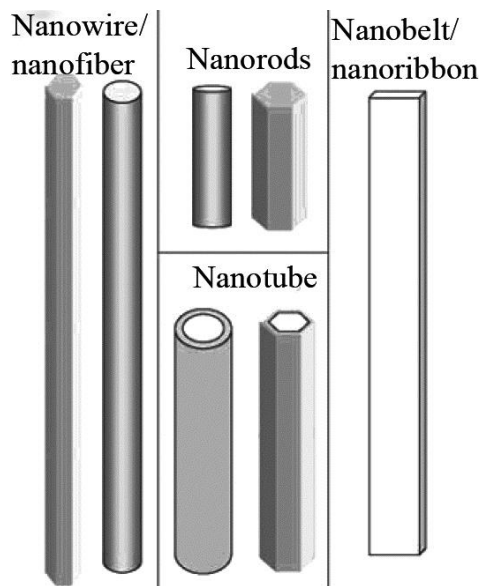


Figure 1.3: Models for selected  $\text{TiO}_2$  Q1D nanostructures.

$\text{TiO}_2$  exists in many different crystal forms under standard temperature and pressure conditions as well other forms have been reported under high pressure. These include anatase (tetragonal), rutile (tetragonal),  $\text{TiO}_2\text{-B}$  (monoclinic), brookite (orthorhombic),  $\text{TiO}_2\text{-R}$  (ramsdellite-structured),  $\text{TiO}_2\text{-H}$  (hollandite-structured),  $\text{TiO}_2\text{-II}$  (columbite-type) and  $\text{TiO}_2\text{-III}$  (baddeleyite-type) [24]. Anatase, brookite, rutile, and  $\text{TiO}_2\text{-B}$  are known to occur naturally [24]. However, the other phases which only exist under high pressure conditions are not stable under ambient conditions [24]. Rutile is considered as the most stable phase in terms of thermodynamics, whereas anatase,  $\text{TiO}_2\text{-B}$  and brookite are metastable phases which are transformed into rutile when treated at 600-900°C [25]. All

the  $\text{TiO}_2$  phases are formed by stacking co-coordinated  $\text{TiO}_6$  octahedral units with the  $\text{Ti}^{4+}$  ion positioned in the center of the octahedron and six oxygen atoms located at the six corners. The  $\text{TiO}_6$  octahedron stacks via either edge-sharing or corner-sharing of the oxygen atoms (Figure 1.4) [26]. The different phase structure showing differences in the distortion of each octahedron and in the assembly pattern of the octahedral chains is due to the Jahn-Teller effect [27]. The crystallographic and physical properties of anatase, rutile, brookite and  $\text{TiO}_2\text{-B}$  are shown in Table 1.1.

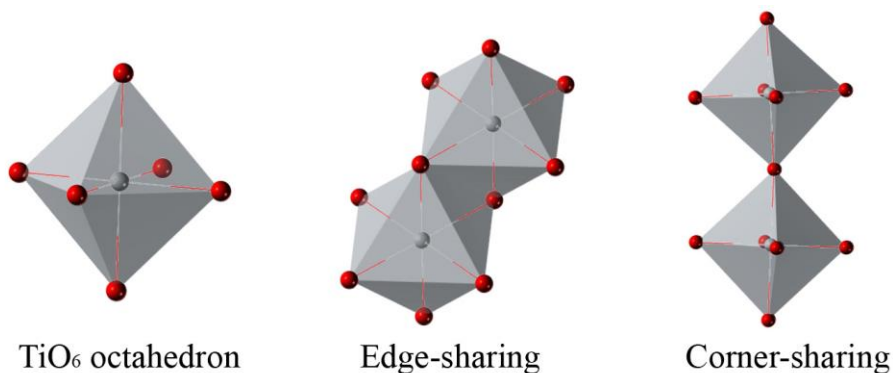


Figure 1.4: Model of  $\text{TiO}_2$  octahedron showing edge-sharing and corner-sharing. Notes: <sup>a</sup> red circles correspond to oxygen atoms, and <sup>b</sup> grey circles correspond to titanium atoms.

Anatase, consisting of a tetragonal structure (Figure 1.5) [11], is predominantly configured with edge-sharing octahedron [28]. Each octahedron in anatase has four sharing edges and each  $\text{O}^{2-}$  ion is closely surrounded by three  $\text{Ti}^{4+}$  ions. Anatase can be synthesized by employing the wet chemical process [25]. The wet chemical process usually leads to the formation of anatase nanoparticles because anatase is relatively thermodynamically stable when the size is confined to the nanoscale level [25].

Table 1.1: Properties of anatase, rutile, brookite and TiO<sub>2</sub>-B [11, 28, 29].

Property	Anatase	Rutile	Brookite	TiO <sub>2</sub> -B
Crystal structure	Tetragonal	Tetragonal	Orthorhombic	Monoclinic
Space group	$I\frac{4}{a}md$	$P\frac{4_2}{m}nm$	Pbca	$C\frac{2}{m}$
Lattice parameters (Å)	a 3.78, c 9.51	a 4.59, c 2.96	a 5.46, b 9.18, c 5.14	a 1.218, b 3.741, c 6.525, $\beta$ 107.05°
Bandgap (eV)	3.20	3.01	3.13	3.19
Hardness (Mohs Scale)	5.5–6	6–6.5	5.5–6	Unknown
Solubility in H <sub>2</sub> O	Insoluble	Insoluble	Insoluble	Insoluble
Density	3.89	4.25	4.13	Unknown
Melting point (°C)	Changes to rutile	1855	Changes to rutile	Changes to rutile

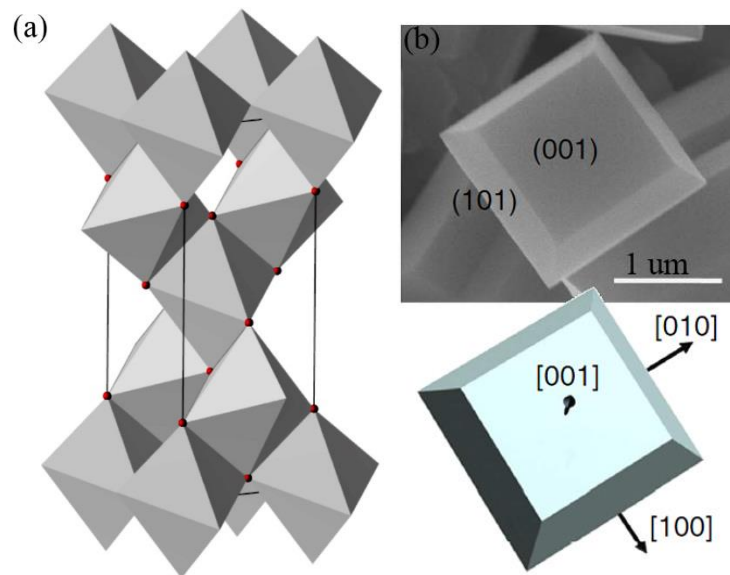


Figure 1.5: Anatase structure and SEM image: (a) Anatase unit cell and (b) SEM image (up) and the model (below) of truncated octahedron-shaped anatase crystal with exposed {001} and {101} facets [9].

Note: red circles correspond to oxygen atoms.

Rutile also has a tetragonal structural configuration; however, the c-axis is shorter in comparison to the anatase structure (Figure 1.6) [11]. Rutile is composed predominantly

of corner-sharing octahedron units [28] with octahedral apices connected to each other by edge-sharing chains parallel to the z-axis and the chains cross-linked in a corner-sharing manner. The  $\{011\}$  and  $\{100\}$  crystal face families in the rutile phase (Figure 1.6) have the lowest energy and thus, is a trunked octahedron that is the mostly observed morphology [30]. Rutile production through solution phase synthesis or transformation of other phases at 600-900°C is primarily due to its thermodynamic stability when compared to the other phases [25].

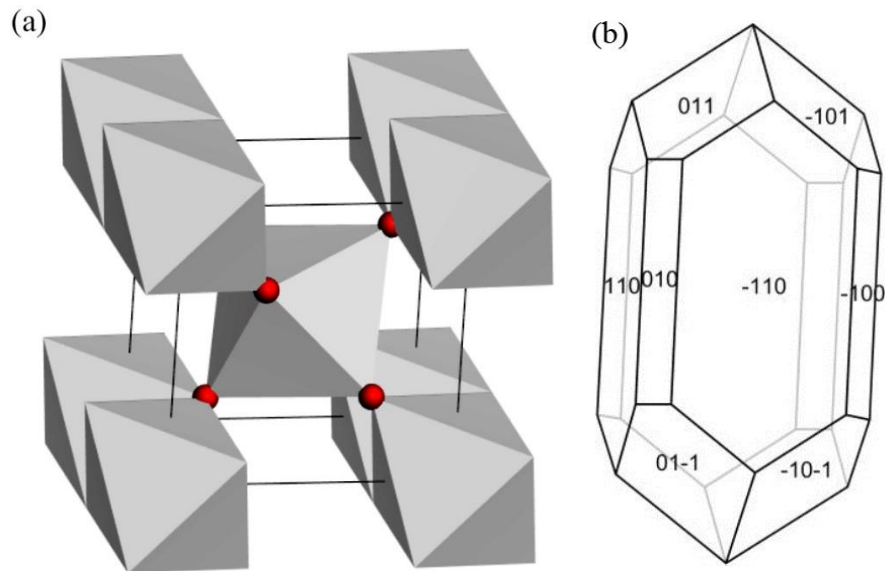


Figure 1.6: Rutile structure: (a) Rutile unit cell and (b) Rutile JCrystal crystal structure model [11].

Notes: <sup>a</sup> red circles correspond to oxygen atoms, and <sup>b</sup> JCrystal is a Java application for creating, editing, displaying and deploying crystal shapes [11].

TiO<sub>2</sub> brookite orthorhombic structure (Figure 1.7) is composed of large unit cells [11]. The structure consists of distorted TiO<sub>6</sub> octahedrons which are connected by both edge- and corner-sharing to construct a framework as shown in Figure 1.7. Although brookite is synthesized through the wet chemical process, it normally coexists with the rutile or anatase phases [28].

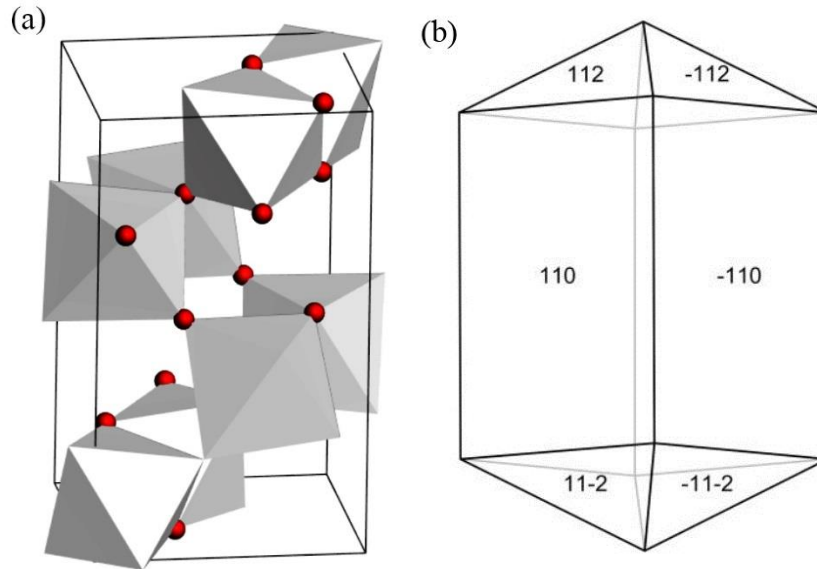


Figure 1.7: Brookite structure: (a) Brookite unit cell and (b) Brookite JCrystal structure model [11].

TiO<sub>2</sub>-B is constructed with large unit cells (Figure 1.8) having a monoclinic structure with a particularly long a-axis [30, 31]. TiO<sub>2</sub>-B is composed of corrugated sheets with edge- and corner-sharing TiO<sub>6</sub> octahedrons. These sheets pile up to construct a 3D framework. TiO<sub>2</sub>-B can be synthesized by proton exchange and subsequent dehydration of layered titanates at a temperature of approximately 300°C [31, 32]. TiO<sub>2</sub>-B can be transformed into anatase or rutile at high temperatures because of its thermodynamic instability [31, 32].

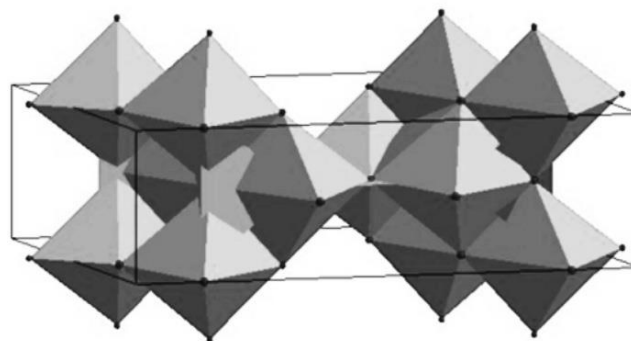


Figure 1.8: TiO<sub>2</sub>-B unit cell [30].



#### 1.4. TiO<sub>2</sub> nanomaterials synthesis

Synthesis of TiO<sub>2</sub> nanostructures can be accomplished by employing various methods such as sol–gel, chemical and physical vapor deposition (CVD and PVD), hydro/solvothermal, direct oxidation, surfactant-controlled approach and the electrochemical route. A brief overview of various methods is discussed in the following sections.

##### *1.4.1. Sol-gel method*

The sol-gel method is widely applied for synthesizing various ceramic materials [5]. In general, a colloidal suspension is produced from the hydrolysis and polymerization reaction of a precursor molecule [5]. Subsequently, complete polymerization and loss of solvent leads to the formation of a solid gel phase. The solid gel is then easily cast into the desired shape such as nanofilms and nanofibers. Furthermore, the wet gel is transformed into a dense ceramic by drying and heating treatment.

TiO<sub>2</sub> nanomaterials usually result from the hydrolysis of a titanium (IV) precursor. In a typical procedure to produce TiO<sub>2</sub> nanoparticles [5], a TiO<sub>2</sub> sol solution is produced by slowly mixing a precursor such as titanium isopropoxide (TTIP) in an alcoholic solution containing water. The 3D polymeric skeletons with close packing were developed by forming Ti-O-Ti chains. Next, the mixture is heated at 90-100°C for 6 h to produce the gel. Subsequent heating the gel at 400°C for 2 h is used to improve the crystallinity of the TiO<sub>2</sub> anatase nanoparticles.

The combination of the sol-gel method and an anodic alumina membrane template with long nanopores is useful in producing TiO<sub>2</sub> nanowires (Figure 1.9) [33]. A brief description of the process involves dipping porous anodic alumina membrane into a boiling TiO<sub>2</sub> sol followed by drying and heating. After heating at 500°C, the TiO<sub>2</sub> sol is converted into anatase TiO<sub>2</sub>. Next, the anodic alumina membrane template is removed by placing the combined TiO<sub>2</sub>/alumina membrane template into a H<sub>3</sub>PO<sub>4</sub> aqueous solution.

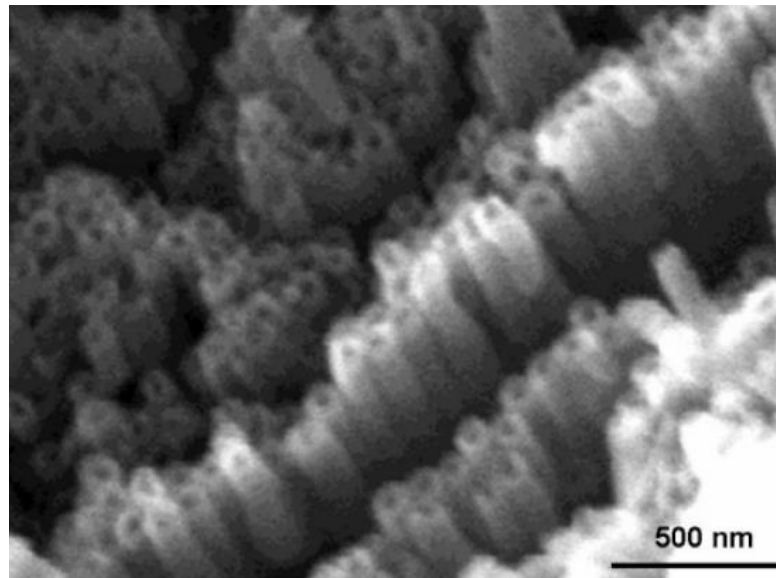


Figure 1.9: Anatase TiO<sub>2</sub> nanotubes SEM image prepared by combining the sol-gel and template methods [33].

Notes: <sup>a</sup> Synthesized using anodic alumina membrane template and TiO<sub>2</sub> sol, and <sup>b</sup> drying and heating at 60°C for 12 h, and <sup>c</sup> anodic alumina membrane template was removed in a 5wt% H<sub>3</sub>PO<sub>4</sub> solution at room temperature for 3 h.

#### 1.4.2. Sol method

The sol method is a non-hydrolytic sol-gel process. The method involves reacting titanium chloride with a metal alkoxide such as titanium alkoxide (Eq. 1.1).



where  $\text{RO}^-$  is an alkoxide. The reaction results in the formation of Ti-O-Ti bridges. The alkoxide groups can be either titanium alkoxides or the products formed by in-situ reacting titanium chloride with alcohols. Zhu et al. [34] reported mixing  $\text{TiF}_4$  with benzyl alcohol to produce an organic-rich titanium precursor. Next, the mixture is placed in an autoclave at  $160^\circ\text{C}$  for 24 h with the subsequent formation of anatase nanosheets (Figure 1.10).

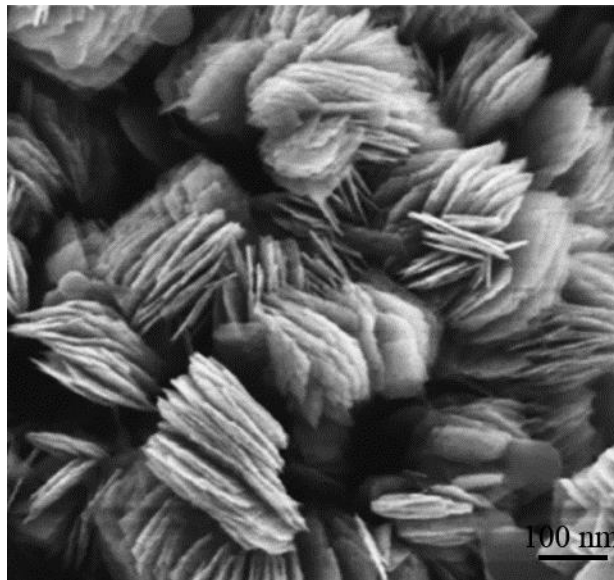


Figure 1.10:  $\text{TiO}_2$  anatase nanosheet SEM image [34].  
Note: Synthesized using  $\text{TiF}_4$  and benzyl alcohol at  $160^\circ\text{C}$  for 24 h.

#### 1.4.3. Hydrothermal method

Hydrothermal synthesis is widely employed for producing small particles in the ceramic industry. The method is performed in aqueous solution under controlled temperature and/or pressure conditions. The autoclave reactor consists of steel pressure vessels with or without a Teflon liner (Figure 1.11). The temperature can be set to  $300^\circ\text{C}$

by controlling the pressure. The morphology for the prepared TiO<sub>2</sub> nanomaterials depends on the type of solution, pH, temperature and the reaction time [5].



Figure 1.11: Commercially available magnetically stirred steel pressure vessel configured with pressure control and an external pump to control the gas flow [35].

Q1D TiO<sub>2</sub> nanomaterials have also been produced using the hydrothermal method (Figure 1.12). This widely used method employs treating TiO<sub>2</sub> particles in a 5-15 M NaOH aqueous solution at 110-200°C for 24-120 h [36-42]. The transformation of TiO<sub>2</sub> powder into nanotubes involves shearing, exfoliation, or delamination of lamellar nanosheets from a crystalline precursor [36]. The lamellar nanosheets edges have many atoms with dangling bonds which are not stable [36]. Next, the lamellar nanosheets bent and scrolled into Q1D nanotubes or nanowire (Figure 1.12) to saturate the dangling bonds [36]. The detailed mechanism is discussed in Section 1.5.4.

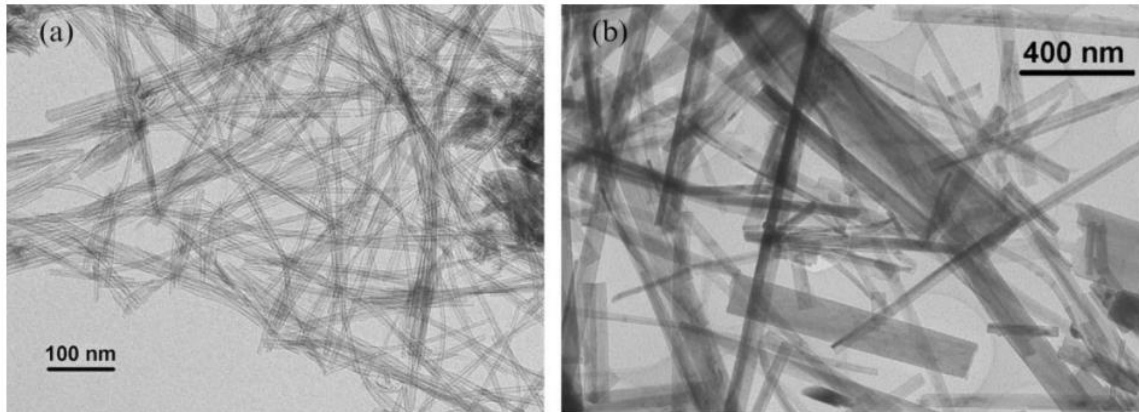


Figure 1.12: Quasi-one-dimension  $\text{TiO}_2$  nanostructure TEM images (a)  $\text{TiO}_2$  nanotubes synthesized using 10 M NaOH at  $140^\circ\text{C}$ , and (b) Anatase  $\text{TiO}_2$  nanowire synthesized using 10 M NaOH at  $190^\circ\text{C}$  [37].

#### 1.4.4. Solvothermal method

The solvothermal method is identical to the hydrothermal method except the solvent used is non-aqueous (e.g. toluene). The solvothermal method has better control of the reaction temperature, size, shape and crystallinity of  $\text{TiO}_2$  products [30]. The temperature can be increased much higher due to employing organic solvents with high boiling points. Solvents with different physical and chemical properties can affect the diffusion behavior, solubility, reactivity of the reactants which in turn influence crystallization and the crystal morphology of the final products [30]. Kim et. al. [38] reported that  $\text{TiO}_2$  nanorods were produced by mixing titanium isopropoxide with anhydrous toluene and oleic acid at  $250^\circ\text{C}$  for 20 h (Figure 1.13).

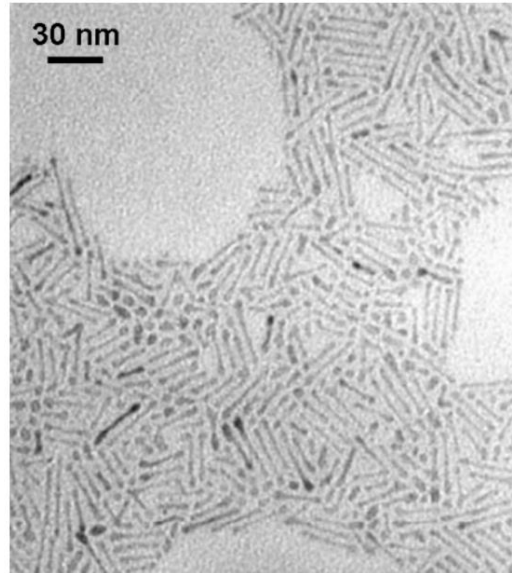


Figure 1.13: Nanorods TEM image synthesized using a solvothermal method [38]. Note:  $\text{TiO}_2$  nanorods were synthesized by mixing titanium isopropoxide, anhydrous toluene and oleic acid at  $250^\circ\text{C}$  for 20 h.

#### 1.4.5. Chemical/physical vapor deposition

Vapor deposition involves producing a vapor which is condensed onto a heated solid. The process is usually executed in a vacuum chamber. The method is designated as a physical vapor deposition (PVD) if the final product does not involve a chemical reaction, otherwise the process is designated as a chemical vapor deposition (CVD).

Producing  $\text{TiO}_2$  nanowires using a simple PVD method is illustrated in the SEM image shown in Figure 1.14 [39]. In a typical synthesis process, 1.5 g of source material (pure Ti metal powder) and a Si (100) substrate are separately placed on 2 graphite boats in a horizontal tube furnace. In this system, the source Ti powder is in the high-temperature zone and the Si (100) substrate is in the low-temperature zone. The furnace is set at  $1050^\circ\text{C}$  in the high-temperature zone and  $850^\circ\text{C}$  in the low-temperature zone. The PVD process is initiated when an  $\text{Ar}/\text{O}_2$  mixture gas flowing at a pressure of 40,000 Pa (300 Torr) is used to convert Ti into a layer of  $\text{TiO}_2$  nanowires [39].

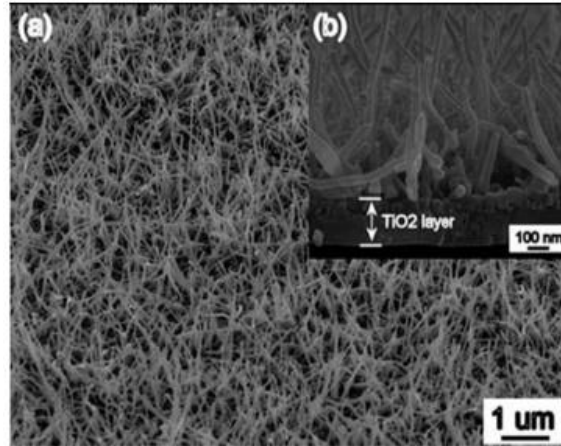


Figure 1.14: SEM images of TiO<sub>2</sub> nanowires SEM images grown on a Si(100) substrate using the PVD method [39].

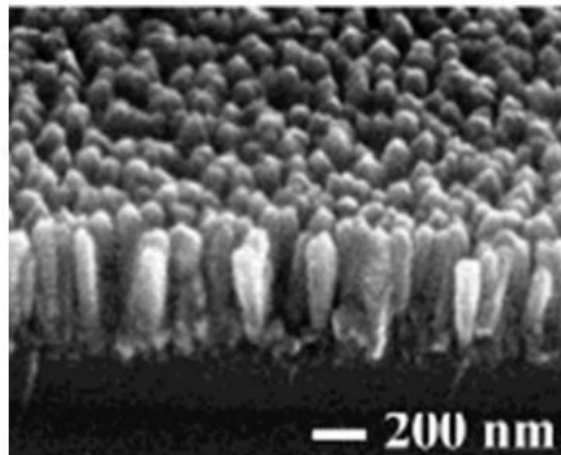


Figure 1.15: TiO<sub>2</sub> anatase nanorods SEM image [40].  
Note: CVD conditions set at 560°C and 667 Pa (5 Torr) [40].

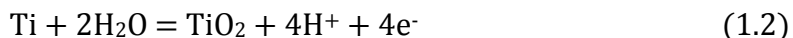
Evidence of producing TiO<sub>2</sub> anatase nanorods by growing them on silica substrates using the CVD method is shown in Figure 1.15 [40]. By using a N<sub>2</sub>/O<sub>2</sub> mixture gas carrying, Wu and Yu [40] demonstrated the vapors of the titanium acetylacetonate (Ti(C<sub>5</sub>H<sub>7</sub>O<sub>2</sub>)<sub>4</sub>) precursor were used to produce nanorods at a relative low temperature ranging between 200-230°C. The precursor reacts and is grown on a relatively high temperature (500-700°C) silica substrate surface. The phase and morphology of the TiO<sub>2</sub> products are tunable by adjusting the substrate temperature and pressure [40]. For

example, at 560°C and 630°C with a pressure at 667 Pa (5 Torr) leads to the production of anatase and rutile TiO<sub>2</sub> nanorods, respectively. However, at different conditions of 535°C and under 480 Pa (3.6 Torr), the results demonstrated the production of TiO<sub>2</sub> nanowalls.

#### 1.4.6. Electrochemical methods

The electrochemical methods include electrodeposition and electrochemical etching/anodization. Electrodeposition is commonly used to produce a TiO<sub>2</sub> nanocoating on a substrate by the action of reducing titanium ions in an electrolyte at the cathode surface. TiO<sub>2</sub> nanowires coating can be synthesized using a template such as an alumina membrane on Al substrate. Typically, titanium deposits into the pores of the template utilizing 0.2 M TiCl<sub>3</sub> solution as the electrolyte [41]. Anatase TiO<sub>2</sub> nanowires are produced after heating the Ti infused alumina membrane coating at 500°C for 4 h in the open furnace (Figure 1.16). Next, the alumina membranes are partly removed by a chemical etching process in a 3 M NaOH for 5 min.

Besides the electrodeposition method, electrochemical etching/anodization method is a versatile process which allows the production of a dense and well defined TiO<sub>2</sub> nanomaterial onto titanium surface [1, 30, 42, 43]. When titanium metal is exposed to a sufficiently high anodic voltage in a cell, electrochemical oxidation produces Ti<sup>4+</sup> (Ti → Ti<sup>4+</sup> + 4e<sup>-</sup>). Next, the Ti<sup>4+</sup> ions react with O<sup>2-</sup> in the electrolyte (Eq. 1.2) to form a compact TiO<sub>2</sub> layer [27, 43, 44].





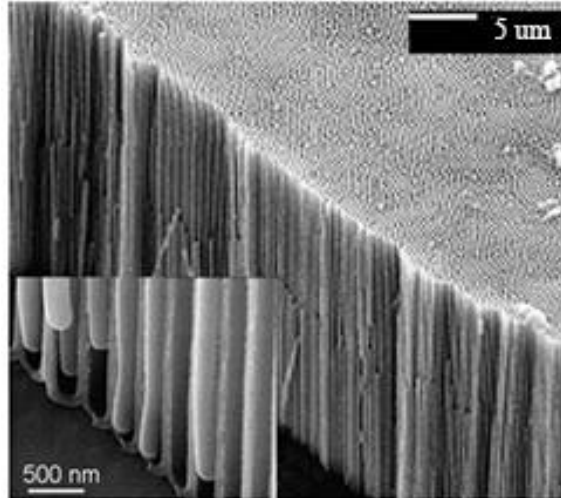


Figure 1.16: SEM images of TiO<sub>2</sub> nanowires produced using a electrodeposition method [41].

#### *1.4.7. Direct oxidation method*

Oxidizing titanium metal can be employed to produce TiO<sub>2</sub> nanomaterials. For example, TiO<sub>2</sub> nanorods on a titanium plate were produced by oxidation using 30% H<sub>2</sub>O<sub>2</sub> aqueous solution at 78°C for 72 h [45]. The TiO<sub>2</sub> nanorods phase structure is controllable by adding inorganic salts such as NaF, NaCl or NaSO<sub>4</sub> [45]. Pure anatase nanorods are produced by adding NaF or NaSO<sub>4</sub>, while pure rutile nanorods are produced by adding NaCl.

#### *1.4.8. Surfactant-controlled method*

With the assistance of surfactants, anisotropic growth of TiO<sub>2</sub> nanostructures is accomplished by the hydrolysis of metal alkoxides. Surfactants have the ability to select the crystal facet and manipulate the final structure of TiO<sub>2</sub> nanomaterials, since they modify the surface energy of desired facets [30]. For example, Cozzoli et al.[46]

reported growing anatase TiO<sub>2</sub> nanorods by the hydrolysis of titanium tetraisopropoxide using oleic acid as the surfactant.

#### *1.4.9. Other methods*

Sonication has been employed to produce TiO<sub>2</sub> nanostructure [5]. In addition, microwaves have been used to prepare TiO<sub>2</sub> nanomaterials [5]. The main advantages of using microwaves are rapid heat transfer as well as volumetric and selective heating.

### **1.5.Preparation of quasi-one-dimension TiO<sub>2</sub> nanostructure**

#### *1.5.1. Why quasi-one-dimension TiO<sub>2</sub> nanostructure?*

Q1D nanostructures are able to provide high electron mobility, high SSA and excellent mechanical strength [1]. For many applications, maximizing the SSA is crucial in increasing the overall efficiency. Decrease the TiO<sub>2</sub> dimension from bulk TiO<sub>2</sub> to the Q1D TiO<sub>2</sub> nanomaterials results in a large increase in the SSA coupled with enhanced electronic properties [1]. Fast charge transportation along TiO<sub>2</sub> Q1D nanostructure is able to improve the overall photocatalytic efficiency [1, 47]. In addition, TiO<sub>2</sub> Q1D nanostructures allow for a higher control of the chemical and physical behaviors for applications by manipulating the morphology [1]. For example, a free-standing membrane consisting of vertically oriented, both-side-open TiO<sub>2</sub> nanotubes was reported and used as micro-photoreactors (Figure 1.17) [48].

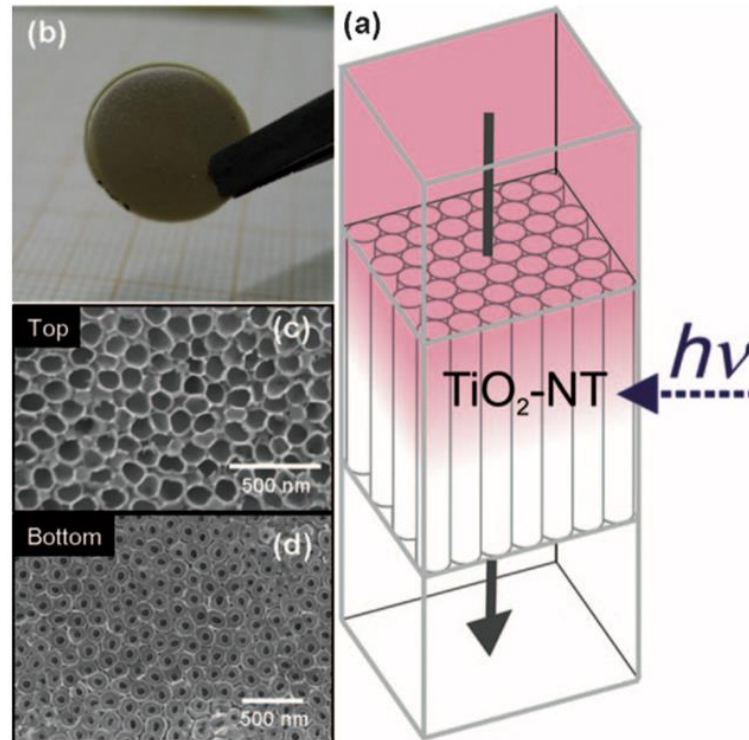


Figure 1.17:  $\text{TiO}_2$  nanotube membrane [1]. (a) flow through a membrane consisting of vertically oriented, both-side-open  $\text{TiO}_2$  nanotubes, (b) image of the membrane, (c) top view of SEM images of a  $\text{TiO}_2$  membrane, and (d) bottom view of SEM image of a  $\text{TiO}_2$  membrane.

### 1.5.2. Growth of quasi-one-dimension $\text{TiO}_2$ nanostructure

Rapid growth in one direction is crucial in obtaining Q1D  $\text{TiO}_2$  nanostructures during the evolution of nanocrystal [29]. Synthesis of Q1D  $\text{TiO}_2$  nanostructures have been achieved by various approaches including sol-gel methods, template-assisted methods, hydro/solvothermal approaches, and electrochemical means [29, 43]. In the previous section for synthesis of  $\text{TiO}_2$  nanomaterials, many examples were discussed for producing  $\text{TiO}_2$  Q1D nanomaterials. Hydrothermal method is a simple approach for scale-up without the use of any templates and surfactants [43]. The hydrothermal process is a soft-chemical technique as the reactions occur at relatively low temperatures. The morphology and crystal structure are controllable by manipulating the synthesis

parameters such as reaction temperature and alkaline concentration [37, 43]. This protocol has been employed in this study and is discussed in detail below.

### *1.5.3. Alkaline hydrothermal method and its parameters*

The hydrothermal synthesis protocol involves the treatment of a TiO<sub>2</sub> precursor with concentrated alkaline solutions sealed in a Teflon®-lined stainless steel autoclave at elevated temperatures (110-200°C) for 24-120 h [44]. Subsequently, the powders were washed with 0.1 M HCl, then distilled water for at least 5 times until pH was close to 7 and calcinated from 300-500°C to increase the crystallinity of the product.

The TiO<sub>2</sub> precursor can be hydrothermal treated with various hydrothermal solutions such as NaOH, KOH and Na<sub>2</sub>S. However, the precursor incompletely reacts with either KOH or Na<sub>2</sub>S even after mixing for 2 weeks. Therefore, the NaOH solution is preferred as a hydrothermal solution. Hydrothermal treatment times varies from 24 h to 120 h [37]. For potential application and scale-up in industry, short time synthesis is usually preferred. In this project, we only consider 24 or 48 h as the reaction time.

Hydrothermal temperature, TiO<sub>2</sub> to NaOH molar ratio significantly affects the product morphology, SSA, crystal structure, bandgap and photocatalytic activities [37]. Bavykin et. al. [37] demonstrated the average diameter of the nanotubes is dependent on the hydrothermal temperature and on the TiO<sub>2</sub> precursor/sodium hydroxide molar ratio. Increasing the temperatures from 120°C to 150°C caused an increase of the average nanotube diameter [37]. Subsequent increase in the temperatures resulted in a change in crystal form from nanotube to nanowire with an average diameter of 75 nm, a wide distribution in diameter and a length longer than 10 μm [37]. The increase of the TiO<sub>2</sub> to

NaOH molar ratio resulted in an average diameter increase of the nanotubes and a decrease in the SSA.

#### *1.5.4. Quasi-one-dimension $\text{TiO}_2$ nanostructure formation mechanisms for alkaline hydrothermal method*

The formation mechanisms for hollow structure (nanotube) and nonhollow structure (nanoribbons and nanowire) are different. The general accepted theory is that  $\text{TiO}_2$  nanotubes are formed through a 3-step process: 1. the liberation of individual  $\text{TiO}_6$  octahedron, 2. recrystallization of  $\text{TiO}_6$  octahedron into lamellar sheet (nanosheets) (Figure 1.18) and 3. scrolling of the lamellar sheet into nanotubes (Figure 1.19) [36, 49]. The onion-like morphologies concurrently produced with the nanotubes. The concentrated NaOH aqueous solution causes the liberation of individual  $\text{TiO}_6$  octahedron into the solution through the cleavage of Ti-O-Ti bonds of the  $\text{TiO}_2$  precursor. The lamellar sheet then formed via fusing the  $\text{TiO}_6$  octahedrons through the formation of hydroxyl bridges between the Ti atoms along both the [001] and [010] axes [49]. The driving force for lamellar sheet scrolling into nanotube is attributed to the reduction of the high surface energy of the nanosheet caused by the saturated dangling bonds on the nanosheets [36].

Non-hollow  $\text{TiO}_2$  Q1D nanostructure can be formed when the curving of lamellar sheets is inhibited [37, 50]. During hydrothermal process, NaOH reacts with  $\text{TiO}_2$  crystallites and free the  $\text{TiO}_6$  octahedron. The  $\text{TiO}_6$  octahedron assembles into lamellar sheets. The concentration of  $\text{Ti}^{4+}$  in the solution impacts the latter process. Wu et al.[51] proposed that the lamellar sheets curve around the b axis to form nanotubes when the  $\text{Ti}^{4+}$

concentration is less than  $3.3 \text{ molm}^{-3}$  (Figure 1.20). However, when  $\text{Ti}^{4+}$  concentration exceeds  $3.3 \text{ molm}^{-3}$ , curving along the b axis is inhibited. The inhibition of the curving allows the lamellar sheets structures to thicken along a and b axis and lengthen along c axis. Finally, lamellar sheets structures are growing to produce nanorods or nanowires.

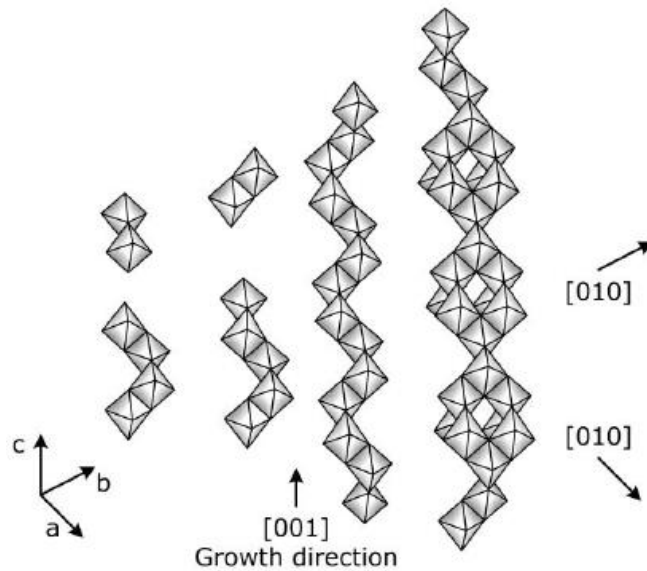


Figure 1.18: Lamellar sheet formation [49].

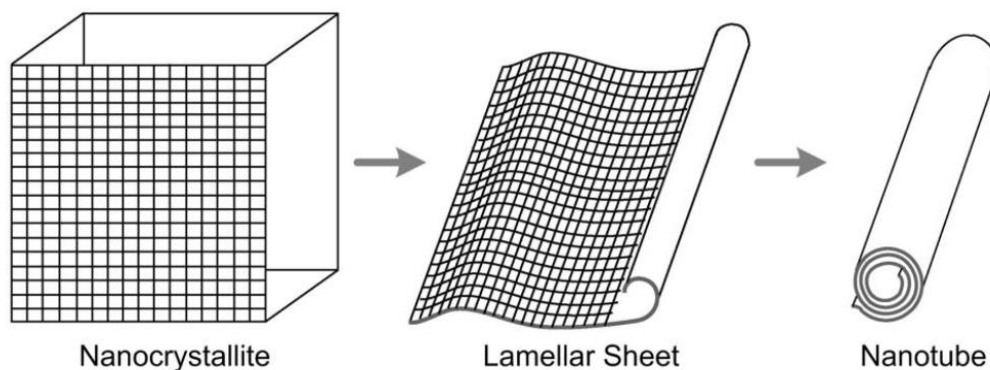


Figure 1.19: Proposed mechanism of formation of  $\text{TiO}_2$  nanotubes [36].

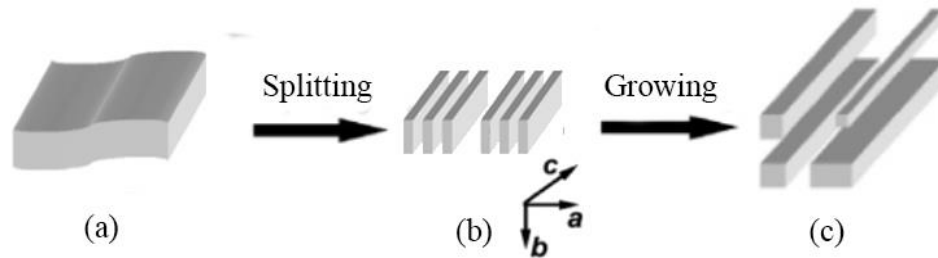


Figure 1.20: Nanowires formation process. (a).  $\text{TiO}_2$  precursor, (b). lamellar sheets and, (c) non-hollow  $\text{TiO}_2$  nanowires.

## 1.6. Plasma thin film and its applications

### 1.6.1. Advantages of $\text{TiO}_2$ thin film or coating

$\text{TiO}_2$  powders show many disadvantages such as the need for separation or filtration steps [4], the problematic use in continuous flow systems and the agglomeration of the particles. Thin film deposition techniques of  $\text{TiO}_2$  overcame these disadvantages (Figure 1.21). In such systems, the photocatalysts are immobilized on the walls of the reactor installed in a solar parabolic concentrator (Figure 1.22). Sol-gel, electrochemical deposition, magnetron sputtering, atomic layer deposition, chemical vapor deposition (CVD), physical vapor deposition (PVD) and plasma-assisted deposition processes [52] has been widely applied to prepare thin film [53].

The plasma-assisted deposition processes generally include two categories: Plasma enhanced chemical vapor deposition (PECVD) and magnetron sputter deposition. Plasma-assisted deposition processes have increased significant interests in industrial use mainly due to their following:

- (1). Low temperature deposition when compared to conventional PVD and CVD processes. For example, silicon nitride coating can be deposited by PECVD at  $300^\circ\text{C}$ . Whereas the conventional CVD process requires  $900^\circ\text{C}$  [52].

- (2). A broad range of experimental parameters (e.g. pressure, gas flow, excitation frequency, power) can be adjusted to optimize the films composition and microstructure [54].
- (3). High deposition rates ( $1 \text{ nm}\cdot\text{s}^{-1}$  -  $40 \text{ }\mu\text{m}\cdot\text{s}^{-1}$ ). The high deposition rate allows a reliable low-cost fabrication [54].
- (4). Plasma-assisted deposition allows uniform coating on different substrate shapes (flat, hemispherical, long fibers, cylindrical shapes, the interior of tubes, etc.) [54].
- (5). Plasma-assisted deposition films shows better mechanical properties (e.g. adhesion, stress compensation, abrasion, and wear resistance) when compared to their PVD counterparts [54].
- (6). Plasma-assisted deposition allowing doping to optimize the photocatalytic activities of the thin film [54].

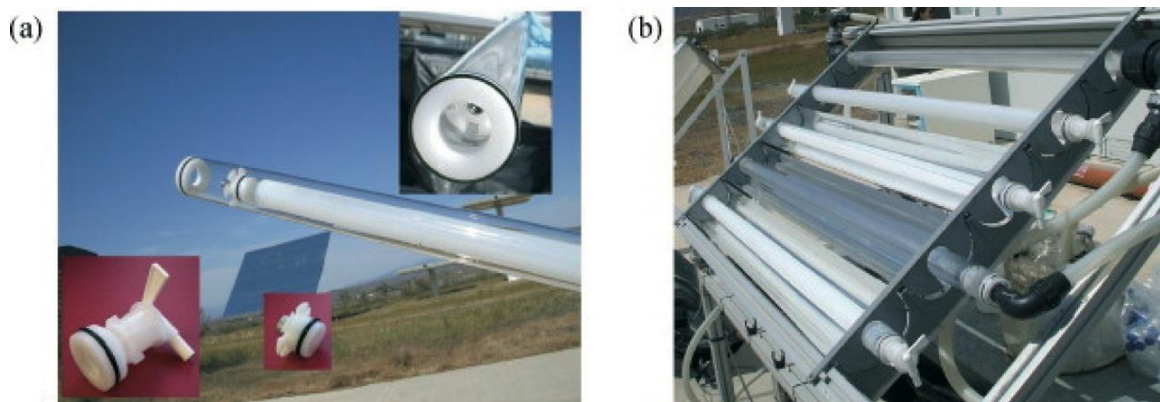


Figure 1.21: (a)  $\text{TiO}_2$  coated glass cylinders using sol-gel method and annealed at  $500^\circ\text{C}$ , and (b) a plug flow system for water purification [55].



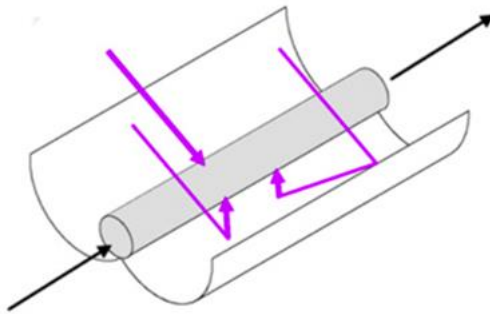


Figure 1.22: Design concept for solar parabolic concentrators [56].

### 1.6.2. Plasma enhanced chemical vapor deposition (PECVD)

PECVD is a method for film preparation using gas phase precursors activated in a glow discharge environment [54]. Indeed, by using a plasma which is a reactive medium, the CVD process which requires fragmentation of the precursor will take place at a much lower temperature because of the collisions with electrons produced in plasma.

The PECVD process can be conducted in both low pressure and atmospheric pressure. In particular, the atmospheric-pressure plasma processes (e.g. APPJ) (Figure 1.23) [57, 58] and dielectric barrier discharges (DBD) plasma [59] have become the most promising candidate systems to replace the thermal CVD or sol-gel processes which are employed for the deposition of functional coatings [57, 58]. This is due to the low cost, high deposition rate, low temperature, one step process, easy implementation, and in-line process capabilities. The careful selection of the plasma source, the titanium precursor, precursor carrier gas allows the deposition of well-adherent and dense  $\text{TiO}_2$  coatings with tunable properties at low temperature [60]. The low temperature condition allows a wide choice of substrates without damaging them (e.g. optical fiber glasses, nickel films and a carbon-polymer composites) [60, 61].

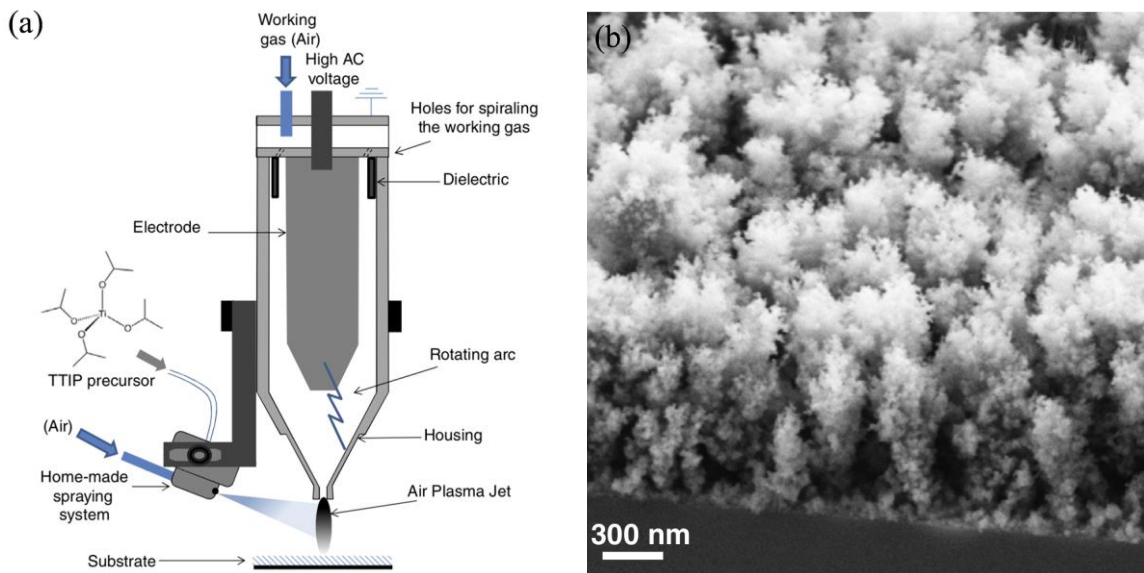


Figure 1.23: (a) Illustration of an open-air APPJ setups for depositing  $\text{TiO}_2$  coating on a flat substrate, and (b) SEM image of the cross section of atmospheric pressure plasma jet (APPJ)  $\text{TiO}_2$  coating with porous structure [58].

Fakhouri et. al. [58] used an open-air APPJ and TTIP as precursor (Figure 1.23a) to deposit photocatalytic  $\text{TiO}_2$  coatings with a high porosity and high SSA at a high deposition rate ( $20\text{-}40\ \mu\text{m}\cdot\text{s}^{-1}$ ). In an open-air APPJ system, the porosity and crystallinity of the  $\text{TiO}_2$  coating was significantly controlled by varying the deposition parameters such as the pulse frequency, working gas flow rate and the post annealing temperature [58]. A APPJ  $\text{TiO}_2$  coating deposited at 23 kHz and  $2400\ \text{L}\cdot\text{s}^{-1}$  was characterized with a high SSA porous structure (Figure 1.23b) and a significant enhancement of photocatalytic efficiency for the degradation of RhB when compared to an N-doped  $\text{TiO}_2$  coating which was deposited by reactive radio frequency (RF) magnetron sputtering [58, 62].

Nie et. al. [59] synthesized nanocrystalline anatase  $\text{TiO}_2$  using  $\text{TiCl}_4$  and  $\text{O}_2$  as precursors by an atmospheric cold DBD plasma (Figure 1.24a). The size of the  $\text{TiO}_2$  nanocrystal attained was 10-15 nm (Figure 1.24b) when plasma energy density was set at  $5.9\ \text{kJ}\cdot\text{L}^{-1}$ . They observed particles size decreased with increasing the plasma energy

density. The DBD plasma process is promising, due to a single-step, low cost, easy to control and simple equipment for the discharge.

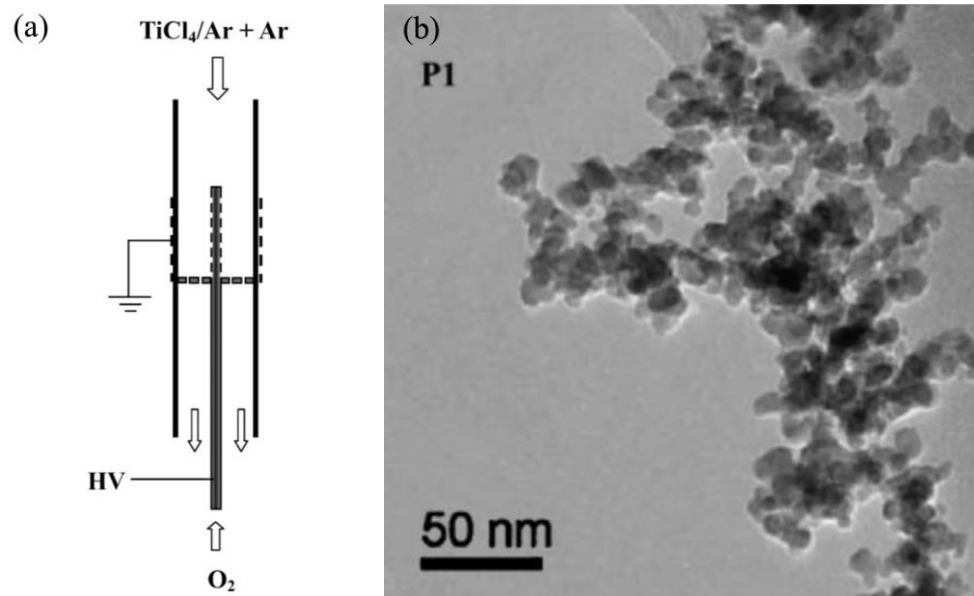


Figure 1.24: (a) The schematic of dielectric barrier discharges (DBD) reactor for synthesizing anatase  $\text{TiO}_2$ , and (b) transmission electron microscopy (TEM) image of DBD  $\text{TiO}_2$  nanocrystal [59].

### 1.6.3. Magnetron sputter deposition

Magnetron sputter deposition is utilized heavily in industry and which provides the possibility to deposit metals, but also oxides, nitrides, alloys etc. [52]. In the case of physical magnetron sputtering [52], the bombarding ions (i.e. argon ions at 500-1000 V) physically sputter the target metallic atoms which then are transferred to and deposited on a substrate. In the case of reactive magnetron sputtering, a reactive gas (i.e.  $\text{O}_2$  and  $\text{N}_2$ ) whose dissociation products chemically react with the target (Ti) was supplied in addition to the bombarding ions. For example, physical magnetron sputtering of a Ti target with argon as bombarding gas results in the formation of Ti thin film. If  $\text{O}_2$  gas is supplied as reactive gas,  $\text{TiO}_2$  thin film can be synthesized [62]. Fakhouri et. al. [62] synthesized N-

doped TiO<sub>2</sub> thin films on Si substrates (Figure 1.25) by reactive RF magnetron sputtering using a dual reactive gas mixture of N<sub>2</sub> and O<sub>2</sub>.

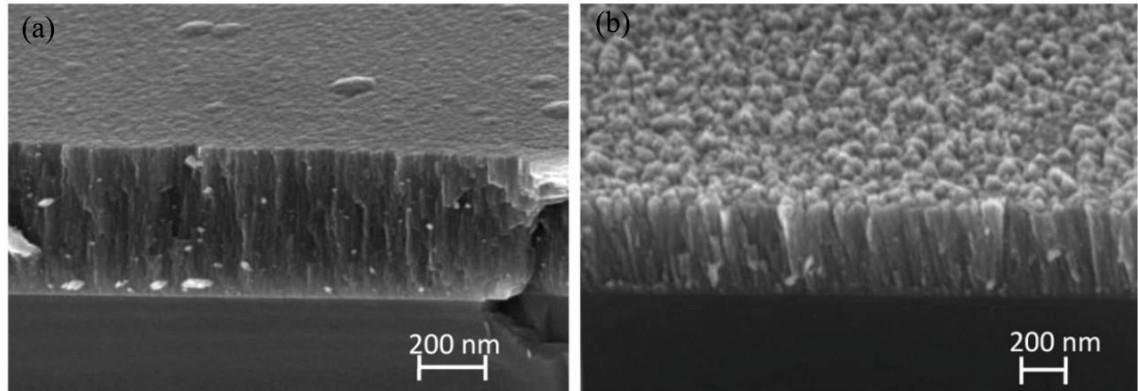


Figure 1.25: Scan electron microscope (SEM) images of TiO<sub>2</sub> coatings synthesized by reactive radio frequency magnetron sputtering at different pressures (a) 3 mTorr, and (b) 14 mTorr [62].

Note: 1 mTorr represents 0.13 Pa (units for pressure).

## 1.7. Modifications of TiO<sub>2</sub> nanomaterials

The majority of pure semiconductors are characterized with a low quantum yield, optical response, utilization rate of visible light. The low photocatalytic efficiency becomes a challenge in designing and developing photocatalysts for practical applications. Fortunately, the modification of pure semiconductors is a facile strategy to enhance their overall efficiency. The mechanism for the modification includes [4, 6, 56]: (1). modifying the crystal structure and morphology, (2). narrowing bandgap, (3). suppressing charge recombination, and (4). enhancing charge transfer.

### 1.7.1. Modifying TiO<sub>2</sub> crystal structure and morphology

The TiO<sub>2</sub> crystal structure and morphology can significantly affect the photocatalytic properties [63]. For pure phase, anatase phase is more active than the rutile phase. The

poor photocatalytic activities of rutile are due to the intrinsic defects in the rutile structure where the electrons are trapped. Meanwhile, the photocatalytic activity of biphasic anatase-rutile photocatalysts increases significantly when compared to any pure phases of TiO<sub>2</sub> [64]. When the two crystal phases are combined, electron migration across the anatase-rutile phase junction facilitates the separation of photogenerated holes and electrons with an increase in the photocatalytic activity (Figure 1.26) [64, 65].

The particle size and morphology strongly affect the dynamics of e<sup>-</sup>-h<sup>+</sup> recombination (e.g. bulk and surface recombination) [66-69]. Generally, bulk charge recombination is dominant in the well-crystallized large-size semiconductor particles [66]. A decrease in the particle size is closely correlated to a significant decrease in the bulk charge recombination, an increase of the SSA and improved photocatalytic activities [66]. However, according to Okura and Kaneko [70], increasing the SSA beyond a threshold value could lead to enhanced surface defects and surface charge recombination with a subsequent negative effect on photocatalysis. Therefore, a trade-off between bulk charge recombination and surface charge combination must be evaluated before designing a photocatalyst [5].

TiO<sub>2</sub> 2D nanostructures (nanosheets, nanoplates) and Q1D nanostructures (nanowire, nanotube, nanoribbon, nanorod) also facilitate the charge transfer inside the crystals to the surface and subsequently enhance the charge separation. Atomic scale thickness, smaller diameter and large surface area allow shorter charge transfer distance and time [5, 7, 71, 72]. Thus, the bulk charge recombination will be impeded to some extent.

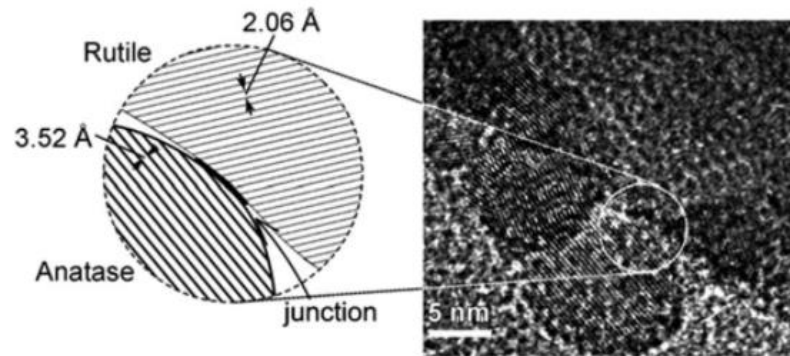


Figure 1.26: Anatase-rutile phase junction structure [73].

### 1.7.2. Metal and nonmetal doping

One of the effective solutions to enhance photocatalytic efficiency is to create an impurity in the forbidden band via metal and nonmetal doping [4, 6, 56]. Doping narrows the wide bandgap of  $\text{TiO}_2$  and expands  $\text{TiO}_2$  optical response into a visible-light region. Researchers have reported that metal doping (Sn, Fe, Mo, Ru, Os, Re, V and Rh ion doping) can significantly increase the photocatalytic activities under visible light [12, 64]. The mechanism of visible-light-driven photocatalysts using metal ion doping is illustrated in Figure 1.27 [63]. An appropriate doping element creates either a donor level above the original valence band or an acceptor level below the original conduction band [63]. These new levels narrow the original band to expand the photocatalysts optical response into the visible light region [63]. In addition, the doping ions serve as a recombination inhibitor by trapping electrons or holes. This in return promotes the charge separation required for the photocatalytic reaction [63].

Unlike metal-ion dopants, nonmetal-ion dopants shift the valence band edge upward without forming any donor or acceptor levels in the forbidden band. The up-shifting of valence band edge results in a narrowed band gap (Figure 1.28) [63]. Various nonmetal

ions (e.g. C, N, S) were used to dope  $\text{TiO}_2$  [63, 74]. To date, the N doping is most efficient and most widely investigated [75, 76]. In N-doped  $\text{TiO}_2$ , the substitution of N for O leads to the mixing of the 2p states of N with the 2p of O [63]. The narrowing bandgap resulted in N-doped  $\text{TiO}_2$  having much higher photocatalytic activities in the visible irradiation when compared to pure  $\text{TiO}_2$ .

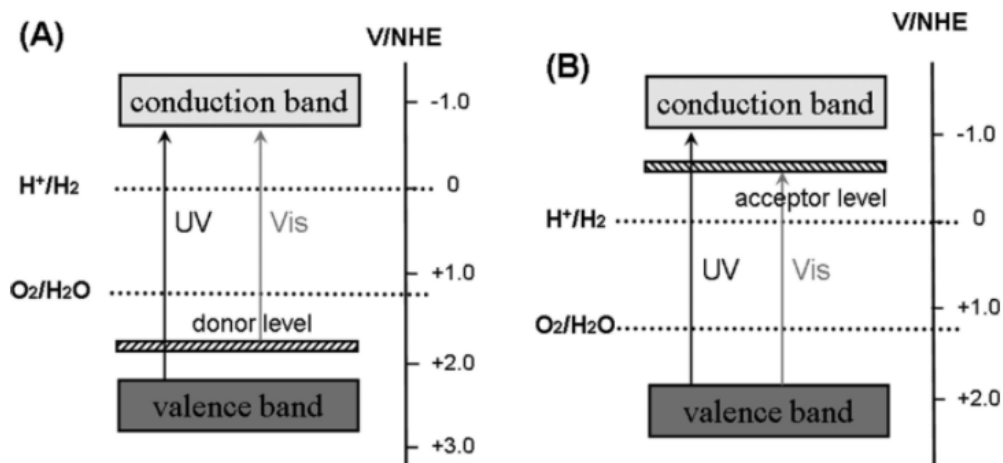


Figure 1.27: Donor level and acceptor level in forbidden band by doping metal ion [63].

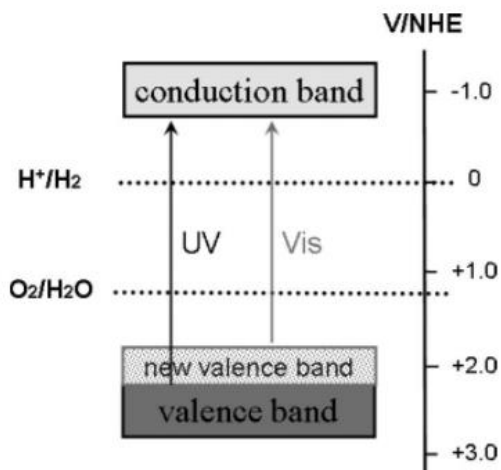


Figure 1.28: Valence band shifting by doping nonmetal ions [63].

### 1.7.3. Depositing noble metals

Deposition of noble metals (Ag, Pt, Au and Pd) on the surface of TiO<sub>2</sub> nanostructure can significantly improve the photocatalytic activities [19, 77, 78]. Noble metals serve as electron trap to delay the recombination of the e<sup>-</sup>-h<sup>+</sup> pair [20, 79]. Figure 1.29 illustrates the electron trapping properties at the Schottky barrier between the metal particle and a semiconductor surface [20, 80]. The photoexcited electrons migrate to the metal particles and are trapped in metal particles due to the Schottky barrier, whereas the holes in TiO<sub>2</sub> is free to transfer to semiconductor surface and react with reactants [20, 80]. The Pt-TiO<sub>2</sub> system is significantly efficient to evolve H<sub>2</sub> gas, due to electron trapping and catalytic effect of Pt [20, 81].

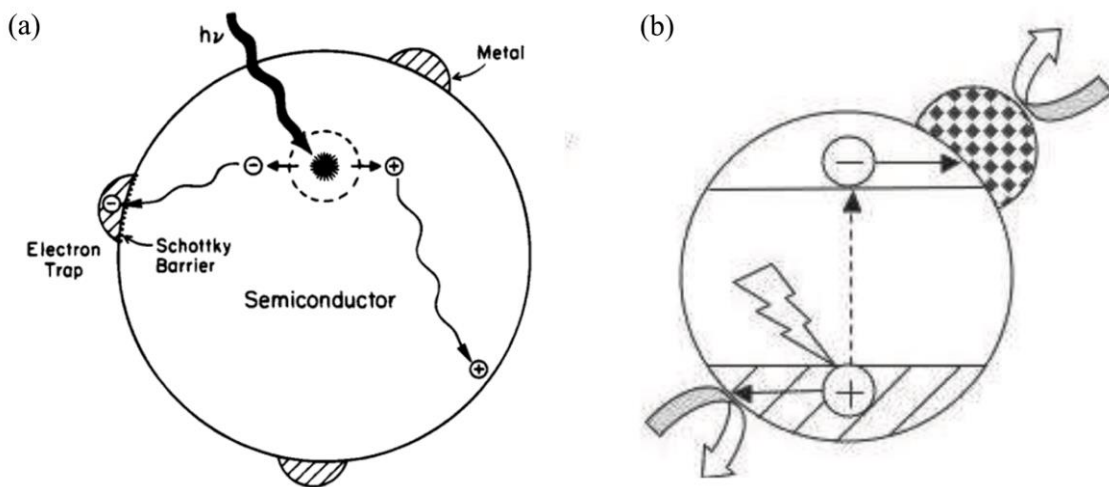


Figure 1.29: Metal modified semiconductor [20].

### 1.7.4. Semiconductor coupling

The semiconductor coupling is another effective method to improve photocatalytic activity due to an enhanced charge separation by forming a heterojunction structure [20, 82]. Coupling TiO<sub>2</sub> with CdS having a narrow bandgap of 2.5 eV improves its



photocatalytic activity in the visible light region [15]. The charge separation is shown in Figure 1.30. The photogenerated electrons in CdS are transferred to TiO<sub>2</sub> conductive band, whereas holes remain in CdS valence band. This charge transfer facilitates the charge separation and retards the charge recombination. In addition to CdS, other semiconductors such as CdSe, Fe<sub>2</sub>O<sub>3</sub> possessing a smaller bandgap and coupled with a proper band edge position are characterized with a more negative potential to reduce reactants or a more positive potential to oxidize reactants (Figure 1.31). These semiconductors can couple with TiO<sub>2</sub> and subsequently improve the photocatalytic efficiency [83, 84].

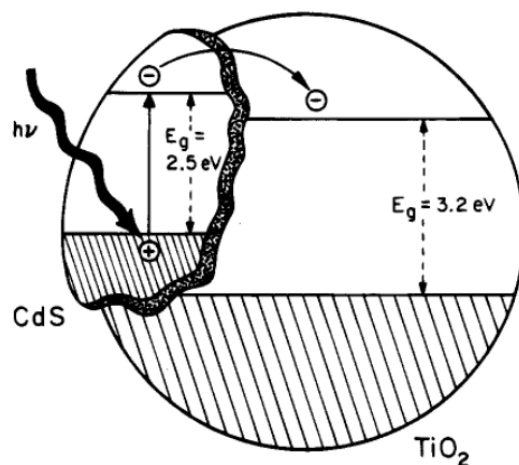


Figure 1.30: Illustrative diagrams of the electron transfer in the CdS/TiO<sub>2</sub> system [20].

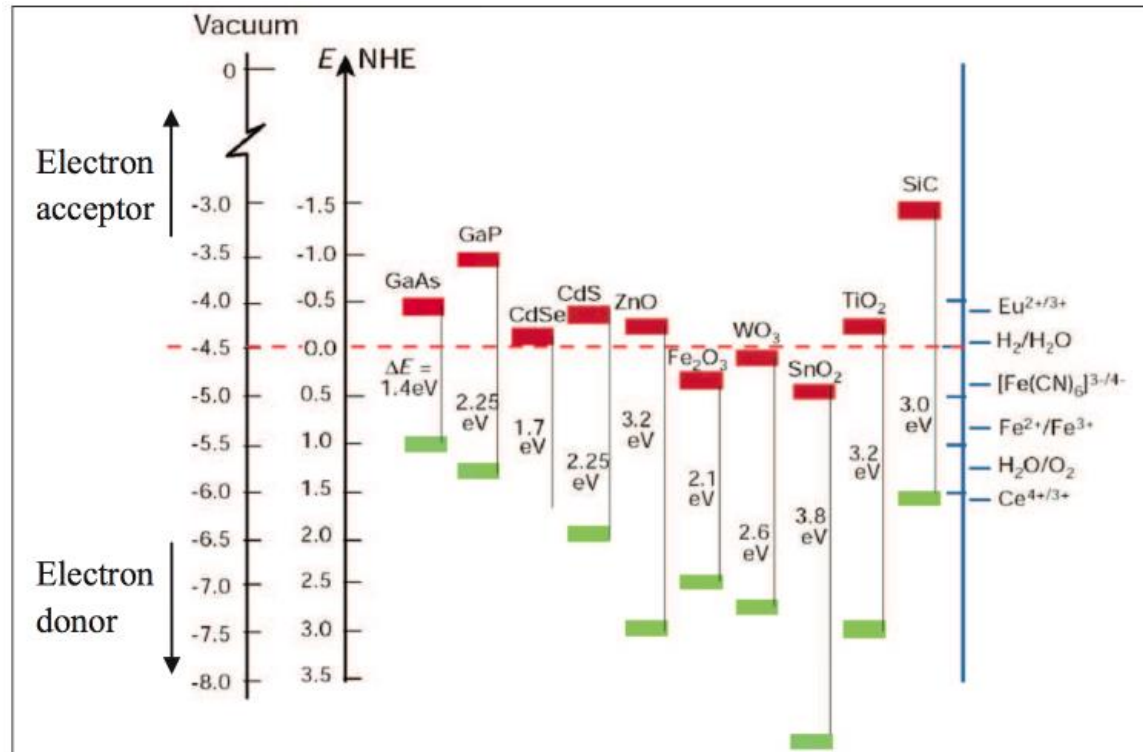


Figure 1.31: Bandgap edge position for different semiconductors in aqueous solution at pH = 1 [85].

#### 1.7.5. Enhancing $\text{TiO}_2$ with carbon materials

Incorporating  $\text{TiO}_2$  into carbon nanomaterials significantly increases the activity of  $\text{TiO}_2$  for the photocatalysis of organic pollutants such as phenol and methyl orange [86]. In recent years, increasing interest in using graphene (Figure 1.32), a 2D carbon atoms sheet, is primarily due to its unique physical and chemical properties. Graphene is characterized with a high charge carrier mobility ( $15000 \text{ cm}^2 \cdot \text{V}^{-1} \cdot \text{s}^{-1}$ ), high SSA (up to  $2630 \text{ m}^2 \cdot \text{g}^{-1}$ ), high thermal conductivity (approximately  $5000 \text{ W} \cdot \text{m}^{-1} \cdot \text{°C}^{-1}$ ), and a tunable bandgap by chemical doping [87-89]. These excellent properties are leading reasons why graphene modified  $\text{TiO}_2$  photocatalysts can find promising applications for air and water purification [16, 90, 91]. A general morphology of graphene modified  $\text{TiO}_2$  nanotube composites is shown in Figure 1.33 [47]. The  $\text{TiO}_2$  nanotubes disperse on the graphene

sheets maintains a direct contact with the graphene sheets. The graphene sheets functions by improving the TiO<sub>2</sub> photocatalytic activities through the following three aspects [16, 92-94]:

1. Enhancing photocatalysts adsorptivity to adsorb pollutant molecules. Graphene has indeed a high SSA and adsorbs organic pollutant molecules efficiently through the  $\pi$ - $\pi$  conjugation [47]. For example, the phenol has the same aromatic compounds as graphene. The  $\pi$ - $\pi$  conjugation between phenol and graphene facilitates the adsorption of chemicals such as phenol on graphene.

2. Extending light absorption. Graphene renders a red shift in the photo-responding range and improves the utilization of light [16, 92-94].

3. Suppressing the charge recombination [16, 92-94]. Graphene serves as an electron scavenger that receives electrons from the TiO<sub>2</sub> and provides a fast electron transfer route due to its high charge carrier mobility [16, 92-94]. The photogenerated  $e^-$  in TiO<sub>2</sub> are transferred to graphene nanosheet, whereas  $h^+$  remain in TiO<sub>2</sub> [16, 92-94]. The electrons on graphene are transferred to electron acceptors and the holes remain in TiO<sub>2</sub> are transferred to electron donors. In this case, an effective charge separation and transportation are obtained.

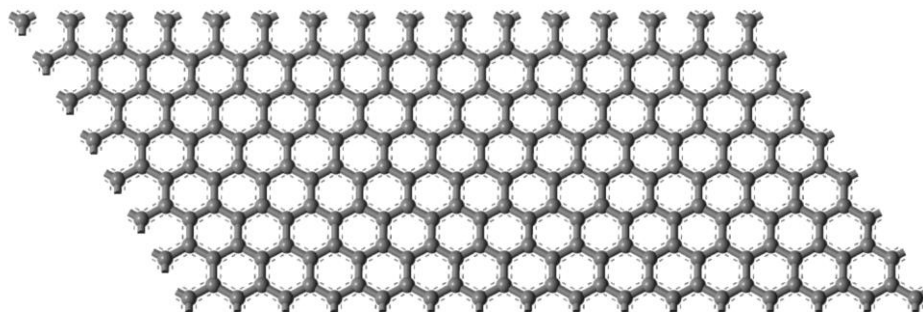


Figure 1.32: Graphene nanosheet composed of one atomic carbon layer.

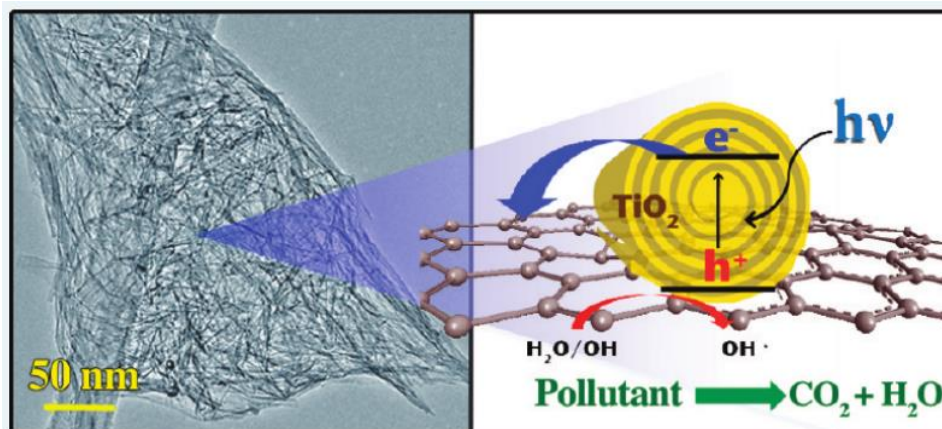


Figure 1.33: TEM image of graphene modified TiO<sub>2</sub> nanotubes (left) and its schematic figure for mechanism of charge transfer and separation (right) [47].

### 1.8. Summary of the research objectives

In Chapter 1, the first objective in this thesis is to provide an overview of the principle of photocatalysis, TiO<sub>2</sub> morphologies and crystallographic structure, phase structures, synthesis methods and modification of TiO<sub>2</sub> for improving photocatalytic activities in the UV light as well as visible light.

In Chapter 2, the second objective is to provide an overview of the chemicals, instruments for characterization and the GO and Q1D TiO<sub>2</sub> synthesis process.

The subsequent chapters are organized in manuscript format. In Chapter 3, the first part of third objective is to evaluate the impact of the hydrothermal reaction conditions on the phase structure, crystal size, specific surface area (SSA) and bandgap. The second part of the third objective is to optimize the reaction conditions for maximizing and minimizing bandgap using a 3-factor 3-level Box Behnken design (BBD).

In Chapter 4, the first part of fourth objective is to optimize hydrothermal conditions for synthesizing Q1D TiO<sub>2</sub> with the maximum photodegradation of aqueous hazardous pollutants using the BBD. The aqueous hazardous pollutants examined in this chapter

will include rhodamine b (RhB), methyl orange (MO), methylene blue (MB) and phenol. Next, the second part of fourth objective is to optimize hydrothermal conditions for synthesizing Q1D TiO<sub>2</sub> with the maximum photocatalytic H<sub>2</sub> production rate using BBD models.

In Chapter 5, the first part of the fifth objective is to optimize the RGO atomic O/C ratio for synthesizing RGO-TiO<sub>2</sub> nanorods (TNRs) composites photocatalyst (designated as GT) with the maximum photodegradation of aqueous hazardous pollutants under UV light condition. Next, based on the optimum RGO atomic O/C ratio obtained, second part of fifth objective is to synthesize a hierarchical three-dimensional (3D) Ag nanoparticle-RGO-TiO<sub>2</sub> nanorods (TNRs) (designated as Ag-GT) thin films photocatalyst with optimum Ag content for degrading aqueous hazardous pollutants under visible irradiation.

In Chapter 6, the first part of sixth objective is to examine micrometer thick Ag nanoparticles (NPs) modified TiO<sub>2</sub> (Ag-TiO<sub>2</sub>) coatings synthesized using a single and facile non-equilibrium atmospheric pressure plasma jet (APPJ) with different concentrations of Ag NPs (0-0.7 wt%). The second part of sixth objective is to examine the effect of the Ag concentration (0-0.7 wt%), air gas flow rate and the discharge pulse frequency on the coating phase structure, crystal size and photocatalytic activity. The third part of sixth objective is to investigate photocatalytic activity efficiency by examining the photodegradation of rhodamine b (RhB) and trace pharmaceutical compounds, namely carbamazepine (CBZ), venlafaxine (VLX) and bezafibrate (BZF), using a solar simulator.

**1.9. References**

- [1] P. Roy, S. Berger, P. Schmuki, TiO<sub>2</sub> nanotubes: synthesis and applications, *Angew. Chem. Int. Ed.* 50 (2011) 2904-2939.
- [2] A. Fujishima, K. Honda, Electrochemical photolysis of water at a semiconductor electrode, *Nature* 238 (1972) 37-38.
- [3] K. Hashimoto, H. Irie, A. Fujishima, TiO<sub>2</sub> photocatalysis: a historical overview and future prospects, *Jpn. J. Appl. Phys.* 44 (2005) 8269-8285.
- [4] F. Han, V.S.R. Kambala, M. Srinivasan, D. Rajarathnam, R. Naidu, Tailored titanium dioxide photocatalysts for the degradation of organic dyes in wastewater treatment: a review, *Appl. Catal., A Applied* 359 (2009) 25-40.
- [5] X. Chen, S.S. Mao, Titanium dioxide nanomaterials: Synthesis, properties, modifications, and applications, *Chem. Rev.* 107 (2007) 2891-2959.
- [6] C.P. Sajjan, S. Wageh, A.A. Al Ghamdi, J. Yu, S. Cao, TiO<sub>2</sub> nanosheets with exposed {001} facets for photocatalytic applications, *Nano Res.* 9 (2016) 3-27.
- [7] N. Roy, Y. Sohn, D. Pradhan, Synergy of low-energy {101} and high-energy {001} TiO<sub>2</sub> crystal facets for enhanced photocatalysis, *ACS Nano* 7 (2013) 2532-2540.
- [8] Z. Zhao, H. Zhao, Z. Sun, H. Zhao, P. Du, M. Zheng, J. Zhao, H. Fan, J. Zhao, H. Fan, Phase control of hierarchically structured mesoporous anatase TiO<sub>2</sub> microspheres covered with {001} facets, *J. Mater. Chem.* 22 (2012) 21965.
- [9] S. Yang, B.X. Yang, L. Wu, Y.H. Li, P. Liu, H. Zhao, Y.Y. Yu, X.Q. Gong, H.G. Yang, Titania single crystals with a curved surface, *Nat. Commun.* 5 (2014) 5355.

- [10] V.V. Pokropivny, V.V. Skorokhod, Classification of nanostructures by dimensionality and concept of surface forms engineering in nanomaterial science, *Mater. Sci. Eng. C* 27 (2007) 990-993.
- [11] D.L. Morgan, Alkaline hydrothermal treatment of titanate nanostructures, in: E.R. Waclawik, E. Waclawik (Eds.), Queensland University of Technology, 2010.
- [12] S. George, S. Pokhrel, Z. Ji, B.L. Henderson, T. Xia, L. Li, J.I. Zink, A.E. Nel, L. Mädler, Role of Fe doping in tuning the band gap of TiO<sub>2</sub> for the photo-oxidation-induced cytotoxicity paradigm, *J. Am. Chem. Soc.* 133 (2011) 11270-11278.
- [13] M. Batzill, E.H. Morales, U. Diebold, Influence of nitrogen doping on the defect formation and surface properties of TiO<sub>2</sub> rutile and anatase, *Phys. Rev. Lett.* 96 (2006) 026103-026104.
- [14] S. Linic, P. Christopher, D.B. Ingram, Plasmonic-metal nanostructures for efficient conversion of solar to chemical energy, *Nat. Mater.* 10 (2011) 911-921.
- [15] N. Qin, Y. Liu, W. Wu, L. Shen, X. Chen, Z. Li, L. Wu, One-dimensional CdS/TiO<sub>2</sub> nanofiber composites as efficient visible-light-driven photocatalysts for selective organic transformation: synthesis, characterization, and performance, *Langmuir* 31 (2015) 1203-1209.
- [16] X. Li, J. Yu, S. Wageh, A.A. Al Ghamdi, J. Xie, Graphene in photocatalysis: a review, *Small* 12 (2016) 6640-6696.
- [17] C. Chen, W. Cai, M. Long, B. Zhou, Y. Wu, D. Wu, Y. Feng, Synthesis of visible-light responsive graphene oxide/TiO<sub>2</sub> composites with p/n heterojunction, *ACS Nano* 4 (2010) 6425-6432.

- [18] A.A. Ismail, D.W. Bahnemann, Photochemical splitting of water for hydrogen production by photocatalysis: A review, *Sol. Energy Mater. Sol. Cells* 128 (2014) 85-101.
- [19] M. Murdoch, G.I.N. Waterhouse, M.A. Nadeem, J.B. Metson, M.A. Keane, R.F. Howe, J. Llorca, H. Idriss, The effect of gold loading and particle size on photocatalytic hydrogen production from ethanol over Au/TiO<sub>2</sub> nanoparticles, *Nat. Chem.* 3 (2011) 489-492.
- [20] A.L. Linsebigler, G. Lu, J.T. Yates, Photocatalysis on TiO<sub>2</sub> surfaces: Principles, mechanisms, and selected results, *Chem. Rev.* 95 (1995) 735-758.
- [21] N.F. Mott, Conduction in non-crystalline materials, *Philos. Mag.* 19 (1969) 835-852.
- [22] M. Pelaez, N.T. Nolan, S.C. Pillai, M.K. Seery, P. Falaras, A.G. Kontos, P.S.M. Dunlop, J.W.J. Hamilton, J.A. Byrne, K. O'Shea, M.H. Entezari, D.D. Dionysiou, A review on the visible light active titanium dioxide photocatalysts for environmental applications, *Appl. Catal., B Environ.* 125 (2012) 331-349.
- [23] R.E. Olsen, Synthesis, characterization, and application of high surface area, mesoporous, stabilized anatase TiO<sub>2</sub> catalyst supports, in, Brigham Young University, 2013.
- [24] V. Swamy, J.D. Gale, L.S. Dubrovinsky, Atomistic simulation of the crystal structures and bulk moduli of TiO<sub>2</sub> polymorphs, *J. Phys. Chem. Solids* 62 (2001) 887-895.
- [25] H.Y. Zhu, Y. Lan, X.P. Gao, S.P. Ringer, Z.F. Zheng, D.Y. Song, J.C. Zhao, Phase transition between nanostructures of titanate and titanium dioxides via simple wet-chemical reactions., *J. Am. Chem. Soc.* 127 (2005) 6730-6736.



- [26] V.B. Damodaran, D. Bhatnagar, V. Leszczak, K.C. Popat, Titania nanostructures: a biomedical perspective, *RSC Adv.* 5 (2015) 37149-37171.
- [27] K.I. Kugel, D.I. Khomskii, The Jahn-Teller effect and magnetism: transition metal compounds, *Sov. Phys. Uspekhi* 25 (1982) 231.
- [28] D. Reyes-Coronado, G. Rodriguez-Gattorno, M.E. Espinosa-Pesqueira, C. Cab, R. de Coss, G. Oskam, Phase-pure TiO<sub>2</sub> nanoparticles: anatase, brookite and rutile, *Nanotechnology* 19 (2008) 145605.
- [29] D. Yang, H. Liu, Z. Zheng, Y. Yuan, J.-c. Zhao, E.R. Waclawik, X. Ke, H. Zhu, An efficient photocatalyst structure: TiO<sub>2</sub>(B) nanofibers with a shell of anatase nanocrystals, *J. Am. Chem. Soc.* 131 (2009) 17885-17893.
- [30] X. Wang, Z. Li, J. Shi, Y. Yu, One-dimensional titanium dioxide nanomaterials: Nanowires, nanorods, and nanobelts, *Chem. Rev.* 114 (2014) 9346-9384.
- [31] A.R. Armstrong, G. Armstrong, J. Canales, P.G. Bruce, TiO<sub>2</sub>-B nanowires, *Angew. Chem.* 116 (2004) 2336-2338.
- [32] H.-L. Kuo, C.-Y. Kuo, C.-H. Liu, J.-H. Chao, C.-H. Lin, A highly active bi-crystalline photocatalyst consisting of TiO<sub>2</sub> (B) nanotube and anatase particle for producing H<sub>2</sub> gas from neat ethanol, *Catal. Lett.* 113 (2007) 7.
- [33] S.M. Liu, L.M. Gan, L.H. Liu, W.D. Zhang, H.C. Zeng, Synthesis of single-crystalline TiO<sub>2</sub> nanotubes, *Chem. Mater.* 14 (2002) 1391.
- [34] J. Zhu, J. Wang, F. Lv, S. Xiao, C. Nuckolls, H. Li, Synthesis and self-assembly of photonic materials from nanocrystalline titania sheets, *J. Am. Chem. Soc.* 135 (2013) 4719.

- [35] K. Byrappa, K. Byrappa, T. Adschiri, T. Adschiri, Hydrothermal technology for nanotechnology, *Prog. Cryst. Growth Charact. Mater.* 53 (2007) 117-166.
- [36] Y.Q. Wang, G.Q. Hu, X.F. Duan, H.L. Sun, Q.K. Xue, Microstructure and formation mechanism of titanium dioxide nanotubes, *Chem. Phys. Lett.* 365 (2002) 427-431.
- [37] D.V. Bavykin, V.N. Parmon, A.A. Lapkin, F.C. Walsh, The effect of hydrothermal conditions on the mesoporous structure of TiO<sub>2</sub> nanotubes, *J. Mater. Chem.* 14 (2004) 3370-3378.
- [38] C.-S. Kim, B.K. Moon, J.-H. Park, B.-C. Choi, H.-J. Seo, Solvothermal synthesis of nanocrystalline TiO<sub>2</sub> in toluene with surfactant, *J. Cryst. Growth* 257 (2003) 309-315.
- [39] J.-M. Wu, H.C. Shih, W.-T. Wu, Electron field emission from single crystalline TiO<sub>2</sub> nanowires prepared by thermal evaporation, *Chem. Phys. Lett.* 413 (2005) 490-494.
- [40] J.-J. Wu, C.-C. Yu, Aligned TiO<sub>2</sub> nanorods and nanowalls, *J. Phys. Chem. B* 108 (2004) 3377-3379.
- [41] S. Liu, K. Huang, Straightforward fabrication of highly ordered TiO<sub>2</sub> nanowire arrays in AAM on aluminum substrate, *Sol. Energy Mater. Sol. Cells* 85 (2005).
- [42] H. Lee, T.-H. Park, D.-J. Jang, Preparation of anatase TiO<sub>2</sub> nanotube arrays dominated by highly reactive facets via anodization for high photocatalytic performances, *New J. Chem.* 40 (2016) 8737-8744.
- [43] Y. Tang, Y. Zhang, J. Deng, J. Wei, H.L. Tam, B.K. Chandran, Z. Dong, Z. Chen, X. Chen, Mechanical force-driven growth of elongated bending TiO<sub>2</sub>-based nanotubular materials for ultrafast rechargeable lithium ion batteries, *Adv. Mater.* 26 (2014) 6111-6118.

- [44] T. Kasuga, M. Hiramatsu, A. Hoson, T. Sekino, K. Niihara, Formation of titanium oxide nanotube, *Langmuir* 14 (1998) 3160-3163.
- [45] J.-M. Wu, S. Hayakawa, K. Tsuru, A. Osaka, Porous titania films prepared from interactions of titanium with hydrogen peroxide solution, *Scr. Mater.* 46 (2002) 101-106.
- [46] P.D. Cozzoli, A. Kornowski, H. Weller, Low-temperature synthesis of soluble and processable organic-capped anatase TiO<sub>2</sub> nanorods, *J. Am. Chem. Soc.* 125 (2003) 14539-14548.
- [47] S.D. Perera, R.G. Mariano, K. Vu, N. Nour, O. Seitz, Y. Chabal, K.J. Balkus Jr., Hydrothermal synthesis of graphene-TiO<sub>2</sub> nanotube composites with enhanced photocatalytic activity, *ACS Catal.* 2 (2012) 949-956.
- [48] S.P. Albu, A. Ghicov, J.M. Macak, R. Hahn, P. Schmuki, Self-organized, free-standing TiO<sub>2</sub> nanotube membrane for flow-through photocatalytic applications, *Nano Lett.* 7 (2007) 1286-1289.
- [49] A. Chemseddine, T. Moritz, Nanostructuring titania: control over nanocrystal structure, size, shape, and organization, *Eur. J. Inorg. Chem.* 1999 (1999) 235-245.
- [50] J. Huang, Y. Cao, Q. Huang, H. He, Y. Liu, W. Guo, M. Hong, High-temperature formation of titanate nanotubes and the transformation mechanism of nanotubes into nanowires, *Cryst. Growth Des.* 9 (2009) 3632-3637.
- [51] D. Wu, J. Liu, X. Zhao, A. Li, Y. Chen, N. Ming, Sequence of events for the formation of titanate nanotubes, nanofibers, nanowires, and nanobelts, *Chem. Mater.* 18 (2006) 547-553.
- [52] M.A. Lieberman, A.J. Lichtenberg, Principles of plasma discharges and materials processing, John Wiley & Sons, 2005.

- [53] A. Essakhi, A. Löfberg, P. Supiot, B. Mutel, S. Paul, V. Le Courtois, E. Bordes-Richard, Coating metallic foams and structured reactors by VO<sub>x</sub>/TiO<sub>2</sub> oxidation catalyst: Application of RPECVD, Elsevier, 2010.
- [54] L. Martinu, D. Poitras, Plasma deposition of optical films and coatings: a review, *J. Vac. Sci. Technol. A* 18 (2000) 2619-2645.
- [55] D.A. Keane, K.G. McGuigan, P.F. Ibáñez, M.I. Polo-López, J.A. Byrne, P.S.M. Dunlop, K. O'Shea, D.D. Dionysiou, S.C. Pillai, Solar photocatalysis for water disinfection: Materials and reactor design, *Catal. Sci. Technol.* 4 (2014) 1211-1216.
- [56] S. Malato, P. Fernández-Ibáñez, M.I. Maldonado, J. Blanco, W. Gernjak, Decontamination and disinfection of water by solar photocatalysis: Recent overview and trends, *Catal. Today* 147 (2009) 1-59.
- [57] D. Ben Salem, O. Carton, H. Fakhouri, J. Pulpytel, F. Arefi-Khonsari, Deposition of water stable plasma polymerized acrylic acid/MBA organic coatings by atmospheric pressure air plasma jet, *Plasma Processes Polym.* 11 (2014) 269-278.
- [58] H. Fakhouri, D.B. Salem, O. Carton, J. Pulpytel, F. Arefi-Khonsari, Highly efficient photocatalytic TiO<sub>2</sub> coatings deposited by open air atmospheric pressure plasma jet with aerosolized TTIP precursor, *J. Phys. D: Appl. Phys.* 47 (2014) 265301-265311.
- [59] L.-H. Nie, C. Shi, Y. Xu, Q.-H. Wu, A.-M. Zhu, Atmospheric cold plasmas for synthesizing nanocrystalline anatase TiO<sub>2</sub> using dielectric barrier discharges, *Plasma Processes Polym.* 4 (2007) 574-582.
- [60] K. Baba, S. Bulou, P. Choquet, N.D. Boscher, Photocatalytic anatase TiO<sub>2</sub> thin films on polymer optical fiber using atmospheric-pressure plasma, *ACS Appl. Mater. Interfaces* 9 (2017) 13733-13741.

- [61] M. Robotti, S. Dosta, M. Gardon, I.G. Cano, J.M. Guilemany, M. Kourasi, B. Mellor, R. Wills, Enhancing the performance of common electrode materials by means of atmospheric plasma spray coatings, *J. Energy Storage* 5 (2016) 127-133.
- [62] H. Fakhouri, J. Pulpytel, W. Smith, A. Zolfaghari, H.R. Mortaheb, F. Meshkini, R. Jafari, E. Sutter, F. Arefi-Khonsari, Control of the visible and UV light water splitting and photocatalysis of nitrogen doped TiO<sub>2</sub> thin films deposited by reactive magnetron sputtering, *Appl. Catal., B Environ.* 144 (2014) 12-21.
- [63] X. Chen, S. Shen, L. Guo, S.S. Mao, Semiconductor-based photocatalytic hydrogen generation, *Chem. Rev.* 110 (2010) 6503-6570.
- [64] G. Tian, H. Fu, L. Jing, B. Xin, K. Pan, Preparation and characterization of stable biphasic TiO<sub>2</sub> photocatalyst with high crystallinity, large surface area, and enhanced photoactivity, *J. Phys. Chem. C* 112 (2008) 3083-3089.
- [65] D.C. Hurum, A.G. Agrios, K.A. Gray, T. Rajh, M.C. Thurnauer, Explaining the enhanced photocatalytic activity of degussa p25 mixed-phase TiO<sub>2</sub> using EPR, *J. Phys. Chem. B* 107 (2003) 4545-4549.
- [66] Z. Zhang, C.-C. Wang, R. Zakaria, J.Y. Ying, Role of particle size in nanocrystalline TiO<sub>2</sub>-based photocatalysts, *J. Phys. Chem. B* 102 (1998) 10871-10878.
- [67] M. Kong, Y. Li, X. Chen, T. Tian, P. Fang, F. Zheng, X. Zhao, Tuning the relative concentration ratio of bulk defects to surface defects in TiO<sub>2</sub> nanocrystals leads to high photocatalytic efficiency, *J. Am. Chem. Soc.* 133 (2011) 16414-16417.
- [68] W. Choi, A. Termin, M.R. Hoffmann, The role of metal ion dopants in quantum-sized TiO<sub>2</sub>: correlation between photoreactivity and charge carrier recombination dynamics, *J. Phys. Chem.* 98 (1994) 13669-13679.

- [69] N. Serpone, D. Lawless, R. Khairutdinov, E. Pelizzetti, Subnanosecond relaxation dynamics in TiO<sub>2</sub> colloidal sols (particle sizes  $R_p = 1.0\text{-}13.4$  nm). Relevance to heterogeneous photocatalysis, *J. Phys. Chem.* 99 (1995) 16655-16661.
- [70] I. Okura, M. Kaneko, *Photocatalysis science and technology*, Springer and Kodansha, Japan, 2002.
- [71] T. Tachikawa, S. Yamashita, T. Majima, Evidence for crystal-face-dependent TiO<sub>2</sub> photocatalysis from single-molecule imaging and kinetic analysis, *J. Am. Chem. Soc.* 133 (2011) 7197-7204.
- [72] J.L. Giocondi, P.A. Salvador, G.S. Rohrer, The origin of photochemical anisotropy in SrTiO<sub>3</sub>, *Top. Catal.* 44 (2007) 529-533.
- [73] J. Zhang, Q. Xu, Z. Feng, M. Li, C. Li, Importance of the relationship between surface phases and photocatalytic activity of TiO<sub>2</sub>, *Angew. Chem. Int. Ed.* 47 (2008) 1766-1769.
- [74] A. Zaleska, Doped-TiO<sub>2</sub>: a review, *Recent Pat. Eng.* 2 (2008) 157-164.
- [75] R. Asahi, T. Morikawa, T. Ohwaki, K. Aoki, Y. Taga, Visible-light photocatalysis in nitrogen-doped titanium oxides, *Science* 293 (2001) 269-271.
- [76] G. Modugno, Efficient photochemical water splitting by a chemically modified n-TiO<sub>2</sub>, *Science* 297 (2002) 2240-2243.
- [77] V. Subramanian, E.E. Wolf, P.V. Kamat, Catalysis with TiO<sub>2</sub>/gold level nanocomposites. effect of metal particle size on the Fermi equilibration, *J. Am. Chem. Soc.* 126 (2004) 4943-4950.

- [78] Y.-C. Liang, C.-C. Wang, C.-C. Kei, Y.-C. Hsueh, W.-H. Cho, T.-P. Perng, Photocatalysis of Ag-loaded TiO<sub>2</sub> nanotube arrays formed by atomic layer deposition, *J. Phys. Chem. C* 115 (2011) 9498-9502.
- [79] D.W. Bahnemann, M. Hilgendorff, R. Memming, Charge carrier dynamics at TiO<sub>2</sub> particles: reactivity of free and trapped holes, *J. Phys. Chem. B* 101 (1997) 4265-4275.
- [80] P. Chinnamuthu, J.C. Dhar, A. Mondal, A. Bhattacharyya, N.K. Singh, Ultraviolet detection using TiO<sub>2</sub> nanowire array with Ag schottky contact, *J. Phys. D: Appl. Phys.* 45 (2012) 135102-135106.
- [81] J. Yu, L. Qi, M. Jaroniec, Hydrogen production by photocatalytic water splitting over Pt/TiO<sub>2</sub> nanosheets with exposed (001) facets, *J. Phys. Chem. C* 114 (2010) 13118-13125.
- [82] R. Dagherir, P. Drogui, D. Robert, Modified TiO<sub>2</sub> for environmental photocatalytic applications: a review, *Ind. Eng. Chem. Res.* 52 (2013) 3581-3599.
- [83] P. Zhou, J. Yu, M. Jaroniec, All-solid-state Z-scheme photocatalytic systems, *Adv. Mater.* 26 (2014) 4920-4935.
- [84] K. Iwashina, A. Iwase, Y.H. Ng, R. Amal, A. Kudo, Z-schematic water splitting into H<sub>2</sub> and O<sub>2</sub> using metal sulfide as a hydrogen-evolving photocatalyst and reduced graphene oxide as a solid-state electron mediator, *J. Am. Chem. Soc.* 137 (2015) 604-607.
- [85] M. Gratzel, Photoelectrochemical cells, *Nature* 414 (2001) 338-344.
- [86] A. Di Paola, E. Garcia-Lopez, G. Marci, L. Palmisano, A survey of photocatalytic materials for environmental remediation, *J. Hazard. Mater.* 211-212 (2012) 3-29.

- [87] K.S. Novoselov, V.I.F. ko, L. Colombo, P.R. Gellert, M.G. Schwab, K. Kim, A roadmap for graphene, *Nature* 490 (2012) 192-200.
- [88] Z. Chen, W. Ren, L. Gao, B. Liu, S. Pei, H.M. Cheng, Three-dimensional flexible and conductive interconnected graphene networks grown by chemical vapour deposition, *Nat. Mater.* 10 (2011) 424-428.
- [89] Y. Zhu, S. Murali, M.D. Stoller, K.J. Ganesh, W. Cai, P.J. Ferreira, A. Pirkle, R.M. Wallace, K.A. Cychoz, M. Thommes, D. Su, E.A. Stach, R.S. Ruoff, Carbon-based supercapacitors produced by activation of graphene, *Science* 332 (2011) 1537-1541.
- [90] J. Yu, S. Wang, J. Low, W. Xiao, Enhanced photocatalytic performance of direct Z-scheme g-C<sub>3</sub>N<sub>4</sub>-TiO<sub>2</sub> photocatalysts for the decomposition of formaldehyde in air, *Phys. Chem. Chem. Phys.* 15 (2013) 16883-16890.
- [91] T. Lv, L. Pan, X. Liu, T. Lu, G. Zhu, Z. Sun, C.Q. Sun, One-step synthesis of CdS-TiO<sub>2</sub>-chemically reduced graphene oxide composites via microwave-assisted reaction for visible-light photocatalytic degradation of methyl orange, *Catal. Sci. Technol.* 2 (2012) 754-758.
- [92] H. Zhang, X. Lv, Y. Li, Y. Wang, J. Li, P25-graphene composite as a high performance photocatalyst, *ACS Nano* 4 (2010) 380-386.
- [93] Y.-K. Kim, D.-H. Min, UV protection of reduced graphene oxide films by TiO<sub>2</sub> nanoparticle incorporation, *Nanoscale* 5 (2013) 3638-3635.
- [94] Z. Fan, J. Yan, L. Zhi, Q. Zhang, T. Wei, J. Feng, M. Zhang, W. Qian, F. Wei, A three-dimensional carbon nanotube/graphene sandwich and its application as electrode in supercapacitors, *Adv. Mater.* 22 (2010) 3723-3728.



## MATERIALS AND EXPERIMENTAL METHODS

### 2.1. Introduction

In this chapter, the chemicals, instruments used to characterize the photocatalysts and the synthesis processes used to synthesize some materials which will be used in whole thesis are detailed in this chapter. This chapter includes three sections:

- a) Chemicals
- b) Analytical and characterization instruments
- c) GO and Q1D TiO<sub>2</sub> synthesis processes

Note: The chemicals, instruments and the detailed process in this chapter are referenced in subsequent chapters.

### 2.2. Chemicals

Commercial TiO<sub>2</sub> nanoparticles (P25) were purchased from Degussa (Evonik Industries, Germany). Graphite flakes (325 mesh, 99.9995%) and KMnO<sub>4</sub> (99.0%) were purchased from Alfa Aesar (MA, United States). H<sub>3</sub>PO<sub>4</sub> (85%), H<sub>2</sub>SO<sub>4</sub> (98%), H<sub>2</sub>O<sub>2</sub> (30%), ethanol (95%), NaOH (97%) and HCl (37 wt%) were purchased from Fischer Scientific (Ontario, Canada). Hydrazine hydrate (50-60%), dialysis bags (proteins M.W. cut-off > 12,000 Da), methyl orange (MO; 85%), phenol (99.5%), and methylene blue (MB; 99.5%) were purchased from Sigma-Aldrich (Ontario, Canada). TTIP (TiO<sub>4</sub>C<sub>12</sub>H<sub>28</sub>, 97% purity), phosphate buffer (Na<sub>2</sub>HPO<sub>4</sub>/NaH<sub>2</sub>PO<sub>4</sub>, acetone (99.9% purity), ethyl alcohol (95% purity), RhB (97% purity), venlafaxine (VLX) (purity >99%), bezafibrate (BZF) (purity >99%) and carbamazepine (CBZ) (purity >99%) were purchased from Sigma

Aldrich (Saint-Quentin-Fallavier, Vendor location – France). Ag NPs (99.5% purity) were procured from Sigma Aldrich (Saint-Quentin-Fallavier-Vendor location – France, add city). Nitrogen (99.995% purity) and air (99.5% purity) were purchased from Air Liquide (Paris, France). Si (100) wafers were purchased from Siegert Wafer (Aachen, Germany).

### **2.3. Characterization instruments and processes**

#### *2.3.1. Electron microscopy*

The morphology and nanostructure were investigated using high-resolution transmission electron microscopy (HRTEM) (JEOL 3010, Japan) which allows for direct imaging the atomic structure [1] of the sample. The sample was prepared by ultrasonically dispersing the photocatalyst in ethanol. Next, 5 uL of sample solution was deposited on a carbon film and dried at a temperature of 25°C. The HRTEM was configured to operate at 300 kV with a high resolution of 0.17 nm.

Field emission scanning electron microscope (FESEM) (Thermo Fisher Scientific, MA., United States) and Energy dispersive X-ray (EDX) (Thermo Fisher Scientific, MA., United States) analysis were employed to examine the surface morphology and sample elemental composition. The photocatalyst sample was dispersed ultrasonically in ethanol and a small amount of the solution (20 uL) was deposited and dried on aluminum film at room temperature. The instrument scanning of the surface of materials using a focused electron beam allows the researcher to gather information related to the sample's surface topography and composition (EDX).

### 2.3.2. Raman spectra

Structural fingerprinting of a sample was examined using an Alpha300 RA argon laser Raman spectrometer (WITec, Germany) equipped with a 532-nm laser. The Raman spectra with a high signal/noise ratio was recorded from 100 to 3000  $\text{cm}^{-1}$  with the accumulation times set as 40 s and integration time as 0.5 s. In this study, the phase of  $\text{TiO}_2$  sample and the degree of order of reduced graphene oxide (RGO) samples were analyzed using Raman spectroscopy.

### 2.3.3. X-ray diffraction (XRD) analysis

The phase structure and elemental composition were determined using XRD analysis. XRD was performed with an X-ray diffractometer (Rigaku, MI, United States) equipped with a  $\text{Cu K}\alpha$  radiation source (0.154 nm). The XRD patterns were collected using step scans with a step of  $0.01^\circ 2\theta$  and a count time of 0.2 s per step between  $10^\circ$  and  $80^\circ 2\theta$ .

### 2.3.4. Diffuse reflectance UV-visible spectroscopy (DRS) and dye concentration

The sample optical response in the UV and visible region was analyzed using Diffuse reflectance UV-visible spectroscopy (DRS). The DRS was obtained using a Cary 300 UV-visible (Agilent Technologies, United States). Next, the DRS was converted to into an absorption spectra using the Kubelka Munk function [2]. The absorption spectra were used to determine the bandgap for each sample.

### 2.3.5. X-ray photoelectron spectroscopy (XPS)

XPS measurements were performed using a VG Scientific (Thermo Electron Corporation, MA, United States) ESCALAB 210 electron spectrometer using Mg K $\alpha$  radiation ( $h\nu = 1253.6$  eV, 300 W) under a vacuum of  $2 \times 10^{-8}$  Pa. High resolution C 1s spectra were recorded at approximately 284.7 eV and deconvoluted into different chemical functional group [3, 4]. Error of electron binding energies of chemical groups was less than 0.2 eV.

### 2.3.6. Brunauer–Emmett–Teller (BET) and specific surface area (SSA)

Nitrogen adsorption–desorption isotherms were determined at 77K using a Micromeritics ASAP 2020 Brunauer–Emmett–Teller (BET) analyzer (Micromeritics Instrument Corp. GA, United States). The instrument was used to determine the SSA.

### 2.3.7. High performance liquid chromatograph (HPLC)

The residual phenol concentration was determined using a high-performance liquid chromatograph (HPLC) (Dionex Ultimate 3000, Sunnyvale, CA) equipped with a UV–visible photodiode array detector set at 274 nm and configured with an Acclaim C18 - 3  $\mu\text{m}$  - 2.1 mm (ID)  $\times$  100 mm (length) column (Dionex, Sunnyvale, CA). The analysis was conducted at 45°C with an acetonitrile-water mixture (1:4) eluent (Fisher Scientific, Ottawa, ON) at a flow rate set at 0.4 mL min $^{-1}$  as described in an earlier study [5]. The phenol detection limit was 5.0  $\mu\text{g}\cdot\text{L}^{-1}$ .

### 2.3.8. Gas chromatograph (GC)

Hydrogen concentration was determined using a gas chromatograph (GC) (Varian CP-3800) installed with a 2m long x 2mm I.D. Carbon Shin Column (Alltech, Deerfield, IL) and a thermal conductivity detector (TCD) at 200°C. The oven and injector temperatures were set at 200°C and 150°C, respectively. N<sub>2</sub> gas was used as a carrier gas at a flowrate of 15 mL·min<sup>-1</sup>.

### 2.3.9. Photoelectrochemical measurements

The charge carrier's transportation and separation were measured using photoelectrochemical measurements which were conducted using a CHI 704D (CHI Instrument inc, Texas) with a standard three-electrode cell. One side of cell is constructed from quartz for UV-light transmission. Platinum wire was used as the counter electrode and a saturated calomel electrode (SCE) was used as a reference electrode. For the working electrode, 0.25 g photocatalyst solution was mixed with 0.06 g polyethylene glycol (PEG, molecular weight 20 000) and 1 mL deionized water to form a slurry. The slurry afterward was coated onto a 2 cm x 1.2 cm F-doped SnO<sub>2</sub>-coated (FTO) glass electrode using a doctor blade method [6, 7]. The electrode was annealing at 450°C for 30 minutes. The measurements were performed in a 1 M Na<sub>2</sub>SO<sub>4</sub> aqueous solution as electrolyte. A 300-nm monochromatic UV light with an average intensity of 9 mW·cm<sup>-2</sup> was used as the source. In addition, a visible light with a KenKo L41 UV filter (≥410 nm) with an average intensity of 2 mW·cm<sup>-2</sup> was used as visible light source.

## 2.3.10. Photocatalytic reactor

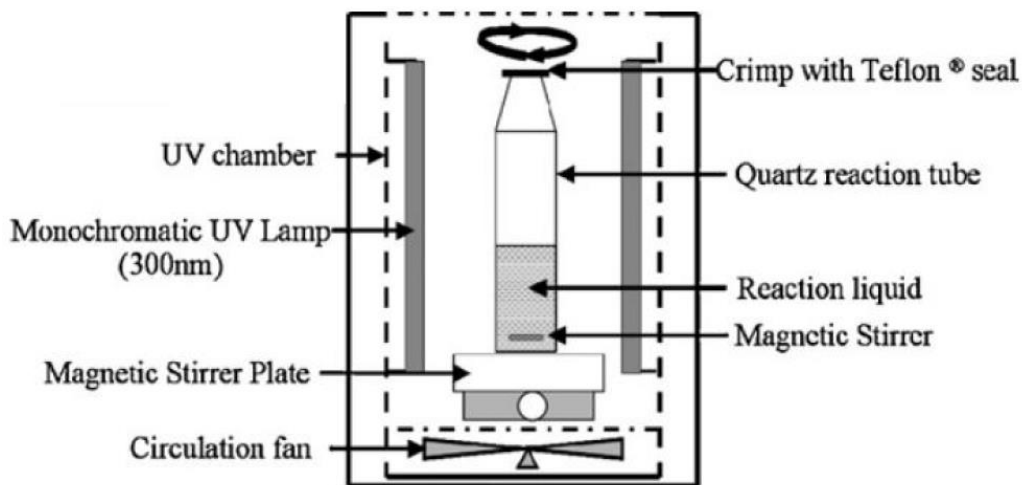


Figure 2.1: Schematic diagram of photocatalytic reactor [5].

The photocatalytic experiments were conducted using quartz tubes (25 mm ID  $\times$  250 mm length) (Technical Glass Products Inc., Painesville, OH) sealed with aluminum crimp caps and Teflon® lined rubber septa. The sealed photocatalytic reaction tubes were placed in a modified Rayonet RPR-100 UV photocatalytic chamber (Figure 2.1) (Southern New England Ultraviolet Co., Branford, CT). The chamber was installed with sixteen monochromatic (300 nm) UV lamps (Southern New England Ultraviolet Co., Branford, CT) on the outer perimeter of the reactor with a rotating inner carousel as described in a previous study by Ray *et al.* [5]. The quartz tubes in triplicates were placed on the rotating carousel and the reaction mixture was magnetically stirred to maintain the photocatalyst in suspension, minimize particle agglomeration and mass transfer limitation. The average intensity of irradiance emitted from the lamps was 9  $\text{mW}\cdot\text{cm}^{-2}$ . The light intensity was measured using a light intensity meter equipped with a

300 nm UV sensor (UV Process Supply, Chicago, IL). The reactor temperature was maintained at  $37 \pm 2^\circ\text{C}$ .

### *2.3.11. Optical emission spectroscopy of plasma*

Plasma emission were sampled using an optical fiber located downstream at 10 mm from the nozzle exit of the torch and connected to an optical emission spectrometer (OES) (Ocean Optics USB2000 Pro, FL, United States) configured with a  $300 \text{ gmm}^{-1}$  grating in the UV-visible spectrum range and a  $25 \mu\text{m}$  slit. The OES spectra were recorded in the range of 200 nm to 1100 nm to identify the excited chemical species in the plasma with and without the presence of the titanium isopropoxide (TTIP) precursor including Ag NPs.

### *2.3.12. Thin film photocatalytic activity test*

The photocatalytic activity was conducted using two methods based on the chemicals under consideration. In the first test, RhB (initial concentration  $5 \text{ mg}\cdot\text{L}^{-1}$ ) degradation was examined at room temperature.

The  $\text{TiO}_2$  thin film samples, deposited on  $9 \times 25 \text{ mm}^2$  glass substrates were placed in a UV grade reactor cell with a diameter of 35 mm and a height of 20 mm facing the irradiation light source (Figure 2.2). The solution (10 ml) was circulated at a flow rate of  $0.5 \text{ mL}\cdot\text{s}^{-1}$  using a peristaltic pump (Masterflex, model# 7553-75, Gelsenkirchen, Germany) connected to the radiated photocatalytic cell. The RhB solution was stirred for 60 min. under dark conditions to ensure adsorption/desorption equilibrium of the chemicals onto the catalyst. A 125 W (Philips) white light source was used to irradiate the samples. During the RhB photocatalytic degradation experiments, samples were

removed, and the absorbance was monitored using a spectrophotometer (Maya 2000+, Ocean Optics, FL, United States) set at 554 nm.

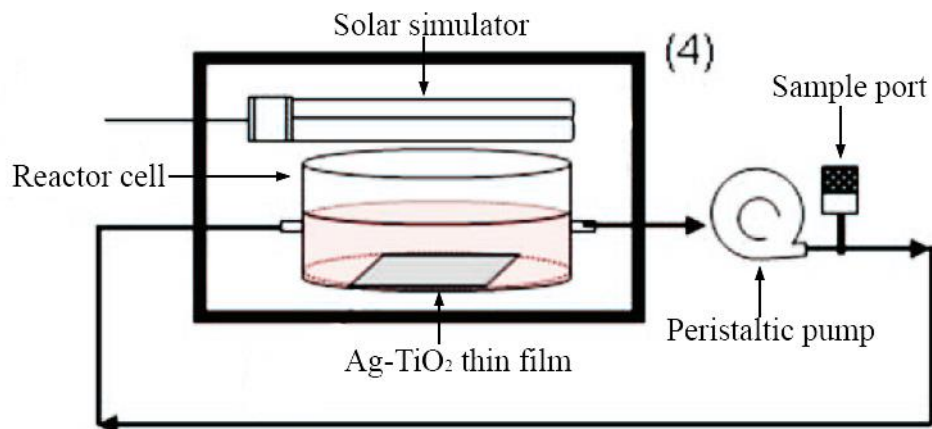


Figure 2.2: Photodegradation of organic wastewater contaminants (OWCs) using solar simulator.

In the second procedure, the degradation of VLX, BZF and CBZ was monitored at room temperature. All three compounds are persistent in the environment due to resistance to conventional treatment technologies [8-10]. The coated slide samples were immersed in a 90 mm x 50 mm Pyrex glass dish containing 30 mL of DI water spiked with a stock solution ( $1 \text{ mg}\cdot\text{L}^{-1}$ ) containing the three pharmaceutical compounds with each at an initial concentration of  $100 \text{ }\mu\text{g}\cdot\text{L}^{-1}$ . The three pharmaceutical compounds standards (purity > 99%) were purchased from Sigma-Aldrich, and used as received stock solution. Experiments were performed at neutral pH=7 using a 1 mM PBS saline. The pharmaceutical compounds solution was stirred for 60 min under dark conditions to ensure adsorption/desorption equilibrium of the chemicals onto the catalyst. Next, the equilibrated solution was irradiated using a solar simulator for 60 min. During stirring the reaction mixture, 0.3 mL samples were removed periodically for further analysis.



Uniform and continuous irradiation for the photocatalytic reaction was achieved using a 150 W ozone-free Xe arc lamp solar simulator (Sciencetech Inc, SS150W, Canada) with a sharp cut off at 256 nm and an output spectrum equivalent to natural sunlight at 48.2° latitudes at sea level. The incident irradiance, as measured by a spectroradiometer (International Light, Model ILT 900R, MA, USA), was approximately  $500 \text{ W}\cdot\text{m}^{-2}$  integrated in the wavelength range of 280-950 nm. Pharmaceutical compounds were monitored and quantified by high performance liquid chromatography (HPLC) (1100 series HPLC, Agilent, Les Ulis, France) configured with a ACE-RP phenyl column (2.1 mm×250 mm) (Aberdeen, Scotland) coupled to a mass spectrometer (Q-ToF MS, Waters Premier, MA, USA) following a method reported by Zucker et al. [11]. The analysis was conducted at 45°C with a water-methanol (1:9) mixture eluent. The eluent was adjusted to pH 3 using formic acid. The HPLC flowrate was set at  $0.5 \text{ mL}\cdot\text{min}^{-1}$ . The mass spectrometer was set in positive mode with a detection limit of  $0.1 \mu\text{g}\cdot\text{L}^{-1}$ .

## **2.4. Graphene oxide (GO) and quasi-one-dimension (Q1D) TiO<sub>2</sub> synthesis**

### *2.4.1. Synthesis of graphene oxide (GO)*

GO was synthesized using an improved Hummer's method [12]. Briefly, a 9:1 mixture of concentrated H<sub>2</sub>SO<sub>4</sub>/H<sub>3</sub>PO<sub>4</sub> (360:40 ml), graphite flakes (3.0 g) and KMnO<sub>4</sub> (18.0 g) were mixed using a magnetic stirrer in a 1 L beaker for 1h at 20°C. Next, the black mixture was heated at 50°C for 12 h. The reaction mixture cooled to room temperature and subsequently mixed with ice flakes (500 mL). 5 mL of 30% H<sub>2</sub>O<sub>2</sub> was added to the dark brown mixture and the mixture was converted into a golden yellow color. The golden yellow solid was collected after 2-h centrifugation (5000 rpm) using Sorvall ST 16 centrifuge (Thermo Scientific, On.). Then, the solid was washed with

deionized water (200 mL), followed by washing with 30% HCl (200 mL) and subsequently with 6 washes of ethanol (200 mL). After each washing, the mixture was centrifuged (5000 rpm for 2 h) and the supernatant decanted. Finally, the yellow solid was dialyzed against deionized water using dialysis bags to remove any residual metal ion. The solid in the dialysis bag was collected and vacuum-dried at 60°C to produce GO powder.

#### *2.4.2. Hydrothermal synthesis*

The hydrothermal synthesis liquor containing NaOH and the precursor as TiO<sub>2</sub> NPs (commercial P25, a mixture of anatase (75%) and rutile (25%)) were prepared based on the fact that NaOH readily reacts with the TiO<sub>2</sub> precursor and the commercial availability of P25 TiO<sub>2</sub> NPs.

The Q1D TiO<sub>2</sub> was synthesized using hydrothermal method [13-15]. To prepare Q1D TiO<sub>2</sub> photocatalyst, 2.5 g TiO<sub>2</sub> P25 nanoparticles was homogeneously mixed with 70 ml of 5 M NaOH using a magnetic stirrer for 30 min. Then, the mixture was placed in a 100-mL Teflon® capped bottle. The Teflon® bottle was placed into a stainless-steel bottle then capped, heated at 120°C for 48 h, and subsequently cooled to room temperature. The resulting paste was centrifuged and rinsed with 0.1 M HCl. The white paste was washed several times with deionized water to attain a pH = 7 and calcined at 400°C for 2 h to produce the Q1D TiO<sub>2</sub>.

### 2.4.3. Plasma process used for deposition

Ag-TiO<sub>2</sub> coating were prepared by introducing TTIP into an open-air atmospheric pressure plasma jet (APPJ) (Plasmatreater AS400, Plasmatreat GmbH, Steinhagen, Germany) by means of an 'in-house' constructed spraying system (Figure 2.3). High deposition rates (10-20  $\mu\text{m}\cdot\text{s}^{-1}$ ) were achieved by spraying a liquid precursor into the plasma torch. The 100 nm Ag NPs concentration was varied from 0 to 0.7 wt.% and dispersed in the liquid precursor. The plasma torch was created using dry compressed air at flow rates set from 1800 to 3000  $\text{L}\cdot\text{h}^{-1}$ . The plasma power was monitored by controlling the pulse frequency of the DC discharge at three level (18 , 21, and 25 kHz) [16]. The detailed parameters were described in work by Fakhouri *et al.* [16]. After configuring the plasma, the TTIP precursor was sprayed into the plasma jet, near the output of the torch, using dry nitrogen, as a carrier gas, at a flow rate of 12  $\text{L}\cdot\text{h}^{-1}$ . The Ag-TiO<sub>2</sub> thin film coatings were formed onto the substrate surface which was placed 10 mm away from the plasma nozzle as described in work by Fakhouri *et al.* [16].

The APPJ is powered using a uni-polar square-wave pulse-width modulation transistor amplifier circuit. The circuit provides electrical power between fully on and fully off at a drive switching frequency from 18 to 25 kHz. The alternating current (AC) pulse voltage was set at 5 kV. The detailed parameter was described in work by Dowling *et al.* [17].

Deposition of the TiO<sub>2</sub> and Ag-TiO<sub>2</sub> thin films were performed on two different substrates. Microscope glass slides were used for optical and photocatalytic measurements while Si (100) wafers were used for structural and analytical

measurements such as X-ray diffraction (XRD) and field emission scanning electron microscopy (FESEM).

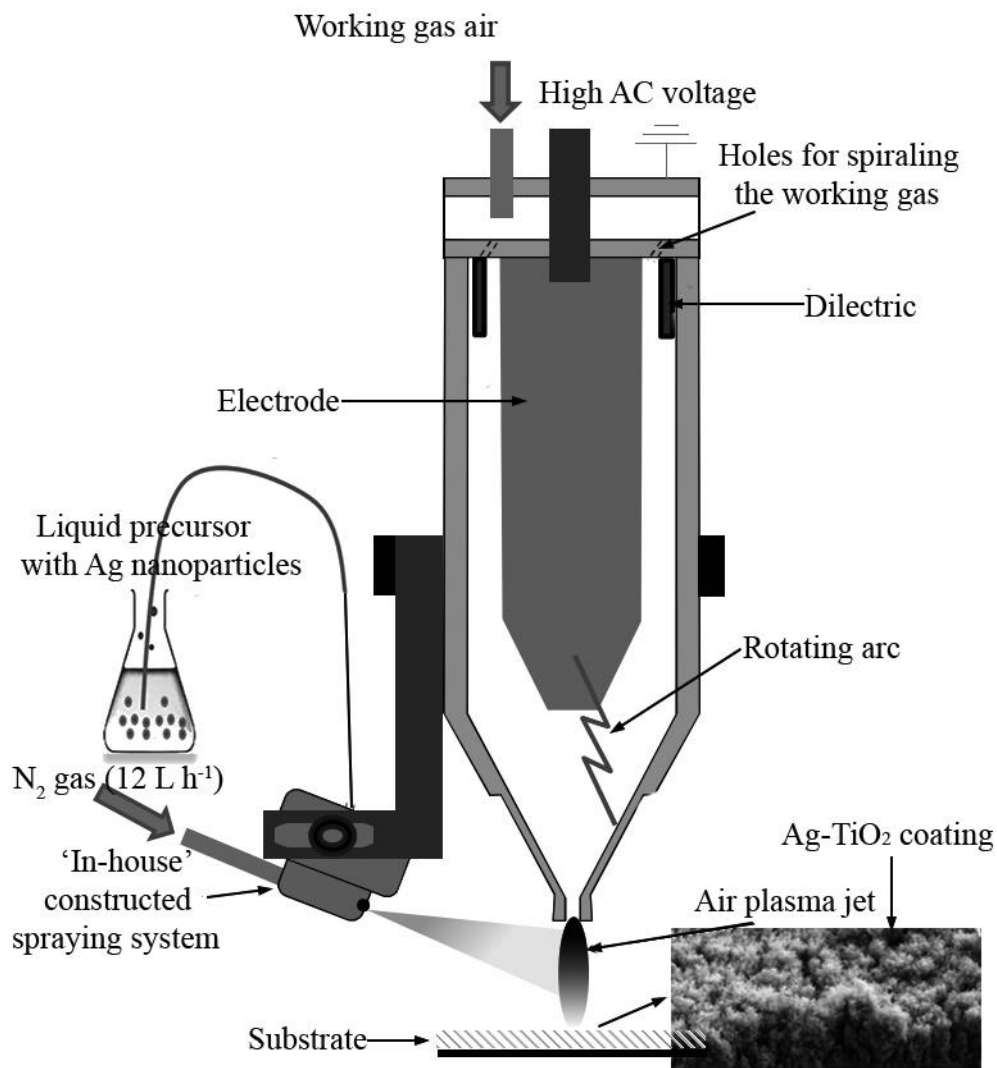


Figure 2.3: Schematic of the atmospheric pressure plasma jet (APPJ) system coupled with an 'in-house' constructed aluminum spraying system.

Prior to deposition, the substrates were ultrasonically cleaned with acetone, ethyl alcohol and then de-ionized water for 20 min each. Pre-treatment with an air plasma at a jet speed of  $10 \text{ m}\cdot\text{min}^{-1}$  and a frequency of 25 kHz was performed to activate the

substrate surface. The substrate temperature was maintained constant during the deposition of the coatings at 200°C except when mentioned otherwise. All the coatings were annealed in ambient air for 1 h at 450°C.

## 2.5. References

- [1] J.C.H. Spence, H.R. Kolar, G. Hembree, C.J. Humphreys, J. Barnard, R. Datta, C. Koch, F.M. Ross, J.F. Justo, Imaging dislocation cores – the way forward, *Philos. Mag.* 86 (2006) 4781-4796.
- [2] R. Lopez, R. Gomez, Band-gap energy estimation from diffuse reflectance measurements on sol–gel and commercial TiO<sub>2</sub>: a comparative study, *J. Sol-Gel Sci. Technol.* 61 (2012) 1-7.
- [3] D.R. Dreyer, S. Park, C.W. Bielawski, R.S. Ruoff, The chemistry of graphene oxide, *Chem. Soc. Rev.* 39 (2010) 228-240.
- [4] P.-G. Ren, D.-X. Yan, X. Ji, T. Chen, Z.-M. Li, Temperature dependence of graphene oxide reduced by hydrazine hydrate., *Nanotechnology* 22 (2011) 055705.
- [5] S. Ray, J.A. Lalman, N. Biswas, Using the Box-Benken technique to statistically model phenol photocatalytic degradation by titanium dioxide nanoparticles, *Chem. Eng. J.* 150 (2009) 15-24.
- [6] G.-S. Kim, H.-K. Seo, V.P. Godble, Y.-S. Kim, O.-B. Yang, H.-S. Shin, Electrophoretic deposition of titanate nanotubes from commercial titania nanoparticles: Application to dye-sensitized solar cells, *Electrochem. Commun.* 8 (2006) 961-966.
- [7] Q. Xiang, J. Yu, M. Jaroniec, Enhanced photocatalytic H<sub>2</sub>-production activity of graphene-modified titania nanosheets, *Nanoscale* 3 (2011) 3670-3679.

- [8] Y. Valcarcel, S. Gonzalez Alonso, J.L. Rodriguez-Gil, A. Gil, M. Catala, Detection of pharmaceutically active compounds in the rivers and tap water of the Madrid Region (Spain) and potential ecotoxicological risk, *Chemosphere* 84 (2011) 1336-1348.
- [9] J.B. Ellis, Pharmaceutical and personal care products (PPCPs) in urban receiving waters, *Environ. Pollut.* 144 (2006) 184-189.
- [10] P. Verlicchi, M. Al Aukidy, E. Zambello, Occurrence of pharmaceutical compounds in urban wastewater: Removal, mass load and environmental risk after a secondary treatment - A review, *Sci. Total Environ.* 429 IS - (2012) 123-155.
- [11] I. Zucker, Y. Lester, D. Avisar, U. Hübner, M. Jekel, Y. Weinberger, H. Mamane, Influence of wastewater particles on ozone degradation of trace organic contaminants., *Environ. Sci. Technol.* 49 (2015) 301-308.
- [12] D.C. Marcano, D.V. Kosynkin, J.M. Berlin, A. Sinitskii, Z. Sun, A. Slesarev, L.B. Alemany, W. Lu, J.M. Tour, Improved synthesis of graphene oxide, *ACS Nano* 4 (2010) 4806-4814.
- [13] T. Kasuga, M. Hiramatsu, A. Hoson, T. Sekino, K. Niihara, Formation of titanium oxide nanotube, *Langmuir* 14 (1998) 3160-3163.
- [14] D.V. Bavykin, V.N. Parmon, A.A. Lapkin, F.C. Walsh, The effect of hydrothermal conditions on the mesoporous structure of TiO<sub>2</sub> nanotubes, *J. Mater. Chem.* 14 (2004) 3370-3378.
- [15] P. Roy, S. Berger, P. Schmuki, TiO<sub>2</sub> nanotubes: synthesis and applications, *Angew. Chem. Int. Ed.* 50 (2011) 2904-2939.

[16] H. Fakhouri, D.B. Salem, O. Carton, J. Pulpytel, F. Arefi-Khonsari, Highly efficient photocatalytic TiO<sub>2</sub> coatings deposited by open air atmospheric pressure plasma jet with aerosolized TTIP precursor, *J. Phys. D: Appl. Phys.* 47 (2014) 265301-265311.

[17] P. Dowling Denis, T. O'Neill Feidhlim, J. Langlais Simon, J. Law Victor, Influence of dc pulsed atmospheric pressure plasma jet processing conditions on polymer activation, *Plasma Processes Polym.* 8 (2011) 718-727.

# THE IMPACT OF HYDROTHERMAL FACTORS ON QUASI-ONE-DIMENSION TIO<sub>2</sub> NANOSTRUCTURE, CRYSTAL SIZE AND BANDGAP

## Synopsis

Quasi-one-dimensional TiO<sub>2</sub> nanostructure (Q1D TiO<sub>2</sub>) synthesized using a hydrothermal method showed significant differences in the crystal phase, crystal size and bandgap properties under different hydrothermal synthesis conditions. The hydrothermal reaction conditions were optimized for maximizing and minimizing bandgap using a 3-factor 3-level Box Behnken design (BBD). The factors investigated include temperature, NaOH concentration and TiO<sub>2</sub> concentration. A quadratic response surface model predicted the optimized conditions for maximum and minimum bandgap were 3.31 eV and 3.05 eV, respectively. The BBD analysis and use of other statistical tools provided evidence showing the temperature and NaOH concentration significantly affected the crystal phase and Q1D TiO<sub>2</sub> bandgap. Pure anatase was associated with a higher bandgap, whereas the biphasic anatase-rutile and anatase-TiO<sub>2</sub>-B phases were linked with decreasing bandgap. In addition, the impact of crystal size and SSA on the bandgap was due to the size quantization effect. Decreasing the crystal size (increasing SSA) is closely linked with increasing the bandgap. These factors are significant because they can be controlled to engineer Q1D TiO<sub>2</sub> based compounds with controllable crystal phase, crystal size, specific surface area (SSA) and bandgap.



### 3.1. Introduction

The discovery of photo-electrochemical splitting of water on n-TiO<sub>2</sub> electrodes in 1972 [1] triggered much attention in examining the photoelectrolysis of water to hydrogen (H<sub>2</sub>) and oxygen (O<sub>2</sub>). Other applications include employing n-TiO<sub>2</sub> in wet solar cells [2] and for the photodegradation of hazardous organics pollutants into carbon dioxide plus water [3-6]. Quasi-one-dimensional (Q1D) TiO<sub>2</sub> nanomaterials have shown significant potential in these applications because of their high electron mobility, large specific surface area (SSA) and high mechanical strength [7-11]. Among the different approaches used to synthesize Q1D TiO<sub>2</sub>, the alkaline hydrothermal method is a relatively easy process for producing Q1D TiO<sub>2</sub> with varied bandgap energies [7-19]. Bandgap energies are crucial in determining the Q1D TiO<sub>2</sub> photocatalytic efficiency [7, 19].

The band gap is significantly affected by factors such as phase structure, temperature and crystal size. Phase structure is a major factor affecting the Q1D TiO<sub>2</sub> bandgap. TiO<sub>2</sub> has an optical bandgap value for different crystal phases. For TiO<sub>2</sub>, the band gap is 3.2 eV for anatase, 3.0 eV for rutile, 3.1 eV for brookite and 3.2 eV for TiO<sub>2</sub>-B [10, 16, 20]. Work by Bavykin et al. [8] has shown that during the alkaline hydrothermal process, TiO<sub>2</sub> precursors (anatase, rutile, TiO<sub>2</sub>-B, brookite and amorphous) were reconstructed into Q1D TiO<sub>2</sub> by producing and consecutively wrapping titanite nanosheets. Different crystal phase structures can be produced during hydrothermal processing [7-18]. Zhu et al. [9] claimed that the anatase phase was produced when using 15 M NaOH at a temperature between 20°C and 200°C for 48 h. In other studies, Kou et al. [16] reported TiO<sub>2</sub>-B nanotubes were obtained when the conditions were set by employing 10 M

NaOH at 120°C for 96-168 h. In these studies, researchers used selected synthesis conditions to produce Q1D TiO<sub>2</sub> structures with varied phase structures. An existing research gap which requires addressing is the assessment of different synthesis conditions on the phase structure and bandgap for Q1D TiO<sub>2</sub> nanostructures.

TiO<sub>2</sub> band structure changes is also affected by crystal size which is comparable to the electron wavelength [21]. This observation, designated as the size quantization effect [10, 21], causes the TiO<sub>2</sub> bandgap to shift to larger values or shorter wavelengths for decreasing crystal sizes [10]. Many studies have shown Q1D TiO<sub>2</sub> diameters ranging from 5 nm to 200 nm can be controlled using selected hydrothermal temperatures and suitable TiO<sub>2</sub> to NaOH molar ratios [8, 12, 13]. Bavykin et al. [8] reported the average Q1D TiO<sub>2</sub> diameter increased with an increase in the temperature from 120°C to 150°C and increasing the TiO<sub>2</sub> to NaOH weight ratio. Adjusting the temperature and NaOH:TiO<sub>2</sub> weight ratio are expected to impact the crystal size and subsequently, the bandgap based on the size quantization effect [10].

The lack of research data describing the role of different hydrothermal synthesis process parameters on the Q1D TiO<sub>2</sub> phase structure and its bandgap is the motivating factor for conducting this study. The first part of the third objective is to evaluate the influence of the hydrothermal synthesis factors on the Q1D TiO<sub>2</sub> phase structure, crystal size, SSA and bandgap [19]. The second part of the third objective is to employ a BBD to optimize the process conditions leading to maximum and minimum Q1D TiO<sub>2</sub> bandgap. The three hydrothermal synthesis factors under consideration will include temperature, NaOH concentration and TiO<sub>2</sub> precursor concentration.

## 3.2. Experimental

### 3.2.1. Preparation of the quasi-one-dimension TiO<sub>2</sub> photocatalyst

Q1D TiO<sub>2</sub> photocatalyst was prepared using the process described in Chapter 2 (Section 2.4.2). Briefly, homogeneously mix a specified quantity of TiO<sub>2</sub> NPs (Aeroxide TiO<sub>2</sub> P25, Evonik Industries, Germany) with 70 mL of a NaOH solution. The resulting suspension was transferred into a 100-mL Teflon lined stainless-steel autoclave. The autoclave was maintained at a desired temperature (Table 3.1) for 48 h and subsequently, cooled to room temperature. Next, the suspension was centrifuged to obtain a white precipitate. The precipitate was washed with 1 L of 0.1 M HCl for 24 h at room temperature. The white precipitate was repeatedly washed (5 times) with deionized water. The washed mixture was centrifuged after each wash. Finally, the collected white precipitate was calcined at 400°C for 2 h to produce Q1D TiO<sub>2</sub> [16]. The selected experimental levels were based on previous studies (Table 3.1) [8].

Table 3.1: Three selected factors and three level.

Level	Factors		
	Temperature (°C)	NaOH concentration (M)	TiO <sub>2</sub> concentration (g·L <sup>-1</sup> )
-1	120	5	14
0	150	10	43
1	190	15	100

### 3.2.2. Characterization studies

Details of all the characterization studies are described in Chapter 2. The Q1D TiO<sub>2</sub> morphology was examined using field emission scanning electron microscopy (FESEM) (JEOL, Japan) and high resolution transmission electron microscopy (HRTEM) (300kV,

JEOL 3010, Japan). X-ray diffraction (XRD) analysis of the samples was conducted using an X-ray diffractometer (Rigaku, MI) equipped with Cu K $\alpha$  radiation source. UV-visible spectra analysis was performed using a Cary 300 UV-visible (Agilent Technologies, Santa Clara, CA). The wavelength accuracy and resolution for the Cary 300 UV-visible were  $\pm 0.04$  nm (at 486 nm) and  $\leq 0.193$  nm, respectively. The bandgap response was calculated based on diffuse reflectance UV-visible spectroscopy studies. The diffuse reflectance spectra were converted into a corresponding absorption spectra using the modified Kubelka Munk function  $(F(R)E)^{1/2}$  [22]. Frequent use of diffuse reflectance UV-visible spectroscopy to determine the bandgap in solid materials is justified based on past research [22]. The bandgap ( $E_g$ ) for each experiment is shown in Table 3.2. The photoluminescence spectra were conducted at room temperature using a Varian Cary Eclipse Fluorescence Spectrophotometer (Mississauga, ON). Nitrogen adsorption–desorption isotherms were determined at 77K with a Micromeritics ASAP 2020 Brunauer–Emmett–Teller (BET) analyzer (Micromeritics Instrument Corp. GA, United States).

### *3.2.3. Experimental design, optimization study and statistical analysis*

A three factor three level BBD was constructed with three central points to determine the hydrothermal synthesis factors for evaluating the bandgap. The BBD is unique because it is rotatable and does not comprise an embedded factorial or fractional factorial design. The BBD experimental conditions were selected at the midpoints of edges of the space and at the center.

Each experimental factor was varied at a low level (designated as -1), a central level (designated as 0) and a high level (designated as +1) (Table 3.1). The method is constructed using 12 experimental points (#1-#12) plus three central points (#13-#15) and each condition under triplicate conditions (Table 3.2). The three central point experiments, designated as #13, #14 and #15 under the same conditions, were performed to evaluate the magnitude of error in the experimental analysis. The experimental factors and bandgap (response variable) were modeled using Minitab (Minitab Inc., State College, PA) to fit a full quadratic equation (Eq. 3.1):

$$E_g = a_0 + \sum_{i=1}^3 a_i X_i + \sum_{i=1}^3 a_{ii} X_i^2 + \sum_{i=1}^3 \sum_{i < j=2}^3 a_{ij} X_i X_j \quad (3.1)$$

where  $X_i$ 's are input variables which influence the response variable  $E_g$ ,  $a_0$  is an offset term,  $a_i$  is the  $i^{\text{th}}$  linear coefficient,  $a_{ii}$  is the quadratic coefficient, and  $a_{ij}$  is the  $ij^{\text{th}}$  interaction coefficient. The  $X_i$  correspond to the experimental factors ( $X_1 = \text{temperature}$ ,  $X_2 = \text{NaOH concentration}$ ,  $X_3 = \text{TiO}_2 \text{ concentration}$ ) (Table 3.2).

An analysis of variance (ANOVA) was performed using the responses for each experiment (#1-#15) (Table 3.2). The coefficient values for the full quadratic model were calculated using a multiple regression analysis. Only significant terms with p values  $< 0.05$  were included into the final model. A normal distribution plot together with the Anderson-Darling (AD) [23] statistic was used to determining the deviation of the residuals from a normal distribution. The D-optimality analysis [24] was performed to obtain optimal conditions for the three factors under consideration (maximize and minimize the bandgap  $E_g$ ).

Table 3.2: Design matrix for experimental factors and responses of bandgap  $E_g$  at different factor levels.

Expt. # <sup>a</sup>	Factors <sup>b</sup>			Response			
	T (°C)	NaOH (M)	TiO <sub>2</sub> (g·L <sup>-1</sup> )	Bandgap $E_g$ (eV) <sup>c</sup>			
				$E_{g1}$	$E_{g2}$	$E_{g3}$	Mean $E_g$
1	120	5	43	3.071	3.063	3.068	3.067±0.004
2	190	5	43	3.271	3.274	3.277	3.274±0.003
3	120	15	43	3.254	3.258	3.261	3.258±0.003
4	190	15	43	3.214	3.202	3.215	3.210±0.007
5	120	10	14	3.289	3.293	3.298	3.293±0.004
6	190	10	14	3.208	3.196	3.206	3.203±0.006
7	120	10	100	3.270	3.262	3.264	3.262±0.004
8	190	10	100	3.239	3.219	3.228	3.229±0.009
9	150	5	14	3.303	3.299	3.293	3.298±0.005
10	150	15	14	3.268	3.268	3.272	3.271±0.002
11	150	5	100	3.270	3.259	3.277	3.269±0.008
12	150	15	100	3.268	3.270	3.276	3.271±0.004
13	150	10	43	3.274	3.278	3.284	3.279±0.005
14	150	10	43	3.283	3.287	3.284	3.285±0.002
15	150	10	43	3.293	3.287	3.291	3.290±0.003

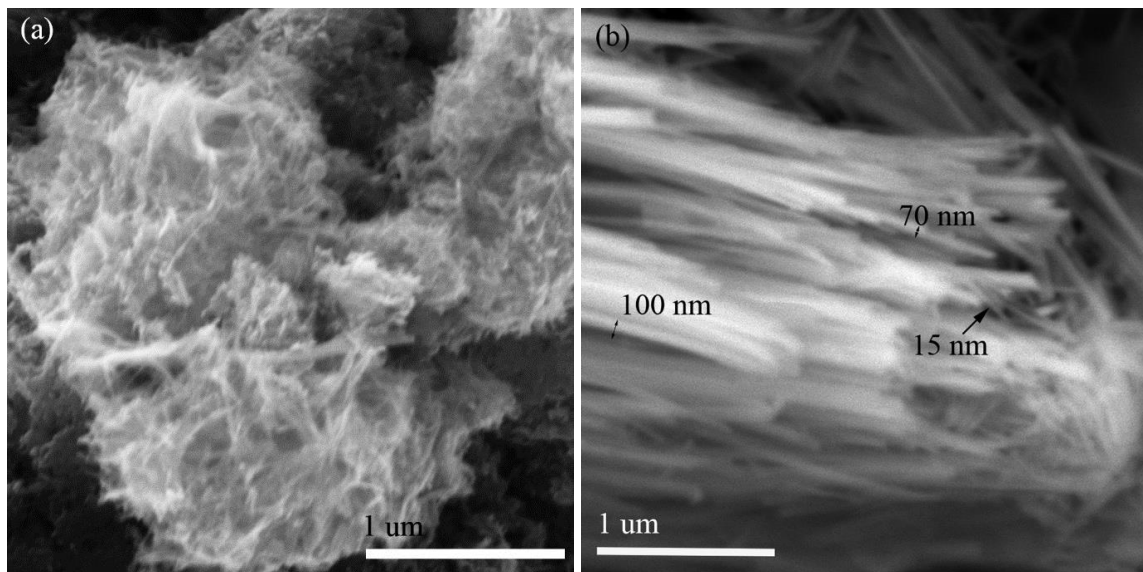
Notes: <sup>a</sup> Expt. # represents one experimental condition, <sup>b</sup> T, NaOH and TiO<sub>2</sub> represents temperature, NaOH concentration and TiO<sub>2</sub> concentration, respectively, and <sup>c</sup>  $E_g$  represents bandgap.  $E_{g1}$ ,  $E_{g2}$  and  $E_{g3}$  are replicates results for  $E_g$ .

### 3.3. Results and discussion

#### 3.3.1. Morphology

FESEM and HRTEM images for selected Q1D TiO<sub>2</sub> samples are shown in Figure 3.1. Q1D TiO<sub>2</sub> samples (nanorods and nanowires) synthesized at different hydrothermal conditions which were randomly distributed showed significant differences in the crystal sizes. The FESEM image for sample #1 (120°C, 5 M and 43 g·L<sup>-1</sup>) (Figure 3.1a) indicate a mixture of nanorods and nanowires with length of approximately 100 nm (Figure 3.1c). Lattice fringes with 0.35 nm spacing (Figure 3.1c) indicate the Q1D TiO<sub>2</sub> sample #1 contains anatase [25]. Nanowire morphology with length up to 3 μm was detected in

sample #8 (190°C, 10 M and 100 g·L<sup>-1</sup>) (Figure 3.1b and d). The lattice fringes with 0.62 nm spacing indicate the TiO<sub>2</sub> nanowire (sample #8) consisted of the TiO<sub>2</sub>-B phase [26]. The FESEM image for sample #9 (190°C, 5 M and 43 g·L<sup>-1</sup>) (Figure 3.1e) indicate a nanowire with length of hundreds of nanometers. The FESEM image for sample #4 (190°C, 15 M and 14 g·L<sup>-1</sup>) (Figure 3.1f) indicate a nanowire with length of micrometers. Sample #4 shows a wide distribution of diameter from 10 nm to hundreds of nanometers. Lower temperature and NaOH concentration were associated with smaller diameter and crystal size (Sample #1). However, higher temperature and NaOH concentration were linked to larger diameter (Sample # 4 and 6), length (sample #9) and crystal size. The FESEM images indicate the hydrothermal synthesis factors significantly impacted the Q1D TiO<sub>2</sub> diameter and crystal size (further discussed in this chapter Section 3.3.6).



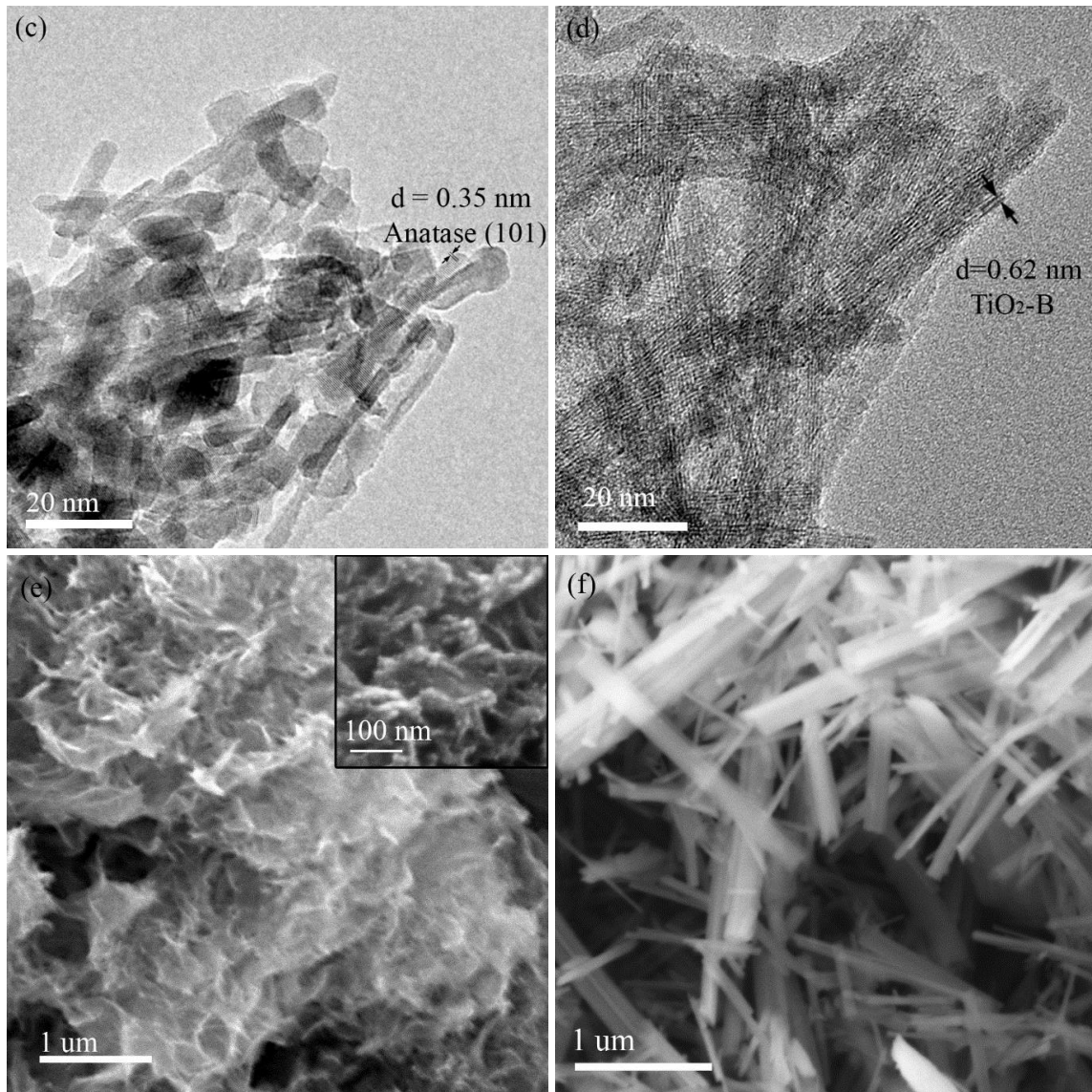


Figure 3.1: Q1D  $\text{TiO}_2$  field emission scanning electron microscopy (FESEM) and high resolution transmission electron microscopy (HRTEM) images (a) FESEM image for sample #1 synthesized at  $120^\circ\text{C}$ , 5 M NaOH and  $43 \text{ g}\cdot\text{L}^{-1}$ , (b) FESEM image for sample #8 synthesized at  $190^\circ\text{C}$ , 10 M and  $100 \text{ g}\cdot\text{L}^{-1}$ , (c) HRTEM image sample #1 synthesized at  $120^\circ\text{C}$ , 5 M NaOH and  $43 \text{ g}\cdot\text{L}^{-1}$ , (d) HRTEM image for sample #8 synthesized at  $190^\circ\text{C}$ , 10 M and  $100 \text{ g}\cdot\text{L}^{-1}$ , (e) FESEM image for sample #9 synthesized at  $150^\circ\text{C}$ , 5 M NaOH and  $14 \text{ g}\cdot\text{L}^{-1}$ , and (f) FESEM image for sample #4 synthesized at  $190^\circ\text{C}$ , 15 M NaOH and  $14 \text{ g}\cdot\text{L}^{-1}$ .

Note: d represents lattice interplanar spacing.

During the hydrothermal process, the NaOH reacted with  $\text{TiO}_2$  crystallites and produced free  $\text{TiO}_6$  octahedron by cleaving the Ti-O-Ti bonds of the  $\text{TiO}_2$  precursor [8,



27, 28]. The  $\text{TiO}_6$  octahedron was subsequently assembled into lamellar structures via the formation of hydroxyl bridges between the Ti atoms [27, 28]. Next, Q1D  $\text{TiO}_2$  (nanotubes, nanorods and nanowires) was produced by scrolling or growing the lamellar structures [8, 29]. The driving force for scrolling lamellar structures into nanotubes or growing to nanorods or nanowires is attributed to the reduction of the high surface energy which was caused by the saturated dangling bonds on the lamellar structures [27].

### 3.3.2. Bandgap (eV)

Diffuse reflectance UV-visible spectroscopy (DRS) was employed to examine the optical response of the starting material  $\text{TiO}_2$  nanoparticles and the resulting Q1D  $\text{TiO}_2$  (Figure 3.2a). A wide optical absorption below a critical value of approximately 410 nm was observed in both samples [30]. This broad band assignment is attributed to the band-band electron transition of the  $\text{TiO}_2$  nanocrystals based on its band gap energy [30, 31]. A red-shift and enhanced light absorption between 300 to 400 nm was observed for the Q1D  $\text{TiO}_2$  sample #1 when compared to  $\text{TiO}_2$  nanoparticles. The diffuse reflectance spectra was converted into a corresponding absorption spectra (Figure 3.2b) by plotting  $(F(R)*E)^{1/2}$  versus E (where  $F(R) = a_{Km}$  is the Kubelka Munk function [22] and E is the photon energy). Extrapolating the straight line portion of the UV-visible spectra to  $(F(R)*E)^{1/2}=0$  was used to determine the bandgap. A  $3.067\pm 0.003\text{eV}$  value for the Q1D  $\text{TiO}_2$  sample #1 was less than that for the  $\text{TiO}_2$  nanoparticles bandgap of  $3.282\pm 0.006\text{eV}$ . In this study, the bandgap energies for the 15 BBD samples (ranging from  $3.067\pm 0.003\text{eV}$  to  $3.298\pm 0.004\text{eV}$ ) are shown in Table 3.2. The observed change in the

bandgap for different samples was due to the changes in crystal phase and size under different hydrothermal conditions.

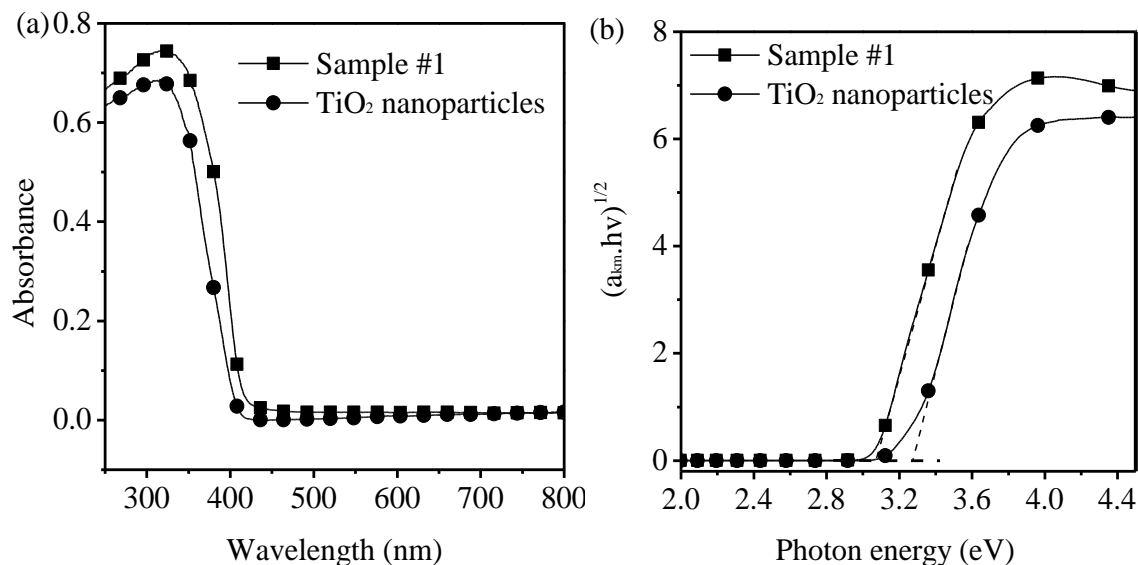


Figure 3.2: Diffuse reflectance UV-visible spectroscopy and  $(a_{km}hv)^{1/2}$  versus absorbed energy profiles for sample #1 (120°C using 5 M NaOH and 43 g·L<sup>-1</sup> TiO<sub>2</sub> nanoparticles) and TiO<sub>2</sub> nanoparticles. (a) Diffuse reflectance UV-visible spectroscopy data, and (b)  $(a_{km}hv)^{1/2}$  versus absorbed energy profiles.

### 3.3.3. Analysis of the experimental design

#### 3.3.3.1. Impacts of factor variables on the bandgap

The bandgap for all the Q1D TiO<sub>2</sub> samples are shown in Table 3.2 and the main effect of 3 hydrothermal synthesis factors on the bandgap is shown in Figure 3.3. Decreasing temperature (120°C) and NaOH concentration (5M) were linked to the lowest bandgap. A mid-level temperature set at 150°C as well as the mid-level NaOH concentration of 10 M were closely linked to increasing the bandgap. Either increasing or decreasing temperatures (NaOH concentrations) resulted in decreasing the bandgap. Interaction plots at all level factor categories (Figure 3.3b) indicate a similar pattern as that shown in the main effect plot.

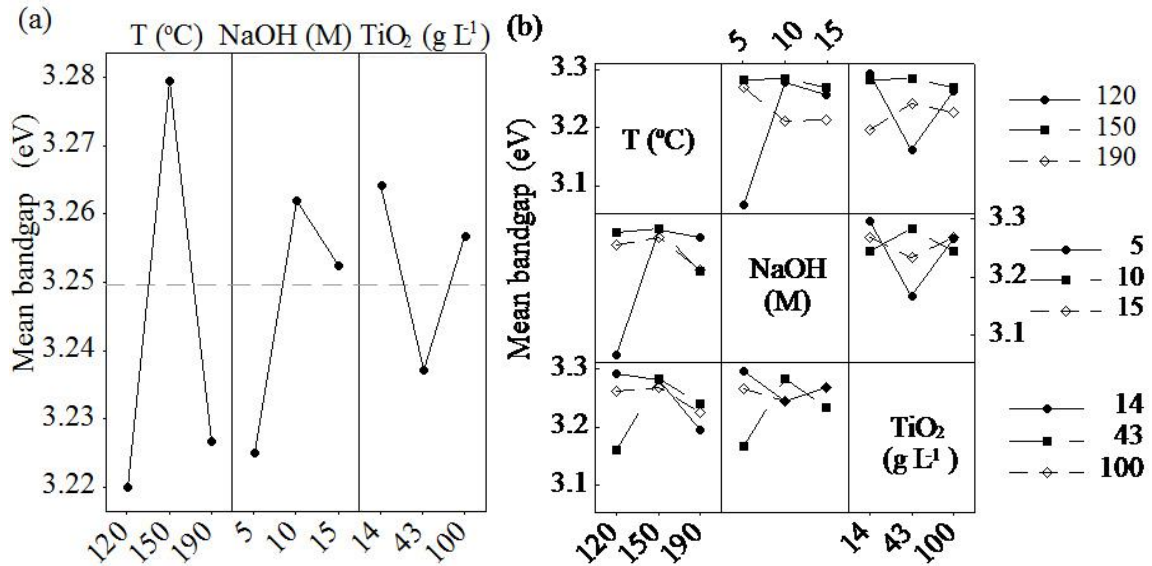


Figure 3.3: Three-level Box-Behnken design (BBD) plots for: (a) Main effects for bandgap, and (b) two-factor effects for bandgap.  
 Note: T, NaOH and TiO<sub>2</sub> represent temperature, NaOH concentration and TiO<sub>2</sub> concentration, respectively.

### 3.3.3.2. Model fitting using analysis of variance (ANOVA)

An ANOVA was employed to evaluate the significance of the full quadratic model and to determine the significance and adequacy of the model. The ANOVA result (Table 3.3) for the bandgap ( $E_g$ ) response shows that the model is statistically significant with a p-value less than 0.05. The model F-value of 6.97 which was greater than the F-critical value of 2.01 at an  $\alpha$  value = 0.05 indicate the full quadratic fit model was significant [24, 32-34]. Note terms with p-values < 0.05 are statistically significant whereas terms with a p-value > 0.05 are insignificant. TiO<sub>2</sub> concentration (g·L<sup>-1</sup>), NaOH concentration (M) x NaOH concentration (M) and TiO<sub>2</sub> concentration (g·L<sup>-1</sup>) x TiO<sub>2</sub> concentration (g·L<sup>-1</sup>) with p-values more than 0.05 are statistically insignificant indicate these the variables did not affect the full quadratic model [24, 32-34].

Table 3.3: ANOVA results of the experimental response at each factor level.

Source	DF <sup>a</sup>	Seq. SS <sup>b</sup>	MS <sup>c</sup>	F-value	p-value
Model	9	0.09347	0.01039	6.97	0
X <sub>1</sub>	1	0.00035	0.00035	0.23	0
X <sub>2</sub>	1	0.00206	0.00206	1.39	0.001
X <sub>3</sub>	1	0.00029	0.00029	0.2	0.620
X <sub>1</sub> <sup>2</sup>	1	0.03601	0.03601	24.18	0
X <sub>2</sub> <sup>2</sup>	1	0.00742	0.00742	4.98	0.146
X <sub>3</sub> <sup>2</sup>	3	0.00365	0.00365	2.45	0.255
X <sub>1</sub> X <sub>2</sub>	1	0.04115	0.04115	27.63	0
X <sub>1</sub> X <sub>3</sub>	1	0.00015	0.00015	0.1	0.046
X <sub>2</sub> X <sub>3</sub>	1	0.00001	0.00001	0	0.007
Error	35	0.05216	0.00008		
Total	44	0.14559			

Notes: <sup>a</sup> DF = degrees of freedom, <sup>b</sup> Seq. SS = sequential sum of square, <sup>c</sup> MS = mean square, and <sup>d</sup> X<sub>1</sub> = Temperature; X<sub>2</sub> = NaOH concentration; X<sub>3</sub> = TiO<sub>2</sub> concentration.

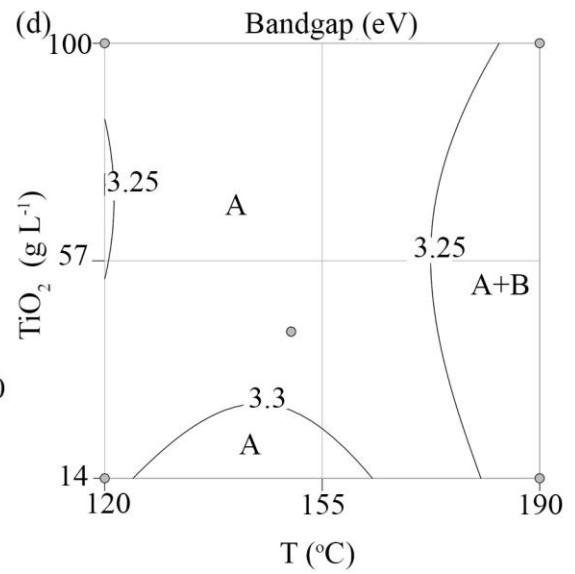
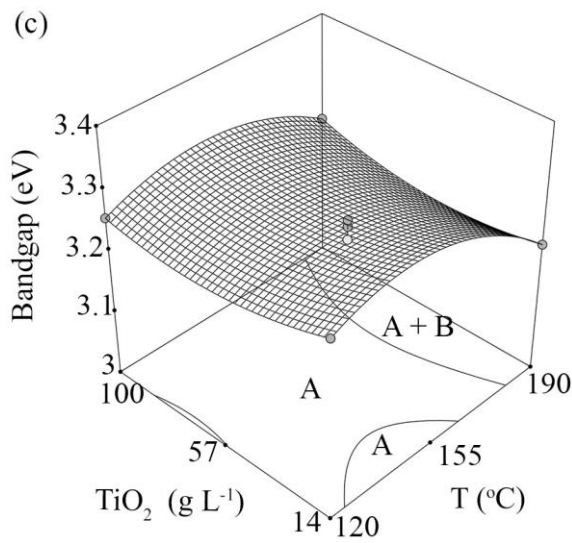
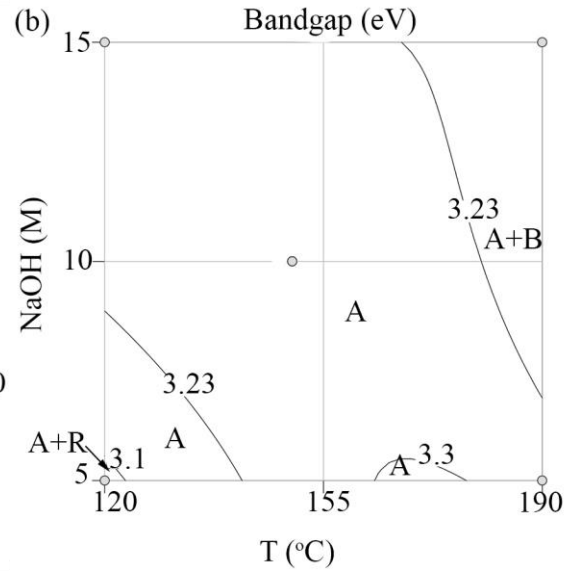
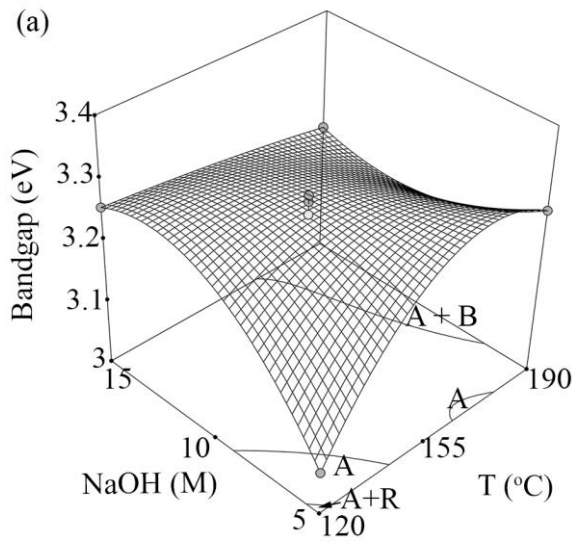
A full quadratic model was simplified using a stepwise procedure such as a backwards elimination method. Other stepwise procedures include forward selection and stepwise regression. The backwards elimination method is advantageous because of considerable predictability. The method is employed to delete statistically insignificant terms with p values > 0.05 in the full model [24]. The refined model (Eq. 3.2) with an F-value of 6.97 (> the critical level (6.7, p < 0.00)) is statistical significant.

$$E_g = 3.2742 - 0.01648X_1 - 0.0111X_2 - 0.01882X_1X_2 + 0.00881X_1X_3 + 0.1171X_2X_3 - 0.02798X_1^2 \quad (3.2)$$

where  $E_g$  is the bandgap (eV),  $X_1$ ,  $X_2$  and  $X_3$  represent temperature (°C), NaOH concentration (M) and TiO<sub>2</sub> concentration (g·L<sup>-1</sup>), respectively.

### 3.3.3.3. Factor interaction plots

Describing interactions between the experimental factors was based on data in the surface and contour plots. Interaction between temperature and NaOH concentration (Figure 3.4a and Figure 3.4b) suggests that a biphasic anatase-rutile (see phase analysis in Figure 3.8) with the minimum bandgap ( $3.067 \pm 0.004 \text{ eV}$ ) was observed for the Q1D  $\text{TiO}_2$  sample synthesized at  $120^\circ\text{C}$  and 5 M NaOH. The pure anatase was obtained with increasing bandgap when increasing the temperature ( $120\text{-}170^\circ\text{C}$ ) and NaOH concentration (5-15 M) were increased. However, high NaOH concentrations reaching 10 M and 15 M along with a relative high temperature set at  $190^\circ\text{C}$  contributed to a biphasic anatase- $\text{TiO}_2$ -B phase structure and decreasing the bandgap (ranging from  $3.203 \pm 0.005$  to  $3.228 \pm 0.008 \text{ eV}$ ). Interaction between temperature and  $\text{TiO}_2$  concentration (Figure 3.4c and Figure 3.4d) is a strong indication that variations in the  $\text{TiO}_2$  concentration under consideration did not affect the bandgap. However, temperature alone affected the bandgap in all level  $\text{TiO}_2$  concentration. Relative high temperatures ( $>170^\circ\text{C}$ ) (Figure 3.4c and Figure 3.4d) were associated with decreasing the bandgap ( $3.203 \pm 0.006$  -  $3.229 \pm 0.009 \text{ eV}$ ). Interaction between NaOH and  $\text{TiO}_2$  concentrations (Figure 3.4e and Figure 3.4f) confirmed that the  $\text{TiO}_2$  concentration did not affect the bandgap and the phase structure. When the temperature was set at  $150^\circ\text{C}$  (Figure 3.4c and Figure 3.4d), the bandgap varied between  $3.269 \pm 0.008$  and  $3.298 \pm 0.005 \text{ eV}$  along with variation in the  $\text{TiO}_2$  concentration and NaOH concentration.



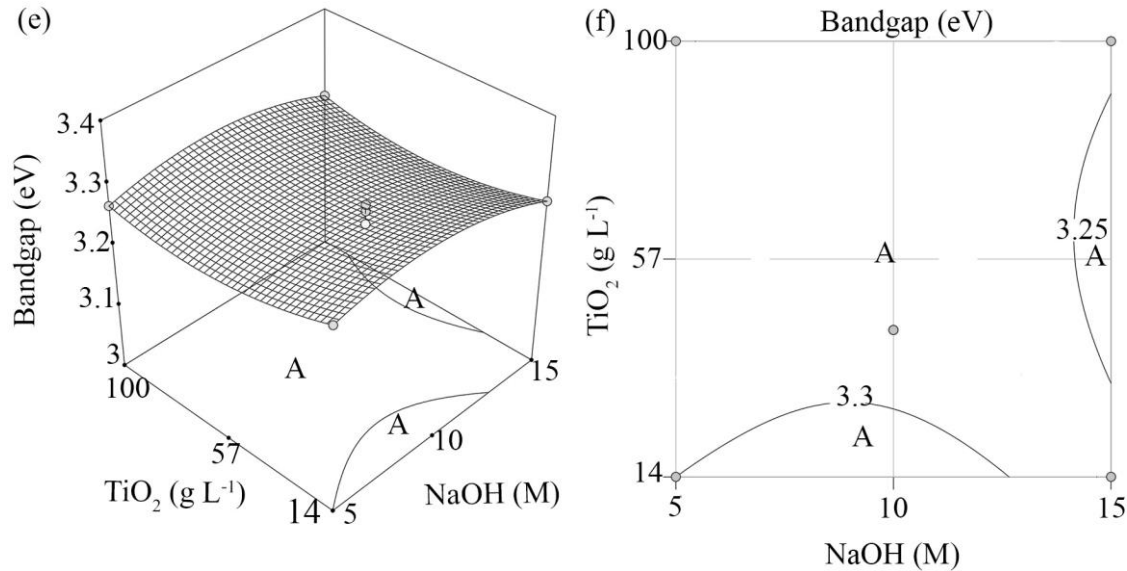


Figure 3.4: Bandgap response surface and contour plots for various factors: (a) and (b) hydrothermal temperature and NaOH concentration with a  $\text{TiO}_2$  concentration at  $43 \text{ g}\cdot\text{L}^{-1}$ , (c) and (d) hydrothermal temperature and  $\text{TiO}_2$  concentration with a NaOH concentration at 10 M, and (e) and (f) NaOH concentration and  $\text{TiO}_2$  concentration with a temperature at  $150^\circ\text{C}$ .

Note: A, R and B represent anatase, rutile and  $\text{TiO}_2\text{-B}$ , respectively.

#### 3.3.4. Response model verification, optimization and validation

The regression coefficient  $R^2$  value for the bandgap model was 0.936. The  $R^2$  value indicate the bandgap values predicted using the model correlated reasonably well with the experimental data. A scatter plot of the experimental values versus the predicted values calculated using the model equation illustrates a reasonable correlation at each level (Figure 3.5a). Evaluating the adequacy of fit between the model and the experimental data was conducted using the Anderson-Darling (AD) statistic (Figure 3.5b) [35]. The AD statistic was 0.488 for the  $E_g$  model. This value which is less than the critical AD value of 0.735 for a sample size of 45 at a 5% level of significance [35] suggest the residuals p-value of 0.213 ( $>$  the critical value of 0.05) was able to meet the normal distribution requirement.

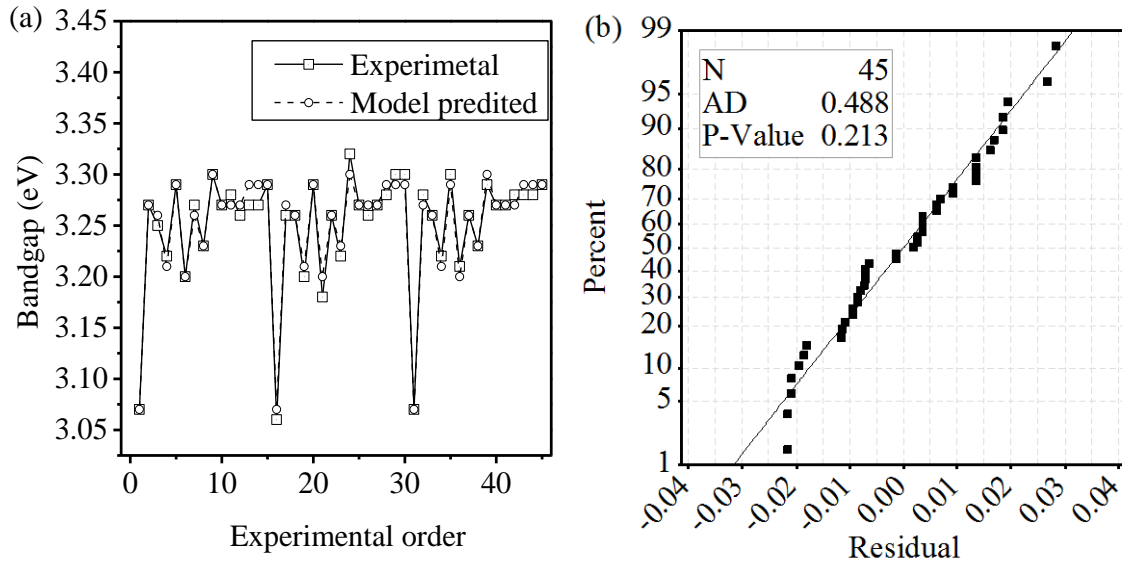


Figure 3.5: Evaluating the accuracy of the response surface model. (a) Scatter plot of the bandgap values versus the experimental order (45 experiments). (b) Anderson-Darling normality plot of residuals.

Notes: <sup>a</sup> N = the number of experiments that was conducted in this study, <sup>b</sup> P-Value = level of confidence, and <sup>c</sup> AD = Anderson-Darling statistic.

The D-optimality was used to locate the region of maximum and minimum response (bandgap). Within the factor space under consideration, the D-optimality value can vary from 0 (completely undesirable) to 1 (completely desirable) using the numerical optimization function in the Minitab<sup>®</sup> software. Values for temperature, NaOH and TiO<sub>2</sub> concentrations at the maximum and minimum bandgap values were identified at the largest D-optimality index (Figure 3.6). A maximum bandgap of 3.31 eV was predicted at a D-optimality value of 0.8740 under conditions set at 150°C, 12 M NaOH and 14 g·L<sup>-1</sup> TiO<sub>2</sub>. In comparison, a minimum bandgap of 3.05 eV was predicted at a D-optimality value of 0.854 at 120°C, 5 M NaOH and 63 g·L<sup>-1</sup> TiO<sub>2</sub>. Validating the model predicted maximum and minimum bandgap values under the optimized hydrothermal conditions revealed experimental maximum and minimum bandgap of 3.305±0.004 eV and



3.044±0.002 eV, respectively. The experimental band gap values were slightly underestimated when compared to the values predicted by the model.

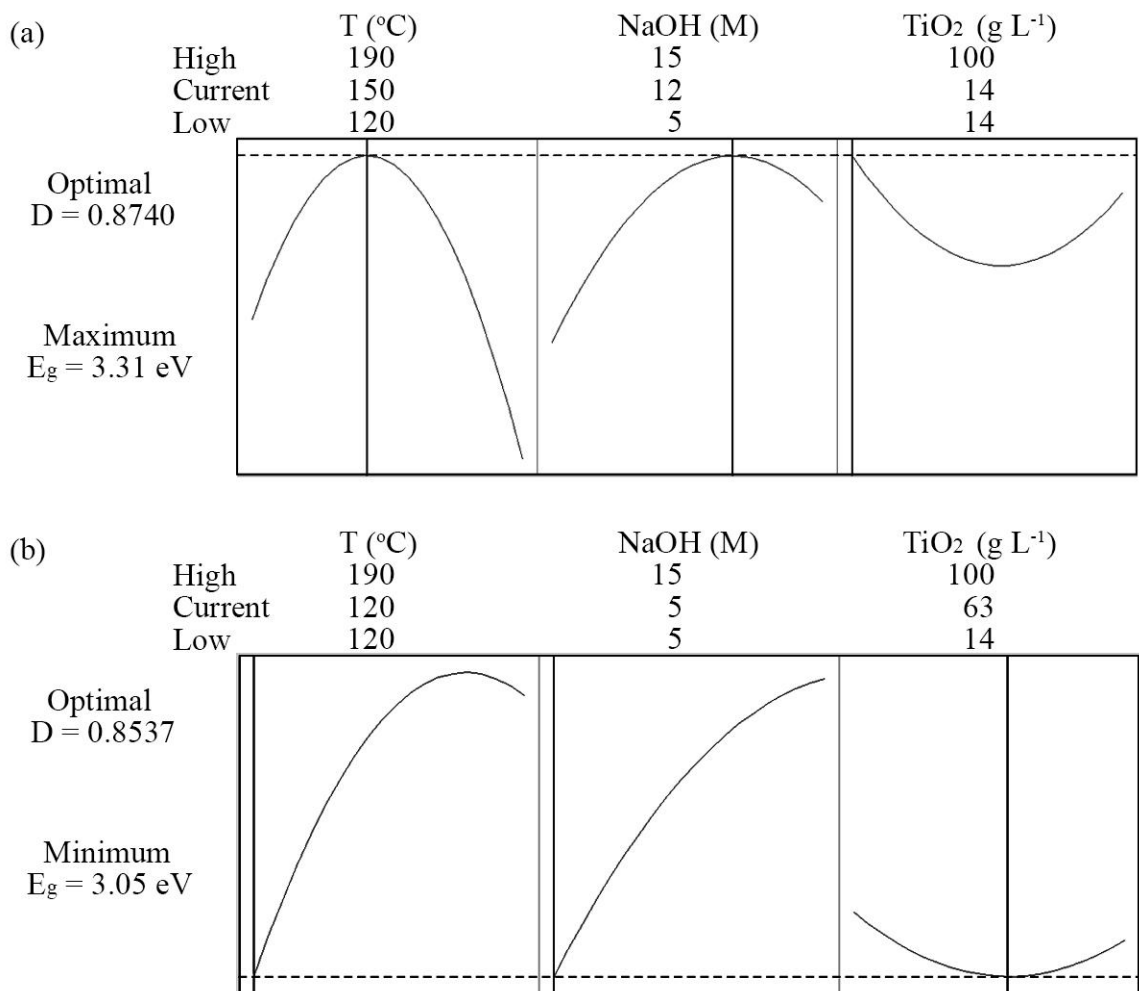
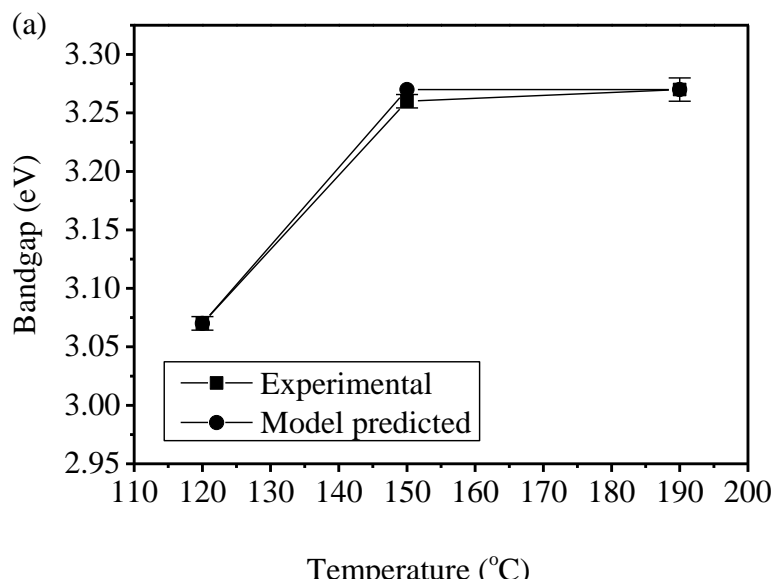


Figure 3.6: Optimality plot to locate optimum factor levels for (a) maximized response bandgap E<sub>g</sub>, and (b) minimized bandgap E<sub>g</sub>.

The accuracy of the model within the experimental factors under consideration was examined by conducting three additional experiments. The experimental results together with the predicted values were obtained by varying a single factor (Figure 3.7). The model predicted values were close to the experimental values for the temperature ranging

from 120°C to 190°C (Figure 3.7a), although the model predicted bandgap values were slightly overestimated at 150°C. For the NaOH concentration, the predicted values were comparable to the experimental points with a slight overestimate at 5 M NaOH and a slight underestimate at 15 M NaOH (Figure 3.7b). For the TiO<sub>2</sub> concentration, the model predicted values were comparable to the observed values with a slightly overestimate at 43 g·L<sup>-1</sup> TiO<sub>2</sub> (Figure 3.7c). Notably, the model predicted trend for varying each factor were close to the experimental observations.



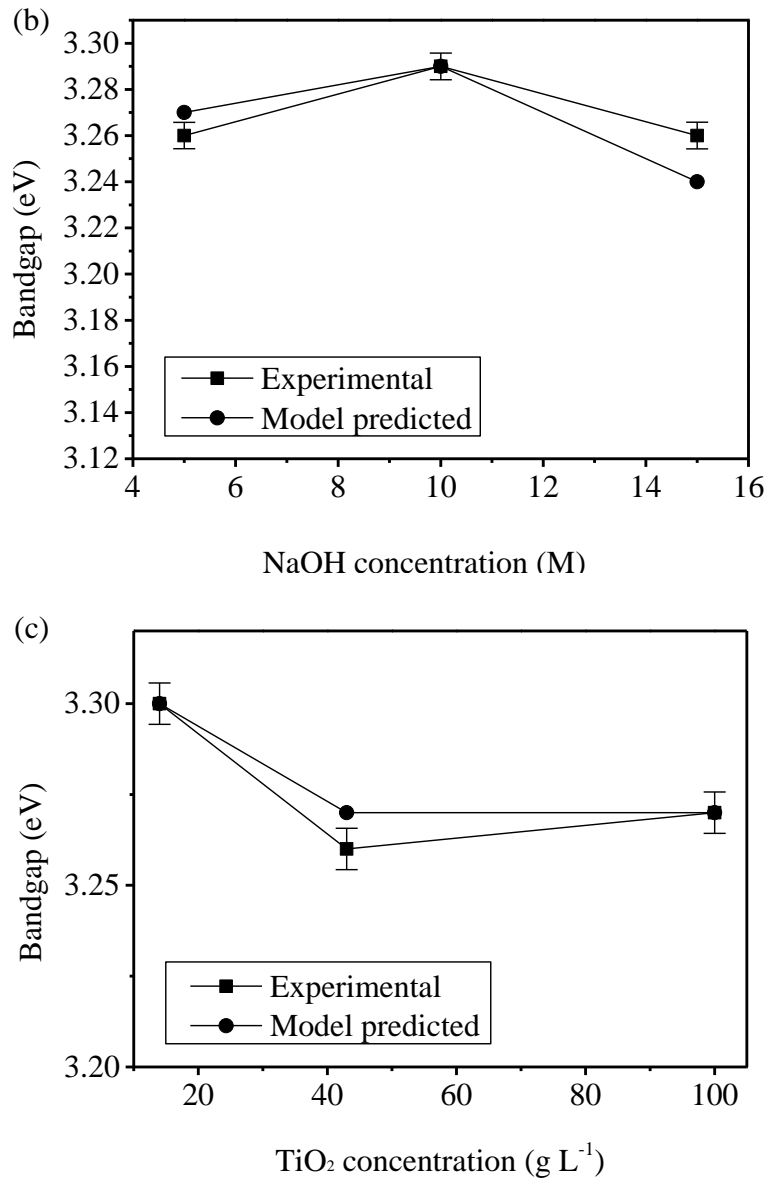


Figure 3.7: Validation study of the response surface model for the different factors under consideration. (a) Bandgap versus temperature at experimental condition set at 5 M NaOH and 43 g·L<sup>-1</sup> TiO<sub>2</sub> concentration, (b) Bandgap versus NaOH concentration at experimental condition set at 150°C and 43 g·L<sup>-1</sup> TiO<sub>2</sub>, and (c) Bandgap versus TiO<sub>2</sub> mass at experimental condition set at 150°C and 5 M NaOH.

### 3.3.5. Phase structure analysis

Evaluating the impact of the crystal phase structure on the bandgap was performed using XRD. The XRD patterns (Figure 3.8a) for selected BBD samples #1, #2 and #6

and the phase structure for all the samples are listed in Table 3.4. The anatase [36], rutile [20, 31] and TiO<sub>2</sub>-B [16, 37] phases were detected in selected samples with the anatase phase observed in all the Q1D TiO<sub>2</sub> samples. Sample #2, #3, #5, #7, #9, #10, #11, #12, #13, #14 and #15 consisted of pure anatase with bandgap ranging from 3.258±0.003 to 3.298±0.004 eV. The biphasic anatase-rutile structure dominated the Q1D TiO<sub>2</sub> sample #1 while the biphasic anatase-TiO<sub>2</sub>-B was dominant in sample #4, #6 and #8. This difference in phase change which is also shown in Figure 3.4 illustrates the impacts of hydrothermal synthesis factors affecting the phase structure and bandgap. Temperature and NaOH concentration were significant factors affecting the Q1D TiO<sub>2</sub> phase structure. At a relative lower temperature (120°C) and a low NaOH concentration (5 M), a biphasic anatase-rutile structure was observed in sample #1. Sample #1 was the only experimental design condition with the same biphasic anatase-rutile structure as TiO<sub>2</sub> NPs (P25) [31, 38, 39]. The low bandgap (3.067±0.004 eV) for the bi-phasic anatase-rutile structure is attributed to rutile which has a relative narrow bandgap of 3.0 eV [20, 40]. Increasing the temperature and NaOH concentration resulted in the production of a pure anatase structure with a relative high bandgap value (3.258±0.003-3.298±0.005 eV). When the temperature was set at 190°C with the NaOH concentration at 10 M or 15 M, the TiO<sub>2</sub>-B phase (3.20 eV) was predominant in samples #4, #6 and #8 together with a small quantity of the anatase phase. The existence of TiO<sub>2</sub>-B lowered the bandgap range from 3.203±0.006 to 3.229±0.009 eV, since TiO<sub>2</sub>-B has a bandgap of 3.20 eV [16, 41]. A few studies have shown existence of the TiO<sub>2</sub>-B phase when using temperatures and a NaOH concentration of 150-190°C and 10 M, respectively [17, 41].

Photoluminescence studies (Figure 3.8b) for selected samples and the control (TiO<sub>2</sub> NPs) further demonstrated that the phase structure had the fundamental effect on bandgap. All the samples showing the peak at 3.4 eV was due to the anatase fundamental band-to-band transition [42-44]. The tail from 3.1 to 3.4 eV in addition to the peak at 3.4 eV is assigned to the exciton trapped at shallow level defects for sample #15 [42, 43]. However, the biphasic anatase-rutile (samples #1 and commercial TiO<sub>2</sub> NPs) and biphasic anatase-TiO<sub>2</sub>-B (such as samples #4) showed broader peak with a tail from 2.9 to 3.4 eV in addition to the anatase peak at 3.4 eV when compared to pure anatase (#15). This long tail is attributed to the lower band-to-band transition of rutile and TiO<sub>2</sub>-B crystal phase [45]. The band from 2.4 to 2.6 eV is due to the oxygen vacancies which behaved as the centers of indirect recombination [43].

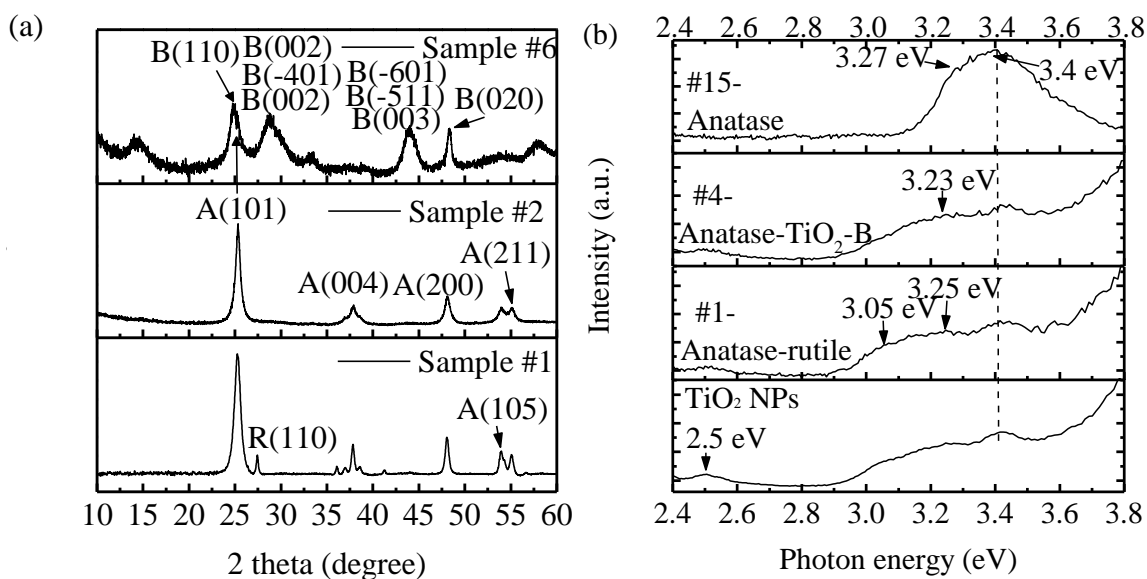


Figure 3.8: (a) XRD pattern for samples #1, #2, and #6, and (b) Photoluminescence spectra for samples #1, #4, #15 and TiO<sub>2</sub> nanoparticles (NPs) excited by 300 nm (4.13 eV) irradiation.

Notes: <sup>a</sup> Synthesis parameter details are listed in Table 3.2, <sup>b</sup> A(101) peak is positioned on the shoulder, and <sup>c</sup> A, R and B represent anatase, rutile and TiO<sub>2</sub>-B, respectively.

Table 3.4. Phase structures and corresponding bandgap energies for all BBD samples

Sample #	Phase	Bandgap (eV)
2, 3, 5, 7 and 9-15	Anatase	3.258±0.003 - 3.298±0.004
1	Anatase and rutile	3.067±0.004
4, 6, 8	Anatase and TiO <sub>2</sub> -B	3.203±0.006 - 3.229±0.009

### 3.3.6. Crystal size and specific surface area (SSA)

The mean crystal sizes (L, nm) for sample #1-15 (Table 3.5) were calculated using Scherrer equation (Eq. 3.3) and the XRD data (data not shown).

$$L = K\lambda / \beta \cdot \cos\theta \quad [46] \quad (3.3)$$

where K,  $\lambda$  and  $\beta$  represent the shape factor (0.89), the wavelength of XRD radiation (0.154 nm) and the half maximum of a full peak, respectively.

The main effect of hydrothermal synthesis factors on the mean crystal size are shown in Figure 3.9a. The synthesis temperature and NaOH concentration significantly affected the crystal size, whereas, the TiO<sub>2</sub> precursor concentration did not impact the crystal size. Decreasing crystal size was closely linked with lower temperatures and lower NaOH concentrations. Increasing the hydrothermal temperature from 120°C to 190°C or NaOH concentration from 5 M to 15 M resulted in an increase in the mean Q1D TiO<sub>2</sub> crystal size from 9.5±0.1 nm to 58.3±0.3 nm. The interaction plots (Figure 3.9b) indicate a similar pattern as shown in the main effect plot. This observation is consistent with work reported by Bavykin et al. [8]

Table 3.5: Design matrix for experimental factors and responses of mean crystal size and BET SSA at different factor levels.

Expt. # <sup>a</sup>	Factors <sup>b</sup>			Mean crystal size L (nm)	BET SSA (m <sup>2</sup> g <sup>-1</sup> )
	T (°C)	NaOH (M)	TiO <sub>2</sub> (g·L <sup>-1</sup> )		
1	120	5	43	9.5±0.1	181±5
2	190	5	43	21.5±0.2	123±5
3	120	15	43	19.9±0.1	137±3
4	190	15	43	57.2±0.4	36±3
5	120	10	14	18.2±0.1	145±5
6	190	10	14	46.4±0.3	72±3
7	120	10	100	17.6±0.2	149±5
8	190	10	100	48.2±0.3	39±3
9	150	5	14	16.9±0.2	172±5
10	150	15	14	58.3±0.3	60±3
11	150	5	100	21.2±0.2	139±4
12	150	15	100	18.8±0.2	137±5
13	150	10	43	19.5±0.2	150±4
14	150	10	43	19.8±0.2	151±5
15	150	10	43	20.5±0.2	148±5

Notes: <sup>a</sup> Expt. # represents one experimental condition, and <sup>b</sup> T, NaOH and TiO<sub>2</sub> represents temperature, NaOH concentration and TiO<sub>2</sub> concentration, respectively.

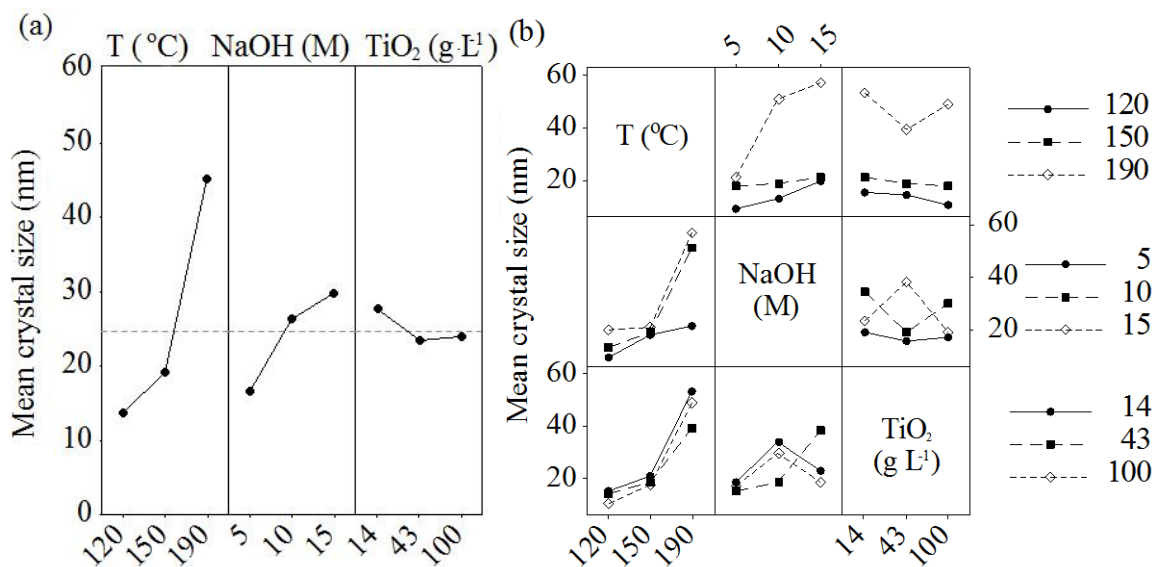


Figure 3.9: (a) main effects, and (b) interaction plots for mean crystal size (nm).

Note: T = temperature; NaOH = NaOH concentration and TiO<sub>2</sub> = TiO<sub>2</sub> concentration.

The BET SSA for all the BBD samples, the main effects and interaction plots of the three hydrothermal synthesis factors on the mean BET SSA are shown in Table 3.5 and Figure 3.10, respectively. The contrasting date trend in Figure 3.10 for the BET SAA with the trend for the mean crystal size in Figure 3.9 suggests since the high BET SSA was closely linked to the small crystal size for the Q1D TiO<sub>2</sub> nanostructure. Increasing the BET SSA was closely correlated with decreasing temperatures and decreasing NaOH concentration. The highest BET SSA was  $181 \pm 5 \text{ m}^2 \text{ g}^{-1}$  for Q1D TiO<sub>2</sub> sample #1 synthesized at 120°C, 5 M NaOH and  $43 \text{ g} \cdot \text{L}^{-1}$  while the lowest BET SSA was observed for sample #4 synthesized at 190°C, 15 M NaOH and  $43 \text{ g} \cdot \text{L}^{-1}$  TiO<sub>2</sub>. The TiO<sub>2</sub> concentration did not impact the BET SSA. The interaction plots (Figure 3.10b) indicate a similar pattern as shown in the main effect plot. A larger BET SSA value was observed with decreasing temperatures as well as decreasing the NaOH concentration.

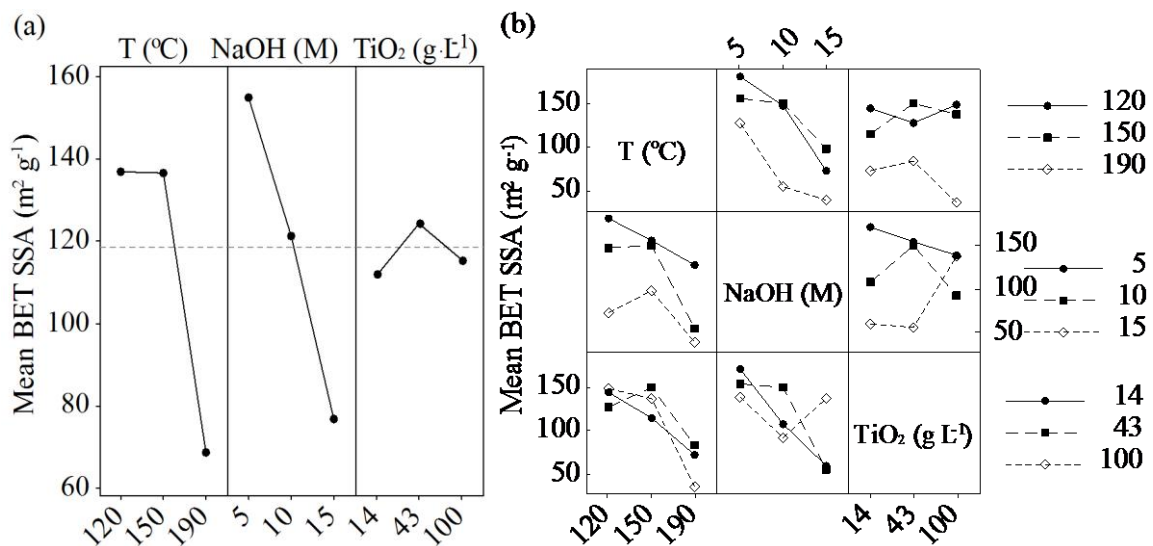


Figure 3.10: (a) main effects and, and (b) interaction plots for mean BET SSA ( $\text{m}^2 \text{ g}^{-1}$ ). Note: T = temperature; NaOH = NaOH concentration and TiO<sub>2</sub> = TiO<sub>2</sub> concentration.



### 3.3.7. Effects of crystal size/specific surface area on Q1D TiO<sub>2</sub> bandgap

Interaction between temperature and the NaOH concentration on bandgap, mean crystal size and BET SSA is shown in Figure 3.11. The trend for bandgap was relatively the same as that for BET SSA, whereas an opposite trend was observed for the mean crystal size. One exception observed at 120°C and 5 M NaOH was a biphasic anatase-rutile structure with the lowest bandgap of 3.067±0.004 eV. This exception is due to difference in the phase structure. For the Q1D TiO<sub>2</sub> samples synthesized at 150°C, a decrease in mean crystal size which was observed from 21.2±0.2 to 16.9±0.2 nm (an increase in BET SSA) resulted in increasing the bandgap from 3.265±0.008 eV to 3.2967±0.005 eV. This bandgap decrease is due to the size quantization effect [10, 21]. Smaller crystal size was closely linked to a larger bandgap according to size quantization effect [10, 21]. From the Figure 11, the mean bandgap, E (eV), is:

$$E = 3.4188 - 0.00727 \times L \quad (18 \leq L \leq 21 \text{ and } T = 150 \text{ } ^\circ\text{C}) \quad (3.4)$$

Where L (nm) is the mean crystal sizes and T is temperature. In addition, the Q1D TiO<sub>2</sub> synthesized at 190°C further demonstrated that decreasing the crystal size from 57.2±0.4 to 21.5±0.2 nm (increasing the BET SSA) was closely correlated with increasing the bandgap from 3.203±0.005 to 3.274±0.002 eV. The mean bandgap, E (eV), is

$$E = 3.307 - 0.00178 \times L \quad (21 \leq L \leq 58 \text{ and } T = 190 \text{ } ^\circ\text{C}) \quad (3.5)$$

Where L (nm) is the mean crystal sizes and T is temperature.

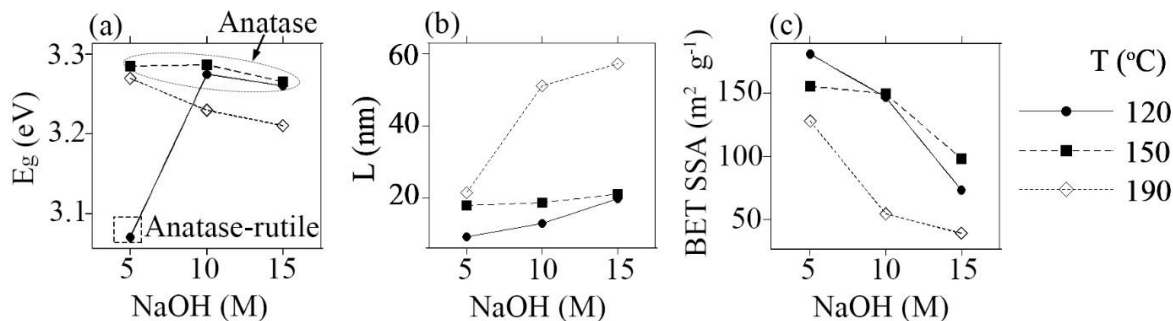


Figure 3.11: Interaction between temperature and NaOH concentration on (a). bandgap, (b). mean crystal size (L) and (c). BET SSA.

Note: L, T and NaOH represent mean crystal size, temperature and NaOH concentration, respectively.

### 3.4. Conclusions

A statistical model was developed to evaluate the effects of the hydrothermal synthesis factors on the Q1D TiO<sub>2</sub> bandgap. The AD statistic indicated an adequate fit of the statistical model to the experimental data. The model predicted optimized hydrothermal conditions for maximum and minimum bandgap. The temperature and NaOH concentration significantly affected the Q1D TiO<sub>2</sub> bandgap, phase, crystal size and SSA, whereas the TiO<sub>2</sub> concentration effect was negligible. The phase structure was the main reason for changes in bandgap. When compared to pure anatase, decreasing bandgap was observed for the biphasic anatase-rutile and anatase-TiO<sub>2</sub>-B structures. In addition, lower temperature and NaOH concentration were associated with decreasing crystal size and increasing SSA. The correlation between decreasing the crystal size (increasing the SSA) with increasing bandgap was due to the size quantization effect. The statistical model developed in this work can be employed to produce Q1D TiO<sub>2</sub> with controllable bandgap, phase, mean crystal size and BET SSA for photocatalytic applications.

**3.5. References**

- [1] A. Fujishima, K. Honda, Electrochemical photolysis of water at a semiconductor electrode, *Nature* 238 (1972) 37-38.
- [2] B. O'Regan, M. Gratzel, A low-cost, high-efficiency solar cell based on dye-sensitized colloidal TiO<sub>2</sub> films, *Nature* 353 (1991) 737-740.
- [3] J. Miao, R. Zhang, L. Zhang, Photocatalytic degradations of three dyes with different chemical structures using ball-milled TiO<sub>2</sub>, *Mater. Res. Bull.* 97 (2018) 109-114.
- [4] M. Stodolny, R. Zagrodnik, G. Nowaczyk, S. Jurga, Size-controlled synthesis of anatase nanobrush structures with higher crystal density, *Mater. Res. Bull.* 94 (2017) 335-341.
- [5] S. Malato, P. Fernández-Ibáñez, M.I. Maldonado, J. Blanco, W. Gernjak, Decontamination and disinfection of water by solar photocatalysis: Recent overview and trends, *Catal. Today* 147 (2009) 1-59.
- [6] A. Di Paola, E. Garcia-Lopez, G. Marci, L. Palmisano, A survey of photocatalytic materials for environmental remediation, *J. Hazard. Mater.* 211-212 (2012) 3-29.
- [7] P. Roy, S. Berger, P. Schmuki, TiO<sub>2</sub> nanotubes: synthesis and applications, *Angew. Chem. Int. Ed.* 50 (2011) 2904-2939.
- [8] D.V. Bavykin, V.N. Parmon, A.A. Lapkin, F.C. Walsh, The effect of hydrothermal conditions on the mesoporous structure of TiO<sub>2</sub> nanotubes, *J. Mater. Chem.* 14 (2004) 3370-3378.
- [9] H.Y. Zhu, Y. Lan, X.P. Gao, S.P. Ringer, Z.F. Zheng, D.Y. Song, J.C. Zhao, Phase transition between nanostructures of titanate and titanium dioxides via simple wet-chemical reactions., *J. Am. Chem. Soc.* 127 (2005) 6730-6736.

- [10] X. Chen, S.S. Mao, Titanium dioxide nanomaterials: Synthesis, properties, modifications, and applications, *Chem. Rev.* 107 (2007) 2891-2959.
- [11] B. Chen, J. Hou, K. Lu, Formation mechanism of TiO<sub>2</sub> nanotubes and their applications in photoelectrochemical water splitting and supercapacitors, *Langmuir* 29 (2013) 5911-5919.
- [12] T. Kasuga, M. Hiramatsu, A. Hoson, T. Sekino, K. Niihara, Formation of titanium oxide nanotube, *Langmuir* 14 (1998) 3160-3163.
- [13] Y. Tang, Y. Zhang, J. Deng, J. Wei, H.L. Tam, B.K. Chandran, Z. Dong, Z. Chen, X. Chen, Mechanical force-driven growth of elongated bending TiO<sub>2</sub>-based nanotubular materials for ultrafast rechargeable lithium ion batteries, *Adv. Mater.* 26 (2014) 6111-6118.
- [14] Y.V. Kolenko, K.A. Kovnir, A.I. Gavrillov, Hydrothermal synthesis and characterization of nanorods of various titanates and titanium dioxide, *J. Phys. Chem. B* 110 (2006) 4030-4038.
- [15] H.-W. Shim, D.K. Lee, I.S. Cho, K.S. Hong, D.-W. Kim, Facile hydrothermal synthesis of porous TiO<sub>2</sub> nanowire electrodes with high-rate capability for Li ion batteries, *Nanotechnology* 21 (2010) 255706-255709.
- [16] H.-L. Kuo, C.-Y. Kuo, C.-H. Liu, J.-H. Chao, C.-H. Lin, A highly active bi-crystalline photocatalyst consisting of TiO<sub>2</sub> (B) nanotube and anatase particle for producing H<sub>2</sub> gas from neat ethanol, *Catal. Lett.* 113 (2007) 7.
- [17] A.R. Armstrong, G. Armstrong, J. Canales, P.G. Bruce, TiO<sub>2</sub>-B nanowires, *Angew. Chem.* 116 (2004) 2336-2338.

- [18] S. Preda, M. Rutar, P. Umek, M. Zaharescu, A study of thermal properties of sodium titanate nanotubes synthesized by microwave-assisted hydrothermal method, *Mater. Res. Bull.* 71 (2015) 98-105.
- [19] T. Peng, S. Ray, S.S. Veeravalli, J.A. Lalman, F. Arefi-Khonsari, The role of hydrothermal conditions in determining 1D TiO<sub>2</sub> nanomaterials bandgap energies and crystal phases, *Mater. Res. Bull.* 105 (2018) 104-113.
- [20] D. Reyes-Coronado, G. Rodriguez-Gattorno, M.E. Espinosa-Pesqueira, C. Cab, R. de Coss, G. Oskam, Phase-pure TiO<sub>2</sub> nanoparticles: anatase, brookite and rutile, *Nanotechnology* 19 (2008) 145605.
- [21] I. Okura, M. Kaneko, *Photocatalysis science and technology*, Springer and Kodansha, Japan, 2002.
- [22] R. Lopez, R. Gomez, Band-gap energy estimation from diffuse reflectance measurements on sol-gel and commercial TiO<sub>2</sub>: a comparative study, *J. Sol-Gel Sci. Technol.* 61 (2012) 1-7.
- [23] S. Ray, J.A. Lalman, N. Biswas, Using the Box-Benkhen technique to statistically model phenol photocatalytic degradation by titanium dioxide nanoparticles, *Chem. Eng. J.* 150 (2009) 15-24.
- [24] S.R. Shanmugam, S.R. Chaganti, J.A. Lalman, D.D. Heath, Statistical optimization of conditions for minimum H<sub>2</sub> consumption in mixed anaerobic cultures: effect on homoacetogenesis and methanogenesis, *Int. J. Hydrogen Energ.* 39 (2014) 15433-15445.
- [25] J. Zhang, Q. Xu, Z. Feng, M. Li, C. Li, Importance of the relationship between surface phases and photocatalytic activity of TiO<sub>2</sub>, *Angew. Chem. Int. Ed.* 47 (2008) 1766-1769.

- [26] T. Kogure, T. Umezawa, Y. Kotani, A. Matsuda, M. Tatsumisago, T. Minami, Formation of TiO<sub>2</sub>(B) nanocrystallites in sol - gel - derived SiO<sub>2</sub> - TiO<sub>2</sub> film, *J. Am. Ceram. Soc.* 82 (1999) 3248-3250.
- [27] Y.Q. Wang, G.Q. Hu, X.F. Duan, H.L. Sun, Q.K. Xue, Microstructure and formation mechanism of titanium dioxide nanotubes, *Chem. Phys. Lett.* 365 (2002) 427-431.
- [28] A. Chemseddine, T. Moritz, Nanostructuring titania: control over nanocrystal structure, size, shape, and organization, *Eur. J. Inorg. Chem.* 1999 (1999) 235-245.
- [29] J. Huang, Y. Cao, Q. Huang, H. He, Y. Liu, W. Guo, M. Hong, High-temperature formation of titanate nanotubes and the transformation mechanism of nanotubes into nanowires, *Cryst. Growth Des.* 9 (2009) 3632-3637.
- [30] H. Luo, C. Wang, Y. Yan, Synthesis of mesostructured titania with controlled crystalline framework, *Chem. Mater.* 15 (2003) 3841-3846.
- [31] H. Zhang, J.F. Banfield, Understanding polymorphic phase transformation behavior during growth of nanocrystalline aggregates: insights from TiO<sub>2</sub>, *J. Phys. Chem. B* 104 (2000) 3481-3487.
- [32] S.S. Veeravalli, S.R. Chaganti, J.A. Lalman, D.D. Heath, Optimizing hydrogen production from a switchgrass steam exploded liquor using a mixed anaerobic culture in an upflow anaerobic sludge blanket reactor, *Int. J. Hydrogen Energ.* 39 (2014) 3160-3175.
- [33] Z. Lai, M. Zhu, X. Yang, J. Wang, S. Li, Optimization of key factors affecting hydrogen production from sugarcane bagasse by a thermophilic anaerobic pure culture, *Biotechnol. Biofuels* 7 (2014) 131-111.

- [34] A. Reungsang, S. Pattra, S. Sittijunda, Optimization of key factors affecting methane production from acidic effluent coming from the sugarcane juice hydrogen fermentation process, *Energies* 5 (2012) 4746-4757.
- [35] M.A. Stephens, EDF statistics for goodness of fit and some comparisons, *J. Am. Stat. Assoc.* 69 (1974) 730.
- [36] H. Cheng, J. Ma, Z. Zhao, L. Qi, Hydrothermal preparation of uniform nanosize rutile and anatase particles, *Chem. Mater.* 7 (1995) 663-671.
- [37] T.P. Feist, P.K. Davies, The soft chemical synthesis of TiO<sub>2</sub> (B) from layered titanates, *J. Solid State Chem.* 101 (1992) 275-295.
- [38] M.C. Hidalgo, M. Maicu, J.A. Navío, G. Colón, Photocatalytic properties of surface modified platinised TiO<sub>2</sub>: effects of particle size and structural composition, *Catal. Today* 129 (2007) 43-49.
- [39] G. Tian, H. Fu, L. Jing, B. Xin, K. Pan, Preparation and characterization of stable biphasic TiO<sub>2</sub> photocatalyst with high crystallinity, large surface area, and enhanced photoactivity, *J. Phys. Chem. C* 112 (2008) 3083-3089.
- [40] S.-D. Mo, W.Y. Ching, Electronic and optical properties of three phases of titanium dioxide: Rutile, anatase, and brookite, *Phys. Rev. B* 51 (1995) 13023-13032.
- [41] D. Yang, H. Liu, Z. Zheng, Y. Yuan, J.-c. Zhao, E.R. Waclawik, X. Ke, H. Zhu, An efficient photocatalyst structure: TiO<sub>2</sub>(B) nanofibers with a shell of anatase nanocrystals, *J. Am. Chem. Soc.* 131 (2009) 17885-17893.
- [42] D. Pan, N. Zhao, Q. Wang, S. Jiang, X. Ji, L. An, Facile synthesis and characterization of luminescent TiO<sub>2</sub> nanocrystals, *Adv. Mater.* 17 (2005) 1991-1995.

- [43] B. Liu, L. Wen, X. Zhao, The photoluminescence spectroscopic study of anatase  $\text{TiO}_2$  prepared by magnetron sputtering, *Mater. Chem. Phys.* 106 (2007) 350-353.
- [44] J. Liqiang, S. Xiaojun, X. Baifu, W. Baiqi, C. Weimin, F. Honggang, The preparation and characterization of La doped  $\text{TiO}_2$  nanoparticles and their photocatalytic activity, *J. Solid State Chem.* 177 (2004) 3375-3382.
- [45] H. Nakajima, T. Mori, Q. Shen, T. Toyoda, Photoluminescence study of mixtures of anatase and rutile  $\text{TiO}_2$  nanoparticles: Influence of charge transfer between the nanoparticles on their photoluminescence excitation bands, *Chem. Phys. Lett.* 409 (2005) 81-84.
- [46] A. Monshi, M.R. Foroughi, M.R. Monshi, Modified Scherrer equation to estimate more accurately nano-crystallite size using XRD, *World J. Nano Sci. Eng.* 02 (2012) 154-160.



## **OPTIMIZING QUASI-ONE-DIMENSION TIO<sub>2</sub> PHOTOCATALYST: PHOTODEGRADING AQUEOUS ORGANIC POLLUTANTS AND PHOTOCATALYTIC HYDROGEN PRODUCTION**

### **Synopsis**

Q1D TiO<sub>2</sub> nanomaterials have attracted attention in photocatalytic applications because TiO<sub>2</sub> possess both high oxidative and reduction potential. In this study, Q1D TiO<sub>2</sub> samples with different phase structure, crystal size and specific surface area (SSA) were produced using a hydrothermal method by varying the reaction conditions (temperature, alkaline concentration and the TiO<sub>2</sub> precursor concentration). A 3-factor 3-level Box Behnken design (BBD) with three replicates (15 conditions) at the center point was employed to evaluate and optimize the hydrothermal synthesis factors for photocatalytic activities in terms of photodegrading organic pollutants and photocatalytic H<sub>2</sub> production.

The BBD demonstrated that the temperature and the NaOH concentration significantly affected the Q1D TiO<sub>2</sub> crystal size, phase structure, bandgap and subsequently photocatalytic activity based on the photocatalysis of organic pollutants and photocatalytic H<sub>2</sub> production. The organic pollutants examined in this study include rhodamine B (RhB), phenol, methyl orange (MO) and methylene blue (MB). Lower temperature (120°C) and lower NaOH (5 M) concentration was linked to producing a biphasic anatase-rutile structure with optimum photodegradation rate. However, the optimum conditions for maximizing H<sub>2</sub> production rate of Q1D TiO<sub>2</sub> was found at 126°C, 15 M NaOH and 49 gL<sup>-1</sup> TiO<sub>2</sub>. The Q1D TiO<sub>2</sub> containing an anatase phase with mean

crystal size of  $20.1 \pm 0.2$  nm showed maximum  $H_2$  production rate of  $475 \pm 12 \mu\text{mol} \cdot \text{h}^{-1}$  (quantum efficiency ( $\epsilon$ ) =  $20.2 \pm 0.5\%$ ). This  $\epsilon$  value is 5-fold of the value using Pt-TiO<sub>2</sub> photocatalyst ( $\epsilon=4\%$ ) in a pure water substrate. Under a higher temperature (190°C) and with  $\geq 10$  M NaOH concentration, the presence of TiO<sub>2</sub>-B phase resulted in the lowest photocatalytic activity in terms of photocatalysis of organic pollutants and photocatalytic  $H_2$  production.

#### 4.1. Introduction

Titanium dioxide (TiO<sub>2</sub>) is a widely studied and efficient photocatalyst for degrading organic pollutants and  $H_2$  production [1-6]. The TiO<sub>2</sub> photocatalytic properties are strongly dependent on properties such as phase structure, crystal size and specific surface area (SSA) [7-9]. Hydrothermal synthesis factors such as reaction temperature and the TiO<sub>2</sub> to NaOH molar ratio can significantly affect the Q1D TiO<sub>2</sub> phase structure, crystal size and SSA as discussed in Chapter 3 [10-12]. However, the impact of individual factor and factors in combination on the photocatalytic characteristics of Q1D TiO<sub>2</sub> has not been addressed in the past studies [13].

Many studies have reported improved photocatalytic activities for Q1D TiO<sub>2</sub> synthesized under different hydrothermal synthesis factors when compared to TiO<sub>2</sub> nanoparticles [3, 12, 14-19]. Recently, Kuo *et al.* [2] reported that 1% Pt/TiO<sub>2</sub> nanotubes (TNTs) synthesized at a relatively low temperature were 20% more effective in producing  $H_2$  gas from ethanol when compared to a 1% Pt/TiO<sub>2</sub> nanoparticle photocatalyst using UV light. Perera *et al.* [12] synthesized reduced graphene oxide (RGO)-TNTs composites using a one-step alkaline hydrothermal process. These

researchers reported Q1D TiO<sub>2</sub> such as TNT were homogeneously dispersed between RGO sheets with the composites showing significant improvements in the photocatalysis of malachite green dye under UV light when compared to TiO<sub>2</sub> nanoparticles [12]. However, these and other researchers did not address the impact of hydrothermal synthesis factors on Q1D TiO<sub>2</sub> photocatalytic activities [2, 3, 12, 14-19].

The work carried out is to execute the fourth objective. The first part of the fourth objective (Section 4.3) was to optimize selected hydrothermal process conditions for the maximum photocatalytic activity of Q1D TiO<sub>2</sub> in terms of photolysis organic pollutants. The second part of the fourth objective (Section 4.4) was to optimize selected hydrothermal process conditions for the maximum photocatalytic H<sub>2</sub> production rate.

## **4.2. Photocatalytic experiments**

### *4.2.1. Preparation of the Q1D nanometric TiO<sub>2</sub> photocatalyst*

Q1D TiO<sub>2</sub> photocatalyst was prepared by homogeneously mixing a specified quantity of TiO<sub>2</sub> nanoparticles (Aeroxide TiO<sub>2</sub> P25, Evonik Corporation, Parsippany, New Jersey) with 70 mL of a NaOH solution. Table 4.1 list the reaction temperature, NaOH concentration and TiO<sub>2</sub> concentration for hydrothermal process. The mixture was poured into a 100 mL Teflon® capped container. The Teflon® container was placed into a stainless-steel bomb, capped and heated to a desired temperature for 48 h and subsequently, cooled to room temperature. The resulting product was centrifuged and rinsed with 0.1 M HCl solution. The white paste was repeatedly washed (5 times) with deionized water and calcinated at 400°C for 2 h to produce Q1D TiO<sub>2</sub> [2].

Table 4.1: Levels of the selected hydrothermal synthesis factors.

Levels	Factors		
	A	B	C
	T (°C)	NaOH (M)	TiO <sub>2</sub> (g·L <sup>-1</sup> )
-1	120	5	14
0	150	10	43
+1	190	15	100

Note: T, NaOH and TiO<sub>2</sub> represent temperature, NaOH and TiO<sub>2</sub> concentration.

#### 4.2.2. Photocatalysis of selected organic pollutants

The photodegrading organic pollutants experiments were conducted using the photoreactor configuration described in Chapter 2 (Section 2.3.10).

The reaction mixture consisted of 0.1 g·L<sup>-1</sup> of photocatalysts and a specific model pollutant concentration. The model pollutants examined in the study include RhB (purity: 95%), phenol (purity: 99.5%), MO (purity: 85%) and MB (purity: 82%). All aqueous organic pollutants used in the photocatalysis study were purchased from Sigma-Aldrich (ON, Canada). The concentration of RhB, MO, phenol and MB in the reaction mixture was 10 mg·L<sup>-1</sup>, 20 mg·L<sup>-1</sup>, 20 mg·L<sup>-1</sup>, 10 mg·L<sup>-1</sup>, respectively. The reaction mixture (50 mL) containing a specific model pollutant and photocatalyst was ultrasonicated for 15 mins and left under dark conditions with magnetic stirring for 1 h to establish an adsorption-desorption equilibrium. The reaction mixture in quartz tubes was thereafter exposed to UV light for a specific duration. The duration of exposure to UV was maintained at 15 minutes for all experiments. A fixed amount of the reaction mixture (5 mL) was withdrawn at specific time intervals (of 3-5 minutes). The sample was centrifuged (5,000 rpm for 10 minutes) and filtered using a 0.1 µm polyvinylidene difluoride (PVDF) filter (Sigma-Aldrich, Oakville, ON) to separate the photocatalyst

from the reaction mixture. The residual aqueous organic pollutants concentration (C) in the filtrate was determined by measuring the optical absorbance at 554 nm, 464 nm and 664 nm for RhB, MO and MB, respectively, using a UV–visible spectrophotometer. The detection limits for RhB, MO and MB were  $1 \mu\text{g}\cdot\text{L}^{-1}$ . The residual phenol concentration was determined using a high-performance liquid chromatograph (HPLC) (Dionex Ultimate 3000, Sunnyvale, CA). The HPLC configuration details were described in Chapter 2 (Section 2.3.7). The residual concentration of the pollutant was used to determine the reaction rate of decoloration or disappearance, termed hereafter as the apparent reaction rate. The apparent reaction rate was modeled using a pseudo-first order rate equation (Eq. 4.1) [20-23].

$$\frac{-dC}{dt} = kC \quad (4.1)$$

where k is the apparent reaction rate constant ( $\text{min}^{-1}$ ), C is the organic pollutant concentration ( $\text{mg}\cdot\text{L}^{-1}$ ) and  $-dC/dt$  is the pseudo-first order reaction rate.

#### *4.2.3. Photocatalytic hydrogen production*

The photocatalytic experiments conducted using the photoreactor are described in Chapter 2 (Section 2.3.10).

The 50-mL reaction mixture in sealed quartz tube contains  $0.2 \text{ g}\cdot\text{L}^{-1}$  of the photocatalyst and 20% (v/v) ethanol. The reaction mixture was purged with nitrogen ( $\text{N}_2$ ) gas to remove oxygen. Next, the reaction mixture was ultrasonicated and magnetically stirred under dark condition for 1 h before initiation of the reaction with UV light. Then,

the reaction mixture was exposed to UV light and kept at  $37\pm 2^\circ\text{C}$ . At specific time intervals, the  $\text{H}_2$  concentration was determined using a gas chromatograph (GC) (Varian CP-3800). The GC configuration was described in Chapter 2 (Section 2.3.8).  $\text{N}_2$  gas was used as a carrier gas at a flowrate of  $15 \text{ mL min}^{-1}$ . The photocatalyst reaction mixture was irradiated for 5 h using a 300-nm monochromatic UV light with an average intensity of  $9 \text{ mW}\cdot\text{cm}^{-2}$ . The irradiation area for each tube was  $58 \text{ cm}^2$ .

The quantum efficiency ( $\epsilon$ ) was calculated using equations (Eq. 4.2) and (Eq. 4.3) [24].

$$N = \frac{E\lambda}{hc} = \frac{9 \times 10^{-3} \times 58 \times 3600 \times 300 \times 10^{-9}}{6.626 \times 10^{-34} \times 3 \times 10^8} = 2.83 \times 10^{21} \quad (4.2)$$

$$\begin{aligned} \epsilon &= \frac{2 \times \text{the number of evolved hydrogen molecules}}{\text{the number of incident photons}} \times 100\% \\ &= \frac{2 \times 6.02 \times 10^{23} \times H_2 \text{ production rate} \times 1h}{2.83 \times 10^{21}} \times 100\% \end{aligned} \quad (4.3)$$

Where N is the photon number in 1 h; E is the energy rate of incident photons;  $\lambda$  is the wavelength in nm; h is Planck's constant; and c is the photon velocity.

### **4.3. The impact of hydrothermal factors on the photodegradation of aqueous organic pollutants**

The morphology, crystal size, crystal phase, bandgap and SSA of the samples were described in Chapter 3 using field emission scanning electron microscope (FESEM

(JEOL, Japan), high-resolution transmission electron microscopy (HRTEM) (300 kV, JEOL 3010, Japan), X-ray diffraction (XRD) analysis Raman spectra analysis, UV-visible spectra analysis, Nitrogen adsorption–desorption isotherms. The Q1D TiO<sub>2</sub> phase structure, crystal size and SSA which were affected by hydrothermal factors strongly impact the photocatalytic activities. In this chapter, the main results from Chapter 3 will be used.

*4.3.1. Selecting model chemicals to assess implementing photodegradation as a technology for treating wastewater effluents and drinking water supplies*

Industrial development coupled with acceleration in population growth rate has led to the occurrence of toxic organic pollutants in wastewater effluents and drinking water supplies. RhB, MO and MB are produced as aqueous pollutants in textile, leather, paper, plastic and dye industries. Phenol has been classified with carcinogenic, teratogenic, and mutagenic properties for more than 30 years [21]. Exposure to these toxic organic pollutants is linked to serious concerns such as environmental damage and human diseases [25]. Conventional municipal biological wastewater treatment facilities are ineffective in removing toxic organic pollutants [26-28]. In addition, operational costs and the generation of secondary toxic pollutants are major problems associated with municipal biological treatment [29, 30]. Advanced oxidation processes such as ozone (O<sub>3</sub>), O<sub>3</sub>/H<sub>2</sub>O<sub>2</sub>, Fenton and photo-Fenton are promising technologies for the degradation of toxic organic pollutants [31]. However, major disadvantages of these processes include incomplete degradation and the production of toxic byproducts. Photocatalysis

based on TiO<sub>2</sub> is an emerging technology which can overcome these problems [26, 27, 31-35].

The advantage of using dyes such as RhB, MO and MB is easily measuring their concentration by using UV-visible spectroscopy and subsequently the apparent degradation rate [36]. However, the dye decolorization and decomposition might be caused by dye sensitization [36]. In the case of dye sensitization, the dye is excited by irradiation. Phenol can be excited by irradiation with short wavelength (<270 nm) [37]. In this study, a 300-nm monochrome UV light were employed as irradiation source. The degradation of phenol was closely linked to photoreaction catalyzed by photocatalyst.

#### *4.3.2. Experimental design and statistical analysis*

A three factor three level BBD was used to determine the experimental conditions for hydrothermal synthesis of the Q1D TiO<sub>2</sub> photocatalyst capable of maximizing the apparent reaction rate constant (min<sup>-1</sup>). Accordingly, the apparent reaction rate constant (min<sup>-1</sup>) was selected as a response variable and RhB was selected as a model pollutant for the optimization study. The hydrothermal conditions for synthesis of Q1D TiO<sub>2</sub>, namely, temperature (°C), NaOH concentration (M) and TiO<sub>2</sub> concentration (g·L<sup>-1</sup>) were the selected experimental factors for the optimization study. Each experimental factor was varied at a low level (designated as -1), a central level (designated as 0) and a high level (designated as +1) (Table 4.1). The method is defined with three center points and 12 experimental points with three replicates under each condition (Table 4.2). A full quadratic model was evaluated for the response function and the apparent reaction rate constant (min<sup>-1</sup>) was analyzed statistically using Minitab 15 (Minitab Inc., State College,



PA). Three experiments (triplicates) designated as #13 to #15 under the same conditions were performed at the center points to evaluate the magnitude of error in the experimental analysis.

Table 4.2: Design matrix for the hydrothermal synthesis factors and responses (apparent reaction rate constant) at different factor levels.

Sample #	Factors <sup>a</sup>			Response	Phase <sup>b</sup>
	T (°C)	NaOH (M)	TiO <sub>2</sub> (g·L <sup>-1</sup> )	Apparent reaction rate constant (k) (min <sup>-1</sup> )	
1	120	5	43	0.4227±0.0107	A+R
2	190	5	43	0.2962±0.0102	A
3	120	15	43	0.1703±0.0053	A
4	190	15	43	0.0936±0.0007	A+B
5	120	10	14	0.2596±0.0039	A
6	190	10	14	0.1171±0.0041	A+B
7	120	10	100	0.1832±0.0037	A
8	190	10	100	0.1268±0.0017	A+B
9	150	5	14	0.2569±0.0039	A
10	150	15	14	0.1703±0.0093	A
11	150	5	100	0.1993±0.0013	A
12	150	15	100	0.1525±0.0081	A
13	150	10	43	0.1906±0.0062	A
14	150	10	43	0.2062±0.0076	A
15	150	10	43	0.2187±0.0099	A

Notes: <sup>a</sup> T, NaOH and TiO<sub>2</sub> represent temperature, NaOH and TiO<sub>2</sub> concentration, and <sup>b</sup> A, R and B correspond to anatase, rutile and TiO<sub>2</sub>-B, respectively.

#### 4.3.3. Rhodamine b photocatalysis

Under the different hydrothermal factors, the Q1D TiO<sub>2</sub> samples showed differences in the photocatalytic efficiency with respect to the discoloration or disappearance of RhB. Profiles for the residual RhB concentration versus time and the corresponding apparent reaction rate constant, k ( $kt = -\ln(C/C_0)$ ), are shown in Figure 4.1 for selected samples (Table 4.3). Control experiments were performed with P25 nanoparticles and without a photocatalyst. The average apparent RhB photocatalysis rate constant value (designated as “apparent RhB k”) was 0.003 min<sup>-1</sup> without a photocatalyst; however, with the

addition of P25 nanoparticles, the average value increased to  $0.3483 \pm 0.0051 \text{ min}^{-1}$ . Only the Q1D  $\text{TiO}_2$  photocatalyst synthesized under conditions designated as #1 ( $120^\circ\text{C}$ , 5 M NaOH and  $43 \text{ g}\cdot\text{L}^{-1} \text{ TiO}_2$ ) showed the apparent RhB  $k$  value ( $0.4227 \pm 0.0107 \text{ min}^{-1}$ ) larger than the value for the  $\text{TiO}_2$  P25 photocatalyst (Table 4.3 and Figure 4.1). The average apparent RhB  $k$  value for the sample #4 and sample #9 were  $0.0936 \pm 0.0007 \text{ min}^{-1}$  and  $0.2569 \pm 0.0107 \text{ min}^{-1}$ , respectively. Depending on the hydrothermal synthesis conditions, the average apparent reaction rate constant value,  $k$ , varied from  $0.0936 \pm 0.0007 \text{ min}^{-1}$  to  $0.4227 \pm 0.0039 \text{ min}^{-1}$  (Table 4.2). For sample #1, the enhanced RhB photocatalytic activity was due to the formation of the active biphasic anatase-rutile structure [9, 38] with the Q1D nanostructure [15, 39] synthesized under relatively lower synthesis temperature of  $120^\circ\text{C}$  and lower NaOH concentration of 5 M. The lowest photocatalytic activity was detected for sample #4 containing the  $\text{TiO}_2$ -B phase. Based on the apparent reaction rate constants, the hydrothermal synthesis conditions significantly affected the photocatalytic activity.

Table 4.3: apparent RhB photocatalysis rate constant value ( $k$ ) for selected samples.

<b>Experiment</b>	<b><math>k</math> (<math>\text{min}^{-1}</math>)</b>	<b>Linear regression <math>R^2</math> value</b>
Control (no photocatalyst)	$0.0030 \pm 0.0002$	0.9991
P25	$0.3483 \pm 0.0051$	0.9823
#1	$0.4227 \pm 0.0107$	0.9729
#4	$0.0936 \pm 0.0007$	0.9674
#9	$0.2569 \pm 0.0039$	0.9740

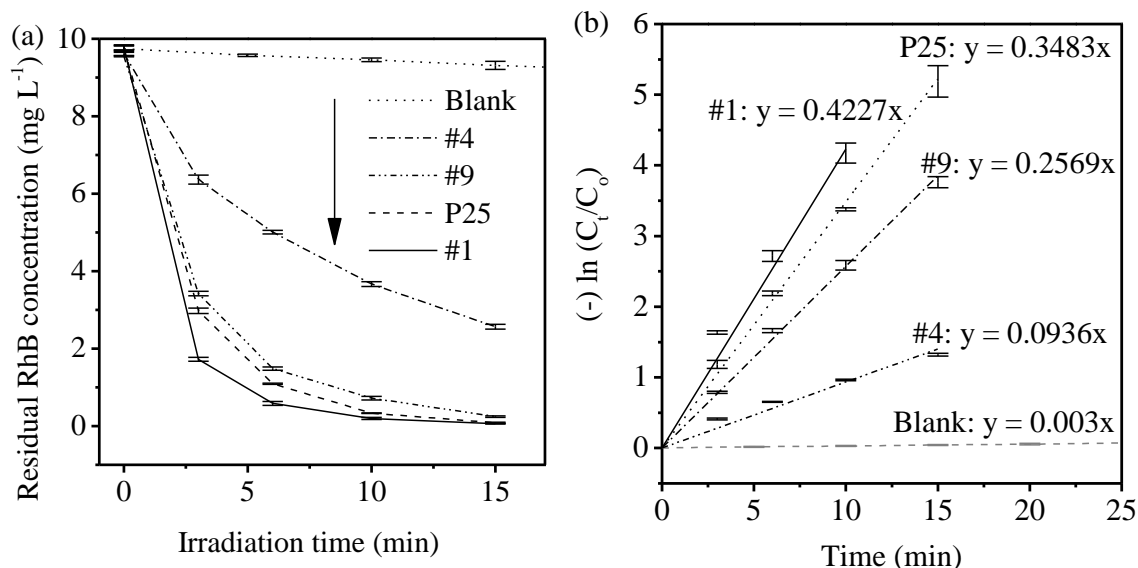


Figure 4.1: RhB photocatalysis concentration profiles and kinetic plots for selected samples. (a) RhB photocatalysis concentration profiles using 300 nm UV light, and (b) apparent reaction rate constant.

Notes: <sup>a</sup> BBD conditions are shown in Table 4.2, <sup>b</sup> blank represents no photocatalyst, and <sup>c</sup> RhB represents rhodamine b.

#### 4.3.4. Impact of hydrothermal conditions on the apparent rhodamine b degradation constant $k$

The main effects plot showing the impact of three hydrothermal synthesis factors on the response apparent RhB  $k$  is illustrated in Figure 4.2a. Increasing the apparent RhB  $k$  was observed with decreasing temperatures to 120°C. A similar trend was observed with decreasing NaOH levels; however, with increasing TiO<sub>2</sub> concentration to 43 g·L<sup>-1</sup>, the apparent RhB  $k$  increased and reached a peak value. The apparent RhB  $k$  value decreased with further increasing the TiO<sub>2</sub> precursor concentration from 43 to 100 g·L<sup>-1</sup> TiO<sub>2</sub>. The interaction plots (Figure 4.2b) indicate a similar pattern as shown in the main effect plot. A larger apparent RhB  $k$  value was obtained at lower temperatures as well as lower NaOH concentration and with the TiO<sub>2</sub> level set at 43 g·L<sup>-1</sup>.

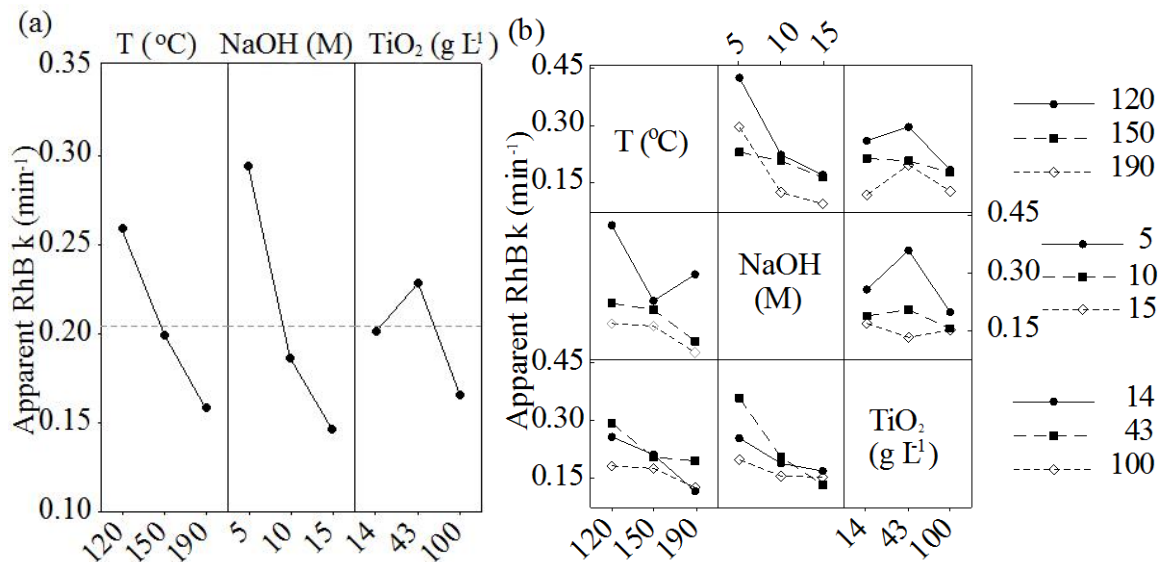


Figure 4.2: (a) main effects, and (b) interaction plots for the different experimental factors.

Notes: <sup>a</sup>. T = temperature; NaOH = NaOH concentration and TiO<sub>2</sub> = TiO<sub>2</sub> concentration, and <sup>b</sup>. apparent RhB k represents “apparent rhodamine b photocatalysis rate constant value”.

#### 4.3.5. Modeling and optimization of hydrothermal synthesis

The impact of varying the hydrothermal synthesis factors, namely, temperature, NaOH concentration and the TiO<sub>2</sub> concentration (Figure 4.2) is crucial for optimizing the Q1D TiO<sub>2</sub> photocatalytic activity. Optimization using a ‘one-factor-at-a-time’ (OFAT) approach is tedious and time-consuming. Furthermore, the OFAT method is unable to account for interactions between the various hydrothermal synthesis factors. In this study, response surface methodology (RSM) was utilized to evaluate the impacts of various hydrothermal synthesis factors on the Q1D TiO<sub>2</sub> photocatalytic activity.

A multiple regression analysis was used to develop a quadratic equation (Eq. 4.4). Eq. 4.4 describes the apparent reaction rate constant (k) for RhB photocatalysis or the apparent RhB k as a function of the hydrothermal process factors.

$$k = 1.184 - 0.00665X_1 - 0.0520X_2 - 0.00102X_3 + 0.000041X_1X_2 + 0.000014X_1X_3 + 0.000103X_2X_3 + 0.000013X_1^2 + 0.001296X_2^2 - 0.000014X_3^2 \quad (4.4)$$

where  $k$  ( $\text{min}^{-1}$ ) is the apparent RhB rate constant,  $X_1$ ,  $X_2$  and  $X_3$  represents the hydrothermal synthesis temperature ( $^{\circ}\text{C}$ ), NaOH concentration (M) and  $\text{TiO}_2$  concentration ( $\text{g}\cdot\text{L}^{-1}$ ), respectively.

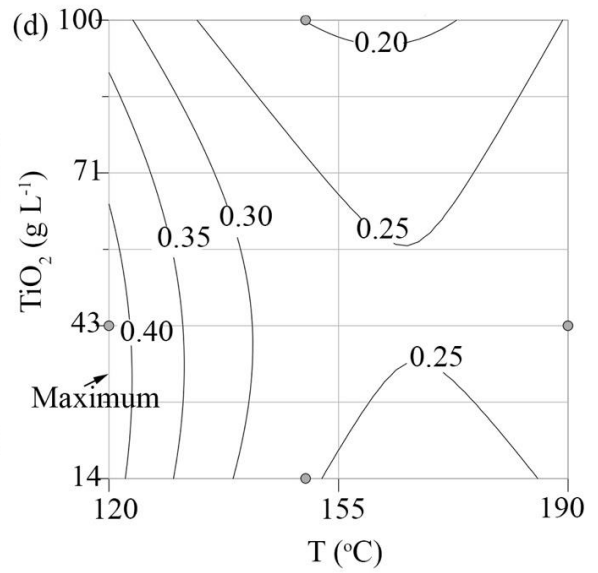
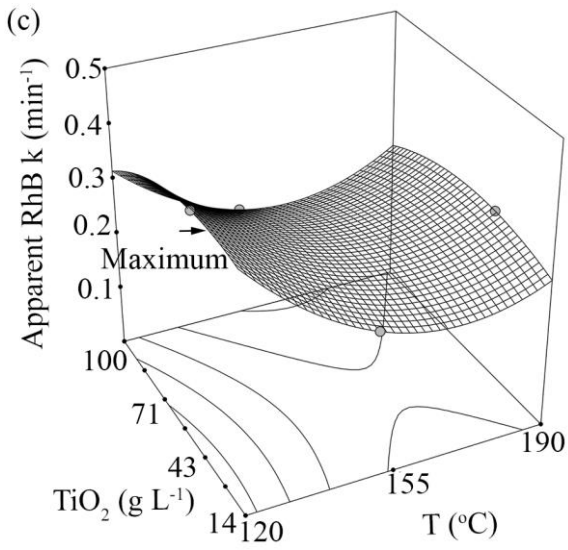
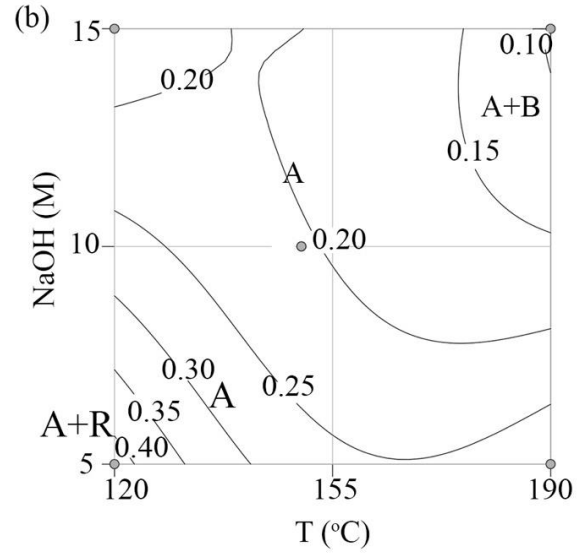
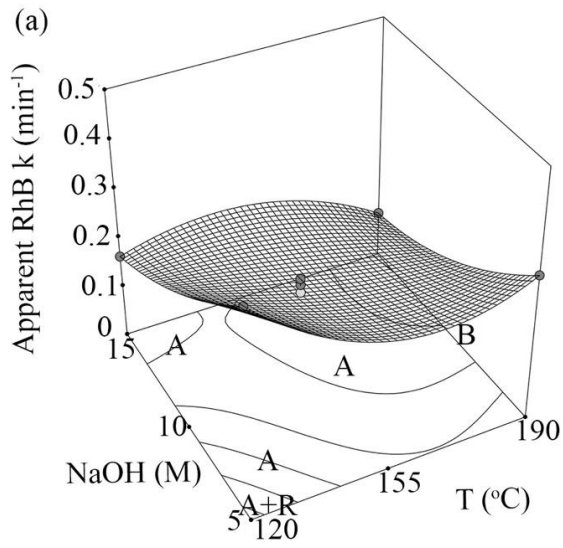
The three-dimensional response surface and the corresponding contour plots of experimental factors and apparent RhB  $k$  is presented in Figure 4.3 with the indication of crystal phase results. The main crystal phase and bandgap results are shown in Table 4.4. The response surface plots indicate interaction between the temperature and NaOH concentration (Figure 4.3a and b) with larger  $k$  values was observed at lower temperatures and lower NaOH concentrations. In addition, the lower temperatures and lower NaOH concentrations which are associated with smaller crystal size (Figure 4.4) resulted in higher SSA and a subsequent increase in the reaction kinetics. The larger  $k$  value was associated with a biphasic anatase-rutile phase structure which showed lowest bandgap. With increasing temperature or NaOH concentration, the rutile phase composition decreased while increasing the anatase phase composition with an enhanced bandgap. The increasing temperature and NaOH concentration which was linked to the increasing crystal size (Figure 4.4) gave rise to decreasing SSA and  $k$  values. When the temperature was set at  $190^{\circ}\text{C}$  with the NaOH concentration at 10 M or 15 M, the  $\text{TiO}_2$ -B phase (large crystal size) was predominant with a low amount of the anatase phase. Anatase is an excellent photocatalyst; however, in combination with the rutile phase, the biphasic anatase-rutile photocatalytic activity is enhanced, such as in the case of  $\text{TiO}_2$

P25 and sample #1. When the two crystal phases are combined, the separation of photogenerated holes and electrons is facilitated with an increase in the photocatalytic activity [9]. Supporting work [38] employing surface enhanced Raman spectroscopy (SERS) has shown that mixed crystal structure TiO<sub>2</sub> with an appropriate proportion of anatase and rutile phase is favorable to increasing TiO<sub>2</sub>-to-molecule charge-transfer as well as interaction between the rutile and anatase phases.

Table 4.4: Phase structures and corresponding bandgap energies for all BBD samples

Sample #	Phase	Bandgap (eV)
1	Anatase-rutile	3.067±0.004
2, 3, 5, 7, 9, 10, 11, 12, 13, 14, 15	Anatase	3.258±0.003 - 3.298±0.004
4, 6, 8	TiO <sub>2</sub> -B-anatase	3.203±0.006 - 3.229±0.009

Higher k values were observed at lower temperatures and TiO<sub>2</sub> concentrations of approximately 35 g·L<sup>-1</sup> (Figure 4.3c and d). The photocatalytic activity of the Q1D TiO<sub>2</sub> structure was slightly affected by the TiO<sub>2</sub> precursor concentration. Enhancing the k value could be achieved at a TiO<sub>2</sub> concentration of 35 g·L<sup>-1</sup>. Interactions between the NaOH and TiO<sub>2</sub> concentrations (Figure 4.3e and f) confirmed that a low NaOH concentration and an appropriate TiO<sub>2</sub> concentration of approximately 35 g·L<sup>-1</sup> TiO<sub>2</sub> were important factors causing an increase in the k value.



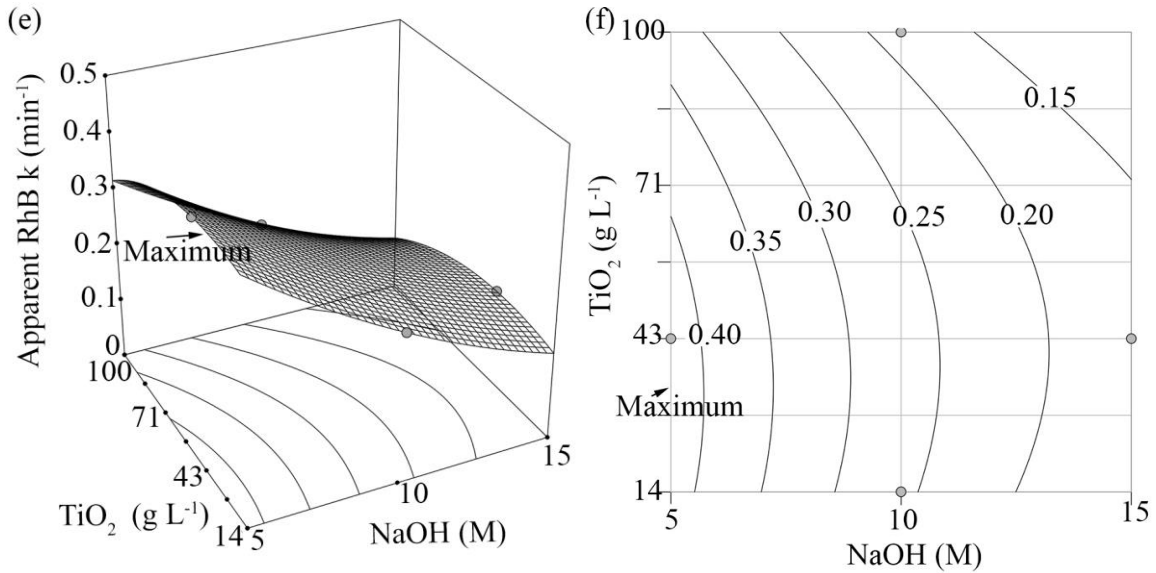


Figure 4.3: Response surface and contour plots for factors affecting the apparent RhB rate constant (min<sup>-1</sup>): (a) and (b) for hydrothermal temperature and NaOH concentration set at 43 g·L<sup>-1</sup> TiO<sub>2</sub>, (c) and (d) for hydrothermal temperature and TiO<sub>2</sub> concentration set at 5 M NaOH concentration, and (e) and (f) for NaOH concentration and TiO<sub>2</sub> concentration set at 120°C temperature.

Notes: <sup>a</sup> The crystal phase for different synthesis condition were discussed in Chapter 3 in detail, <sup>b</sup> apparent RhB  $k$  represents “apparent rhodamine b photocatalysis rate constant value”, and <sup>c</sup> A, B and R represent anatase, TiO<sub>2</sub>-B and rutile phases, respectively.

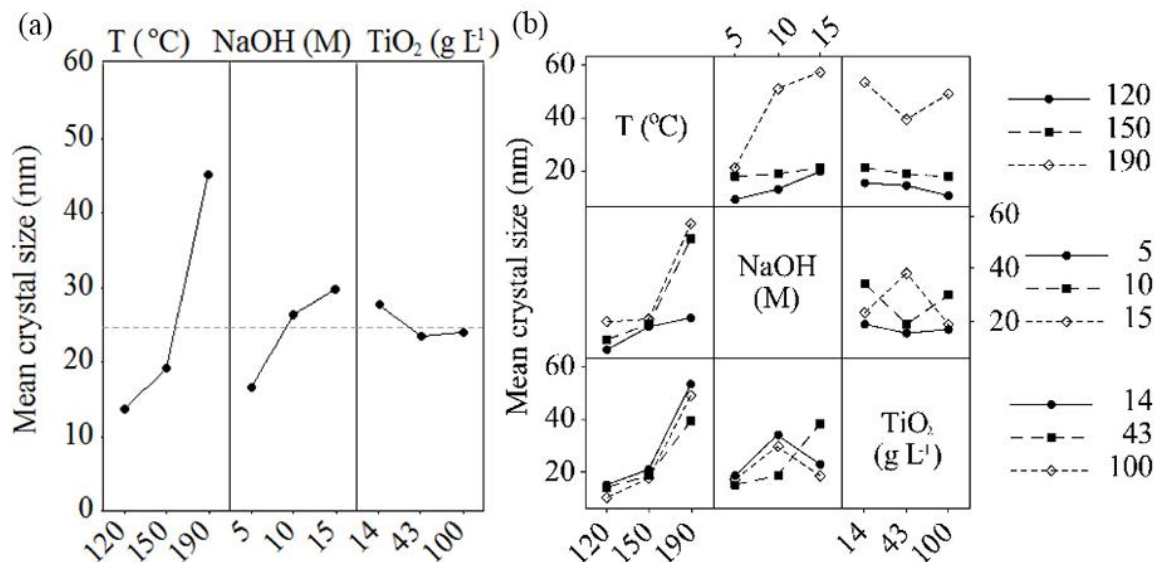


Figure 4.4: (a) Main effect of hydrothermal factors on the crystal size of Q1D TiO<sub>2</sub>, and (b) interaction plots for the effect of different factors on crystal size of Q1D TiO<sub>2</sub>.

Note: The results are from Chapter 3.



Locating the region of maximum response (apparent RhB  $k$ ) was conducted using the D-optimality index. Within the factor space under consideration, the D-optimality index was determined using the Minitab<sup>®</sup> software optimization function. The D-optimality index range from 0 to 1 represents the ideal and worst cases, respectively. The D-optimality plot for the apparent RhB  $k$  for all the different factors beginning from the low factor-level setting is shown in Figure 4.5. A D-optimality value of 0.8990 with a maximum photocatalysis rate (response) of  $0.4412 \text{ min}^{-1}$  was determined under conditions set at  $120^\circ\text{C}$ , 5M NaOH and  $26.0 \text{ g}\cdot\text{L}^{-1} \text{ TiO}_2$ . Additional experiments were conducted to verify the optimum  $k$  value under the optimized hydrothermal conditions at  $120^\circ\text{C}$ , 5M NaOH and  $26.0 \text{ g}\cdot\text{L}^{-1} \text{ TiO}_2$ . The predicted value was slightly underestimated when compared to the observed  $k$  of  $0.4506 \pm 0.0107 \text{ min}^{-1}$ . The apparent RhB  $k$  for Q1D  $\text{TiO}_2$  synthesized using the optimized conditions was approximately 30% larger when compared to the commercial P25 and anatase/ $\text{TiO}_2$ -B prepared using a surfactant molecular self-assembly process [40], respectively.

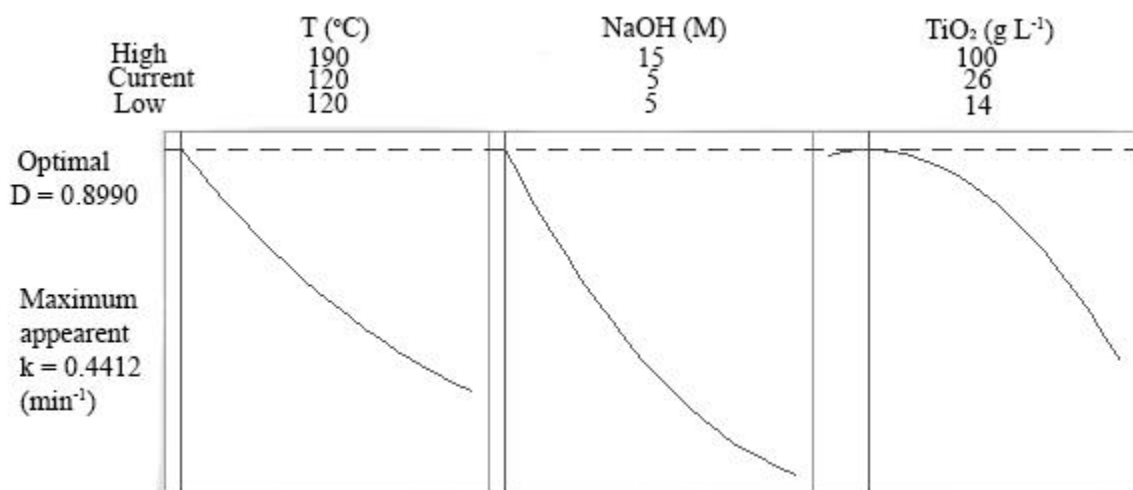


Figure 4.5: Optimality plot to locate optimum factor levels for maximized response  $k$  ( $\text{min}^{-1}$ ).

#### 4.3.6. Response surface model development

An analysis of variance (ANOVA) was employed to evaluate the model full quadratic equation (Eq. 4.4) to determine the significance and adequacy of the model (Table 4.5). Terms with a p-value less than 0.05 are statistically significant, whereas the terms with a p-value greater than 0.05 are insignificant [40-43]. A p-value of 0 (less than 0.05) and F-value (24.46) greater than F-critical value (2.01 at 5% level of significance) for the model indicates that the quadratic model is statistically significant since most of the terms are significant. The F-value of 24.46 for model was greater than the F-critical value of 2.01 (at 5% level of significance) [41-44]. However, temperature (°C) x temperature (°C) and temperature (°C) x NaOH concentration (M) with p-value larger than 0.05 are statistically insignificantly, indicating these two variables had no individual effect on the response (Eq. 4.4). Statistically insignificant terms in the full quadratic model were deleted using a backward elimination method [42]. The final response surface model is designated as equation (Eq. 4.5):

$$k = 0.8 - 0.002081X_1 - 0.04479X_2 - 0.00092X_3 + 0.000014X_1X_3 + 0.000102X_2X_3 + 0.001247X_2^2 - 0.000023X_3^2 \quad (4.5)$$

where  $k$  ( $\text{min}^{-1}$ ) is the apparent RhB photocatalytic rate constant,  $X_1$ ,  $X_2$  and  $X_3$  represents temperature (°C), NaOH concentration (M) and  $\text{TiO}_2$  concentration ( $\text{g}\cdot\text{L}^{-1}$ ), respectively. All terms are statistically significant in equation (Eq. 4.5).

Table 4.5: ANOVA results of the experimental response at each factor level.

Source	DF <sup>a</sup>	Seq. SS <sup>b</sup>	MS <sup>c</sup>	F-value	P-value
Model	9	0.24459	0.02718	24.46	0
X <sub>1</sub>	1	0.04991	0.04991	44.91	0
X <sub>2</sub>	1	0.10955	0.10955	98.58	0
X <sub>3</sub>	1	0.00632	0.00632	5.69	0.023
X <sub>1</sub> <sup>2</sup>	1	0.00281	0.00281	2.53	0.121
X <sub>2</sub> <sup>2</sup>	1	0.01163	0.01163	10.46	0.003
X <sub>3</sub> <sup>2</sup>	3	0.01389	0.01389	12.50	0.001
X <sub>1</sub> X <sub>2</sub>	1	0.00062	0.00062	0.56	0.46
X <sub>1</sub> X <sub>3</sub>	1	0.00535	0.00535	4.82	0.035
X <sub>2</sub> X <sub>3</sub>	1	0.00617	0.00617	5.55	0.024
Error	35	0.03889	0.00111		
Total	44	0.28348			

Notes: <sup>a</sup> DF = degrees of freedom, <sup>b</sup> Seq. SS = sequential sum of square, and <sup>c</sup> MS = mean square.

#### 4.3.7. Response surface model verification

A scatter plot of the experimental values and predicted values from the model equation demonstrated a reasonable correlation for each level (Figure 4.6a). Assessing the adequacy of fitting the model to experimental data was conducted using the Anderson-Darling (AD) statistic. The AD statistic was employed to determine the normal distribution of the residuals (difference between the predicted and experimentally apparent photocatalysis rate constant) (Figure 4.6b) [44]. The AD value (0.231) was below the critical value of the statistic (0.735) for a sample size of 45 and at a 5% level of significance [44, 45]. A p-value (0.793) greater than 0.05 suggest the model prediction fitted reasonably well with the experimental data.

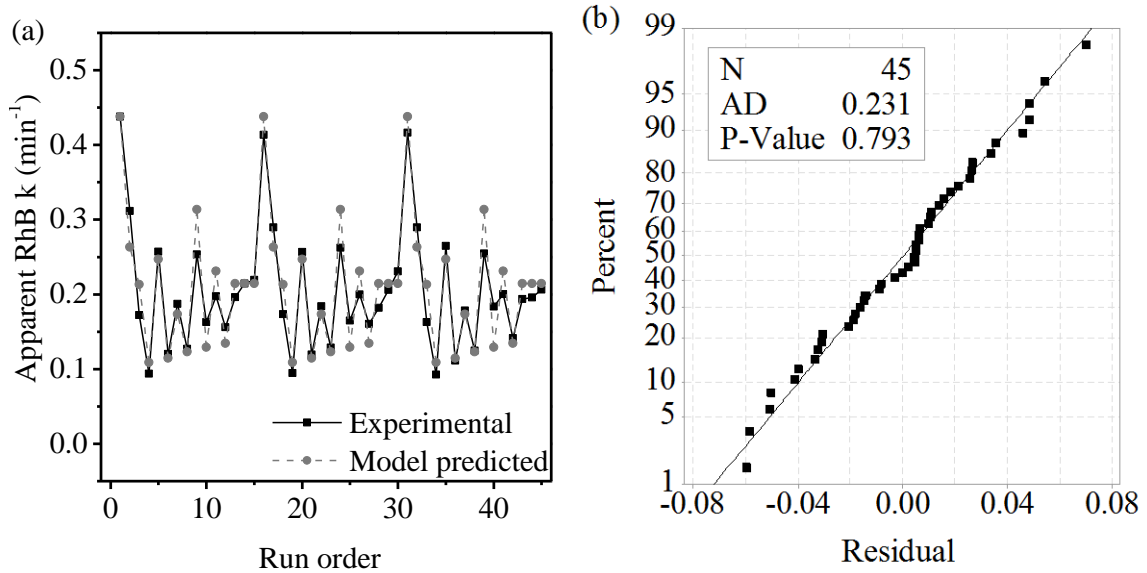
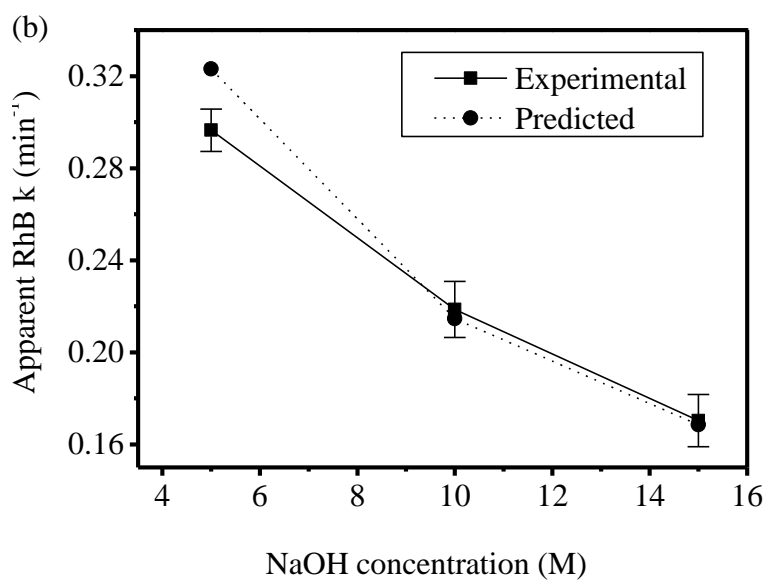
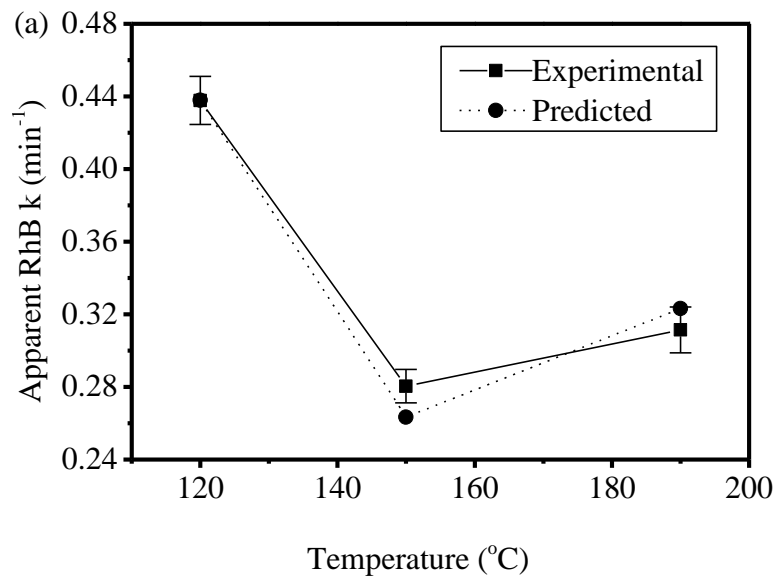


Figure 4.6: Evaluating accuracy of the response surface model. (a) Scatter plot of the apparent RhB  $k$  versus experiment order (45 experiments), and (b) Anderson-Darling normality plot of residuals.

Notes: <sup>a</sup>  $N$  = the number of experiments conducted in this study, <sup>b</sup> P-Value = level of confidence, and <sup>c</sup> AD = Anderson-Darling statistic.

Additional experiments were conducted to validate accuracy of the model within the experimental factors under examination. Each of the three factors was evaluated by employing a separate validation study. The model prediction was in agreement with the experimental results for the temperature ranging from 120°C to 190°C (Figure 4.7a), although the model slightly underestimated and overestimated the apparent RhB  $k$  at 150°C and 190°C, respectively. For the NaOH concentration, the predicted points were consistent with the experimental points with a slight overestimate at 5 M NaOH (Figure 4.7b). For the TiO<sub>2</sub> concentration, the predicted values were slightly underestimated compared to the observed values for each level of TiO<sub>2</sub> concentration (Figure 4.7c). Notably, the trend for varying temperature, the NaOH and TiO<sub>2</sub> concentrations were in agreement with the experimental observations.



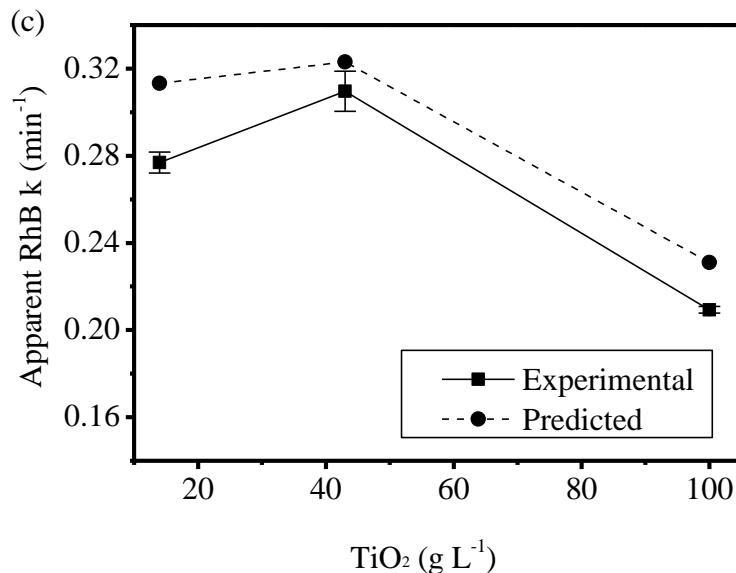
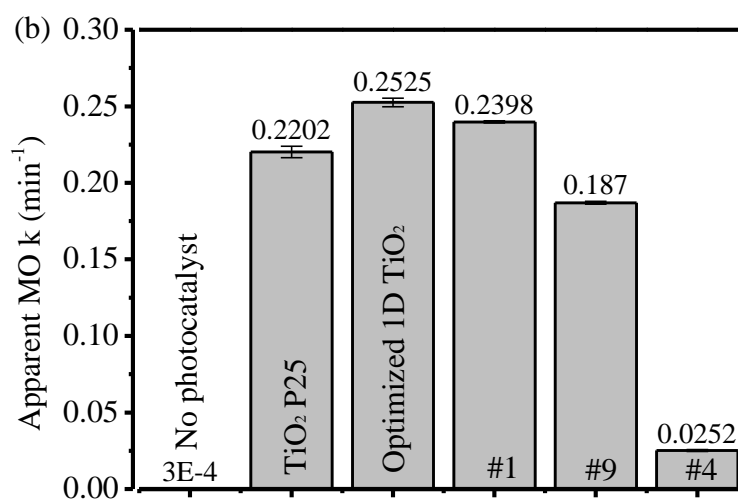
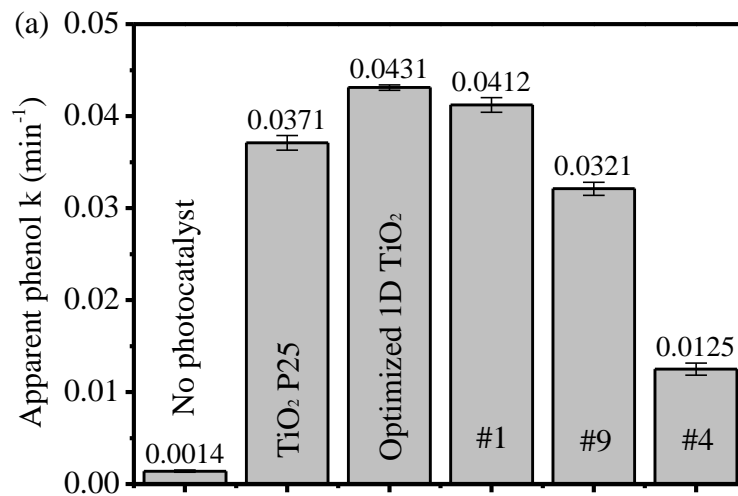


Figure 4.7: Validation study of the response surface model for the varied factors under consideration. (a) apparent RhB  $k$  value versus temperature at experimental conditions set at 5 M NaOH and 43 g·L<sup>-1</sup> TiO<sub>2</sub>, (b) apparent RhB  $k$  versus NaOH concentration at experimental conditions set at 150°C and 43 g·L<sup>-1</sup> TiO<sub>2</sub>, and (c) apparent RhB  $k$  value versus TiO<sub>2</sub> concentration at experimental conditions set at 150°C and 5 M NaOH.

#### 4.3.8. Photocatalysis of other pollutants using the optimized Q1D TiO<sub>2</sub>

The Q1D TiO<sub>2</sub> produced under the optimized conditions was also employed to photodegrade phenol, methyl orange and methylene blue (Figure 4.8). The apparent  $k$  value for each aqueous organic pollutant is shown in Figure 4.8a-c. The data set trend for the apparent  $k$  clearly show that Q1D TiO<sub>2</sub> synthesized under decreasing temperature conditions (e.g. optimized Q1D TiO<sub>2</sub> and sample #1) were correlated with larger  $k$  values. The largest  $k$  value was observed for the optimized Q1D TiO<sub>2</sub>. The apparent  $k$  for phenol, MO and MB when using the optimized Q1D TiO<sub>2</sub> were 1.16, 1.24 and 1.26-fold greater than that of the P25 nanoparticles photocatalyst. The data indicate that the optimized Q1D TiO<sub>2</sub> is a promising photocatalyst for degrading organic pollutants when compared to P25. The small apparent  $k$  of sample #4 for each aqueous organic pollutant clearly indicates TiO<sub>2</sub>-B exerted a negative influence on the photocatalytic activity.



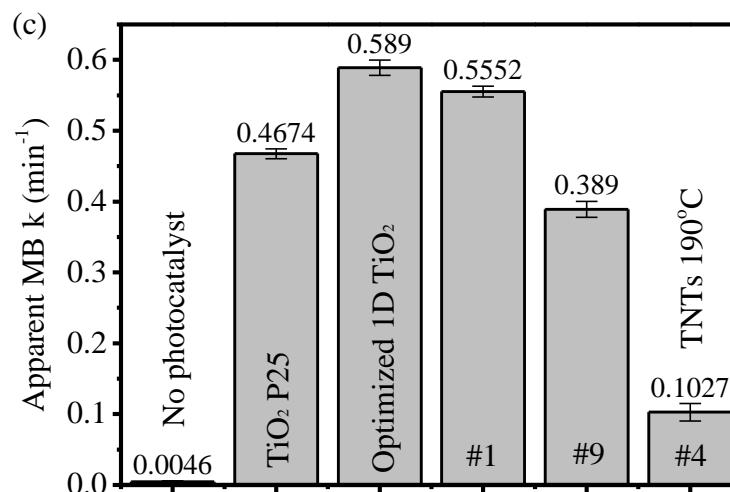


Figure 4.8: Apparent rate constant ( $k$ ) for the different aqueous organic pollutants: (a) phenol, (b) MO, and (c) MB.

Notes: <sup>a</sup> Optimized Q1D TiO<sub>2</sub> were synthesized at 120°C, 5 M NaOH and 26 g·L<sup>-1</sup> TiO<sub>2</sub>, and <sup>b</sup> other samples synthesis conditions are listed Table 4.2.

#### 4.3.9. Photodegradation conclusions

A statistical model was developed to evaluate the effects of the hydrothermal synthesis factors on the photocatalytic activity of Q1D TiO<sub>2</sub> in terms of RhB photocatalysis. The AD statistic indicated an adequate fit of the statistical model to the experimental data. The model predicted a maximum apparent photocatalytic rate constant which was achieved using a biphasic anatase-rutile photocatalyst synthesized at 120°C, 5 M NaOH, and 26 g·L<sup>-1</sup> TiO<sub>2</sub>. The biphasic anatase-rutile structure was favorable for photocatalysis of RhB and other aqueous organic pollutants. The TiO<sub>2</sub>-B phase was produced using a relatively high temperature of 190°C and relatively high NaOH concentrations between 10 to 15 M. This study demonstrated that the TiO<sub>2</sub>-B phase negatively affected the photocatalysis of selected aqueous organic pollutants. When using the optimized biphasic anatase-rutile Q1D TiO<sub>2</sub>, the apparent photocatalysis



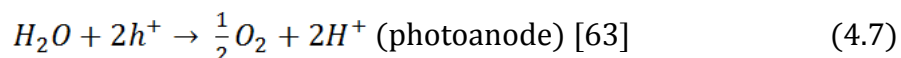
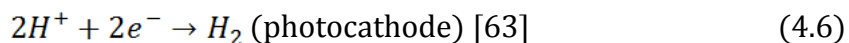
rate constant for phenol, methyl orange and methylene blue under UV light conditions were enhanced by 3-5 fold in comparison to the TiO<sub>2</sub>-B. The study demonstrated using the hydrothermal synthesis of Q1D TiO<sub>2</sub> with controllable phase structure and crystal size was to produce a photocatalyst with optimum photodegrading capabilities.

#### **4.4. The impact of hydrothermal synthesis factors on photocatalytic hydrogen production from water-ethanol mixture**

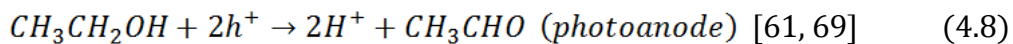
##### *4.4.1. Introduction: Photocatalytic hydrogen production*

Hydrogen is considered as a promising fuel for the future. Q1D TiO<sub>2</sub> nanomaterials have shown significant potential in producing H<sub>2</sub> because of their high electron mobility, large SSA and high mechanical strength [10, 16, 46-48]. Producing Q1D TiO<sub>2</sub> using the alkaline hydrothermal method is a relatively facile process with advantages of large-scale production and varied crystal phase [2, 10, 11, 16, 17, 47-52]. In studies employing the hydrothermal method, Q1D TiO<sub>2</sub> nanomaterials containing anatase [16] or TiO<sub>2</sub>-B [2, 51] were produced under selected conditions. These materials have been utilized to produce hydrogen (H<sub>2</sub>) from the photocatalytic splitting of water or from other substrates such as ethanol [2, 53]. In comparison to TiO<sub>2</sub> nanoparticles, Q1D TiO<sub>2</sub> has shown improved H<sub>2</sub> production from ethanol under UV light conditions [2, 53]. Hydrothermal synthesis factors such as reaction temperature and the TiO<sub>2</sub>-to-NaOH molar ratio can significantly affect the Q1D TiO<sub>2</sub> phase structure, crystal size, SSA [10, 11, 46] and subsequently the H<sub>2</sub> production rate. However, the impact of hydrothermal synthesis factors on the Q1D TiO<sub>2</sub> photocatalytic H<sub>2</sub> production rate and optimization hydrothermal conditions has not been addressed in previous studies.

Many factors affecting the use of photocatalysts to produce H<sub>2</sub> and other fuels include band gap [54, 55], band edge positions [55, 56], charge transfer [57], material stability [58, 59], cocatalyst [60-62], availability [63], complementary metal oxide semiconductor [64, 65] and toxicity [63]. Substrates such as water [57, 66] and ethanol [61] have been used to produce H<sub>2</sub> using photocatalysts. Photocatalyst generates and separates electrons (e<sup>-</sup>) and holes (h<sup>+</sup>) after absorbing photons. Next, the photogenerated electrons reduce H<sup>+</sup> to generate H<sub>2</sub>. The water splitting reaction is described as following half-cell reactions:



In the presence of sacrificial electron donors [67, 68] such as ethanol, the photogenerated holes are consumed by electron donor and subsequently, the recombination of electrons and holes in photocatalyst are suppressed [67, 68]. This significantly increases the H<sub>2</sub> production rate as well as photocatalytic stability [67, 68]. The reaction at the photoanode is described as a water splitting half reaction as follows [61, 69]:



Ethanol, a renewable fuel produced from carbon neutral feedstocks, with a specific heating value of approximately 29.7 MJ·kg<sup>-1</sup> is less when compared to H<sub>2</sub> with a specific heating value of approximately 141.8 MJ·kg<sup>-1</sup> [70]. In addition, the decomposition of

ethanol contributes to a high H<sub>2</sub> production rate and quantum efficiency [71]. Hence, H<sub>2</sub> with a larger energy content is preferred when compared to ethanol as a fuel source.

#### 4.4.2. Experimental design and statistical analysis

The experimental design was based on a 3-factor and 3-level Box-Behnken design (BBD) [40]. The experimental design was used to optimize key process factors (Table 4.1) to improve the H<sub>2</sub> production rate. A total of 15 experimental points (#1 to #15) were conducted with each condition under triplicate (Table 4.6). Experiments, designated as #13, #14 and #15 under the same conditions were conducted as central points to evaluate the magnitude of the error in the study. The experimental factors and H<sub>2</sub> production rate (Y) (response variable) were modeled using Minitab 15 (Minitab Inc., State College, PA) to fit a full quadratic equation (Eq. (4.9)):

$$Y = a_0 + \sum_{i=1}^3 a_i X_i + \sum_{i=1}^3 a_{ii} X_i^2 + \sum_{i=1}^3 \sum_{i < j=2}^3 a_{ij} X_i X_j \quad (4.9)$$

where X<sub>i</sub>'s are input variables which influence the response variable Y, a<sub>0</sub> is an offset term, a<sub>i</sub> is the i<sup>th</sup> linear coefficient, a<sub>ii</sub> is the quadratic coefficient, and a<sub>ij</sub> is the ij<sup>th</sup> interaction coefficient. The X<sub>1</sub>, X<sub>2</sub> and X<sub>3</sub> represent the synthesis temperature, NaOH concentration and TiO<sub>2</sub> concentration, respectively (Table 4.6).

Table 4.6: Design matrix for experimental factors and response (hydrogen production rate, mean crystal size and BET SSA) at different factor levels.

Expt. #	Factors			Response		
	T (°C) (X <sub>1</sub> )	NaOH (M) (X <sub>2</sub> )	TiO <sub>2</sub> (g·L <sup>-1</sup> ) (X <sub>3</sub> )	H <sub>2</sub> production rate (μmol·h <sup>-1</sup> )	Mean crystal size L (nm)	BET SSA (m <sup>2</sup> ·g <sup>-1</sup> )
1	120	5	43	193±7	9.5±0.1	182 ± 5
2	190	5	43	298±10	21.5±0.2	125 ± 5
3	120	15	43	463±14	19.9±0.1	138 ± 3
4	190	15	43	72±4	57.2±0.4	37 ± 3
5	120	10	14	271±8	18.2±0.1	146 ± 5
6	190	10	14	95±4	46.4±0.3	73 ± 3
7	120	10	100	224±8	17.6±0.2	149 ± 5
8	190	10	100	103±5	48.2±0.3	39 ± 3
9	150	5	14	204±8	16.9±0.2	174 ± 5
10	150	15	14	284±10	58.3±0.3	61 ± 3
11	150	5	100	395±13	21.2±0.2	140 ± 4
12	150	15	100	283±10	18.8±0.2	137 ± 5
13	150	10	43	393±13	19.5±0.2	151 ± 4
14	150	10	43	389±12	19.8±0.2	152 ± 5
15	150	10	43	383±8	20.5±0.2	148 ± 5

Note: T, NaOH and TiO<sub>2</sub> represent temperature, NaOH and TiO<sub>2</sub> concentration.

The quadratic model was used to predict reaction conditions which produced Q1D TiO<sub>2</sub> with a maximum H<sub>2</sub> production rate. A D-optimality analysis [41] was performed to find optimal conditions for the three factors under consideration (maximize the H<sub>2</sub> production rate). The coefficient values for fitting the full quadratic model were determined using the experimental response (H<sub>2</sub> production rate) and a multiple regression analysis. An analysis of variance (ANOVA) was conducted using the observed responses for samples #1 to #15) (Table 4.6). Only significant terms with p values < 0.05 were included into the model. A normal distribution plot together with the Anderson-Darling (AD) [21] test was used to determine the adequacy of the model.

#### 4.4.3. Photocatalytic hydrogen production

Significant differences in H<sub>2</sub> production were observed for Q1D TiO<sub>2</sub> samples prepared using different reaction conditions. Hydrogen production versus time profiles are shown in Figure 4.9a for BBD sample #3 plus the control experiment. Control experiments were conducted with P25 nanoparticles and without a photocatalyst. The mean H<sub>2</sub> production rate (Y value) was 0 μmol·h<sup>-1</sup> without a photocatalyst; however, with the addition of P25 nanoparticles, the mean production rate increased to 235±8 μmol·h<sup>-1</sup>. In comparison, the production rate of 463±14 μmol·h<sup>-1</sup> (ε = 19.3±0.6%) for sample #3 (synthesized at 120°C, 15 M NaOH and 43 g·L<sup>-1</sup> TiO<sub>2</sub>) was approximately 2-fold higher than the TiO<sub>2</sub> P25 photocatalyst (ε = 10±0.4%) using ethanol as an electron donor. This ε value was 5-fold of ε value using Pt-TiO<sub>2</sub> as photocatalyst and pure water as substrate under UV light condition [72]. Photocatalytic H<sub>2</sub> production were significantly enhanced using ethanol as electron donor when compared to using water (Figure 4.9b). The H<sub>2</sub> production rates are listed in Table 4.6. The effect of ethanol concentration on H<sub>2</sub> production rate was evaluated using TiO<sub>2</sub> NPs (Figure 4.9b). A 20 v/v% aqueous ethanol level was able to produce the highest H<sub>2</sub> production rate.

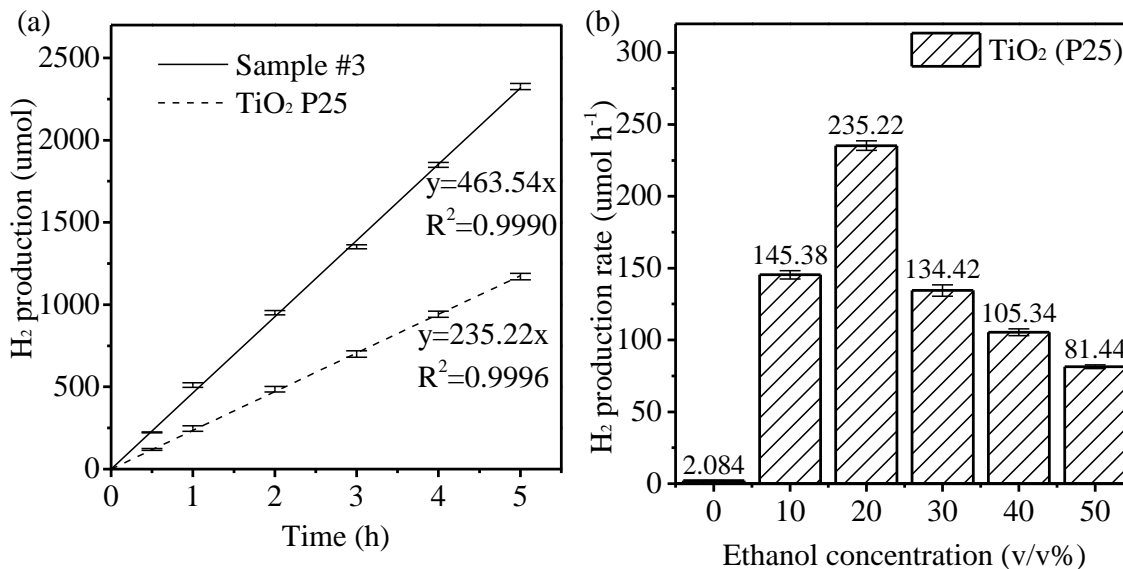


Figure 4.9: (a) Hydrogen production for sample #1 and TiO<sub>2</sub> precursor using 300-nm UV light, and (b) Effect of ethanol concentration on hydrogen production rate for TiO<sub>2</sub> nanoparticles (NPs) (P25).

#### 4.4.4. Impact of hydrothermal conditions on hydrogen production rate

The main effects plot showing the overall impact of three hydrothermal factors for synthesizing Q1D TiO<sub>2</sub> on the response H<sub>2</sub> yield is illustrated in Figure 4.10a. The main effects plots indicate decreasing H<sub>2</sub> yield is correlated with relative high temperature (190°C) and 5 M NaOH concentration. Middle level of TiO<sub>2</sub> concentration is correlated with increasing H<sub>2</sub> yield value. The interaction plots (Figure 4.10b) provide detailed results. A larger H<sub>2</sub> yield value was obtained at lower temperatures as well as higher NaOH concentration and with the TiO<sub>2</sub> level set at 43 g·L<sup>-1</sup>.

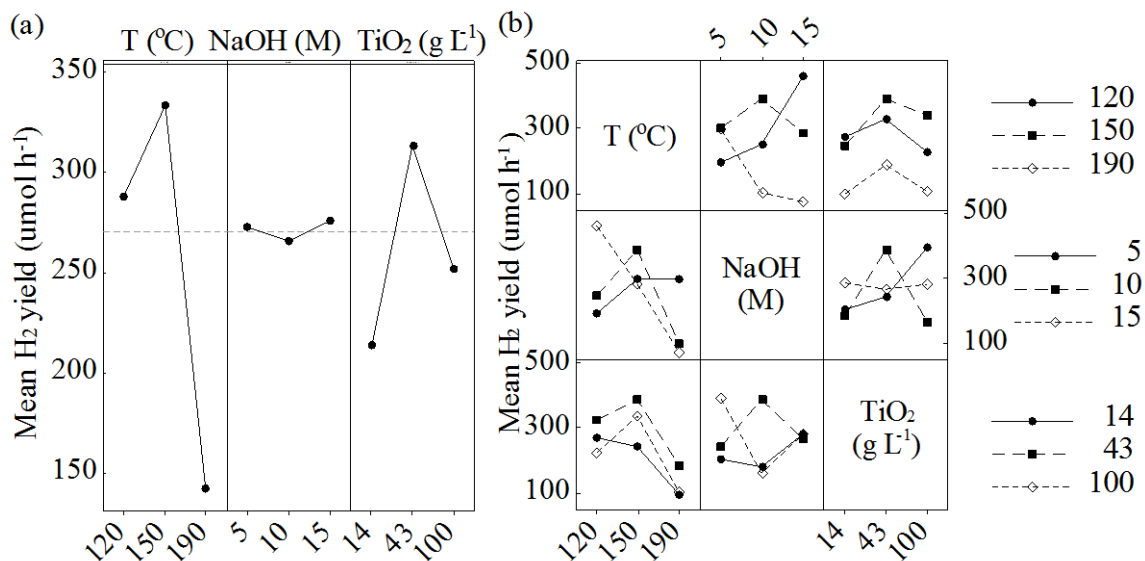


Figure 4.10: Matrix of plots of three factors for hydrogen (H<sub>2</sub>) yield in a three-factor, three-level Box-Behnken design (BBD): (a) main effects for H<sub>2</sub> yield, and (b) two-factor effects for H<sub>2</sub> yield.

Note: T, NaOH and TiO<sub>2</sub> represent temperature, NaOH concentration and TiO<sub>2</sub> concentration, respectively.

#### 4.4.5. Modeling and effects of factors on response variable hydrogen production rate

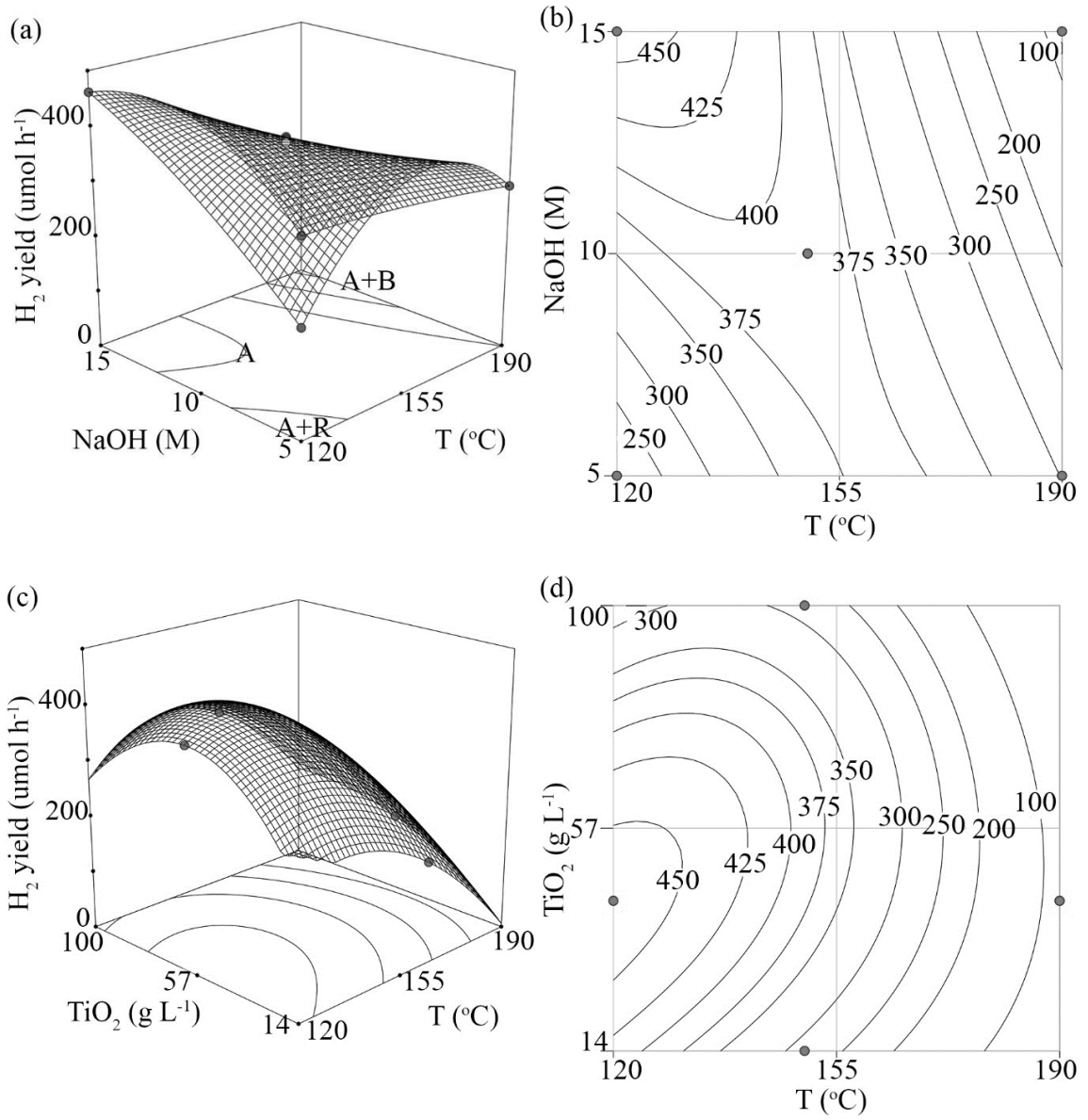
For the response surface optimization study, three sets (replicates) of 15 experiments were conducted to compute the H<sub>2</sub> production rate under 15 conditions (Table 4.6). A multiple regression analysis was used to develop a full quadratic Eq. (4.10) which describes the H<sub>2</sub> production rate, Y, as a function of the hydrothermal process conditions.

$$Y = -2964 + 34.28X_1 + 124.34X_2 + 8.55X_3 - 0.7X_1X_2 + 0.006X_1X_3 - 0.239X_2X_3 - 0.096X_1^2 - 0.269X_2^2 - 0.058X_3^2 \quad (4.10)$$

where Y is the H<sub>2</sub> production rate (μmol·h<sup>-1</sup>), X<sub>1</sub>, X<sub>2</sub> and X<sub>3</sub> represent the reaction temperature (°C), NaOH concentration (M) and TiO<sub>2</sub> concentration (g·L<sup>-1</sup>), respectively.

3D Surface plots and the corresponding contour plots (Figure 4.11) shows the relation among the synthesis factors, phase structure and the H<sub>2</sub> production rate. Interaction between the temperature and the NaOH concentration (Figure 4.11a and b) suggests that both parameters significantly affected the Q1D TiO<sub>2</sub> phase structure and the H<sub>2</sub> production rate. Relative lower temperature at 120°C and a high NaOH concentration at 15 M were closely associate with producing a pure anatase structure with a high H<sub>2</sub> production rate. Increasing temperatures or decreasing NaOH concentrations were correlated with decreasing H<sub>2</sub> production rates. The biphasic anatase-rutile structure, synthesized at 120°C and 5 M NaOH, was linked to a lower H<sub>2</sub> production rate. The biphasic anatase-TiO<sub>2</sub>-B structure synthesized at 190°C and  $\geq 10$  M NaOH showed a significant decrease in the H<sub>2</sub> production rate. These observations indicate the rutile and TiO<sub>2</sub>-B phases are closely correlated with decreasing photocatalytic H<sub>2</sub> evolution activities. Interaction between temperature and TiO<sub>2</sub> concentration (Figure 4.11c and d) and interaction between NaOH concentration and TiO<sub>2</sub> concentration (Figure 4.11e and f) confirmed the decrease of the synthesis temperature and increasing NaOH concentration were closely associated with increasing H<sub>2</sub> production rate. In addition, the surface and contour plots indicate the optimum H<sub>2</sub> production rate was obtained with a TiO<sub>2</sub> concentration of approximately 50 g·L<sup>-1</sup>.





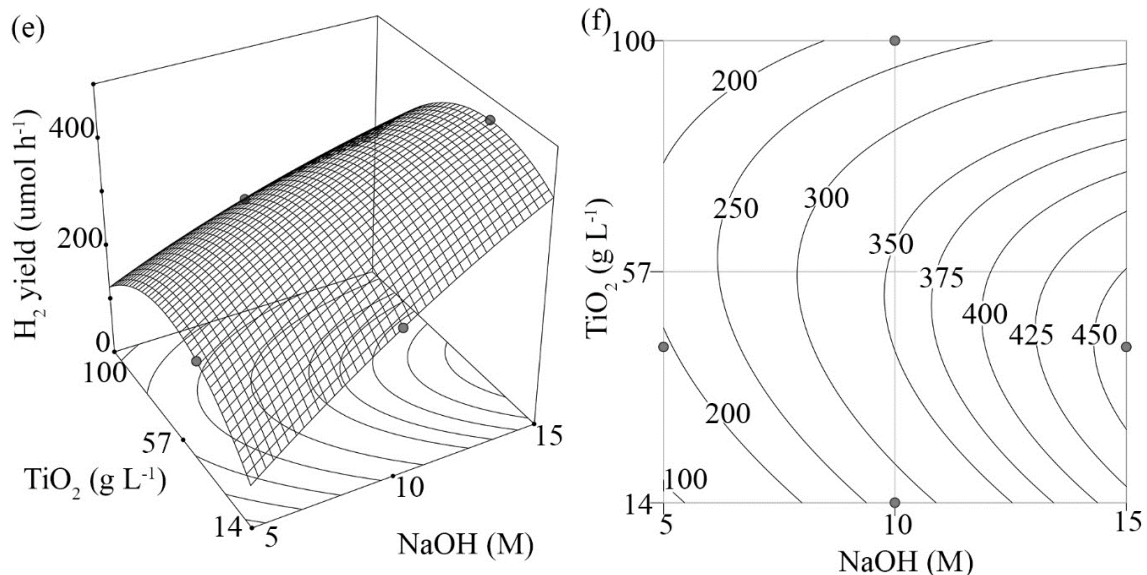


Figure 4.11: 3D Response surface and contour plots for: (a) and (b) Interaction between hydrothermal temperature and NaOH concentration set at 43 g·L<sup>-1</sup> TiO<sub>2</sub>, (c) and (d) Interaction between hydrothermal temperature and TiO<sub>2</sub> concentration set at 15 M NaOH concentration, and (e) and (f) Interaction between NaOH concentration and TiO<sub>2</sub> concentration set at 120°C temperature.

Notes: <sup>a</sup> A, R and B represent anatase, rutile and TiO<sub>2</sub>-B, respectively, and <sup>b</sup> H<sub>2</sub> yield represents H<sub>2</sub> production rate.

The D-optimality index was used to locate the maximum response (Y) region within the factor space under consideration (Figure 4.12). A maximum Y value of 470 μmol·h<sup>-1</sup> was predicted for Q1D TiO<sub>2</sub> synthesized at 126°C, 15 M NaOH and 49 g·L<sup>-1</sup> TiO<sub>2</sub>. Additional experiments were conducted to verify the maximum Y using the Q1D TiO<sub>2</sub> synthesized under the predicted conditions. The predicted value was slightly underestimated when compared to the observed H<sub>2</sub> production rate of 475±12 μmol·h<sup>-1</sup> (ε = 20.2±0.5%). Recall, a pure anatase phase with a mean crystal size of 20.1±0.2 nm and BET SSA of 140±3 m<sup>2</sup>·g<sup>-1</sup> was observed in Q1D TiO<sub>2</sub> synthesized under optimum conditions. The optimum H<sub>2</sub> production rate was approximately 2-fold larger when compared to commercial P25. This H<sub>2</sub> production rate was significantly improved when compared to reported production rates of 348 μmol·h<sup>-1</sup> for reported biphasic anatase-

TiO<sub>2</sub>-B [2]. Note that in this study, 0.02 g photocatalyst was used to obtain a H<sub>2</sub> production rate of 470 μmol·h<sup>-1</sup>. The highest specific H<sub>2</sub> production rate (per g of photocatalyst) reached 23,500 μmol·h<sup>-1</sup>·g<sup>-1</sup> which was significantly enhanced when compared to data reported for pure anatase, pure rutile, flame spray pyrolysis-synthesised TiO<sub>2</sub> and Au/TiO<sub>2</sub> [73].

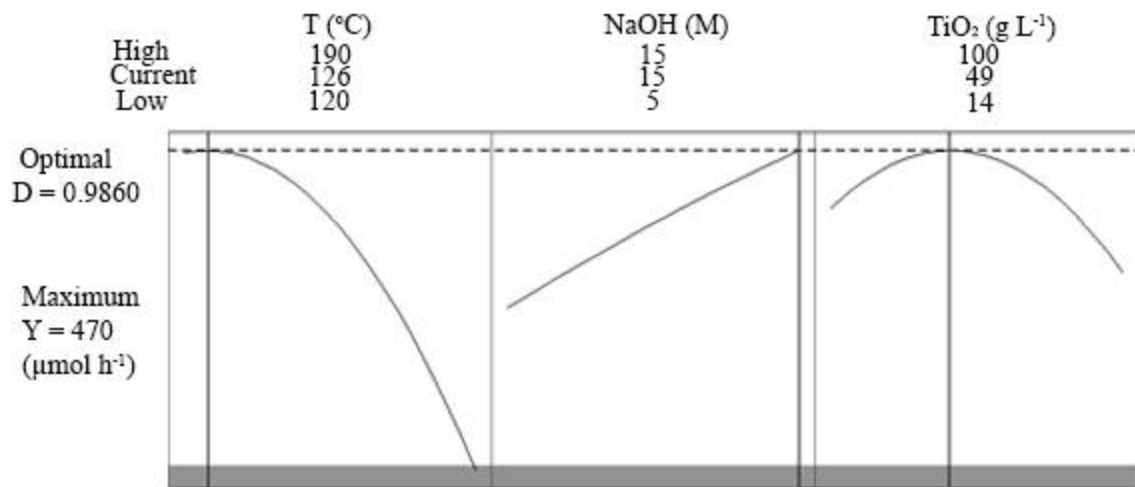


Figure 4.12: Optimality plot to locate optimum factor levels for maximized hydrogen yield (μmol·h<sup>-1</sup>).

Notes: <sup>a</sup> The D-optimality index ranging from 0 to 1 represents the ideal and worst cases, respectively, and <sup>b</sup> Y represents H<sub>2</sub> production rate.

#### 4.4.6. Response surface model development

An analysis of variance (ANOVA) (Table 4.7) was employed to evaluate the model full quadratic equation (Eq. 4.10) was employed to determine the significance and adequacy of the model. The quadratic model with an overall p-value ≤ 0.05 [40-43] and F-value ≤ critical value (2.01 at 5% level of significance) [40-43] indicate the model was statistically significant. However, two variables (X<sub>2</sub><sup>2</sup> and X<sub>1</sub>X<sub>3</sub>) with p-value ≥ 0.05 are statistically insignificant with no individual effect on the full quadratic model. These two

terms were deleted from the full quadratic model using a backward elimination method [41]. The revised response surface model is designated as equation (Eq. 4.11):

$$Y = -2974 + 34.43X_1 + 118.96X_2 + 9.40X_3 - 0.7X_1X_2 - 0.239X_2X_3 - 0.095X_1^2 - 0.058X_3^2 \quad (4.11)$$

where Y is the H<sub>2</sub> production rate (μmol·h<sup>-1</sup>), X<sub>1</sub>, X<sub>2</sub> and X<sub>3</sub> represent temperature (°C), NaOH concentration (M) and TiO<sub>2</sub> concentration (g·L<sup>-1</sup>), respectively.

Table 4.7: ANOVA results of the experimental response at each factor level.

Source	DF <sup>a</sup>	Seq. SS <sup>b</sup>	MS <sup>c</sup>	F-value	P-value
Model	9	593896	65988	96.78	0
X <sub>1</sub>	1	116309	116309	170.58	0
X <sub>2</sub>	1	5352	5352	7.58	0.008
X <sub>3</sub>	1	8961	8961	13.14	0.001
X <sub>1</sub> <sup>2</sup>	1	144590	144590	212.05	0
X <sub>2</sub> <sup>2</sup>	1	501	501	0.73	0.397
X <sub>3</sub> <sup>2</sup>	3	97085	97085	142.38	0
X <sub>1</sub> X <sub>2</sub>	1	181600	181600	266.33	0
X <sub>1</sub> X <sub>3</sub>	1	973	973	1.43	0.240
X <sub>2</sub> X <sub>3</sub>	1	33226	33226	48.73	0
Error	35	23865	682		
Total	44	617760			

Notes: <sup>a</sup> DF = degrees of freedom, <sup>b</sup> Seq. SS = sequential sum of square, <sup>c</sup> MS = mean square, and <sup>d</sup> X<sub>1</sub> = temperature; X<sub>2</sub> = NaOH concentration; X<sub>3</sub> = TiO<sub>2</sub> concentration.

#### 4.4.7. Response surface model verification

A scatter plot comparing the experimental and the model predicted values (Figure 4.13a) indicate a reasonable correlation at each level. The Anderson-Darling (AD) statistic (Figure 4.13b) was employed to assess the adequacy of fitting the model to the experimental data by determining the normal distribution of the residuals (difference between the predicted and experimental values) [44]. An AD value of 0.379 (≤ the

critical value of 0.735 for 45 samples and at a 5% level of significance) [44] and a p-value of 0.391 ( $\geq 0.05$ ) suggest the model's predicted values correlated with the experimental values.

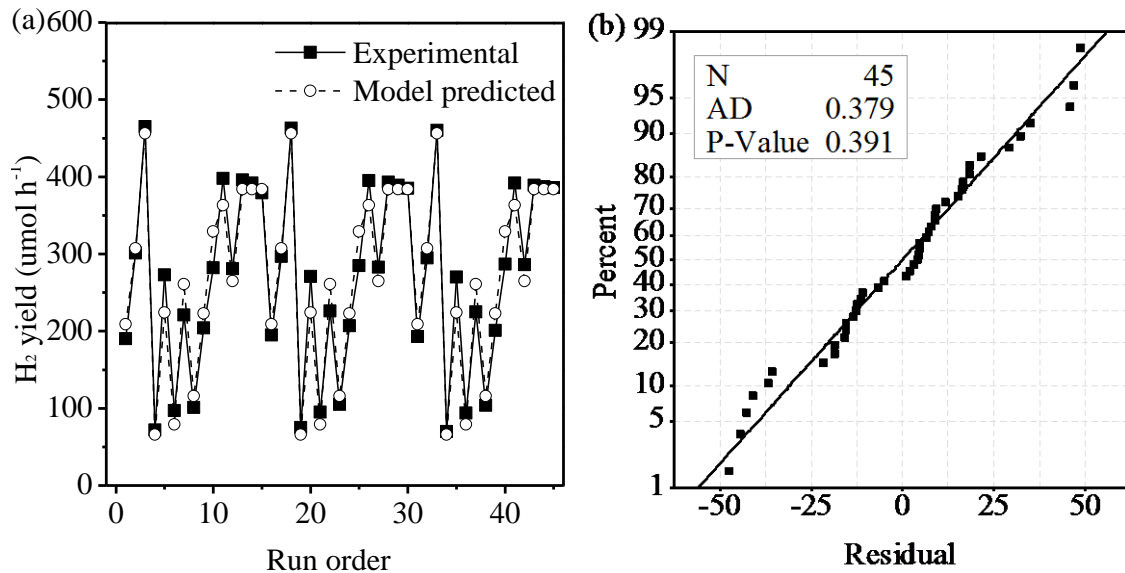
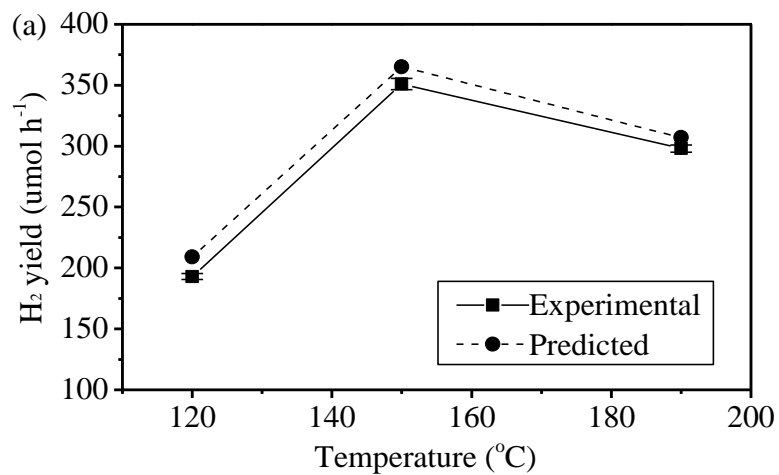


Figure 4.13: Accuracy evaluation of the response surface model. (a) Scatter plot of the hydrogen (H<sub>2</sub>) production rate (μmol·h<sup>-1</sup>) versus experiment order (45 experiments). (b) Anderson-Darling normality plot of residuals.

Notes: <sup>a</sup> N = the number of experiments conducted in this study, <sup>b</sup> P-Value = level of confidence, and <sup>c</sup> AD = Anderson-Darling statistic.



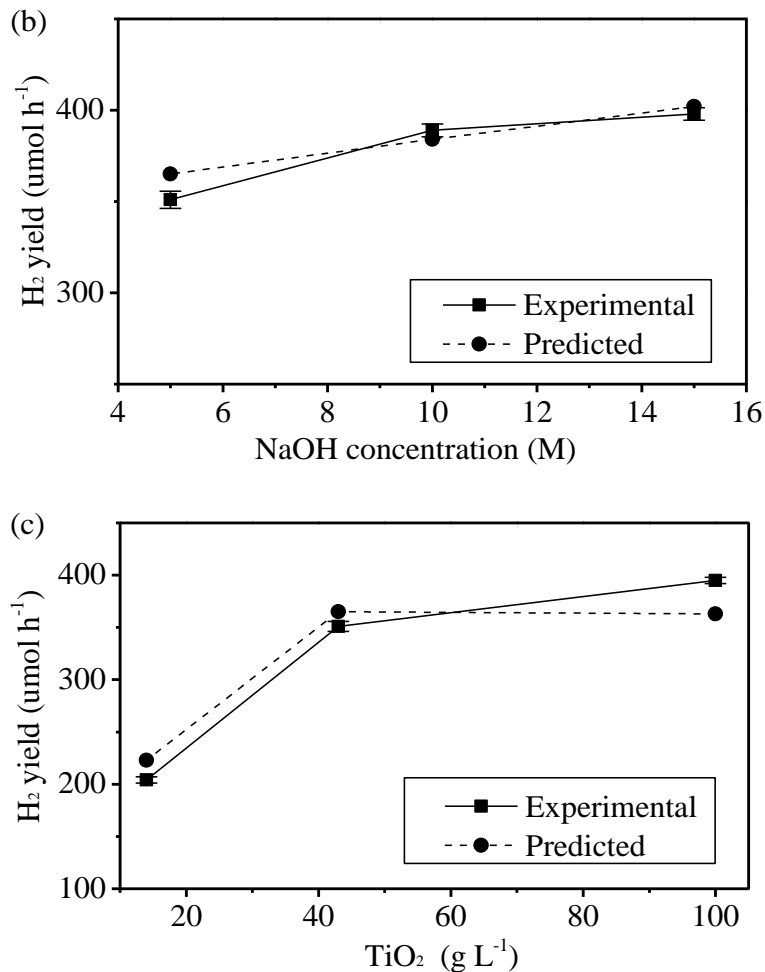


Figure 4.14: Validation study of the response surface model for the varied factors under consideration. (a) hydrogen (H<sub>2</sub>) production rate versus temperature at experimental conditions set at 5 M NaOH and 43 g·L<sup>-1</sup> TiO<sub>2</sub>, (b) H<sub>2</sub> production rate value versus NaOH concentration at experimental conditions set at 150°C and 43 g·L<sup>-1</sup> TiO<sub>2</sub>, and (c) H<sub>2</sub> production rate versus TiO<sub>2</sub> concentration at experimental conditions set at 150°C and 5 M NaOH.

Validation of the model accuracy was examined by varying a single factor in three additional experiments (Figure 4.14). The model predicted trend was comparable to the experimental trend for varying each factor. For the temperature range from 120 to 190°C (Figure 4.14a), the model predicted values were close to the experimental values with a slight overestimate at each temperature level. For the NaOH concentration (Figure 4.14b), the predicted values were in agreement with the experimental data with a slight

overestimate at 5 M NaOH. For the TiO<sub>2</sub> concentration, the model predicted values which were reasonably close to the observed values for each level of TiO<sub>2</sub> concentration with a slight underestimate at 100 g·L<sup>-1</sup> TiO<sub>2</sub> and a slight overestimate at 14 and 43 g·L<sup>-1</sup> (Figure 4.14c).

#### 4.4.8. Phase structure, crystal size and bandgap

XRD analysis and diffuse reflectance UV-visible spectroscopy were used to evaluate the phase structure, crystal size and bandgap for the BBD samples. The XRD patterns for selected BBD samples #1, #3 and #8 are shown in Figure 4.15a and the phase structure is summarized in Table 4.8 for all the samples. The three phase structures observed in this study included pure anatase [74], biphasic anatase-rutile [9, 75, 76] and the biphasic anatase-TiO<sub>2</sub>-B [2] structures (Figure 4.15a). The biphasic anatase-rutile structure, similar to that in P25, was only detected in sample #1 [9, 75, 76], while pure anatase phase and the biphasic anatase-TiO<sub>2</sub>-B structures were observed in a majority of the samples. The mean crystal sizes (L, nm) for sample #1-15 (Table 4.6 and Table 4.8) were calculated using Scherrer equation (Eq. 4.12) and XRD data.

$$L = K\lambda / \beta \cdot \cos\theta \quad [77] \quad (4.12)$$

where K,  $\lambda$  and  $\beta$  represent the shape factor (0.89), the wavelength of XRD radiation (0.154 nm) and the half maximum of a full peak, respectively.

The Kubelka-Munk function was used to transform the diffuse reflectance spectra into the corresponding absorption spectra (Figure 4.15b) [75, 78, 79]. . The bandgap is closely correlated with the phase structure (Table 4.8). The pure anatase (e.g. sample #3)

phase was observed with a large bandgap ranging from  $3.258\pm 0.003$  to  $3.298\pm 0.005$  [80, 81], while the biphasic structure anatase-rutile (sample #1) and anatase-TiO<sub>2</sub>-B (samples #4, #6 and #8) showed decreasing bandgap energies of  $3.067\pm 0.006$  and  $3.210\pm 0.007$ - $3.229\pm 0.009$  eV, respectively.

Table 4.8. Phase structures, bandgap energies and hydrogen yield for all BBD samples.

Sample #	Phase	Bandgap (eV)	Mean L (nm)	BET SSA (m <sup>2</sup> ·g <sup>-1</sup> )	Y (μmol·h <sup>-1</sup> )
1	Anatase and rutile	$3.067\pm 0.006$	$9.5\pm 0.1$	$182\pm 5$	$193\pm 7$
2, 3, 5, 7, 9 and 11-15	Anatase	$3.258\pm 0.003$ - $3.298\pm 0.005$	$16.9\pm 0.2$ - $21.5\pm 0.2$	$125\pm 5$ - $174\pm 5$	$204\pm 8$ - $463\pm 14$
10	Anatase	$3.271\pm 0.004$	$57.2\pm 0.4$	$61\pm 3$	$284\pm 10$
4, 6, 8	Anatase and TiO <sub>2</sub> -B	$3.210\pm 0.007$ - $3.229\pm 0.009$	$46.4\pm 0.3$ - $58.3\pm 0.3$	$37\pm 3$ - $73\pm 3$	$72\pm 4$ - $103\pm 5$

Note: L and Y represent crystal size and H<sub>2</sub> production rate, respectively.

The H<sub>2</sub> production rates, crystal size and BET SSA are summarized in Table 4.8 for BBD Q1D TiO<sub>2</sub> samples synthesized under different reaction conditions. Depending on the hydrothermal synthesis conditions, the H<sub>2</sub> production rates varied from  $72\pm 4$  to  $475\pm 12$  μmol·h<sup>-1</sup>. The phase structure significantly affected the H<sub>2</sub> production rate. Pure anatase (sample #2, #3, #5, #7, #9, #11-15 and optimum) was closely linked with increasing the H<sub>2</sub> production rate while the biphasic anatase-rutile (sample #1) and anatase-TiO<sub>2</sub>-B structures (sample #4, #6 and #8) were associated with decreasing H<sub>2</sub> production rate. The lowest H<sub>2</sub> production rate was detected for the biphasic anatase-TiO<sub>2</sub>-B structure (sample #4, 6 and 8).



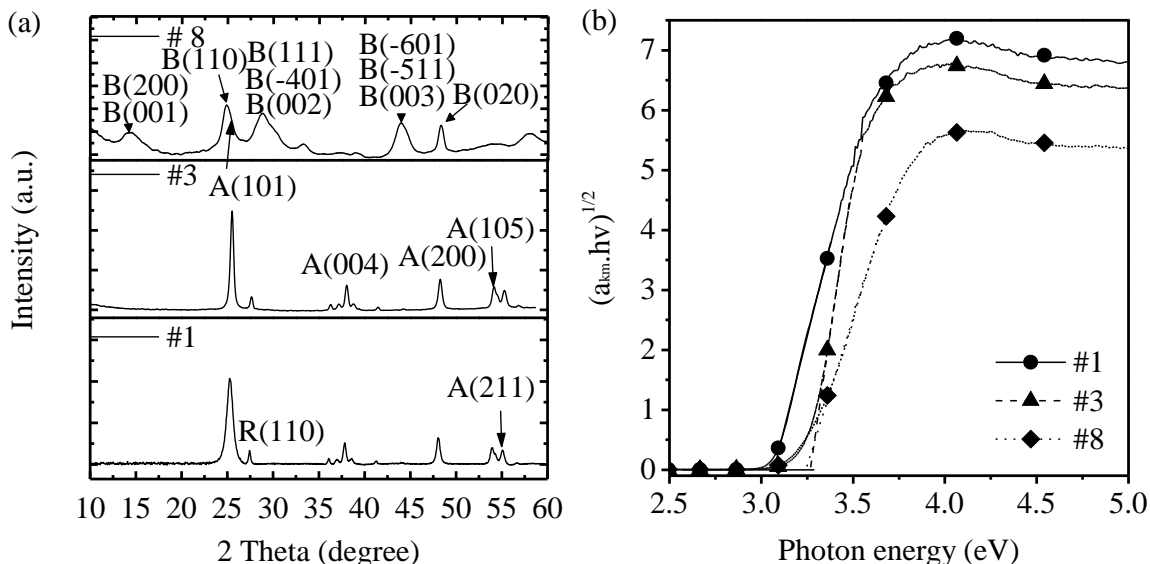


Figure 4.15: X-ray diffraction (XRD) patterns and  $(\alpha_{km}h\nu)^{1/2}$  versus absorbed energy for samples #1, #3, and #8: (a) XRD spectra, and (b)  $(\alpha_{km}h\nu)^{1/2}$  versus absorbed energy profiles.

Notes: <sup>a</sup> Synthesis parameter details are listed in Table 4.6, <sup>b</sup> the A(101) peak is positioned on the shoulder, and <sup>c</sup> A, R and B represents anatase, rutile and TiO<sub>2</sub>-B, respectively.

Plotting the H<sub>2</sub> production rate ( $\mu\text{mol}\cdot\text{h}^{-1}$ ) and BET SSA versus the particle size for pure anatase phase samples (Figure 4.16) suggests the greatest H<sub>2</sub> production rate of  $475\pm 12 \mu\text{mol}\cdot\text{h}^{-1}$  was observed when the mean crystal size was  $20.1\pm 0.2 \text{ nm}$  with BET SSA of  $140\pm 3 \text{ m}^2\cdot\text{g}^{-1}$ . Smaller crystal size was closely linked to a larger BET SSA for Q1D TiO<sub>2</sub> containing anatase. The BET SSA ( $\text{m}^2\cdot\text{g}^{-1}$ ) as a function of the mean crystal size is shown as equation (Eq. 4.13):

$$\text{BET SSA} = 1518 \times L^{-0.7931} \quad (16 \leq L \leq 56 \text{ and } R^2 = 95.6\%) \quad (4.13)$$

where L (nm) is the mean crystal size.

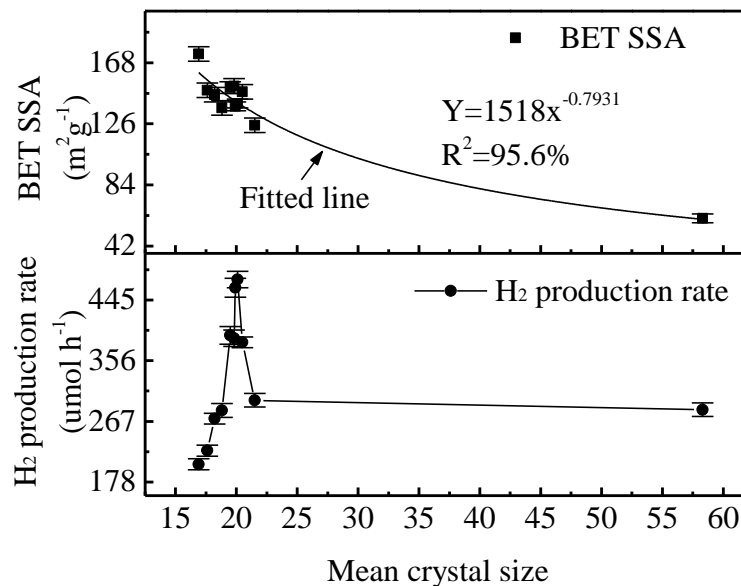


Figure 4.16: Hydrogen production rate and specific surface area versus anatase mean crystal size.

Note: All samples counted in the figure are for the anatase phase.

Increasing the H<sub>2</sub> production rate was closely correlated with decreasing the anatase mean crystal size from  $58.3 \pm 0.3$  to  $20.1 \pm 0.2$  nm. This H<sub>2</sub> production rate increase was due to increasing the SSA [82]. Increasing the SSA was associated with faster rate of e<sup>-</sup> and h<sup>+</sup> surface reaction with substrate. The optimum anatase mean crystal size of  $20.1 \pm 0.2$  nm was correlated with a maximum H<sub>2</sub> production rate. However, note the lower H<sub>2</sub> production rate observed below the optimum anatase mean crystal size was caused by fast e<sup>-</sup>-h<sup>+</sup> recombination [82]. A decrease in H<sub>2</sub> production rate which was correlated with fast e<sup>-</sup>-h<sup>+</sup> recombination at defective sites on the photocatalyst surface [82]. The significant number of defective site was likely due to decreasing the crystal size below an optimum value.

#### 4.4.9. Conclusions: Photocatalytic hydrogen production

Many Q1D TiO<sub>2</sub> shapes ranging from nanorods to nanowires were produced using a hydrothermal method with variable reaction conditions. The reaction temperature and NaOH concentration significantly affected the Q1D TiO<sub>2</sub> phase structure, crystal size, SSA, bandgap and photocatalytic activity. A statistical model was employed to evaluate the effects of the hydrothermal synthesis factors on the photocatalytic activity of Q1D TiO<sub>2</sub> in terms of the H<sub>2</sub> production rate. The AD and validation test indicated an adequate fit of the statistical model to the experimental data under the conditions examined. The model revealed that a relatively low temperature (126°C) and high NaOH concentration (15 M) were closely linked to producing Q1D TiO<sub>2</sub> containing pure anatase. This Q1D TiO<sub>2</sub> sample with an optimum mean crystal size was able to maximize the H<sub>2</sub> production rate. The Q1D TiO<sub>2</sub> with biphasic anatase-rutile and anatase-TiO<sub>2</sub>-B structures was observed with decreasing photocatalytic H<sub>2</sub> production rate. This study demonstrated that Q1D TiO<sub>2</sub> containing a controllable phase structure, and crystal size was able to produce a photocatalyst with a H<sub>2</sub> production rate greater than reported values.

#### 4.5. Conclusions

Q1D TiO<sub>2</sub> photocatalytic activities, in terms of photodegrading organic pollutants and H<sub>2</sub> production, were significantly affected by hydrothermal reaction temperature and NaOH concentration. A biphasic anatase-rutile Q1D TiO<sub>2</sub> structure produced at 120°C temperature and a 5 M NaOH solution was associated with the lowest bandgap and the highest photocatalytic activities for photodegrading aqueous organic pollutant. However, a pure anatase Q1D TiO<sub>2</sub> structure synthesized at 120°C and 15 M NaOH was correlated

with the highest bandgap and photocatalytic H<sub>2</sub> production rate from ethanol. The TiO<sub>2</sub>-B which was predominant at hydrothermal conditions of 190°C and ≥10 M NaOH showed with lowest photocatalytic activities in terms of photodegrading organic pollutants and producing H<sub>2</sub>.

#### 4.6. References

- [1] Q. Wang, T. Hisatomi, Q. Jia, H. Tokudome, M. Zhong, C. Wang, Z. Pan, T. Takata, M. Nakabayashi, N. Shibata, Y. Li, I.D. Sharp, A. Kudo, T. Yamada, K. Domen, Scalable water splitting on particulate photocatalyst sheets with a solar-to-hydrogen energy conversion efficiency exceeding 1%, *Nat. Mater.* 15 (2016) 611-615.
- [2] H.-L. Kuo, C.-Y. Kuo, C.-H. Liu, J.-H. Chao, C.-H. Lin, A highly active bi-crystalline photocatalyst consisting of TiO<sub>2</sub> (B) nanotube and anatase particle for producing H<sub>2</sub> gas from neat ethanol, *Catal. Lett.* 113 (2007) 7.
- [3] G. Wang, H. Wang, Y. Ling, Y. Tang, X. Yang, R.C. Fitzmorris, C. Wang, J.Z. Zhang, Y. Li, Hydrogen-treated TiO<sub>2</sub> nanowire arrays for photoelectrochemical water splitting, *Nano Lett.* 11 (2011) 3026-3033.
- [4] P. Bansal, N. Bhullar, D. Sud, Studies on photodegradation of malachite green using TiO<sub>2</sub>/ZnO photocatalyst, *Desalin. Water Treat.* 12 (2012) 108-113.
- [5] X. Liu, T. Lv, Y. Liu, L. Pan, Z. Sun, TiO<sub>2</sub>-Au composite for efficient UV photocatalytic reduction of Cr(VI), *Desalin. Water Treat.* 51 (2013) 3889-3895.
- [6] Q. Han, Y. Wang, H. Yan, B. Gao, D. Ma, S. Sun, J. Ling, Y. Chu, Photocatalysis of THM precursors in reclaimed water: the application of TiO<sub>2</sub> in UV irradiation, *Desalin. Water Treat.* 57 (2016) 9136-9147.

- [7] A. Mezni, N.B. Saber, M.M. Ibrahim, M. El-Kemary, A. Aldalbahi, P. Feng, L. Samia Smiri, T. Altalhi, Facile synthesis of highly thermally stable TiO<sub>2</sub> photocatalysts, *New J. Chem.* 41 (2017) 5021-5027.
- [8] S. Ray, J.A. Lalman, Fabrication and characterization of an immobilized titanium dioxide (TiO<sub>2</sub>) nanofiber photocatalyst, *Mater. Today: Proc.* 3 (2016) 1582-1591.
- [9] G. Tian, H. Fu, L. Jing, B. Xin, K. Pan, Preparation and characterization of stable biphasic TiO<sub>2</sub> photocatalyst with high crystallinity, large surface area, and enhanced photoactivity, *J. Phys. Chem. C* 112 (2008) 3083-3089.
- [10] D.V. Bavykin, V.N. Parmon, A.A. Lapkin, F.C. Walsh, The effect of hydrothermal conditions on the mesoporous structure of TiO<sub>2</sub> nanotubes, *J. Mater. Chem.* 14 (2004) 3370-3378.
- [11] T. Kasuga, M. Hiramatsu, A. Hoson, T. Sekino, K. Niihara, Formation of titanium oxide nanotube, *Langmuir* 14 (1998) 3160-3163.
- [12] S.D. Perera, R.G. Mariano, K. Vu, N. Nour, O. Seitz, Y. Chabal, K.J. Balkus Jr., Hydrothermal synthesis of graphene-TiO<sub>2</sub> nanotube composites with enhanced photocatalytic activity, *ACS Catal.* 2 (2012) 949-956.
- [13] Z. Yang, B. Wang, H. Cui, H. An, Y. Pan, J. Zhai, Synthesis of crystal-controlled TiO<sub>2</sub> nanorods by a hydrothermal method: rutile and brookite as highly active photocatalysts, *J. Phys. Chem. C* 119 (2015) 16905-16912.
- [14] S. Hoang, S. Guo, N.T. Hahn, A.J. Bard, C.B. Mullins, Visible light driven photoelectrochemical water oxidation on nitrogen-modified TiO<sub>2</sub> nanowires, *Nano Lett.* 12 (2012) 26-32.

- [15] X. Pan, Y. Zhao, S. Liu, C.L. Korzeniewski, S. Wang, Z. Fan, Comparing graphene-TiO<sub>2</sub> nanowire and graphene-TiO<sub>2</sub> nanoparticle composite photocatalysts, *ACS Appl. Mater. Interfaces* 4 (2012) 3944-3950.
- [16] P. Roy, S. Berger, P. Schmuki, TiO<sub>2</sub> nanotubes: synthesis and applications, *Angew. Chem. Int. Ed.* 50 (2011) 2904-2939.
- [17] Y.V. Kolenko, K.A. Kovnir, A.I. Gavrilov, Hydrothermal synthesis and characterization of nanorods of various titanates and titanium dioxide, *J. Phys. Chem. B* 110 (2006) 4030-4038.
- [18] M. Andersson, L. Osterlund, S. Ljungström, A. Palmqvist, Preparation of nanosize anatase and rutile TiO<sub>2</sub> by hydrothermal treatment of microemulsions and their activity for photocatalytic wet oxidation of phenol, *J. Phys. Chem. B* 106 (2002) 10674-10679.
- [19] J.-N. Nian, H. Teng, Hydrothermal synthesis of single-crystalline anatase TiO<sub>2</sub> nanorods with nanotubes as the precursor, *J. Phys. Chem. B* 110 (2006) 4193-4198.
- [20] D. Yang, Y. Sun, Z. Tong, Y. Tian, Y. Li, Synthesis of Ag/TiO<sub>2</sub> nanotube heterojunction with improved visible-light photocatalytic performance inspired by bioadhesion, *J. Phys. Chem. C* 119 (2015) 5827-5835.
- [21] S. Ray, J.A. Lalman, N. Biswas, Using the Box-Benken technique to statistically model phenol photocatalytic degradation by titanium dioxide nanoparticles, *Chem. Eng. J.* 150 (2009) 15-24.
- [22] D. Xu, B. Cheng, S. Cao, J. Yu, Enhanced photocatalytic activity and stability of Z-scheme Ag<sub>2</sub>CrO<sub>4</sub>-GO composite photocatalysts for organic pollutant degradation, *Appl. Catal., B Environ.* 164 (2015) 380-388.

- [23] M. Nasr, R. Viter, C. Eid, R. Habchi, P. Miele, M. Bechelany, Enhanced photocatalytic performance of novel electrospun BN/TiO<sub>2</sub> composite nanofibers, *New J. Chem.* 41 (2016) 81-89.
- [24] J. Liu, Y. Liu, N. Liu, Y. Han, X. Zhang, H. Huang, Y. Lifshitz, S.T. Lee, J. Zhong, Z. Kang, Metal-free efficient photocatalyst for stable visible water splitting via a two-electron pathway, *Science* 347 (2015) 970-974.
- [25] Y. Ling, G. Liao, Y. Xie, J. Yin, J. Huang, W. Feng, L. Li, Coupling photocatalysis with ozonation for enhanced degradation of atenolol by Ag-TiO<sub>2</sub> micro-tube, *J. Photochem. Photobiol. A: Photochem. Rev.* 329 (2016) 280-286.
- [26] J. Sun, L. Qiao, S. Sun, G. Wang, Photocatalytic degradation of orange g on nitrogen-doped TiO<sub>2</sub> catalysts under visible light and sunlight irradiation., *J. Hazard. Mater.* 155 (2008) 312-319.
- [27] I.M. Arabatzis, T. Stergiopoulos, M.C. Bernard, D. Labou, S.G. Neophytides, P. Falaras, Silver-modified titanium dioxide thin films for efficient photodegradation of methyl orange, *Appl. Catal., B Environ.* 42 (2003) 187-201.
- [28] Z. Xiong, J. Ma, W.J. Ng, T.D. Waite, X.S. Zhao, Silver-modified mesoporous TiO<sub>2</sub> photocatalyst for water purification, *Water Res.* 45 (2011) 2095-2103.
- [29] O. Carp, C.L. Huisman, A. Reller, Photoinduced reactivity of titanium dioxide, *Prog. Solid State Chem.* 32 (2004) 33-177.
- [30] U.I. Gaya, A.H. Abdullah, Heterogeneous photocatalytic degradation of organic contaminants over titanium dioxide: A review of fundamentals, progress and problems, *J. Photochem. Photobiol. C: Photochem. Rev.* 9 (2008) 1-12.

- [31] R. Andreozzi, V. Caprio, A. Insola, R. Marotta, Advanced oxidation processes (AOP) for water purification and recovery, *Catal. Today* 53 (1999) 51-59.
- [32] M.F.A. Messih, M.A. Ahmed, A. Soltan, S.S. Anis, Facile approach for homogeneous dispersion of metallic silver nanoparticles on the surface of mesoporous titania for photocatalytic degradation of methylene blue and indigo carmine dyes, *J. Photochem. Photobiol. A: Photochem. Rev.* 335 (2017) 40-51.
- [33] M. Sui, Y. Dong, Z. Wang, F. Wang, H. You, A biocathode-driven photocatalytic fuel cell using an Ag-doped TiO<sub>2</sub>/Ti mesh photoanode for electricity generation and pollutant degradation, *J. Photochem. Photobiol. A: Photochem. Rev.* 348 (2017) 238-245.
- [34] S.S. Boxi, S. Paria, Visible light induced enhanced photocatalytic degradation of organic pollutants in aqueous media using Ag doped hollow TiO<sub>2</sub> nanospheres, *RSC Adv.* 5 (2015) 37657-37668.
- [35] M.K. Seery, R. George, P. Floris, S.C. Pillai, Silver doped titanium dioxide nanomaterials for enhanced visible light photocatalysis, *J. Photochem. Photobiol. A: Photochem. Rev.* 189 (2007) 258-263.
- [36] B. Ohtani, Preparing articles on photocatalysis—Beyond the illusions, misconceptions, and speculation, *Chem. Lett.* 37 (2008) 216-229.
- [37] K. Bustos-Ramirez, C.E. Barrera-Diaz, M. De Icaza, A.L. Martínez-Hernández, C. Velasco-Santos, Photocatalytic activity in phenol removal of water from graphite and graphene oxides: effect of degassing and chemical oxidation in the synthesis process, *J. Chem.* 2015 (2015) 1-10.



- [38] L. Yang, M. Gong, X. Jiang, D. Yin, X. Qin, B. Zhao, W. Ruan, Investigation on SERS of different phase structure TiO<sub>2</sub> nanoparticles, *J. Raman Spectrosc.* 46 (2015) 287-292.
- [39] S. Hoang, S.P. Berglund, N.T. Hahn, A.J. Bard, C.B. Mullins, Enhancing visible light photo-oxidation of water with TiO<sub>2</sub> nanowire arrays via cotreatment with H<sub>2</sub> and NH<sub>3</sub>: synergistic effects between Ti<sup>3+</sup> and N, *J. Am. Chem. Soc.* 134 (2012) 3659-3662.
- [40] S.S. Veeravalli, S.R. Chaganti, J.A. Lalman, D.D. Heath, Optimizing hydrogen production from a switchgrass steam exploded liquor using a mixed anaerobic culture in an upflow anaerobic sludge blanket reactor, *Int. J. Hydrogen Energ.* 39 (2014) 3160-3175.
- [41] S.R. Shanmugam, S.R. Chaganti, J.A. Lalman, D.D. Heath, Statistical optimization of conditions for minimum H<sub>2</sub> consumption in mixed anaerobic cultures: effect on homoacetogenesis and methanogenesis, *Int. J. Hydrogen Energ.* 39 (2014) 15433-15445.
- [42] Z. Lai, M. Zhu, X. Yang, J. Wang, S. Li, Optimization of key factors affecting hydrogen production from sugarcane bagasse by a thermophilic anaerobic pure culture, *Biotechnol. Biofuels* 7 (2014) 131-111.
- [43] A. Reungsang, S. Pattra, S. Sittijunda, Optimization of key factors affecting methane production from acidic effluent coming from the sugarcane juice hydrogen fermentation process, *Energies* 5 (2012) 4746-4757.
- [44] M.A. Stephens, EDF statistics for goodness of fit and some comparisons, *J. Am. Stat. Assoc.* 69 (1974) 730.
- [45] D.C. Montgomery, *Design and analysis of experiments*, John Wiley and Sons, Inc., Arizona State University, 2017.

- [46] H.Y. Zhu, Y. Lan, X.P. Gao, S.P. Ringer, Z.F. Zheng, D.Y. Song, J.C. Zhao, Phase transition between nanostructures of titanate and titanium dioxides via simple wet-chemical reactions., *J. Am. Chem. Soc.* 127 (2005) 6730-6736.
- [47] X. Chen, S.S. Mao, Titanium dioxide nanomaterials: Synthesis, properties, modifications, and applications, *Chem. Rev.* 107 (2007) 2891-2959.
- [48] B. Chen, J. Hou, K. Lu, Formation mechanism of TiO<sub>2</sub> nanotubes and their applications in photoelectrochemical water splitting and supercapacitors, *Langmuir* 29 (2013) 5911-5919.
- [49] Y. Tang, Y. Zhang, J. Deng, J. Wei, H.L. Tam, B.K. Chandran, Z. Dong, Z. Chen, X. Chen, Mechanical force-driven growth of elongated bending TiO<sub>2</sub>-based nanotubular materials for ultrafast rechargeable lithium ion batteries, *Adv. Mater.* 26 (2014) 6111-6118.
- [50] H.-W. Shim, D.K. Lee, I.S. Cho, K.S. Hong, D.-W. Kim, Facile hydrothermal synthesis of porous TiO<sub>2</sub> nanowire electrodes with high-rate capability for Li ion batteries, *Nanotechnology* 21 (2010) 255706-255709.
- [51] A.R. Armstrong, G. Armstrong, J. Canales, P.G. Bruce, TiO<sub>2</sub>-B nanowires, *Angew. Chem.* 116 (2004) 2336-2338.
- [52] S. Preda, M. Rutar, P. Umek, M. Zaharescu, A study of thermal properties of sodium titanate nanotubes synthesized by microwave-assisted hydrothermal method, *Mater. Res. Bull.* 71 (2015) 98-105.
- [53] J. Jitputti, S. Pavasupree, Y. Suzuki, S. Yoshikawa, Synthesis of TiO<sub>2</sub> nanotubes and its photocatalytic activity for H<sub>2</sub> evolution, *Jpn. J. Appl. Phys.* 47 (2008) 751.

- [54] A.M. Hussein, L. Mahoney, R. Peng, H. Kibombo, C.-M. Wu, R.T. Koodali, R. Shende, Mesoporous coupled ZnO/TiO<sub>2</sub> photocatalyst nanocomposites for hydrogen generation, *J. Renew. Sustain. Ener.* 5 (2013) 033118.
- [55] A.L. Linsebigler, G. Lu, J.T. Yates, Photocatalysis on TiO<sub>2</sub> surfaces: Principles, mechanisms, and selected results, *Chem. Rev.* 95 (1995) 735-758.
- [56] J. Zhang, Q. Sun, J. Zheng, X. Zhang, Y. Cui, P. Wang, W. Li, Y. Zhu, The characterization of nitrogen doped TiO<sub>2</sub> photoanodes and its application in the dye sensitized solar cells, *J. Renew. Sustain. Ener.* 3 (2011) 033108.
- [57] Q. Xiang, B. Cheng, J. Yu, Graphene based photocatalysts for solar fuel generation, *Angew. Chem.* 127 (2015) 11508-11524.
- [58] X. Wang, K. Maeda, A. Thomas, K. Takanabe, G. Xin, J.M. Carlsson, K. Domen, M. Antonietti, A metal-free polymeric photocatalyst for hydrogen production from water under visible light, *Nat. Mater.* 8 (2008) 76-80.
- [59] S.-W. Cao, Y.-P. Yuan, J. Fang, M.M. Shahjamali, F.Y.C. Boey, J. Barber, S.C.J. Loo, C. Xue, In-situ growth of CdS quantum dots on g-C<sub>3</sub>N<sub>4</sub> nanosheets for highly efficient photocatalytic hydrogen generation under visible light irradiation, *Int. J. Hydrogen Energ.* 38 (2013) 1258-1266.
- [60] A. Nada, M. Barakat, H. Hamed, N. Mohamed, T. Veziroglu, Studies on the photocatalytic hydrogen production using suspended modified photocatalysts, *Int. J. Hydrogen Energ.* 30 (2005) 687-691.
- [61] M. Murdoch, G.I.N. Waterhouse, M.A. Nadeem, J.B. Metson, M.A. Keane, R.F. Howe, J. Llorca, H. Idriss, The effect of gold loading and particle size on photocatalytic

hydrogen production from ethanol over Au/TiO<sub>2</sub> nanoparticles, *Nat. Chem.* 3 (2011) 489-492.

[62] K. Connelly, A.K. Wahab, H. Idriss, Photoreaction of Au/TiO<sub>2</sub> for hydrogen production from renewables: a review on the synergistic effect between anatase and rutile phases of TiO<sub>2</sub>, *Mater. Renew. Sustain. Ener.* 1 (2012) 401-412.

[63] K. Hashimoto, H. Irie, A. Fujishima, TiO<sub>2</sub> photocatalysis: a historical overview and future prospects, *Jpn. J. Appl. Phys.* 44 (2005) 8269-8285.

[64] N. Qin, Y. Liu, W. Wu, L. Shen, X. Chen, Z. Li, L. Wu, One-dimensional CdS/TiO<sub>2</sub> nanofiber composites as efficient visible-light-driven photocatalysts for selective organic transformation: synthesis, characterization, and performance, *Langmuir* 31 (2015) 1203-1209.

[65] X. Wang, Z. Li, J. Shi, Y. Yu, One-dimensional titanium dioxide nanomaterials: Nanowires, nanorods, and nanobelts, *Chem. Rev.* 114 (2014) 9346-9384.

[66] J.B. Priebe, M. Karnahl, H. Junge, M. Beller, D. Hollmann, A. Brückner, Water reduction with visible light: synergy between optical transitions and electron transfer in Au-TiO<sub>2</sub> catalysts visualized by in situ EPR spectroscopy, *Angew. Chem. Int. Ed.* 52 (2013) 11420-11424.

[67] G. Xie, K. Zhang, B. Guo, Q. Liu, L. Fang, J.R. Gong, Graphene-based materials for hydrogen generation from light-driven water splitting, *Adv. Mater.* 25 (2013) 3820-3839.

[68] V.M. Daskalaki, D.I. Kondarides, Efficient production of hydrogen by photo-induced reforming of glycerol at ambient conditions, *Catal. Today* 144 (2009) 75-80.

- [69] N. Strataki, V. Bekiari, D.I. Kondarides, P. Lianos, Hydrogen production by photocatalytic alcohol reforming employing highly efficient nanocrystalline titania films, *Appl. Catal., B Environ.* 77 (2007) 184-189.
- [70] S. McAllister, J.-Y. Chen, A.C. Fernandez-Pello, *Fundamentals of Combustion Processes*, Springer Science & Business Media, New York, NY, 2011.
- [71] K. Zhang, Q. Liu, H. Wang, R. Zhang, C. Wu, J.R. Gong, TiO<sub>2</sub> single crystal with four-truncated-bipyramid morphology as an efficient photocatalyst for hydrogen production, *Small* 9 (2013) 2452-2459.
- [72] R. Abe, K. Sayama, H. Sugihara, Development of new photocatalytic water splitting into H<sub>2</sub> and O<sub>2</sub> using two different semiconductor photocatalysts and a shuttle redox mediator IO<sup>3-</sup>/I<sup>-</sup>, *J. Phys. Chem. B* 109 (2005) 16052-16061.
- [73] G.L. Chiarello, E. Selli, L. Forni, Photocatalytic hydrogen production over flame spray pyrolysis-synthesised TiO<sub>2</sub> and Au/TiO<sub>2</sub>, *Appl. Catal., B Environ.* 84 (2008) 332-339.
- [74] H. Cheng, J. Ma, Z. Zhao, L. Qi, Hydrothermal preparation of uniform nanosize rutile and anatase particles, *Chem. Mater.* 7 (1995) 663-671.
- [75] H. Zhang, J.F. Banfield, Understanding polymorphic phase transformation behavior during growth of nanocrystalline aggregates: insights from TiO<sub>2</sub>, *J. Phys. Chem. B* 104 (2000) 3481-3487.
- [76] M.C. Hidalgo, M. Maicu, J.A. Navío, G. Colón, Photocatalytic properties of surface modified platinised TiO<sub>2</sub>: effects of particle size and structural composition, *Catal. Today* 129 (2007) 43-49.

- [77] A. Monshi, M.R. Foroughi, M.R. Monshi, Modified Scherrer equation to estimate more accurately nano-crystallite size using XRD, *World J. Nano Sci. Eng.* 02 (2012) 154-160.
- [78] R. Lopez, R. Gomez, Band-gap energy estimation from diffuse reflectance measurements on sol–gel and commercial TiO<sub>2</sub>: a comparative study, *J. Sol-Gel Sci. Technol.* 61 (2012) 1-7.
- [79] H. Luo, C. Wang, Y. Yan, Synthesis of mesostructured titania with controlled crystalline framework, *Chem. Mater.* 15 (2003) 3841-3846.
- [80] J. Tao, T. Luttrell, M. Batzill, A two-dimensional phase of TiO<sub>2</sub> with a reduced bandgap, *Nat. Chem.* 3 (2011) 296-300.
- [81] W. Fan, Q. Lai, Q. Zhang, Y. Wang, Nanocomposites of TiO<sub>2</sub> and reduced graphene oxide as efficient photocatalysts for hydrogen evolution, *J. Phys. Chem. C* 115 (2011) 10694-10701.
- [82] I. Okura, M. Kaneko, *Photocatalysis science and technology*, Springer and Kodansha, Japan, 2002.

**ENHANCED TiO<sub>2</sub> NANORODS PHOTOCATALYSTS WITH  
PARTIALLY REDUCED GRAPHENE OXIDE AND AG  
NANOPARTICLES FOR DEGRADING AQUEOUS HAZARDOUS  
POLLUTANTS**

**Synopsis**

Integrating TiO<sub>2</sub> nanorods (TNRs) with partially reduced graphene oxide (RGO) (designated as GT) was as a photocatalyst composite for degrading aqueous hazardous pollutants. The degree of RGO oxidation played an important role in affecting the photoelectronic and photocatalytic activities of GT composites. The study examined the impact of the degree of RGO oxidation on the photocatalytic activities. The photocatalytic activity of the materials was investigated for photodegrading rhodamine b (RhB), methyl orange (MO), methylene blue (MB) and phenol by using ultraviolet (UV) light. The highest photocatalytic activity was observed when the atomic oxygen-to-carbon (O/C) ratio of RGO was  $0.130 \pm 0.003$ . This study suggested the photocatalytic performance was maximized by preserving a selected amount of the RGO oxygen-containing groups. The work reported in this study on optimizing the RGO based TiO<sub>2</sub> photocatalyst could serve as a promising approach for preparing and optimizing other types of carbon based photocatalysts such as “graphene based CdS”.

Employing highly active photocatalysts and visible light energy is a promising route for removing organic pollutants from drinking water supplies and wastewater effluents. Successful commercial installation of TiO<sub>2</sub> photocatalytic systems for water and wastewater treatment is dependent on enhanced photocatalytic activity under visible

irradiation. In this study, a hierarchical three-dimensional (3D) Ag nanoparticle-RGO-TiO<sub>2</sub> nanorods (TNRs) (designated as Ag-GT) films with optimum RGO atomic O/C ratio and Ag content was synthesized for degrading toxic organic pollutants under visible irradiation. The Ag-GT photocatalyst film was characterized with a significantly high specific surface area (SSA), improved charge separation and visible light absorption. The photocatalytic activity of the film was investigated for the photocurrent and degradation of organic pollutants (RhB, MB, MO and phenol) using visible light. The maximum photocurrent and photodegradation activities were observed for a silver content of 10% in the film photocatalyst.

### 5.1. Introduction

The development of highly active TiO<sub>2</sub> based photocatalysts is an important challenge for remediating polluted water [1-3]. Graphene is widely used to modify TiO<sub>2</sub> photocatalyst [4-8]. Graphene, a two-dimension carbonaceous material [9-12], has attracted much attention for various applications such as energy storage devices [12, 13], photovoltaics [12], and photocatalysis [14] since its discovery in 2004 [15]. Graphene properties include significantly high mobility of charge carriers [12, 16], extremely high thermal conductivity [17], extraordinary elasticity [16, 18], large specific surface area (2630 m<sup>2</sup>g<sup>-1</sup>) [19] and mechanic stability [18]. Graphene is a zero-gap semimetal [20] with a strong capability in accepting, storing and subsequently, shuttling photo-induced electrons to enhance the photocatalytic properties of graphene-based semiconductor nanocomposites [4, 14, 21-23]. The properties of graphene are sensitive to chemical doping and hole doping [24]. The Hummers method [25], involving the oxidization of



graphite, exfoliation of graphite and reduction of graphene oxide (GO) [25], is a cost-effective and widely adopted method to synthesize reduced graphene oxides (RGO). The RGO structure contains lattice defects and residual chemical groups (e.g. oxygen-containing moieties) which degrade the electronic properties when compared to pristine graphene sheets obtained by the mechanical exfoliation method [9, 10]. GO and RGO could be treated as chemically doped or functionalized graphene with oxygen-containing groups and structure distortion [26-28]. The GO and RGO charge mobility property is significantly dependent on the degree of oxidation (the amount of oxygen-containing group on RGO), species of oxygen containing groups and the degree of structural distortion [27-30]. In addition, the oxygen-containing groups serving as ‘anchor sites’ [31] are able to enhance the interaction between RGO and semiconductor oxides [4, 30], and thereby increase the electronic [4, 14] and photocatalytic properties [4, 14].

The discovery of photo-electrochemical water splitting [4, 30] using  $\text{TiO}_2$  electrode in 1972 has triggered more than 45 years of intensive research on developing semiconductor photocatalysts for application in different areas such as  $\text{H}_2$  production [32],  $\text{CO}_2$  reduction [33], hazardous pollutant degradation [34, 35] and bacterial destruction [34, 35]. The photocatalysis reaction involves excitation of a semiconductor such as  $\text{TiO}_2$  with photons having equal or higher energy than the bandgap to produce electron-hole pairs. The electron-hole pairs either recombine or react with adsorbed species. A highly active photocatalyst is characterized by its reaction efficiency as well as suppressing electron-hole combination. The photoactivity of  $\text{TiO}_2$  can be enhanced by coupling with a noble metal, metal ion doping, anion doping and incorporating electron-accepting materials such as graphene [5, 36-40]. These methods have been used to improve charge

transportation, to suppress the charge recombination and to extend the optical absorption to visible light region [5, 36-40]. In particular, incorporating graphene into TiO<sub>2</sub> provides a facile and effective approach to improve the photocatalytic properties [34]. The role of graphene in photocatalysts includes increasing the adsorbability, expanding the light absorption range, changing TiO<sub>2</sub> bandgap and suppressing the electron-hole recombination [4, 7]. Many reports [4, 6-8, 41, 42] on employing graphene-based TiO<sub>2</sub> composites have mainly focused on the effects of the graphene content, photogenerated carrier transportation, RGO adsorption properties and the chemical moieties on the photocatalytic efficiency. However, these studies did not investigate the degree of RGO oxidization on RGO based TiO<sub>2</sub> photocatalyst used in the degradation of aqueous hazardous pollutants. Akhavan et al. (2009 and 2010) [43, 44] demonstrated that bacteria photoinactivation and electron conductivity of RGO based TiO<sub>2</sub> photocatalyst were greatly improved by gradually removing the oxygen-containing groups on RGO. Therefore, the effect of RGO oxidization on photodegrading aqueous hazardous pollutants was assessed in this study.

Furthermore, several researchers have demonstrated improved visible-light photocatalysis using noble-metal-loaded TiO<sub>2</sub> photocatalysts [42, 45-50]. This improvement in photocatalytic activity, which is associated with the extended light absorption range, is due to the surface plasmon resonance (SPR) effect of noble metal NPs [42, 45-50]. The work was carried out to execute the fifth objective in this thesis. The first part of fifth objective, which is addressed in Section 5.3, is to optimize the RGO atomic oxygen-to-carbon (O/C) ratio [51] for synthesizing RGO-TiO<sub>2</sub> nanorods (designated as GT) photocatalyst with maximum photocatalytic activity for

degrading aqueous hazardous pollutants using UV light. The work outlined in Section 5.4 (second part of the fifth objective) is to synthesize a hierarchical three-dimensional (3D) Ag nanoparticle-RGO-TiO<sub>2</sub> nanorods (TNRs) (designated as Ag-GT) thin films photocatalyst with optimum Ag content for degrading aqueous hazardous pollutants under visible irradiation.

## 5.2. Experimental

### 5.2.1. Synthesis of reduced graphene oxide-TiO<sub>2</sub> nanorods (designated as GT) photocatalyst with varied RGO atomic oxygen-to-carbon (O/C) ratio

The TNRs was synthesized using the hydrothermal method using the optimum parameter conditions described in Chapter 4 [52-55]. To prepare the TNRs photocatalyst, 2.5 g TiO<sub>2</sub> P25 nanoparticles was homogeneously mixed with 70 ml of 5 M NaOH by stirring for 30 min. Next, the mixture was placed in a 100-mL Teflon® bottle and capped with a Teflon® cover. The capped Teflon® bottle was placed into a stainless-steel container then capped. The container was heated at 120°C for 48 h and subsequently, cooled to room temperature. The precipitate was separated by centrifugation and subsequently rinsed with 0.1 M HCl. Next, the precipitate was separated again by centrifugation and subsequently washed with deionized water. The centrifuging and washing processes were repeated several times until pH = 7. Next, the precipitate was calcined at 400°C for 2 h to produce the TNRs.

The procedure for synthesizing the GT composites with varied atomic O/C ratio is outlined in Figure 1. Briefly, GO (3wt% (based on per mass of GT composite)) (15 mg) and TNRs (485 mg) were mixed and ultra-sonicated in 100 mL Milli-Q water for 1 h to

ensure re-exfoliating of the GO sheets and dispersing the TNRs between the GO sheets. The GO and TNRs mixture was designated as GOT. Next, 1 ml of hydrazine hydrate was added to the yellow gel. The mixture was maintained at a desired temperature (20°C, 60°C, 80°C, and 95°C) for 1 h to deoxidize (reduce) the GOT to RGO based TNRs (designated as GT). Further deoxidization was conducted by increasing the reaction time to 3 h at 95°C. The resulting product (GT) was isolated by filtration (PTFE 20 um pore size membrane), washed with DI water and 3 times with methanol then dried at 60°C for 12h. The GT produced at 20°C, 60°C and 80°C for 1 h were designated as GT-20, GT-60, GT-80, respectively. The GT reduced samples synthesized at 95°C for 1 h, 2 h and 3 h were designated as GT-95<sup>1h</sup>, GT-95<sup>2h</sup> and GT-95<sup>3h</sup>, respectively.

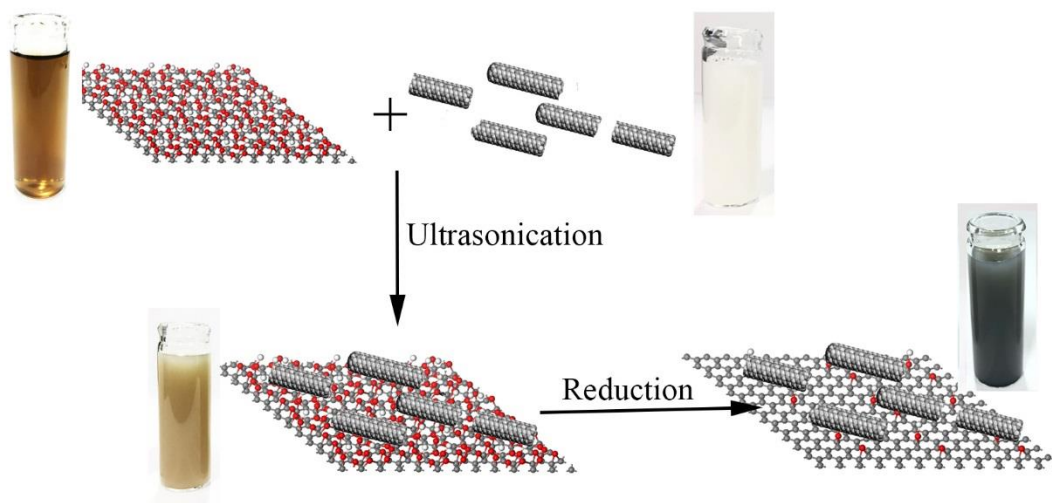


Figure 5.1: Graphene oxide based  $\text{TiO}_2$  nanorods (designated as GOT photocatalyst) and reduced graphene oxide based  $\text{TiO}_2$  nanorods (GT) synthesis process [51].

### 5.2.2. Ag-RGO-TiO<sub>2</sub> nanorods (designated as Ag-GT) synthesis and Ag-GT film preparation

The schematic process employed to synthesize the Ag-GT nanocomposites is shown in Figure 5.2. Briefly, GO (3% w/w) (300 mg) and TNRs (0.97 g) were mixed and ultrasonicated (240 W) in 100 mL deionized water for 1 h to ensure re-exfoliating of the GO and inserting TNRs between the GO sheets. The mixture was mixed with 1 mL of hydrazine hydrate, and was heated at 95°C for 1 h. The RGO-TiO<sub>2</sub> (designated as GT) composite photocatalyst was isolated by filtration (PTFE 20 µm pore size) and washed with DI water and ethanol for 3 times, and subsequently dried at 60°C for 12 h. The silver photocatalysts were synthesized by a deposition–precipitation method (using ethanol as a reducing agent) over the GT photocatalysts. The Ag loading was 5%, 8%, 10%, 12% and 15% and referred as 5%Ag-GT, 8%Ag-GT, 10%Ag-GT, 12%Ag-GT and 15%Ag-GT, respectively. Briefly, 1 g of GT was mixed with 600 mL deionized water, 250 mL ethanol and 5 mL 0.1 M NaOH. The mixture was then stirred for 1 h and heated to 50°C. A specific amount of 9.3 mM AgNO<sub>3</sub> were added to the mixture and kept at 50°C for 3 h. The Ag-GT samples were collected after filtering the mixture and repeated washing with deionized water.

Preparing the Ag-GT film was performed by depositing 0.2 mL of a photocatalyst aqueous solution containing 2 g·L<sup>-1</sup> photocatalyst and 0.25 wt% Nafion (C<sub>7</sub>HF<sub>13</sub>O<sub>5</sub>S·C<sub>2</sub>F<sub>4</sub>) on a 9 × 9 mm<sup>2</sup> glass substrate and subsequently drying at 50°C (Figure 5.2 e). Nafion was used to enhance the mechanical properties of the film. The uniformly coated Ag-GT film with a thickness of several micrometers was formed on the glass substrate.

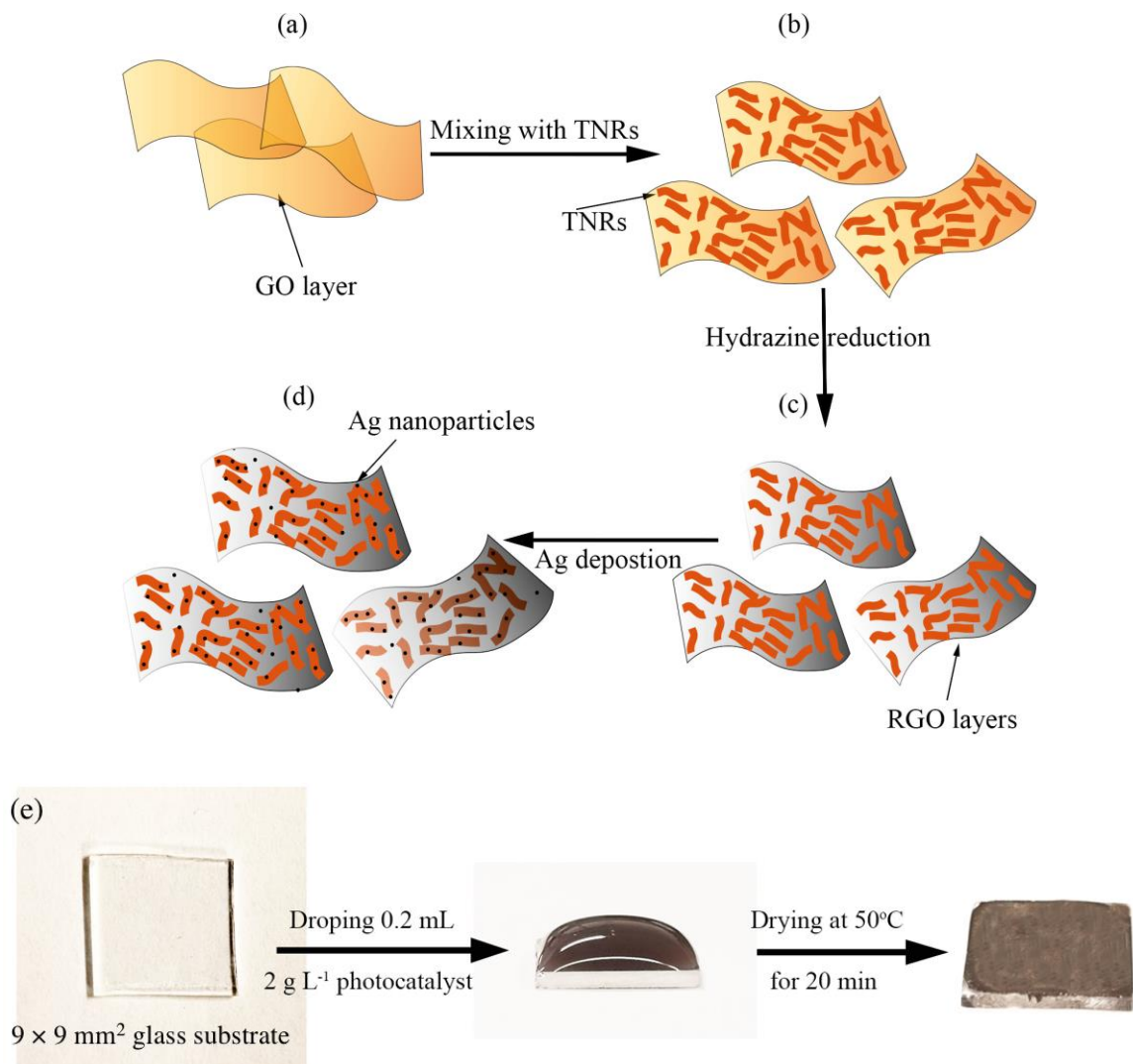


Figure 5.2: Schematic process showing the synthesis of the Ag-GT photocatalyst film. The GO sheets (a) were exfoliated and (b) homogeneously mixed with TNRs using ultrasonication, (c) next, GO-TNRs mixture were reduced to GT and finally, (d) Ag-GT were formed by depositing Ag NPs on GT, and (e) Ag-GT thin film preparation.

### 5.2.3. Characterization studies

The morphology and structure were investigated using high-resolution transmission electron microscopy (HRTEM) (JEOL 3010, Japan). The lattice spacing (d) was measured from a digitized HRTEM image by digital image processing and evaluation was conducted using the Digital Micrograph (Gatan, CA). Field emission scanning

electron microscopy (FESEM) (Thermo Fisher Scientific, MA., United States) and energy dispersive X-ray (EDX) (Thermo Fisher Scientific, MA, United States) analysis were used to examine the surface morphology and composition of the GT sample. The photocatalyst was dispersed ultrasonically in ethanol. Small amount of the solution (20  $\mu$ L) was deposited and dried on aluminum film at room temperature for the FESEM and EDX studies. Raman spectroscopy was conducted using an Alpha300 RA argon laser Raman spectrometer (WITec, Germany) equipped with a 532-nm laser. UV–visible spectra analysis performed using a Cary 300 UV-visible (Agilent Technologies, United States). X-ray photoelectron spectroscopy (XPS) measurements were performed using a VG Scientific ESCALAB 210 electron spectrometer (Thermo Electron Corporation, MA, United States) equipped with a Mg K $\alpha$  radiation source ( $h\nu = 1253.6$  eV, 300 W). X-ray diffraction (XRD) analysis was performed with an X-ray diffractometer (Rigaku, MI, United States) equipped with a Cu K $\alpha$  radiation source. Nitrogen adsorption–desorption isotherms were recorded at 77 K using a Micromeritics ASAP 2020 Brunauer–Emmett–Teller (BET) analyzer (Micromeritics Instrument Corp. GA, United States).

#### *5.2.4. Photoelectrochemical measurements*

Photoelectrochemical measurements were conducted using a CHI 704D (CH Instrument inc, Texas) with a standard three-electrode cell. Platinum wire was used as the counter electrode and a saturated calomel electrode (SCE) was used as a reference electrode. For the GT working electrode, 0.25 g photocatalyst was mixed with 0.06 g polyethylene glycol (PEG, molecular weight 20 000) and 1 mL deionized water to produce a slurry. The slurry was coated onto a 2 cm x 1.2 cm F-doped SnO<sub>2</sub>-coated

(FTO) glass electrode using a doctor blade method [56, 57]. The electrode was annealed at 450°C for 30 minutes. The measurements were performed in a 1 M Na<sub>2</sub>SO<sub>4</sub> aqueous solution as electrolyte. A 300-nm monochromatic UV light with an average intensity of 9 mW cm<sup>-2</sup> was used as the UV light source.

#### 5.2.5. Photocatalytic activity under ultraviolet (UV) light

The photocatalytic experiments were conducted using instruments and the process described in Chapter 2 (Section 2.3.10). The reaction mixture consisted of a specific concentration of organic chemical and 100 mg·L<sup>-1</sup> of photocatalysts. The organic chemicals examined in the study included RhB, phenol, MO and MB. The initial concentration (C<sub>0</sub>) of MO, RhB, phenol and MB was 20 mg·L<sup>-1</sup>, 10 mg·L<sup>-1</sup>, 20 mg·L<sup>-1</sup>, 10 mg·L<sup>-1</sup>, respectively. The 50-mL reaction mixture containing a specific organic chemical plus photocatalyst was ultrasonicated for 15 minutes and subsequently, magnetically stirred under dark conditions for 1 h to attain adsorption-desorption equilibrium. The reaction mixture was exposed to UV light for 10 minutes. A 5-mL reaction mixture was collected at specific time intervals of 2 minutes. The liquid sample was centrifuged (5,000 rpm for 60 minutes) and filtered using a 0.1 µm polyvinylidene difluoride (PVDF) filter (Sigma-Aldrich, Oakville, ON, Canada). The residual RhB, MO and MB concentration (C) in the filtrate was determined by measuring the optical absorbance at 554 nm, 464 nm and 664 nm, respectively, using a UV–Vis spectrophotometer (Agilent Technologies, United States). The detection limit for RhB, MO and MB were 1 µg·L<sup>-1</sup>. The residual phenol concentration was determined using a high performance liquid chromatograph (HPLC) (Dionex Ultimate 3000, Sunnyvale, CA, United States) described



in Chapter 2 (Section 2.3.8). The residual concentration of the chemicals was used to determine the reaction rate of discoloration or disappearance, termed hereafter as apparent reaction rate. The apparent reaction rate was modeled using a pseudo-first order rate equation (Eq. 5.1) [58-60].

$$\frac{-dC}{dt} = kC \quad (5.1)$$

where  $k$  is the apparent reaction rate constant ( $\text{min}^{-1}$ ),  $C$  is the organic chemical concentration ( $\text{mg}\cdot\text{L}^{-1}$ ) and  $-dC/dt$  is the pseudo-first order reaction rate.

#### *5.2.6. Ag-GT film photocatalytic activity under visible irradiation*

The Ag-GT film samples, deposited on glass substrates, were placed in a Pyrex cell ( $25 \text{ mm} \times 10 \text{ mm} \times 10 \text{ mm}$ ) facing the visible light source. The Rhodamine B solution was stirred for 60 minutes under dark conditions to ensure adsorption/desorption equilibrium onto the photocatalyst film. A 125 W (Philips) white light source was used to irradiate the samples. During the Rhodamine B photocatalytic degradation experiments, samples were collected, and the absorbance was monitored using a spectrophotometer (Maya 2000+, Ocean Optics, FL, United States) set at 554 nm. In addition, the photodegradation of phenol, MO and MB was monitored using the same procedure as photodegradation of RhB.

### 5.3. Graphene based $\text{TiO}_2$ nanorods (GT) photocatalyst with optimum RGO atomic oxygen-to-carbon (O/C) ratio

#### 5.3.1. The graphene based $\text{TiO}_2$ nanorods (GT) morphology and phase structure

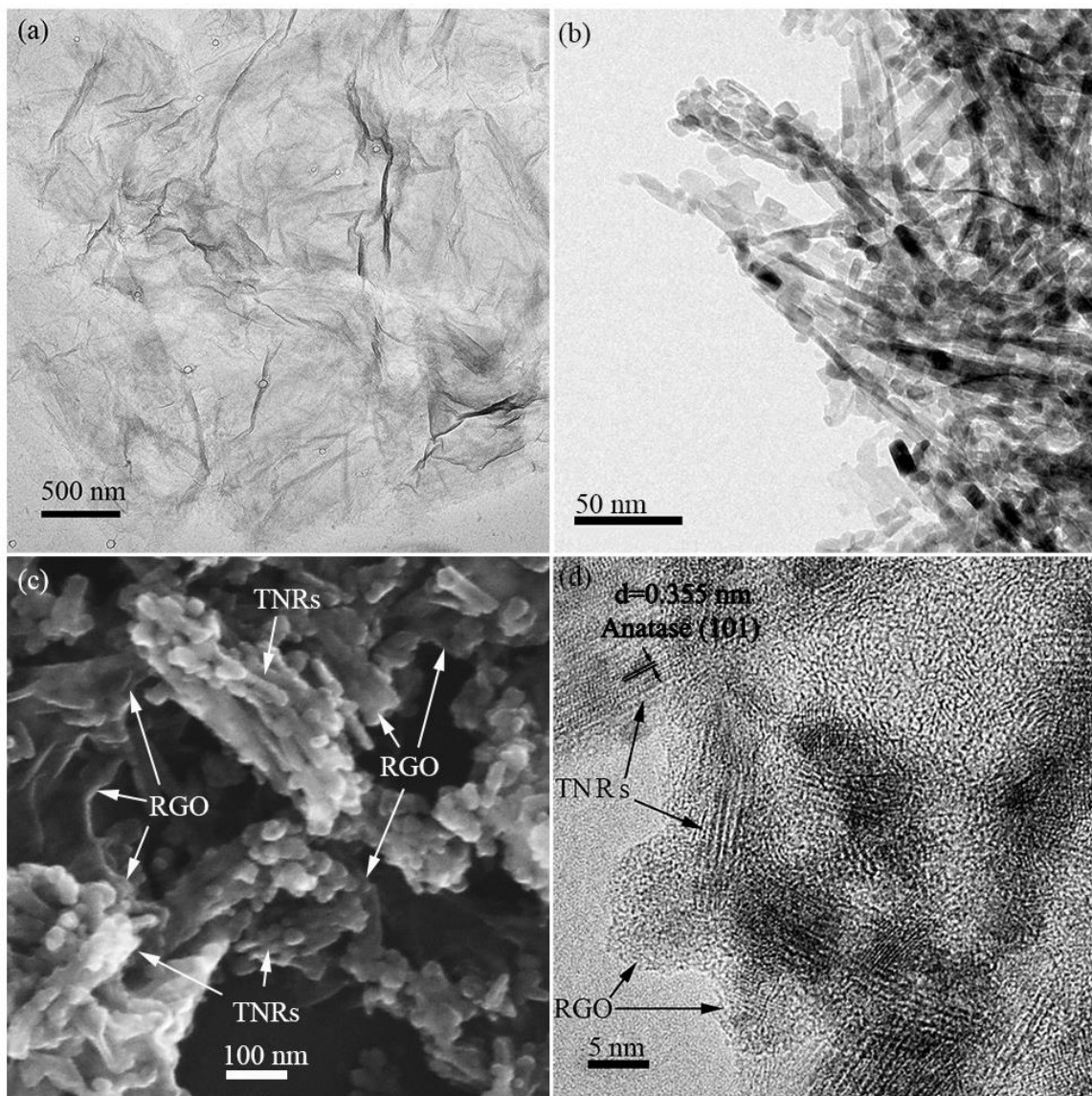


Figure 5.3: Field emission scanning electron microscopy (FESEM) and high-resolution transmission electron microscopy (HRTEM) images: (a) Graphene oxide (GO) HRTEM image, (b)  $\text{TiO}_2$  nanorods (TNRs) TEM image, (c) Reduced graphene oxide based  $\text{TiO}_2$  nanorods synthesized at  $95^\circ\text{C}$  for 1 h ( $\text{GT-95}^{1\text{h}}$ ) FESEM image, and (d)  $\text{GT-95}^{1\text{h}}$  HRTEM image.

Note: d represents lattice interplanar spacing.

TEM images (Figure 5.3 a and b) show GO sheets with some wrinkling patterns and TNRs with an average diameter of approximately 10 nm and lengths ranging from 20 to 50 nm. The FESEM image of commercial TiO<sub>2</sub> nanoparticles (P25) shows that a biphasic anatase-rutile phase structure with an average diameter of 40 nm is larger than the diameter of TNRs (Figure 5.4). After reduction treatment, the sheet morphology was retained in the GT structure (Figure 5.3c). The RGO sheets were fully covered with TNRs. The FESEM results for the GT-95<sup>th</sup> (Figure 5.3c) structure are in agreement with the structures shown in the GT structure illustrated in Figure 5.1.

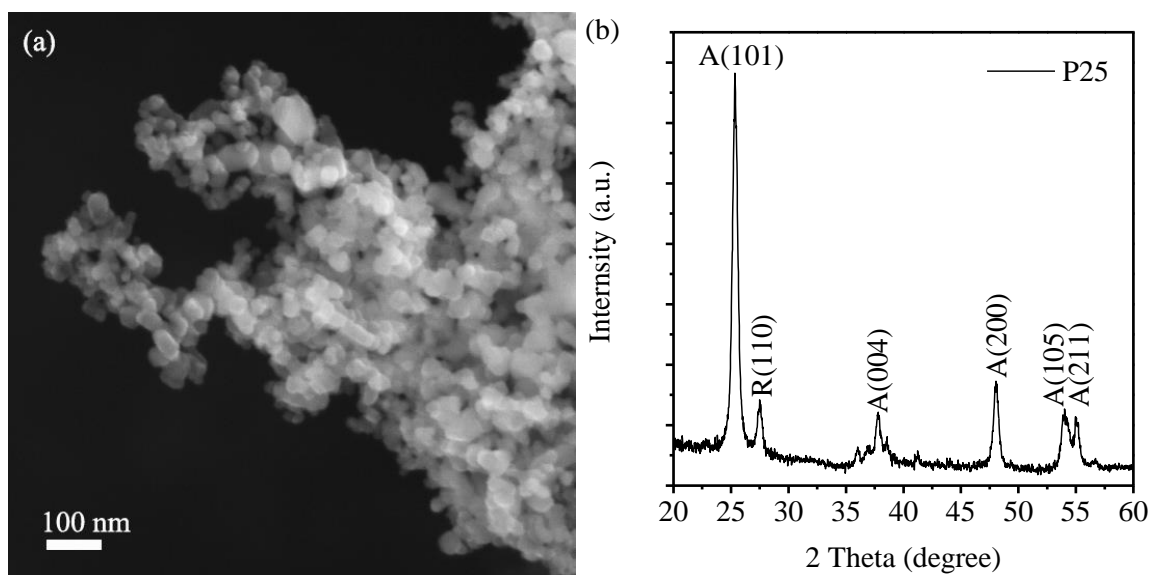


Figure 5.4: (a) Field emission scanning electron microscopy (FESEM), and (b) X-ray diffraction (XRD) for commercial TiO<sub>2</sub> (P25) nanoparticles.

Note: A and R represents anatase and rutile, respectively.

EDX mapping was conducted to analyze GT for C, Ti and O elements. The EDX mapping (Figure 5.5) shows that the intense points were relative intensive for Ti and O elements; however, the lower intensity for C element was likely attributed to the small amount of C (<3 wt% per mass of GT composite) in the GT-95<sup>th</sup> sample. The intense

areas in the EDX map demonstrate the homogeneous dispersion for each element across the particle. This implies homogeneous dispersion of RGO sheets in the GT composites. The HRTEM image (Figure 5.3d) clearly shows that the TNRs attach to the RGO sheets indicated the successful synthesis of GT composites. The lattice spacing  $d = 0.355$  nm on the HRTEM image (Figure 5.3d) suggest the presence of anatase in the TNRs [61, 62].

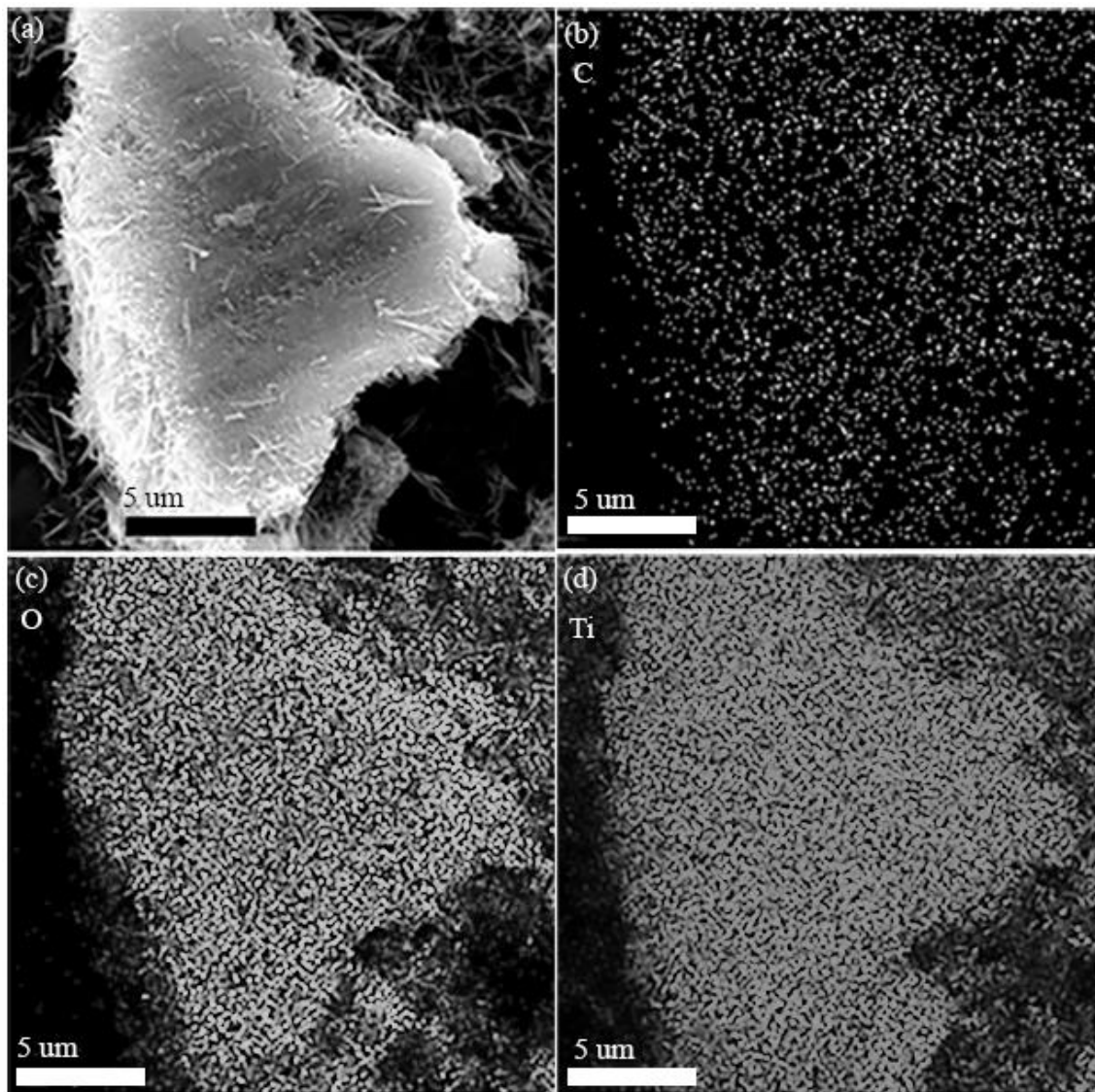


Figure 5.5: Field emission scanning electron microscopy (FESEM) image and energy dispersive X-ray (EDX) patterns for GT-95<sup>1h</sup> samples. (a) GT-95<sup>1h</sup> FESEM image, (b) C element EDX mapping, (c) O element EDX mapping, and (d) Ti element EDX mapping. Note: GT-95<sup>1h</sup> represents enhanced TiO<sub>2</sub> nanorods (TNRs) with reduced graphene oxide (RGO) photocatalyst synthesized at 95°C for 1 h.

The TNRs and its composites XRD patterns are shown in Figure 5.6. All the samples exhibited characteristic anatase and rutile peaks [63]. The intensity pattern indicates the anatase phase was dominant in all the samples with a small amount of the rutile phase. The GOT and GT, GO(002) samples showed a broad band in a range from  $\sim 10^\circ 2\theta$  [64]. The decreasing GO (002) peak intensity suggests the removal of oxygen-containing group was accomplished when GT was produced from the GOT sample. When compared to GOT, all the GT samples containing a graphene (002) peak located at  $26^\circ 2\theta$  suggest that GO was reduced to RGO [21]. The low intensity of the graphene (002) peak was due to the low RGO content in the photocatalyst.

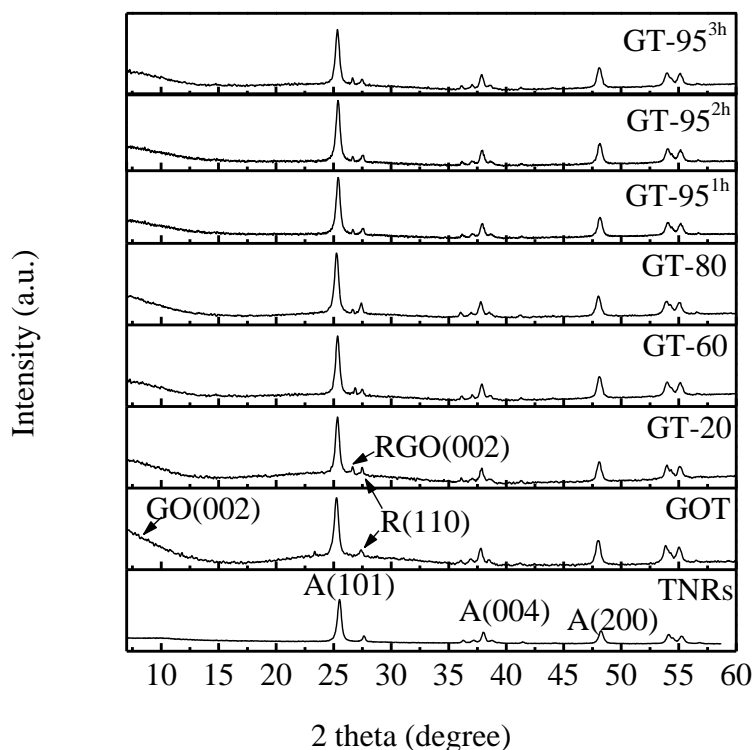


Figure 5.6: X-ray diffraction (XRD) patterns for  $\text{TiO}_2$  nanorods (TNRs) and its composites.

Notes: <sup>a</sup> A and R represent anatase and rutile, respectively, <sup>b</sup> GT represents reduced graphene oxide based  $\text{TiO}_2$  nanorods, <sup>c</sup> GO and RGO represent graphene oxide and reduced graphene oxide, respectively, and <sup>d</sup> the number after GT represents the temperature ( $^\circ\text{C}$ ) condition and time (h) to synthesize the photocatalysts.

5.3.2. *Removing oxygen-containing groups and adjusting the the atomic oxygen-to-carbon (O/C) ratio of reduced graphene oxide (RGO)*

Investigating changes in chemical structure for RGO was conducted using Raman spectroscopy. Peaks for both TiO<sub>2</sub> and carbon nanomaterials were observed for GT (Figure 5.7a) synthesized under different conditions. Peaks at 144 cm<sup>-1</sup> (E<sub>g</sub>), 399 cm<sup>-1</sup> (B<sub>1g</sub>), 513 cm<sup>-1</sup> (A<sub>1g</sub>), and 638 cm<sup>-1</sup> (E<sub>g</sub>) indicate the presence of the anatase phase [65]. The D and G peaks located at ~1347 cm<sup>-1</sup> and ~1600 cm<sup>-1</sup>, respectively, were detected in GOT and GT samples [66]. The D mode, which is observed when sp<sup>3</sup> atoms are present, represents disorder in the crystal structure [67-70]. The G mode which represents order in the crystal structure corresponds to bond stretching of all pairs of sp<sup>2</sup> atoms [67-70]. The D band to the G band integrated intensity ratio (I<sub>D</sub>/I<sub>G</sub>) was used to establish the degree of defects in the GO and RGO structures [21, 66]. The lower integrated I<sub>D</sub>/I<sub>G</sub> ratio of RGO showed an increase in the average size of the sp<sup>2</sup> domains (graphitization and order) upon the reduction of GO [67-70]. The I<sub>D</sub>/I<sub>G</sub> values are tabulated in Figure 5.7b and listed in Table 5.1 showed the following decreasing integrated I<sub>D</sub>/I<sub>G</sub> ratio trend: GOT > GT-20 > GT-60 > GT-80 > GT-95<sup>1h</sup> > GT-95<sup>2h</sup> > GT-95<sup>3h</sup> (Figure 5.7b). The decreasing integrated I<sub>D</sub>/I<sub>G</sub> ratio suggests that the RGO oxygen containing functional group gradually decreased with an increase in temperature and reaction time [71]. This gradual decrease is caused by increasing the reduction reaction rate as the temperature rises and increasing reaction time [72]. According to Perera et al. [21], reduction of the defective GO is a crucial mechanism which can be employed to enhance the RGO electrical properties. In addition, the layer number of RGO sheets was determined based on the position and the shape of the 2D band. The 2D band of single-layer graphene is

located at  $2679\text{ cm}^{-1}$  [44, 73]. An increase in graphene layer numbers (2-5 layers) is closely linked to a significant up-shift in the wavenumber by  $19\text{ cm}^{-1}$  for 2D band [44, 69, 73]. In this study, the 2D bands were observed at  $2683\text{ cm}^{-1}$  for samples (Figure 5.8) that contain GO or RGO. These relatively lower 2D band wavenumbers indicate the samples containing a significant number of single-layer graphene (oxide) sheets.

X-ray photoelectron spectroscopy (XPS) was employed to confirm the trend of oxygen containing group removal. In the deconvoluted C1s spectra (Figure 5.7c), the peaks located at 284.5 and 284.8 eV correspond to the C-C and C=C bonded carbon, respectively, whereas the deconvoluted peaks for C-OH (286.9 eV), C=O (289.0 eV) are attributed to oxygen containing functional groups on the RGO layers [26, 72]. GO and GOT with atomic O/C ratio of  $0.8300\pm 0.0124$  and  $0.8500\pm 0.0075$ , respectively, indicate that mixing GO and  $\text{TiO}_2$  photocatalyst did not affect the GO atomic O/C ratio. However, reduction of GO to RGO decreased the atomic O/C ratio significantly. For C-O and C=O peaks, decreasing the peak intensity was observed with an increase in the reaction temperature and time. This suggests decreasing amounts of the oxygen containing functional groups. The atomic O/C ratios determined using the integrated areas under the C 1s peak are shown in Figure 5.7d. The atomic O/C ratios represents the integrated areas of C-O and C=O divided by the integrated areas of C=C and C-C. Decreasing RGO atomic O/C ratios was observed in the following trend: GOT > GT-20 > GT-60 > GT-80 > GT-95<sup>1h</sup> > GT-95<sup>2h</sup> > GT-95<sup>3h</sup>. The decreasing RGO atomic O/C ratio is consistent with the trend observed for the decreasing  $I_D/I_G$  ratios (Figure 5.7b). The data clearly indicate the GT photocatalysts possess a tunable atomic O/C ratio.

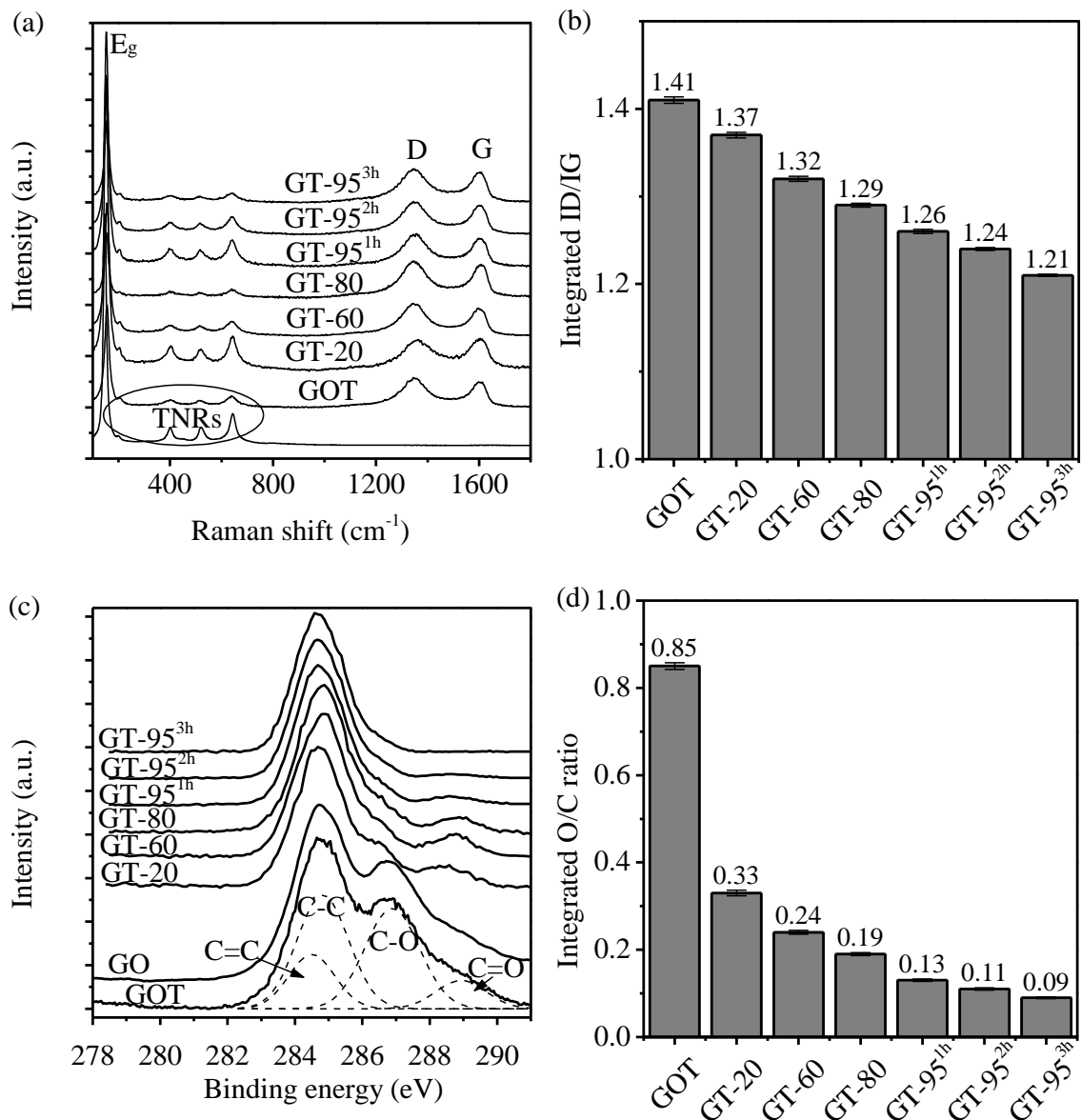


Figure 5.7: Raman spectra and X-ray photoelectron spectroscopy (XPS) for samples. (a) Raman spectra, (b) Integrated intensity ratio  $I_D/I_G$ , (c) C1s X-ray photoelectron spectroscopy (XPS) spectra, and (d) Integrated atomic oxygen-to-carbon (O/C) ratio of reduced graphene oxide (RGO).

Notes: <sup>a</sup> GT represents reduced graphene oxide based TiO<sub>2</sub> nanorods, <sup>b</sup> GOT represents graphene oxide based TiO<sub>2</sub> nanorods, and <sup>c</sup> the number after GT represents the temperature (°C) condition and time (h) to synthesize the photocatalysts.



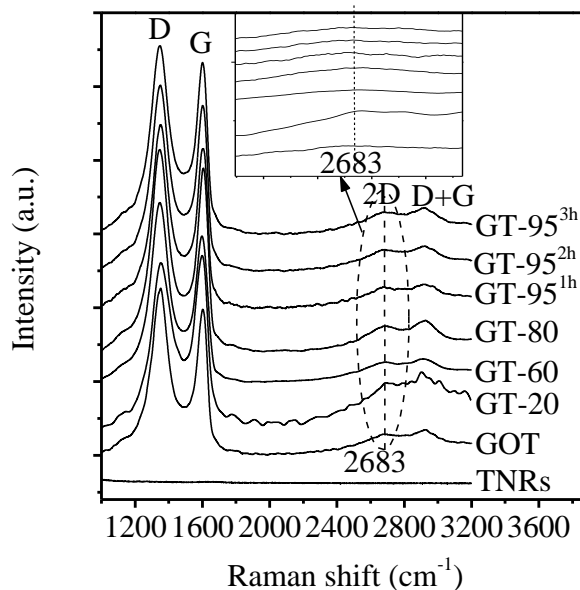


Figure 5.8: Raman spectra for samples.

Notes: <sup>a</sup> D+G band indicates a significant number of defects in graphene sheet, <sup>b</sup> GT produced at 20°C, 60°C and 80°C for 1 h were designated as GT-20, GT-60, GT-80, respectively, and <sup>c</sup> GT samples synthesized at 95°C for 1 h, 2 h and 3 h were designated as GT-95<sup>1h</sup>, GT-95<sup>2h</sup> and GT-95<sup>3h</sup>, respectively.

Table 5.1: Summary of integrated intensity ratio of the D band to the G band ( $I_D/I_G$ ) and atomic oxygen-to-carbon (O/C) ratio for different samples.

	GOT	GT-20	GT-60	GT-80	GT-95 <sup>1h</sup>	GT-95 <sup>2h</sup>	GT-95 <sup>3h</sup>
$I_D/I_G$	1.41± 0.0037	1.37± 0.0032	1.32± 0.0028	1.29± 0.0023	1.26± 0.0023	1.24± 0.0018	1.21± 0.0013
RGO atomic O/C ratio	0.85± 0.0075	0.33± 0.0062	0.24± 0.0045	0.19± 0.0034	0.13± 0.0027	0.11± 0.0025	0.09± 0.0021

Notes: <sup>a</sup> GOT represents graphene oxide based TiO<sub>2</sub> nanorods, <sup>b</sup> GT represents reduced graphene oxide based TiO<sub>2</sub> nanorods, <sup>c</sup> the number after GT represents the temperature (°C) condition and time (h) to synthesize the photocatalysts, <sup>d</sup>  $I_D/I_G$  represents integrated intensity ratio of the D band to the G band, and <sup>e</sup> O/C represents oxygen-to-carbon.

### 5.3.3. Interaction between reduced graphene oxide (RGO) and TiO<sub>2</sub> nanorods (TNRs)

The E<sub>g</sub> vibrational mode peak for selected samples is shown in Figure 5.9. The E<sub>g</sub> peak at 146 cm<sup>-1</sup> is associated with the TNR sample. A blue-shift from 146 cm<sup>-1</sup> to 155 cm<sup>-1</sup> for the GOT E<sub>g</sub> peak was observed when compared to TNRs. The E<sub>g</sub> peak's blue shift which was caused by the phonon confinement effect and likely due to the strain developed at the interface between TiO<sub>2</sub> and GO [21, 74] suggests strong bonding interactions between TNRs and GO [4, 21, 74, 75]. The greatest blue shift among the different samples was observed for GOT which had the strongest interactions between TNRs and GO among all the different samples. However, the degree of blue shift decreased with increasing RGO deoxidization was a function of increasing reaction temperature and time. Notice the blue shift decreased with deoxidization or the decreasing O/C ratio from 0.850±0.007 to 0.090±0.002 was observed for a temperature change from 20°C to 95°C and reaction time change from 1 h to 3 h. The E<sub>g</sub> peak assigned to the GT-95<sup>1h</sup> and GT-95<sup>3h</sup> samples were located at 152 cm<sup>-1</sup> and 150 cm<sup>-1</sup>, respectively, and the E<sub>g</sub> peaks for GT-20, GT-60 and GT-80 were positioned between the E<sub>g</sub> for the GOT and GT-95<sup>1h</sup> samples. The decreasing blue shift suggested that the interaction between RGO and TNWs decreased with decreased with RGO deoxidization. In the XPS Ti2p (Figure 5.10) and C1s spectra (Figure 5.7c), no peaks corresponding to Ti-C and Ti-O-C chemical bonds indicate that the interaction is based on physical and not chemical attachment [44, 76].

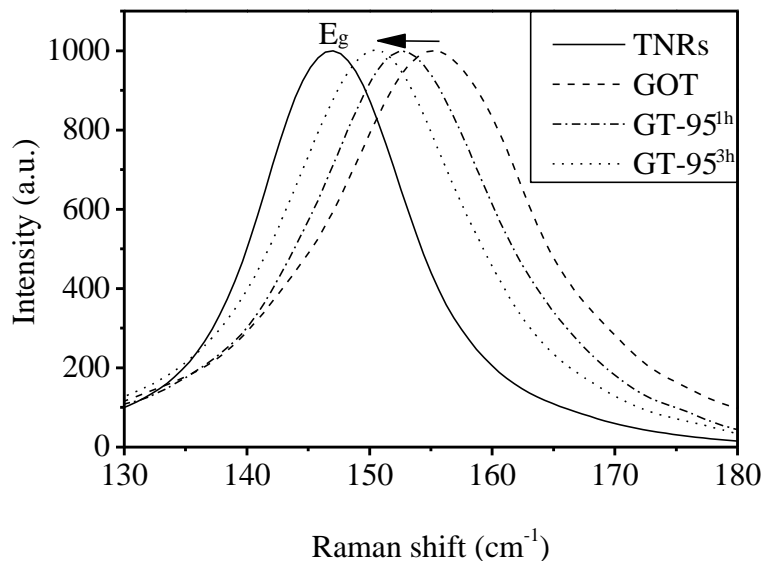


Figure 5.9: Raman spectra for the  $E_g$  peak blue shift.

Notes: <sup>a</sup> TNRs represents  $\text{TiO}_2$  nanorods, <sup>b</sup> GT represents reduced graphene oxide based  $\text{TiO}_2$  nanorods, <sup>c</sup> GOT represents graphene oxide based  $\text{TiO}_2$  nanorods, and <sup>d</sup> the number after GT represents the temperature ( $^\circ\text{C}$ ) condition and time (h) to synthesize the photocatalysts.

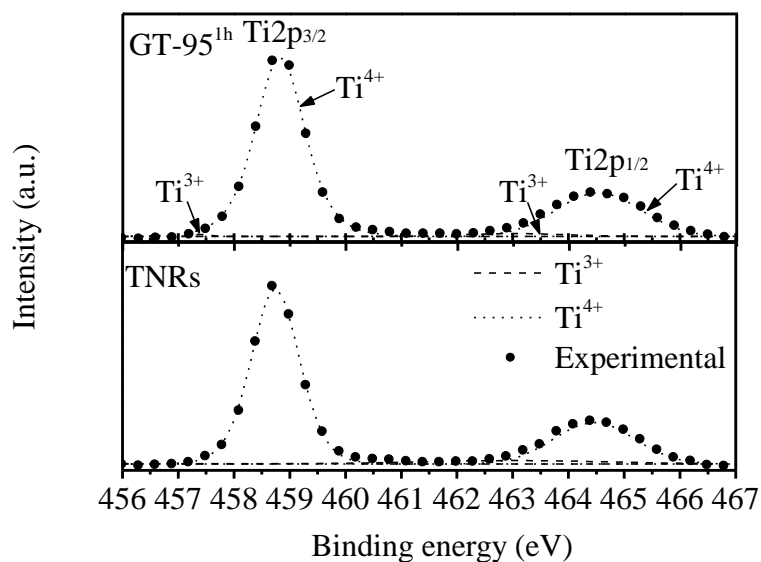


Figure 5.10:  $\text{Ti}2p$  X-ray photoelectron spectroscopy (XPS) spectra for  $\text{TiO}_2$  nanorods (TNRs) and reduced graphene oxide based  $\text{TiO}_2$  nanorods synthesized at  $95^\circ\text{C}$  for 1 h reaction ( $\text{GT-}95^{1\text{h}}$ ).

#### 5.3.4. Optical response and bandgap

The atomic O/C ratio exerted a remarkable influence on the optical properties. Lower bandgap energies resulted in more efficient optical absorption. Diffuse reflectance UV-visible spectroscopy (DRS) (Figure 5.11a) was used to examine the optical response for each sample. The bandgap for each sample was calculated by using the Kubelka Munk function to convert the diffuse reflectance spectra into an absorption spectra (Figure 5.11b) [77]. By adding GO or RGO sheets, a significant increase in optical absorption in the visible light region (Figure 5.11a) was observed for GOT when compared to the TNRs. The optical absorption was further increased by reducing GOT to GT which contained a lower RGO atomic O/C ratio. The greatest optical absorption was observed with GT-95<sup>1h</sup> containing an RGO atomic O/C ratio of  $0.130 \pm 0.003$ . However, further deoxidization by increasing the reaction time to 3 h resulted in a decrease in the optical absorption when compared to GT-95<sup>1h</sup>. The decreased optical response for GT-95<sup>2h</sup> and GT-95<sup>3h</sup> was likely caused by the separation of RGO from TiO<sub>2</sub> due to the decreased interaction between RGO and TiO<sub>2</sub> when excessive deoxidization occurred.

Decreasing GOT bandgap (3.08 eV) was observed by adding GO to TNRs (Figure 5.11b). Further narrowing of the bandgap occurred by continuing deoxidization of RGO. With decreasing RGO atomic O/C ratios from  $0.850 \pm 0.007$  to  $0.130 \pm 0.003$ , the bandgap decreased trend was as follows: GOT (3.04 eV) > GT-20 (2.91 eV) > GT-60 (2.73 eV) > GT-80 (2.65 eV) > GT-95<sup>1h</sup> (2.61 eV) (Figure 5.11b). However, as RGO atomic O/C ratios decreased from  $0.130 \pm 0.003$  to  $0.09 \pm 0.002$ , the bandgap increased to 2.75 eV and 2.87 eV for the GT-95<sup>2h</sup> and the GT-95<sup>3h</sup> samples, respectively. This indicated that an excessive removal of oxygen-containing functional groups caused an increase in the

bandgap. According to Zhang et al. (2010) [78], the chemical bonds of Ti-O-C were responsible for the interaction between TiO<sub>2</sub> and RGO. This interaction narrowed the TiO<sub>2</sub> bandgap [78]. For the GT-95<sup>3h</sup> sample, an excessive removal of the oxygen containing functional groups weakened the interaction between TiO<sub>2</sub> and RGO and this increased the bandgap from 2.61 eV to 2.84 eV.

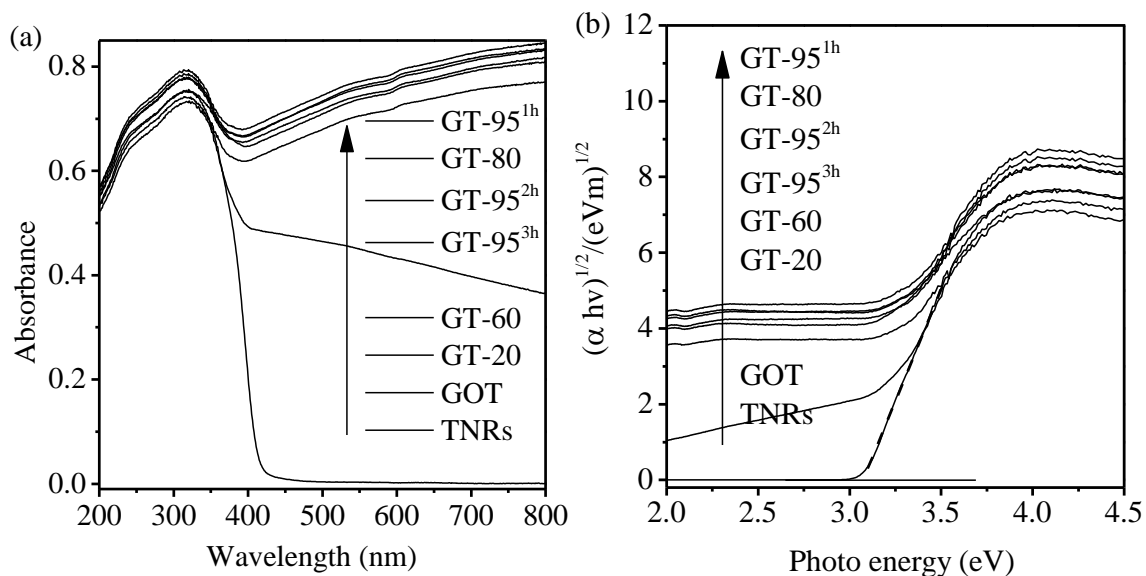


Figure 5.11: Plots for (a) diffuse reflectance UV-visible spectroscopy, and (b)  $(\alpha_{km}hv)^{1/2}$  versus absorbed energy.

Notes: <sup>a</sup> TNRs represents TiO<sub>2</sub> nanorods, <sup>b</sup> GT represents reduced graphene oxide based TiO<sub>2</sub> nanorods, <sup>c</sup> GOT represents graphene oxide based TiO<sub>2</sub> nanorods, and <sup>d</sup> the number after GT represents the temperature (°C) condition and time (h) to synthesize the photocatalysts.

### 5.3.5. Charge transportation and separation

The transit photocurrent responses were examined to illustrate the influence of the RGO atomic O/C ratio on the charge transportation and separation for the GT composites. I-t curves for each sample with an on-off UV-light irradiation source are shown in Figure 5.12. The current for each sample increased when the light source was applied and a rapid decrease to approximately zero was observed after removing the light source.

Incorporation of GO into TNRs resulted in a slight decrease in photocurrent when compared to TNRs. A significant increase in the photocurrent was observed when the GOT sample was reduced to GT. This increase is attributed to enhanced charge carries transfer and separation by incorporating TNR with the highly conductive RGO [78]. The photocurrent continued increasing with a decrease in the RGO atomic O/C ratio from  $0.850\pm 0.007$  to  $0.130\pm 0.003$ . The highest photocurrent for GT-95<sup>lh</sup> was a 12-fold increase when compared to pure TNRs. This photocurrent was approximately 6-fold increase when compared to the UV-assisted TiO<sub>2</sub>-RGO reported by Williams et al. (2008) [5]. The UV-assisted TiO<sub>2</sub>-RGO which showed approximate 2-fold increase when compared to pure TiO<sub>2</sub> was synthesized by photocatalytic reduction of GO under UV light. Akhavan et al. (2009 and 2010) [43, 44] reported that the photocatalytic activity of UV-assisted TiO<sub>2</sub>-RGO was further improved by gradually removing the oxygen-containing groups. This suggestion of removing the oxygen-containing groups was closely linked to an increase in the photocatalytic activity for the RGO based TiO<sub>2</sub> photocatalyst with high atomic O/C ratios. However, the photocurrent decreased sharply with a decrease in the atomic O/C ratio from  $0.130\pm 0.003$  to  $0.090\pm 0.002$ . This decrease is likely due to the excessive loss of the oxygen containing groups leading to weak interactions between RGO and TNRs. The results indicated that preserving an appropriate amount of oxygen containing groups on RGO sheets will manage and hence, maximize the charge-carries transfer and separation processes.

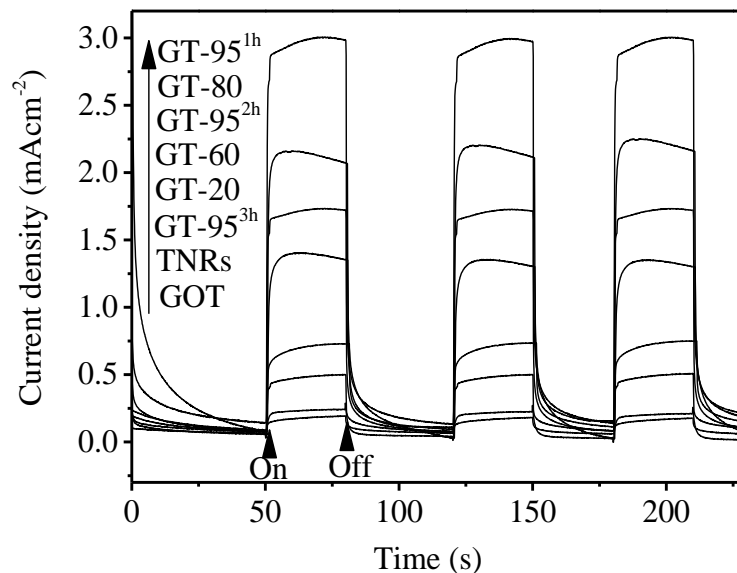


Figure 5.12: Transient photocurrent responses for samples in 1 M  $\text{Na}_2\text{SO}_4$  aqueous solution under ultraviolet-light irradiation (300 nm) at 0.5 V versus saturated calomel electrode (SCE).

Notes: <sup>a</sup> TNRs represents  $\text{TiO}_2$  nanorods, <sup>b</sup> GT represents reduced graphene oxide based  $\text{TiO}_2$  nanorods, <sup>c</sup> GOT represents graphene oxide based  $\text{TiO}_2$  nanorods, and <sup>d</sup> the number after GT represents the temperature ( $^\circ\text{C}$ ) condition and time (h) to synthesize the photocatalysts.

### 5.3.6. Photocatalytic activity

The photocatalytic activities for each sample were characterized using MO as a model pollutant under UV light (Figure 5.13). Two control experiments were conducted without any photocatalyst and with RGO. Approximate 5% and 2% MO was adsorbed onto the GOT and TNRs samples, respectively, after 1-h stirring under dark conditions stirring at  $20^\circ\text{C}$ . This indicates 3% RGO negligibly increased the MO adsorption onto the sample. The apparent first-order MO photocatalysis rate constants (apparent MO  $k$ ) for no photocatalyst ( $0.0003 \pm 0.0001 \text{ min}^{-1}$ ) and RGO ( $0.0053 \pm 0.0012 \text{ min}^{-1}$ ) were significantly less when compared to  $0.2361 \pm 0.0021 \text{ min}^{-1}$  for TNRs and  $0.2202 \pm 0.0025 \text{ min}^{-1}$  for  $\text{TiO}_2$  P25 based on the Tukey's test [79] (Figure 5.13 and Table 5.2).

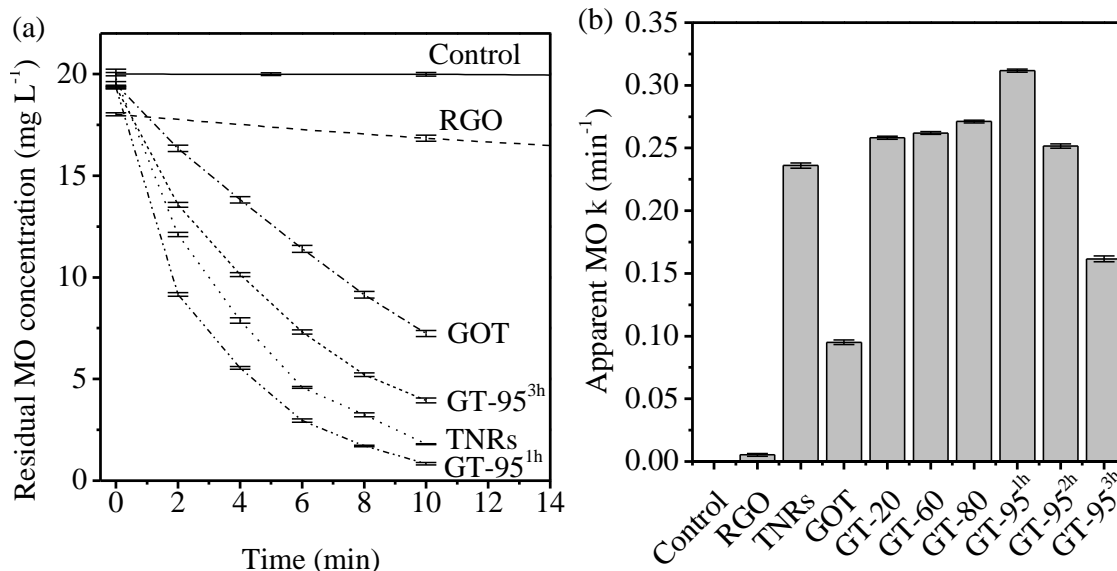


Figure 5.13: Methyl orange photocatalysis using selected photocatalysts under UV light. (a) Residual methyl orange concentration versus time for selected samples. (b) Apparent first-order methyl orange photocatalysis rate constants (apparent MO  $k$ ) ( $\text{min}^{-1}$ ) for a control and selected photocatalysts.

Notes: <sup>a</sup> Control contains no photocatalyst, <sup>b</sup> TNRs represents TiO<sub>2</sub> nanorods, <sup>c</sup> GT represents reduced graphene oxide based TiO<sub>2</sub> nanorods, <sup>d</sup> GOT represents graphene oxide based TiO<sub>2</sub> nanorods, <sup>e</sup> RGO represents reduced graphene oxide, and <sup>f</sup> the number after GT represents the temperature (°C) condition and time (h) to synthesize the photocatalysts.

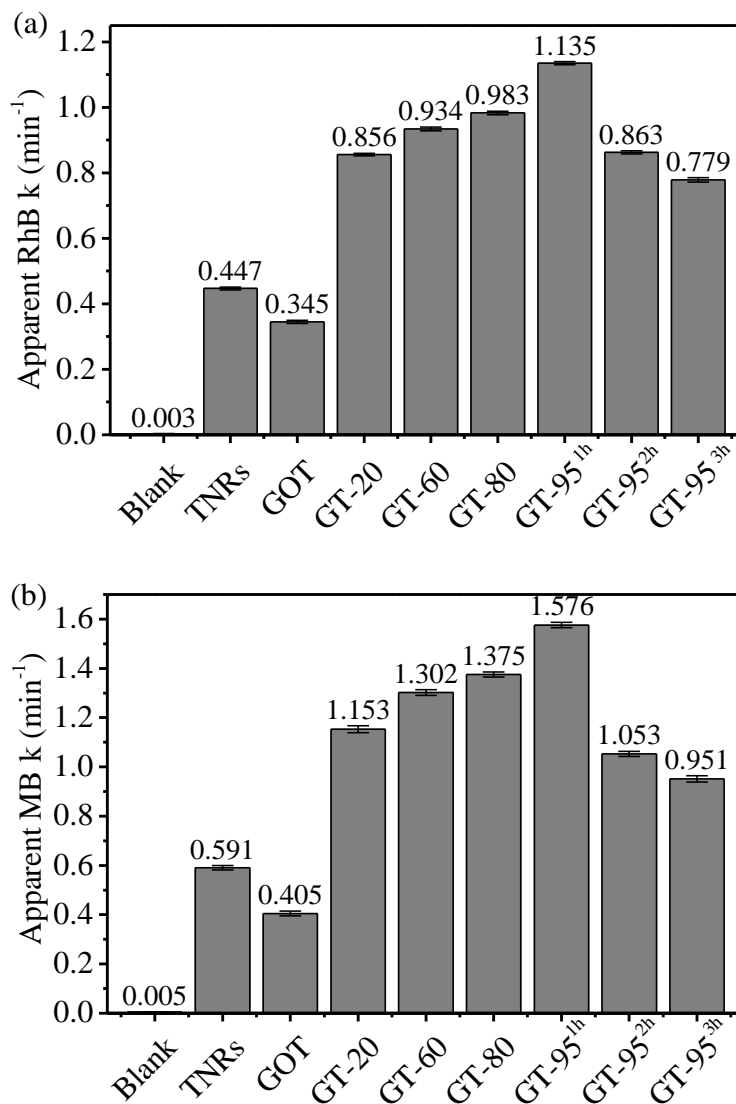
Coupling TNRs with GO caused a sharp decrease in the apparent MO  $k$  to  $0.0951 \pm 0.0019 \text{ min}^{-1}$  when compared to TNRs. This sharp decrease indicates the GO with a high RGO atomic O/C ratio was unfavorable for the photocatalytic process. However, the photocatalytic performance was significantly improved through the reduction of GOT to GT. The apparent MO  $k$  value increased from  $0.0951 \pm 0.0019 \text{ min}^{-1}$  to  $0.3118 \pm 0.0012 \text{ min}^{-1}$  with an increase in reduction temperature up to 95°C for 1 h corresponded to a decrease in the RGO atomic O/C ratio from  $0.850 \pm 0.007$  to  $0.130 \pm 0.003$ . However, at 95°C for 2 h and 3 h, a further decrease in the O/C ratio caused a decrease in the apparent MO  $k$  value to  $0.2516 \pm 0.0018$  and  $0.1616 \pm 0.0023 \text{ min}^{-1}$ , respectively, when compared to GT-95<sup>1h</sup>. This observation indicates the excessive



deoxidization in GT-95<sup>3h</sup> decreased the photocatalytic performance. Data from the photocatalytic studies are consistent with the photocurrent results (Figure 5.12). For photocatalytic and photocurrent studies, the highest photocatalytic activity and transit photocurrent was observed for the GT-95<sup>1h</sup> sample with a moderate atomic O/C ratio of 0.130±0.003.

The bifunctional effect of the RGO atomic O/C ratio on the GT photocatalytic activities was further evaluated by assessing the photocatalysis of RhB, MB and phenol. RhB and MB are cationic dyes, and phenol, a chemical containing a benzene structure, is difficult to be degraded. The apparent first-order photocatalysis rate constant (apparent  $k$ ) values for the different organic chemicals are shown Figure 5.14. When compared to MO photodegradation, the photocatalysis of the selected chemicals followed a similar trend based on Tukey's test [79] (Table 5.2). Addition of GO into TNRs without any reduction resulted in a decrease in the apparent  $k$ , whereas a large improvement was observed after reduction at 20°C for a 1 h exposure time. Improving the apparent  $k$ , was observed by increasing the reduction temperature. The highest apparent  $k$  for each dye was observed when using the GT-95<sup>1h</sup> sample with an atomic O/C ratio of 0.130±0.003. However, a sharp decrease in apparent  $k$  was observed when the atomic O/C ratio reached 0.110±0.002 and 0.090±0.002 for the GT-95<sup>2h</sup> and GT-95<sup>3h</sup> samples, respectively. The optimum photocatalytic activity for the photocatalysis of RhB, MB and phenol increased by factors of approximately 1.5, 1.7 and 1.3, respectively, for the GT-95<sup>1h</sup> sample. Peak photocatalytic activities suggest that the optimum RGO atomic O/C ratio of 0.130±0.003 was observed in the case of GT-95<sup>1h</sup>. This optimized GT-95<sup>1h</sup> showed a significantly shorter half-life ( $t_{1/2}$ ) of approximately 0.44 min for degrading MB when

compared to the  $t_{1/2}$  of P25-RGO (3-4 min) corroborated by Zhang et al. (2010) [78] and Du et al. (2011) [78]. This is an approximate 8-fold improvement. In addition, the optimized GT-95<sup>1h</sup> has an overwhelming advantage over activated carbon based TiO<sub>2</sub> which showed  $t_{1/2}$  of approximately 10 min [1].



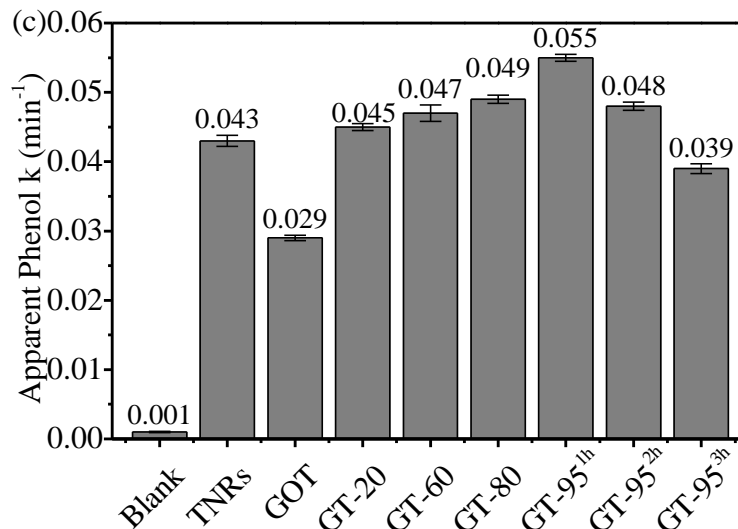


Figure 5.14: Apparent first-order photocatalysis rate constant ( $k$ ) for the photocatalysis under ultraviolet (UV) light irradiation for (a) RhB, (b) MB, and (c) phenol.

Notes: <sup>a</sup> Blank contains no photocatalyst, <sup>b</sup> TNRs represents TiO<sub>2</sub> nanorods, <sup>c</sup> GT represents reduced graphene oxide based TiO<sub>2</sub> nanorods, <sup>d</sup> GOT represents graphene oxide based TiO<sub>2</sub> nanorods, and <sup>e</sup> the number after GT represents the temperature (°C) condition and time (h) to synthesize the photocatalysts.

Table 5.2: Apparent photocatalysis rate constants  $k$  for selected organic chemicals.

Experiment	Apparent photocatalysis rate constant $k$ (min <sup>-1</sup> ) for:			
	MO	RhB	MB	Phenol
Blank	0.0003±0.0001 <sup>J</sup>	0.003±0.0008 <sup>I</sup>	0.0046±0.0004 <sup>I</sup>	0.0014±0.0001 <sup>I</sup>
RGO	0.0053±0.0012 <sup>I</sup>	-	-	-
TNRs	0.2361±0.0021 <sup>F</sup>	0.4470±0.0041 <sup>G</sup>	0.5891±0.0108 <sup>G</sup>	0.0431±0.0008 <sup>F</sup>
GOT	0.0951±0.0019 <sup>H</sup>	0.3455±0.0049 <sup>H</sup>	0.4052±0.0095 <sup>H</sup>	0.0293±0.0004 <sup>H</sup>
GT-20	0.2582±0.0012 <sup>CD</sup>	0.8560±0.0042 <sup>DE</sup>	1.1530±0.0142 <sup>D</sup>	0.0450±0.0005 <sup>E</sup>
GT-60	0.2619±0.0011 <sup>CD</sup>	0.9343±0.0061 <sup>C</sup>	1.3018±0.0110 <sup>C</sup>	0.0469±0.0012 <sup>D</sup>
GT-80	0.2711±0.0011 <sup>B</sup>	0.9830±0.0052 <sup>B</sup>	1.3749±0.0099 <sup>B</sup>	0.0488±0.0006 <sup>BC</sup>
GT-95 <sup>1h</sup>	0.3118±0.0012 <sup>A</sup>	1.1345±0.0052 <sup>A</sup>	1.5758±0.0110 <sup>A</sup>	0.0548±0.0005 <sup>A</sup>
GT-95 <sup>2h</sup>	0.2516±0.0018 <sup>E</sup>	0.8632±0.0048 <sup>DE</sup>	1.0531±0.0101 <sup>E</sup>	0.0481±0.0006 <sup>BC</sup>
GT-95 <sup>3h</sup>	0.1616±0.0023 <sup>G</sup>	0.7793±0.0067 <sup>F</sup>	0.9507±0.0127 <sup>F</sup>	0.0388±0.0007 <sup>G</sup>

Note: A, B, C, D, E, F, G, H, I, J: Means of the terms that do not share a letter in superscript are significantly different in each column according to Tukey's test [80], and A>B>C>D>E>F>G>H>I>J.

5.3.7. *The mechanism of reduced graphene oxide (RGO) atomic oxygen-to-carbon (O/C) ratio*

The mechanistic action for GT containing the oxygen containing groups on RGO could be explained using the scheme shown in Figure 5.15 and Figure 5.16. TNRs are attached on the RGO sheets through the interaction between the oxygen containing groups and TNRs (Figure 5.15) [78]. RGO residual oxygen containing groups -OH and =O are able to interact with TNRs'  $O^{2-}$  and  $Ti^{4+}$ , respectively. Photo-generated electrons are transferred to the highly conductive RGO sheet, and subsequently a reaction is mediated with organic chemicals [21].

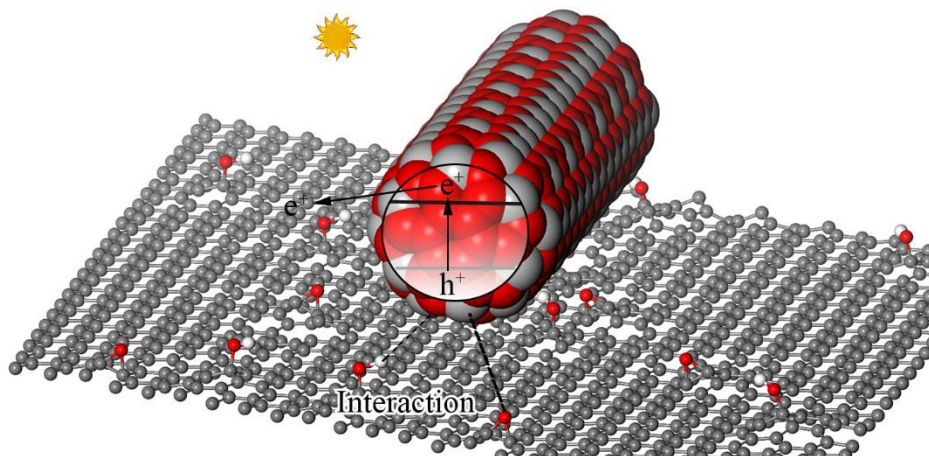


Figure 5.15: Charge transportation and separation on the partially reduced graphene oxide based  $TiO_2$  nanorods (GT) photocatalyst.

GOT (brown color) with the lowest photocatalytic activities was caused by the low GO electron conductivity. Color changing for the sample solution ( $1 \text{ g}\cdot\text{L}^{-1}$ , dispersed in  $H_2O$ ) from brown to grey was observed when reducing GOT to GT (Figure 5.16). Increasing the reduction temperatures conditions from  $20^\circ\text{C}$  to  $95^\circ\text{C}$  for a 1-h reduction time caused a decrease in RGO atomic O/C ratio, darkening sample solution color

(Figure 5.16) and subsequently, an increase in the photocatalytic activity [30, 58, 78]. Increasing the photocatalytic activity was caused by increasing the RGO conductivity [71]. Optimum photocatalytic activity was observed for the GT-95<sup>1h</sup> sample with an RGO atomic O/C ratio of  $0.130 \pm 0.003$ . Increasing the reducing time to 2 h and 3 h at 95°C caused an excessive removal of the oxygen containing groups, a decrease in interaction between RGO and TNRs and a significant decrease in the photocatalytic activity. A change in the reaction mixture color from dark to light grey (GT-95<sup>2h</sup> and GT-95<sup>3h</sup> samples) suggests a significant amount of RGO was separated from the TNRs. Separated RGO was detected floating on the surface of the reaction mixture or settling to the bottom of glass vial (Sample to the right side of Figure 5.16). RGO separation resulted in a sharp decrease in the charge transfer, charge separation and optical response.

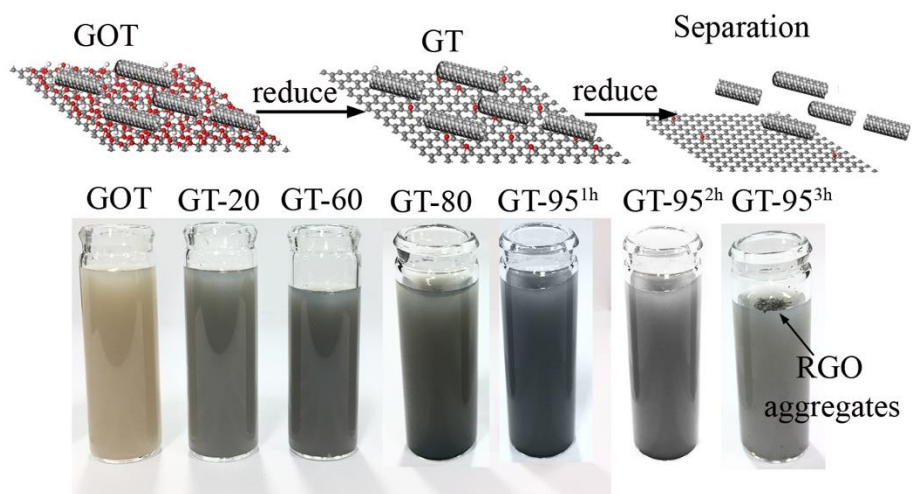


Figure 5.16: Color changes observed with a decrease in the atomic oxygen-to-carbon (O/C) ratio.

Notes: <sup>a</sup> GT represents reduced graphene oxide based TiO<sub>2</sub> nanorod, and <sup>b</sup> GOT represents graphene oxide based TiO<sub>2</sub> nanorods.

Excellent properties such as charge transfer, charge separation and narrow bandgap were detected in the GT-95<sup>1h</sup> sample with an RGO atomic O/C ratio of  $0.130 \pm 0.003$ . In

comparison, in the GT-95<sup>2h</sup> and GT-95<sup>3h</sup> samples, the excessive loss of oxygen containing groups weakened interaction between RGO and TNRs caused less photoactivity. Based on these studies, a balance between reduction and functionalization is crucial in achieving high performance RGO modified TiO<sub>2</sub> photocatalysts.

#### **5.4. Ag-reduced graphene oxide-TiO<sub>2</sub> nanorods (Ag-GT) photocatalyst with optimum Ag loading**

##### *5.4.1. Morphology analysis*

Formation of the hierarchical 3D Ag-GT composite was demonstrated by FESEM and HRTEM (Figure 5.17). The morphology of the GO sheets is shown in Figure 5.17a. The FESEM image for the hierarchical 3D 10%Ag-GT composite (Figure 5.17b) shows that the GO sheet morphology was retained after incorporating TNRs and depositing Ag NPs. The RGO sheets were homogeneously distributed in TNRs matrix. HRTEM images for the 3D 10%Ag-GT composite (Figure 5.17c) indicate that the TNRs were attached to the RGO sheets surface. The TNRs with an average diameter of approximately 6 nm and length of approximately 50 nm were homogeneously decorated with Ag NPs (shown as dark dots in Figure 5.17c and d). The 10%Ag-GT shows an enhanced SSA ( $181 \pm 5 \text{ m}^2 \cdot \text{g}^{-1}$ ) when compared to TiO<sub>2</sub> NPs with a SSA of  $50 \pm 5 \text{ m}^2 \cdot \text{g}^{-1}$ . Ag NPs with an average diameter of 3 nm were grown on the TNRs surface (Figure 5.17). Ag<sup>+</sup> ions introduced after the formation of GT composite were preferably adsorbed on the TiO<sub>2</sub> hydrophilic surface instead of on the hydrophobic RGO sheet surface. During reduction, Ag NPs were homogeneously grown on the TNRs.

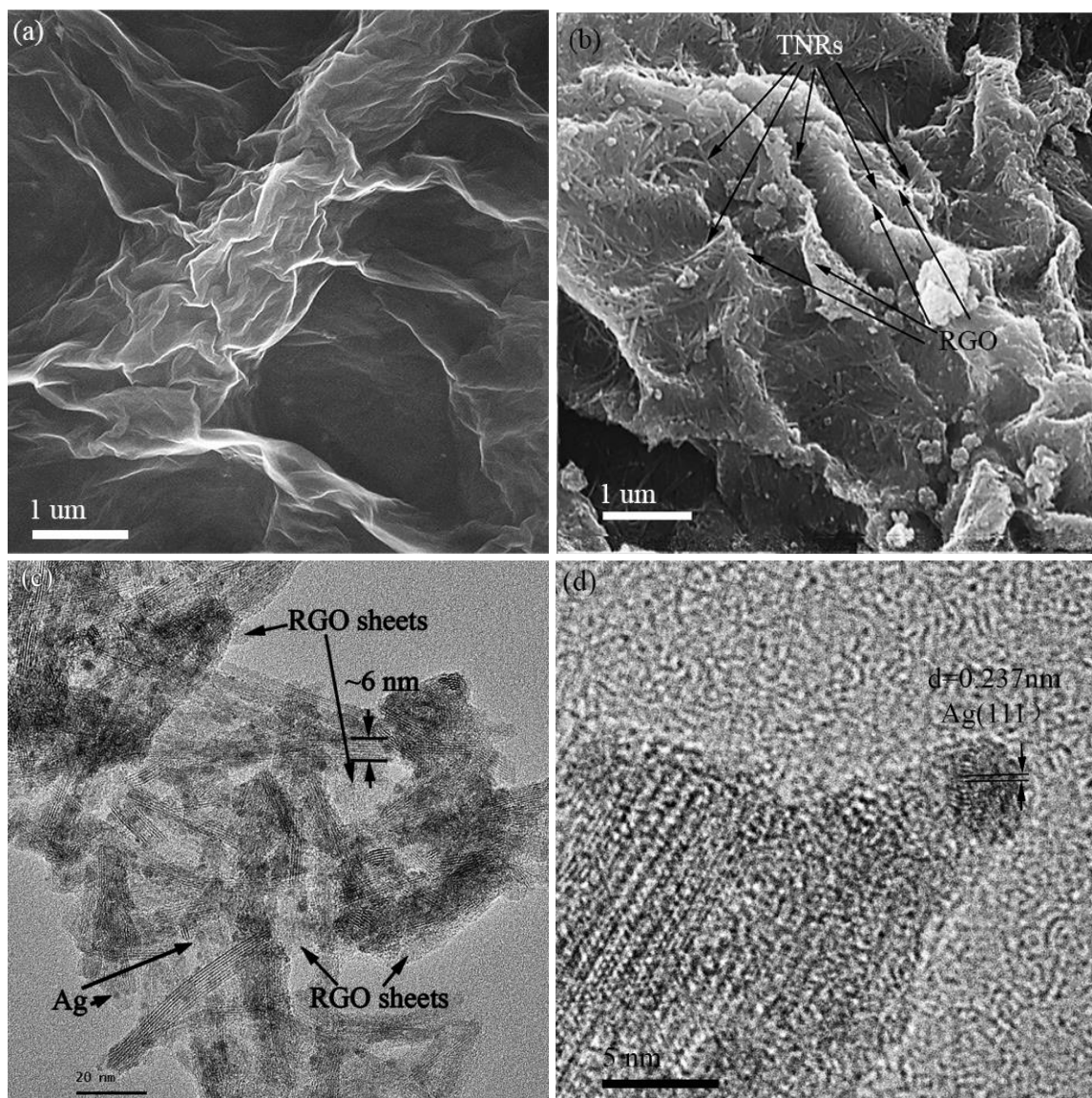


Figure 5.17: Field emission scan electron micrograph (FESEM) and high-resolution transmission electron microscopy (HRTEM) images for GO and 10%Ag-GT. (a) GO FESEM image, (b) 10%Ag-GT FESEM image, (c) 10%Ag-GT HRTEM image, and (d) 10%Ag-GT HRTEM image.

#### 5.4.2. Structure analysis

X-ray diffraction (XRD) analysis was conducted to evaluate the crystal phase for all the samples (Figure 5.18a). The anatase [81] and rutile [63, 82] phases were detected in all the samples. The peaks located at  $2\theta = 25.4^\circ$ ,  $37.9^\circ$  and  $48.1^\circ$  correspond to the (101), (004) and (200) orientation of the anatase  $\text{TiO}_2$  phase, respectively. The peak located at

$2\theta = 25.4^\circ$  correspond to the (110) orientation of the rutile  $\text{TiO}_2$  phase. The Ag characteristic peaks (111) and (200) located at  $2\theta = 38.2^\circ$  and  $44.0^\circ$ , respectively, were detected for the GT samples containing Ag nanoparticles. The increasing Ag peaks intensity was linked to the increase in the Ag content. Raman spectroscopy was employed to confirm the  $\text{TiO}_2$  phase and incorporation of RGO into the  $\text{TiO}_2$  matrix. The peaks [65] at  $144\text{ cm}^{-1}$  ( $E_g$ ),  $399\text{ cm}^{-1}$  ( $B_{1g}$ ),  $513\text{ cm}^{-1}$  ( $A_{1g}$ ), and  $638\text{ cm}^{-1}$  ( $E_g$ ) (Figure 5.18b) indicate the existence of anatase. Moreover, the  $E_g$  peak for GT and Ag-GT shows a blue-shift from  $143\text{ cm}^{-1}$  to  $155\text{ cm}^{-1}$  when compared to TNRs (Figure 5.18c). The  $E_g$  peak blue shift is likely caused by the strain at the interface between the  $\text{TiO}_2$  and RGO sheets [21, 74]. This suggests that TNRs has a strong interaction with RGO sheets [4, 21, 74, 75] (Figure 5.18c). Interaction between TNRs and RGO sheets in the hierarchical 3D Ag-GT is an essential element for efficient charge transfer and separation [21]. In the de-convoluted GO X-ray photoelectron spectroscopy (XPS) C1s spectra (Figure 5.18d), the peak located at 284.5 eV and 250.0 eV corresponds to  $sp^2$  or  $sp^3$  bonded carbon, respectively, while the de-convoluted peaks for C–O (286.5 eV), C=O (287.8 eV) and O–C=O (289.0 eV) at higher binding energies are attributed to oxygen-containing function groups on the RGO layers [24]. The significant decrease in the peak intensities of oxygen functionalities for the 10%Ag-GT composite suggests the successful reduction of GO to RGO.



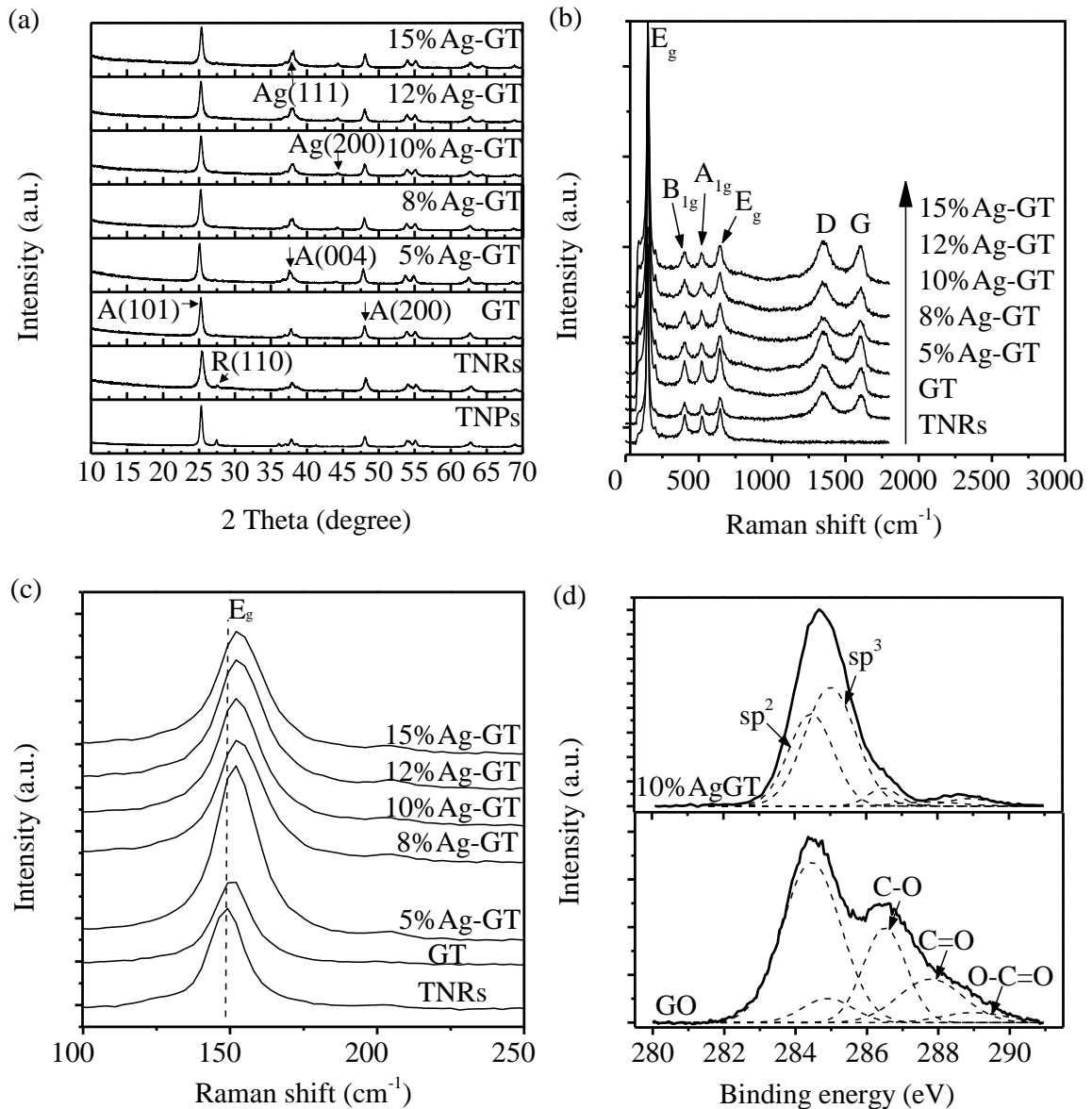


Figure 5.18: X-ray diffraction (XRD) and Raman Spectra. (a) XRD patterns for all samples, (b) the Raman spectra for different samples, (c) E<sub>g</sub> bands, and (d) C1s X-ray photoelectron spectroscopy (XPS) spectra of 10% Ag-GT and TiO<sub>2</sub> nanorods (TNRs) (top) and graphene oxide (GO) (bottom).

#### 5.4.3. Diffuse reflectance UV-visible spectroscopy (DRS) and bandgap

Diffuse reflectance UV-visible spectroscopy (DRS) (Figure 5.19) was used to further examine the optical response of the samples. The diffuse reflectance spectra were converted into a corresponding absorption spectra using the Kubelka Munk function [77]

(Figure 5.19b). All the samples showing a wide optical absorption band at approximately 380 nm [83] is based on the  $\text{TiO}_2$  bandgap of 3.21 eV (Figure 5.19b) [82, 83]. The GT with RGO structure in the  $\text{TiO}_2$  matrix which are associated with increasing visible light absorption and decreasing the bandgap to 2.94 eV, due to the interaction between  $\text{TiO}_2$  and RGO [84]. The 3D Ag-GT photocatalysts showing the largest visible light absorption between 400 to 700 nm and decreased the bandgap to approximately 2.55 eV (Figure 5.19b) was due to the localized SPR absorption of Ag NPs [39, 85, 86]. In addition, increasing the Ag content from 5% to 15% caused an increasing visible light absorption between 400 to 700 nm. The narrowing bandgap for the hierarchical 3D Ag-GT photocatalyst suggests that this composite is favorable for visible-light photocatalysis.

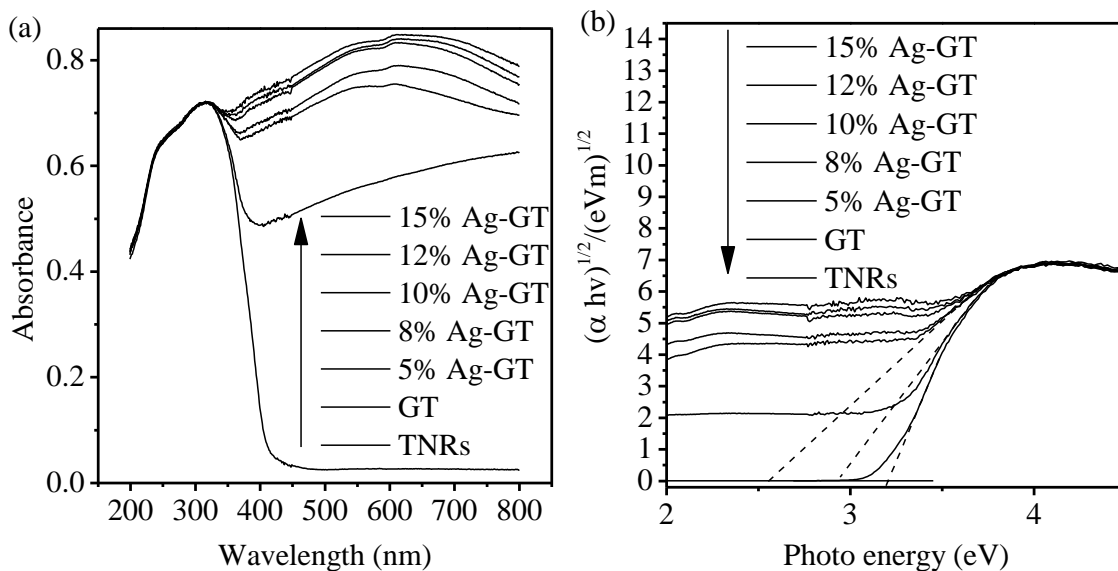


Figure 5.19: (a) UV-visible absorption spectra, and (b) the determination of the indirect interband transition energies for samples.

#### 5.4.4. Photoelectrochemical studies

The transit current responses, I-t curves with an on-off visible light source, were conducted to demonstrate the charge transfer and separation of the photocatalysts (Figure 5.20). The current for each sample was enhanced when the light source was applied and a rapid decrease to approximately zero was subsequently observed by removing the light source. Incorporation of RGO into TNRs significantly increased the photocurrent density. This increase is attributed to enhanced charge carrier transfer and separation by incorporating RGO sheets into TNRs matrix [57]. The photocurrent further increased with depositing Ag NPs. The best photocurrent of approximately  $1.45 \text{ mA}\cdot\text{cm}^{-2}$  was observed for the sample containing 10% Ag. The decreasing photocurrent caused by the Ag content larger than 10% was due to the negative effect of excessive Ag behaving as recombination centers between the photogenerated  $e^-h^+$  [87].

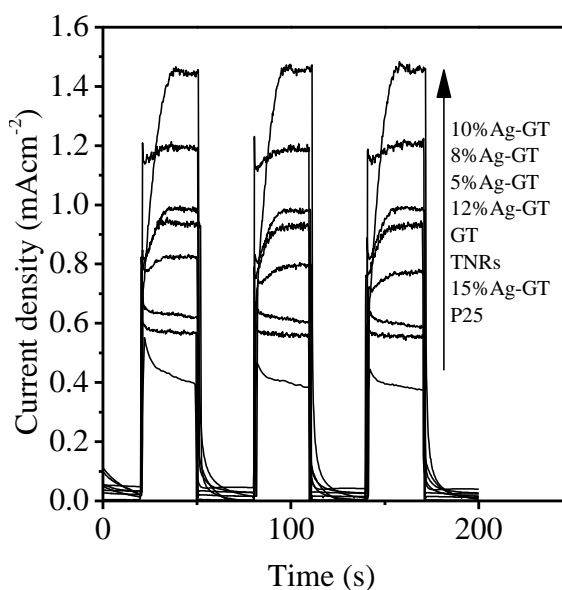


Figure 5.20: Transient photocurrent for samples in 1 M  $\text{Na}_2\text{SO}_4$  aqueous solution under visible-light irradiation ( $\geq 410 \text{ nm}$ ) at 0.5 V versus saturated calomel electrode (SCE).

#### 5.4.5. Photocatalytic activity

The visible light photocatalytic degradation capacity for the different samples was firstly evaluated using RhB as a contaminant target (Figure 5.21). Control experiments were performed with TiO<sub>2</sub> NPs and without a photocatalyst (referred as photolysis). The initial concentration of RhB in deionized water was 5 mg·L<sup>-1</sup> before each experiment. All photocatalysts films showed approximately 10% adsorption of RhB for 1 h of stir under dark condition. Under visible light condition, only approximately 6% of RhB was degraded without the photocatalyst. The average apparent RhB degradation rate constant value (designated as “apparent RhB k”) was 0.016±0.001 h<sup>-1</sup> without a photocatalyst (Figure 5.21b). However, with the addition of a film of photocatalyst, the average k value significantly increased. The apparent k of TiO<sub>2</sub> NPs film was 0.1203±0.0073 h<sup>-1</sup>. The apparent k of TNRs for RhB (0.154±0.0077 h<sup>-1</sup>) was improved by approximately 28.01±0.06% when compared to TiO<sub>2</sub> NPs. In addition, adding RGO into TNRs also caused an enhanced k value. This improvement can be attributed to interaction between TiO<sub>2</sub> and RGO [22]. The largest k values (0.7374±0.011 h<sup>-1</sup>) were observed for Ag-GT samples 10% Ag (degrading 96% of RhB in 4 h). This largest k value was approximately 2.6-fold increase when compared to the k value of 0.288 h<sup>-1</sup> (0.0048 min<sup>-1</sup>) using Ag doped TiO<sub>2</sub> reported by Bensouici et al. [43] The decreasing k value caused by Ag concentrations larger than 10% was due to the negative effect of excessive Ag acting as recombination centers between the photogenerated e<sup>-</sup>-h<sup>+</sup> pairs.

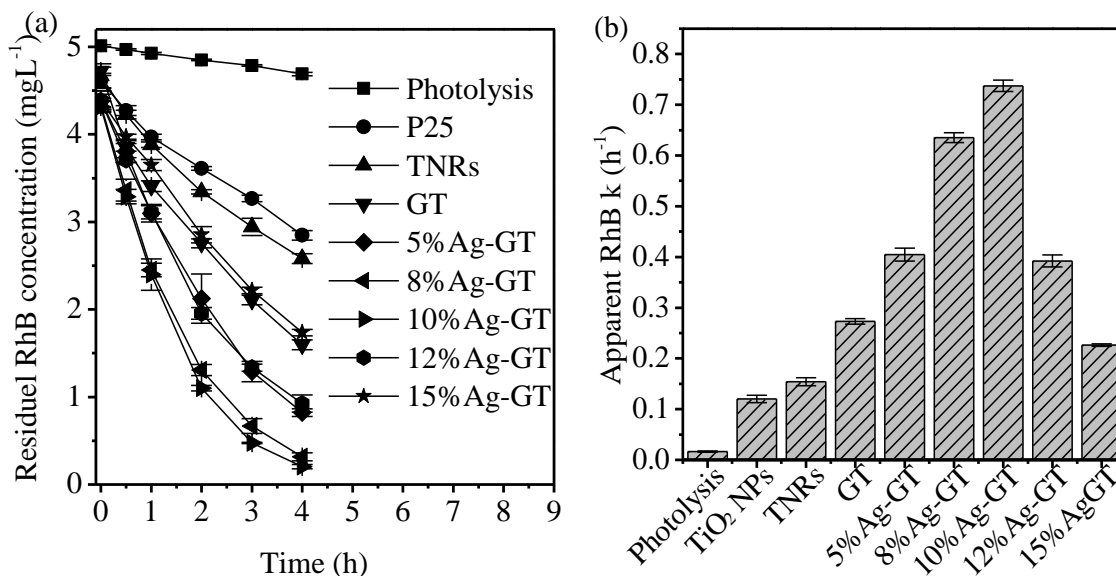


Figure 5.21: Photocatalytic degradation of RhB using photocatalysts under visible light. (a) Residual RhB concentration versus time, and (b) Apparent RhB degradation rate constant (Apparent RhB  $k$ ) ( $\text{h}^{-1}$ ).

The photodegradation of phenol, MO and MB at initial concentration  $5 \text{ mgL}^{-1}$  was conducted using photolysis (irradiation only),  $\text{TiO}_2$  NPs, TNRs and 10%Ag-GT under visible light irradiation. The calculated photodegradation rate constants are shown in Figure 5.22 for each photocatalyst. The results indicate that phenol, MO and MB are not susceptible to photolysis; however, substantial photodegradation by each photocatalyst was observed in the following order:  $\text{MB} > \text{MO} > \text{phenol}$ . Significantly greater photodegradation rates of the tested organic pollutants were observed for the 10%Ag-GT photocatalyst when compared to the unmodified  $\text{TiO}_2$  and GT samples. The highest photodegradation rates observed for phenol, MO and MB by employing 10%Ag-GT photocatalyst were  $0.3091 \pm 0.0195 \text{ h}^{-1}$ ,  $0.6069 \pm 0.0193 \text{ h}^{-1}$  and  $1.2007 \pm 0.0214 \text{ h}^{-1}$ , respectively, corresponds to approximately 9.66 h, 4.91 h and 2.50 h, respectively, based on 95% degradation. These fast degradation rates can be attributed to the fast charge transportation and separation of 3D Ag-GT structure.

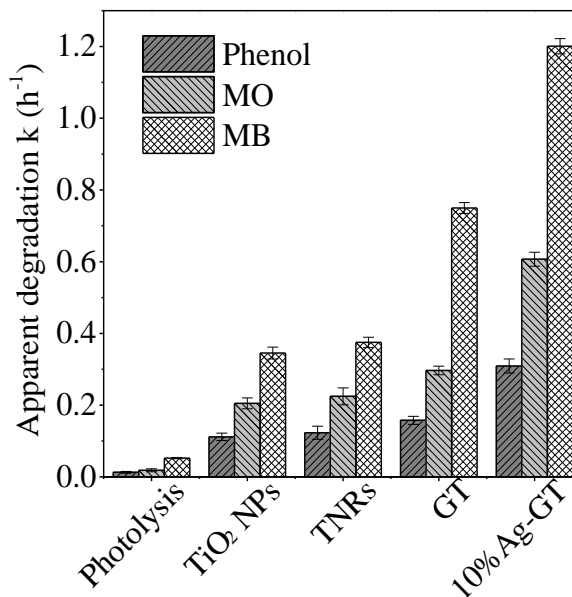


Figure 5.22: Photocatalytic degradation rate constant ( $k$ ) for phenol, methyl orange (MO), and methylene blue (MB) under visible light conditions.

#### 5.4.6. Reaction mechanism

A key factor in achieving a highly active photocatalyst is the unique hierarchical 3D structure of Ag-GT (Figure 5.23) which includes visible-light active, enhanced charge separation and improved SSA. In the unique hierarchical 3-D structure, both RGO [6, 78] and Ag NPs were able to extend the absorption band edge of TiO<sub>2</sub> into the visible light region. The SPR excited electrons from Ag NPs can be transferred to the conduction band of large SSA TNRs and be subsequently transferred to the RGO sheets to produce superoxide anion radicals ( $\bullet\text{O}_2^-$ ) [39]. RGO, an efficient electron sink/transporter, induces electron transfer from the TiO<sub>2</sub> conduction band to itself, while the holes trapped in the TNRs and Ag NPs have a longer lifetime [21, 22, 39, 40]. In particular, 3D Ag-RGO-TNRs (Ag-GT) shows significantly improved photocatalytic activities when compared to Ag-RGO-TiO<sub>2</sub> NPs, because TNRs, in comparison to TiO<sub>2</sub> NPs, have more uniform dispersion on RGO with less agglomeration [57] and have improved charge

transfer along TiO<sub>2</sub> Q1D structure. The electrons are eventually captured by adsorbed molecular oxygen on the RGO sheets surface to produce  $\cdot\text{O}_2^-$ , while the holes accept electrons from H<sub>2</sub>O on the TiO<sub>2</sub> surface to produce hydroxyl radicals ( $\cdot\text{OH}$ ) [88]. Subsequently, these highly reactive radicals oxidize organic molecules such as RhB. The much higher TNRs SSA provided more reactive sites for producing reactive species such as  $\cdot\text{OH}$  when compared to TiO<sub>2</sub> NPs.

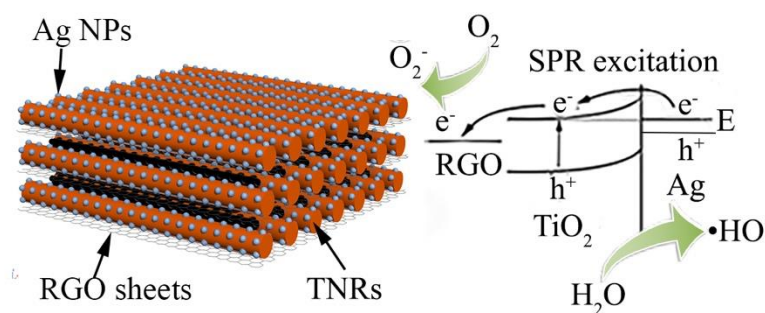


Figure 5.23: A proposed mechanism for the photocatalytic degradation of organic dyes employing the hierarchical three-dimension (3D) Ag-RGO-TiO<sub>2</sub> nanorods (Ag-GT) photocatalyst under visible light irradiation.

## 5.5. Conclusions

A graphene-based TiO<sub>2</sub> (RGO-TNRs; designated as GT) photocatalyst with tunable RGO O/C atomic ratio was produced for degrading aqueous hazardous pollutants under UV irradiation. The optimum RGO atomic O/C ratio of approximately  $0.130 \pm 0.003$  was sufficient to obtain high photocatalytic activities. Extreme cases of either high or low levels of oxygen containing functional groups should be avoided because these conditions are characteristic of giving rise to low photocatalytic activities. An elevated threshold level of the oxygen containing functional groups is characterized by low electron conductivities, while a lower threshold level contributes to a loss of interaction

between RGO and TNRs. This research suggested the importance of partial oxygen functionalization of graphene as a means to enhance semiconductor photocatalysts (e.g.  $\text{TiO}_2$ , CdS and ZnO) for the destruction of hazardous chemicals during drinking water and air pollution treatment.

A hierarchical 3D Ag-GT photocatalyst was successfully synthesized and examined as an advanced photocatalyst. The photocatalyst was effective in degrading toxic organic pollutants under visible light conditions. Both RGO sheets and SPR effect of Ag NPs narrowed the bandgap of TNRs, and therefore significantly extended the light-response range. The unique Q1D structure of TNRs and the RGO significantly were closely linked to the high SSA and efficient charge separation, respectively. As a result, the greater organic pollutant degrading rate was observed when compared to  $\text{TiO}_2$  NPs in the presence of visible-light.

## 5.6. References

- [1] J. Matos, R. Montana, E. Rivero, Influence of activated carbon upon the photocatalytic degradation of methylene blue under UV–vis irradiation, *Environ. Sci. Pollut. Res.* 22 (2015) 784-791.
- [2] N. Singh, M.S. Rana, R.K. Gupta, Modelling studies for photocatalytic degradation of organic dyes using  $\text{TiO}_2$  nanofibers, *Environ. Sci. Pollut. Res.* (2017).
- [3] E.O. Oseghe, P.G. Ndungu, S.B. Jonnalagadda, Synthesis of mesoporous Mn/ $\text{TiO}_2$  nanocomposites and investigating the photocatalytic properties in aqueous systems, *Environ. Sci. Pollut. Res.* 22 (2015) 211-222.



- [4] H. Zhang, X. Lv, Y. Li, Y. Wang, J. Li, P25-graphene composite as a high performance photocatalyst, *ACS Nano* 4 (2010) 380-386.
- [5] G. Williams, B. Seger, P.V. Kamat, TiO<sub>2</sub>-graphene nanocomposites. UV-assisted photocatalytic reduction of graphene oxide, *ACS Nano* 2 (2008) 1487-1491.
- [6] J.S. Lee, K.H. You, C.B. Park, Highly photoactive, low bandgap TiO<sub>2</sub> nanoparticles wrapped by graphene, *Adv. Mater.* 24 (2012) 1084-1088.
- [7] J. Du, X. Lai, N. Yang, J. Zhai, D. Kisailus, F. Su, D. Wang, L. Jiang, Hierarchically ordered macro-mesoporous TiO<sub>2</sub>-graphene composite films: improved mass transfer, reduced charge recombination, and their enhanced photocatalytic activities, *ACS Nano* 5 (2011) 590-596.
- [8] N.J. Bell, Y.H. Ng, A. Du, H. Coster, S.C. Smith, R. Amal, Understanding the enhancement in photoelectrochemical properties of photocatalytically prepared TiO<sub>2</sub>-reduced graphene oxide composite, *J. Phys. Chem. C* 115 (2011) 6004-6009.
- [9] K.S. Novoselov, V.I.F. ko, L. Colombo, P.R. Gellert, M.G. Schwab, K. Kim, A roadmap for graphene, *Nature* 490 (2012) 192-200.
- [10] Z. Chen, W. Ren, L. Gao, B. Liu, S. Pei, H.M. Cheng, Three-dimensional flexible and conductive interconnected graphene networks grown by chemical vapour deposition, *Nat. Mater.* 10 (2011) 424-428.
- [11] A.K. Geim, Graphene: status and prospects, *Science* 324 (2009) 1530-1534.
- [12] F. Bonaccorso, L. Colombo, G. Yu, M. Stoller, V. Tozzini, A.C. Ferrari, R.S. Ruoff, V. Pellegrini, Graphene, related two-dimensional crystals, and hybrid systems for energy conversion and storage, *Science* 347 (2015) 1246501-1246501.

- [13] Y. Zhu, S. Murali, M.D. Stoller, K.J. Ganesh, W. Cai, P.J. Ferreira, A. Pirkle, R.M. Wallace, K.A. Cychoz, M. Thommes, D. Su, E.A. Stach, R.S. Ruoff, Carbon-based supercapacitors produced by activation of graphene, *Science* 332 (2011) 1537-1541.
- [14] X. Li, J. Yu, S. Wageh, A.A. Al Ghamdi, J. Xie, Graphene in photocatalysis: a review, *Small* 12 (2016) 6640-6696.
- [15] K.S. Novoselov, A.K. Geim, S.V. Morozov, D. Jiang, Y. Zhang, S.V. Dubonos, I.V. Grigorieva, A.A. Firsov, Electric field effect in atomically thin carbon films, *Science* 306 (2004) 666-669.
- [16] K.-Y. Chun, Y. Oh, J. Rho, J.-H. Ahn, Y.-J. Kim, H.R. Choi, S. Baik, Highly conductive, printable and stretchable composite films of carbon nanotubes and silver, *Nat. Nanotechnol.* 5 (2010) 853-857.
- [17] A.A. Balandin, S. Ghosh, W. Bao, I. Calizo, D. Teweldebrhan, F. Miao, C.N. Lau, Superior thermal conductivity of single-layer graphene, *Nano Lett.* 8 (2008) 902-907.
- [18] C. Lee, X. Wei, J.W. Kysar, J. Hone, Measurement of the elastic properties and intrinsic strength of monolayer graphene, *Science* 321 (2008) 385-388.
- [19] M.D. Stoller, S. Park, Y. Zhu, J. An, R.S. Ruoff, Graphene-based ultracapacitors, *Nano Lett.* 8 (2008) 3498-3502.
- [20] L. Liu, S. Ryu, M.R. Tomasik, E. Stolyarova, N. Jung, M.S. Hybertsen, M.L. Steigerwald, L.E. Brus, G.W. Flynn, Graphene oxidation: Thickness-dependent etching and strong chemical Doping, *Nano Lett.* 8 (2008) 1965-1970.
- [21] S.D. Perera, R.G. Mariano, K. Vu, N. Nour, O. Seitz, Y. Chabal, K.J. Balkus Jr., Hydrothermal synthesis of graphene-TiO<sub>2</sub> nanotube composites with enhanced photocatalytic activity, *ACS Catal.* 2 (2012) 949-956.

- [22] C. Chen, W. Cai, M. Long, B. Zhou, Y. Wu, D. Wu, Y. Feng, Synthesis of visible-light responsive graphene oxide/TiO<sub>2</sub> composites with p/n heterojunction, *ACS Nano* 4 (2010) 6425-6432.
- [23] X.-Y. Zhang, H.-P. Li, X.-L. Cui, Y. Lin, Graphene/TiO<sub>2</sub> nanocomposites: synthesis, characterization and application in hydrogen evolution from water photocatalytic splitting, *J. Mater. Chem.* 20 (2010) 2801-2806.
- [24] J. Chen, B. Yao, C. Li, G. Shi, An improved Hummers method for eco-friendly synthesis of graphene oxide, *Carbon* 64 (2013) 225-229.
- [25] S. Pei, H.M. Cheng, The reduction of graphene oxide, *Carbon* 50 (2012) 3210-3228.
- [26] D.R. Dreyer, S. Park, C.W. Bielawski, R.S. Ruoff, The chemistry of graphene oxide, *Chem. Soc. Rev.* 39 (2010) 228-240.
- [27] D.W. Boukhvalov, M.I. Katsnelson, Modeling of graphite oxide, *J. Am. Chem. Soc.* 130 (2008) 10697-10701.
- [28] K.A. Mkhoyan, A.W. Contryman, J. Silcox, D.A. Stewart, G. Eda, C. Mattevi, S. Miller, M. Chhowalla, Atomic and electronic structure of graphene-oxide, *Nano Lett.* 9 (2009) 1058-1063.
- [29] D. Wang, D. Choi, J. Li, Z. Yang, Z. Nie, R. Kou, D. Hu, C. Wang, L.V. Saraf, J. Zhang, I.A. Aksay, J. Liu, Self-assembled TiO<sub>2</sub>-graphene hybrid nanostructures for enhanced Li-ion insertion, *ACS Nano* 3 (2009) 907-914.
- [30] Y.-K. Kim, D.-H. Min, UV protection of reduced graphene oxide films by TiO<sub>2</sub> nanoparticle incorporation, *Nanoscale* 5 (2013) 3638-3635.

- [31] D. He, K. Cheng, T. Peng, X. Sun, M. Pan, S. Mu, Bifunctional effect of reduced graphene oxides to support active metal nanoparticles for oxygen reduction reaction and stability, *J. Mater. Chem.* 22 (2012) 21298-21297.
- [32] A. Fujishima, K. Honda, Electrochemical photolysis of water at a semiconductor electrode, *Nature* 238 (1972) 37-38.
- [33] M. Murdoch, G.I.N. Waterhouse, M.A. Nadeem, J.B. Metson, M.A. Keane, R.F. Howe, J. Llorca, H. Idriss, The effect of gold loading and particle size on photocatalytic hydrogen production from ethanol over Au/TiO<sub>2</sub> nanoparticles, *Nat. Chem.* 3 (2011) 489-492.
- [34] M. Pelaez, N.T. Nolan, S.C. Pillai, M.K. Seery, P. Falaras, A.G. Kontos, P.S.M. Dunlop, J.W.J. Hamilton, J.A. Byrne, K. O'Shea, M.H. Entezari, D.D. Dionysiou, A review on the visible light active titanium dioxide photocatalysts for environmental applications, *Appl. Catal., B Environ.* 125 (2012) 331-349.
- [35] S.F. Tahir, C.A. Koh, Catalytic oxidation for air pollution control, *Environ. Sci. Pollut. Res.* 3 (1996) 20-23.
- [36] H. Fakhouri, J. Pulpytel, W. Smith, A. Zolfaghari, H.R. Mortaheb, F. Meshkini, R. Jafari, E. Sutter, F. Arefi-Khonsari, Control of the visible and UV light water splitting and photocatalysis of nitrogen doped TiO<sub>2</sub> thin films deposited by reactive magnetron sputtering, *Appl. Catal., B Environ.* 144 (2014) 12-21.
- [37] W. Smith, H. Fakhouri, J.r.m. Pulpytel, F. Arefi-Khonsari, Control of the optical and crystalline properties of TiO<sub>2</sub> in visible-light active TiO<sub>2</sub>/TiN bi-layer thin-film stacks, *J. Appl. Phys.* 111 (2012) 024301-024311.

- [38] R. Asahi, T. Morikawa, T. Ohwaki, K. Aoki, Y. Taga, Visible-light photocatalysis in nitrogen-doped titanium oxides, *Science* 293 (2001) 269-271.
- [39] Y. Wen, H. Ding, Y. Shan, Preparation and visible light photocatalytic activity of Ag/TiO<sub>2</sub>/graphene nanocomposite, *Nanoscale* 3 (2011) 4411-4417.
- [40] Q. Xiang, B. Cheng, J. Yu, Graphene based photocatalysts for solar fuel generation, *Angew. Chem.* 127 (2015) 11508-11524.
- [41] R. Long, N.J. English, O.V. Prezhdo, Photo-induced charge separation across the graphene–TiO<sub>2</sub> interface is faster than energy losses: A time-domain ab initio analysis, *J. Am. Chem. Soc.* 134 (2012) 14238-14248.
- [42] Q. Wu, H. Zhao, F. Huang, J. Hou, H. Cao, Z. Liu, S. Peng, G. Cao, Impacts of reduced graphene oxide in CdS/CdSe quantum dots co-sensitized solar cells, *J. Phys. Chem. C* 121 (2017) 18430-18438.
- [43] O. Akhavan, E. Ghaderi, Photocatalytic reduction of graphene oxide nanosheets on TiO<sub>2</sub> thin film for photoinactivation of bacteria in solar light irradiation, *J. Phys. Chem. C* 113 (2009) 20214-20220.
- [44] O. Akhavan, M. Abdolahad, A. Esfandiar, M. Mohatashamifar, Photodegradation of graphene oxide sheets by TiO<sub>2</sub> nanoparticles after a photocatalytic reduction, *J. Phys. Chem. C* 114 (2010) 12955-12959.
- [45] Y.-C. Liang, C.-C. Wang, C.-C. Kei, Y.-C. Hsueh, W.-H. Cho, T.-P. Perng, Photocatalysis of Ag-loaded TiO<sub>2</sub> nanotube arrays formed by atomic layer deposition, *J. Phys. Chem. C* 115 (2011) 9498-9502.

- [46] Y. Yang, J. Wen, J. Wei, R. Xiong, J. Shi, C. Pan, Polypyrrole-decorated Ag-TiO<sub>2</sub> nanofibers exhibiting enhanced photocatalytic activity under visible-light illumination, *ACS Appl. Mater. Interfaces* 5 (2013) 6201-6207.
- [47] H. Li, W. Lu, J. Tian, Y. Luo, A.M. Asiri, A.O. Al Youbi, X. Sun, Synthesis and study of plasmon - induced carrier behavior at Ag/TiO<sub>2</sub> nanowires, *Chem. Eur. J.* 18 (2012) 8508-8514.
- [48] Z. Zhang, L. Zhang, M.N. Hedhili, H. Zhang, P. Wang, Plasmonic gold nanocrystals coupled with photonic crystal seamlessly on TiO<sub>2</sub> nanotube photoelectrodes for efficient visible light photoelectrochemical water splitting, *Nano Lett.* 13 (2013) 14-20.
- [49] K. Matsubara, T. Tatsuma, Morphological changes and multicolor photochromism of Ag nanoparticles deposited on single-crystalline TiO<sub>2</sub> surfaces, *Adv. Mater.* 19 (2007) 2802-2806.
- [50] S. Linic, P. Christopher, D.B. Ingram, Plasmonic-metal nanostructures for efficient conversion of solar to chemical energy, *Nat. Mater.* 10 (2011) 911-921.
- [51] T. Peng, J. Zhang, S. Ray, H. Fakhouri, X. Xu, F. Arefi-Khonsari, J.A. Lalman, Enhanced TiO<sub>2</sub> nanorods photocatalysts with partially reduced graphene oxide for degrading aqueous hazardous pollutants, *Environ. Sci. Pollut. Res.* (2018).
- [52] T. Kasuga, M. Hiramatsu, A. Hoson, T. Sekino, K. Niihara, Formation of titanium oxide nanotube, *Langmuir* 14 (1998) 3160-3163.
- [53] H.-L. Kuo, C.-Y. Kuo, C.-H. Liu, J.-H. Chao, C.-H. Lin, A highly active bi-crystalline photocatalyst consisting of TiO<sub>2</sub> (B) nanotube and anatase particle for producing H<sub>2</sub> gas from neat ethanol, *Catal. Lett.* 113 (2007) 7.

- [54] D.V. Bavykin, V.N. Parmon, A.A. Lapkin, F.C. Walsh, The effect of hydrothermal conditions on the mesoporous structure of TiO<sub>2</sub> nanotubes, *J. Mater. Chem.* 14 (2004) 3370-3378.
- [55] P. Roy, S. Berger, P. Schmuki, TiO<sub>2</sub> nanotubes: synthesis and applications, *Angew. Chem. Int. Ed.* 50 (2011) 2904-2939.
- [56] G.-S. Kim, H.-K. Seo, V.P. Godble, Y.-S. Kim, O.-B. Yang, H.-S. Shin, Electrophoretic deposition of titanate nanotubes from commercial titania nanoparticles: Application to dye-sensitized solar cells, *Electrochem. Commun.* 8 (2006) 961-966.
- [57] Q. Xiang, J. Yu, M. Jaroniec, Enhanced photocatalytic H<sub>2</sub>-production activity of graphene-modified titania nanosheets, *Nanoscale* 3 (2011) 3670-3679.
- [58] D. Yang, Y. Sun, Z. Tong, Y. Tian, Y. Li, Synthesis of Ag/TiO<sub>2</sub> nanotube heterojunction with improved visible-light photocatalytic performance inspired by bioadhesion, *J. Phys. Chem. C* 119 (2015) 5827-5835.
- [59] S. Ray, J.A. Lalman, N. Biswas, Using the Box-Benken technique to statistically model phenol photocatalytic degradation by titanium dioxide nanoparticles, *Chem. Eng. J.* 150 (2009) 15-24.
- [60] D. Xu, B. Cheng, S. Cao, J. Yu, Enhanced photocatalytic activity and stability of Z-scheme Ag<sub>2</sub>CrO<sub>4</sub>-GO composite photocatalysts for organic pollutant degradation, *Appl. Catal., B Environ.* 164 (2015) 380-388.
- [61] N. Roy, Y. Sohn, D. Pradhan, Synergy of low-energy {101} and high-energy {001} TiO<sub>2</sub> crystal facets for enhanced photocatalysis, *ACS Nano* 7 (2013) 2532-2540.
- [62] C.P. Sajan, S. Wageh, A.A. Al Ghamdi, J. Yu, S. Cao, TiO<sub>2</sub> nanosheets with exposed {001} facets for photocatalytic applications, *Nano Res.* 9 (2016) 3-27.

- [63] D. Reyes-Coronado, G. Rodriguez-Gattorno, M.E. Espinosa-Pesqueira, C. Cab, R. de Coss, G. Oskam, Phase-pure TiO<sub>2</sub> nanoparticles: anatase, brookite and rutile, *Nanotechnology* 19 (2008) 145605.
- [64] D.C. Marcano, D.V. Kosynkin, J.M. Berlin, A. Sinitskii, Z. Sun, A. Slesarev, L.B. Alemany, W. Lu, J.M. Tour, Improved synthesis of graphene oxide, *ACS Nano* 4 (2010) 4806-4814.
- [65] J.-G. Li, T. Ishigaki, X. Sun, Anatase, brookite, and rutile nanocrystals via redox reactions under mild hydrothermal conditions: phase-selective synthesis and physicochemical properties, *J. Phys. Chem. C* 111 (2007) 4969-4976.
- [66] K.N. Kudin, B. Ozbas, H.C. Schniepp, R.K. Prud'homme, I.A. Aksay, R. Car, Raman spectra of graphite oxide and functionalized graphene sheets, *Nano Lett.* 8 (2008) 36-41.
- [67] F. Tuinstra, J.L. Koenig, Raman spectrum of graphite, *J. Chem. Phys.* 53 (1970) 1126-1130.
- [68] A.C. Ferrari, J. Robertson, Interpretation of Raman spectra of disordered and amorphous carbon, *Phys. Rev. B* 61 (2000) 14095-14107.
- [69] A.C. Ferrari, J.C. Meyer, V. Scardaci, C. Casiraghi, M. Lazzeri, F. Mauri, S. Piscanec, D. Jiang, K.S. Novoselov, S. Roth, A.K. Geim, Raman spectrum of graphene and graphene layers, *Phys. Rev. Lett.* 97 (2006) 187401-187404.
- [70] A.C. Ferrari, Raman spectroscopy of graphene and graphite: Disorder, electron-phonon coupling, doping and nonadiabatic effects, *Solid State Commun.* 143 (2007) 47-57.



- [71] P. Wang, L. Han, C. Zhu, Y. Zhai, S. Dong, Aqueous-phase synthesis of Ag-TiO<sub>2</sub>-reduced graphene oxide and Pt-TiO<sub>2</sub>-reduced graphene oxide hybrid nanostructures and their catalytic properties, *Nano Res.* 4 (2011) 1153-1162.
- [72] P.-G. Ren, D.-X. Yan, X. Ji, T. Chen, Z.-M. Li, Temperature dependence of graphene oxide reduced by hydrazine hydrate., *Nanotechnology* 22 (2011) 055705.
- [73] O. Akhavan, Bacteriorhodopsin as a superior substitute for hydrazine in chemical reduction of single-layer graphene oxide sheets, *Carbon* 81 (2015) 158-166.
- [74] L. Shen, X. Zhang, H. Li, C. Yuan, G. Cao, Design and tailoring of a three-dimensional TiO<sub>2</sub>-graphene-carbon nanotube nanocomposite for fast lithium storage, *J. Phys. Chem. Lett.* 2 (2011) 3096-3101.
- [75] Y.T. Liang, B.K. Vijayan, O. Lyandres, K.A. Gray, M.C. Hersam, Effect of dimensionality on the photocatalytic behavior of carbon-titania nanosheet composites: Charge transfer at nanomaterial interfaces, *J. Phys. Chem. Lett.* 3 (2012) 1760-1765.
- [76] O. Akhavan, E. Ghaderi, Flash photo stimulation of human neural stem cells on graphene/TiO<sub>2</sub> heterojunction for differentiation into neurons, *Nanoscale* 5 (2013) 10316-10311.
- [77] R. Lopez, R. Gomez, Band-gap energy estimation from diffuse reflectance measurements on sol-gel and commercial TiO<sub>2</sub>: a comparative study, *J. Sol-Gel Sci. Technol.* 61 (2012) 1-7.
- [78] Y. Zhang, Z.-R. Tang, X. Fu, Y.-J. Xu, TiO<sub>2</sub>-graphene nanocomposites for gas-phase photocatalytic degradation of volatile aromatic pollutant: is TiO<sub>2</sub>-graphene truly different from other TiO<sub>2</sub>-carbon composite materials?, *ACS Nano* 4 (2010) 7303-7314.

- [79] B.E. Zawacki, S.P. Azen, S.H. Imbus, Y.T. Chang, Multifactorial probit analysis of mortality in burned patients., *Ann. Surg.* 189 (1979) 1-5.
- [80] M.N.G.D. Sharma, Power of Tukey's test for non-additivity, (2017) 1-7.
- [81] H. Cheng, J. Ma, Z. Zhao, L. Qi, Hydrothermal preparation of uniform nanosize rutile and anatase particles, *Chem. Mater.* 7 (1995) 663-671.
- [82] H. Zhang, J.F. Banfield, Understanding polymorphic phase transformation behavior during growth of nanocrystalline aggregates: insights from TiO<sub>2</sub>, *J. Phys. Chem. B* 104 (2000) 3481-3487.
- [83] H. Luo, C. Wang, Y. Yan, Synthesis of mesostructured titania with controlled crystalline framework, *Chem. Mater.* 15 (2003) 3841-3846.
- [84] B.A. Bhanvase, T.P. Shende, S.H. Sonawane, A review on graphene–TiO<sub>2</sub> and doped graphene–TiO<sub>2</sub> nanocomposite photocatalyst for water and wastewater treatment, *Environ. Technol. Rev.* 6 (2016) 1-14.
- [85] K. Awazu, M. Fujimaki, C. Rockstuhl, J. Tominaga, H. Murakami, Y. Ohki, a. Naoya Yoshida, T. Watanabe, A plasmonic photocatalyst consisting of silver nanoparticles embedded in titanium dioxide, *J. Am. Chem. Soc.* 130 (2008) 1676-1680.
- [86] Y. Ohko, T. Tatsuma, T. Fujii, K. Naoi, C. Niwa, Y. Kubota, A. Fujishima, Multicolour photochromism of TiO<sub>2</sub> films loaded with silver nanoparticles, *Nat. Mater.* 2 (2002) 29-31.
- [87] P. Van Viet, B.T. Phan, D. Mott, S. Maenosono, T.T. Sang, C.M. Thi, L.V. Hieu, Silver nanoparticle loaded TiO<sub>2</sub> nanotubes with high photocatalytic and antibacterial activity synthesized by photoreduction method, *J. Photochem. Photobiol. A: Photochem. Rev.* 352 (2018) 106-112.

[88] H. Tian, C. Wan, X. Xue, X. Hu, X. Wang, Effective electron transfer pathway of the ternary TiO<sub>2</sub>/RGO/Ag nanocomposite with enhanced photocatalytic activity under visible light, *Catalysts* 7 (2017) 156-115.

# ONE-STEP DEPOSITION OF NANO-AG-TIO<sub>2</sub> COATINGS BY ATMOSPHERIC PRESSURE PLASMA JET FOR DEGRADING TRACE PHARMACEUTICAL USING SOLAR ENERGY

## Synopsis

In this work, micrometer thick Ag nanoparticles (NPs) modified TiO<sub>2</sub> (Ag-TiO<sub>2</sub>) coatings were deposited in a single and facile step by spraying the precursor solution in a non-equilibrium atmospheric pressure plasma jet (APPJ) with different concentrations of Ag NPs (0-0.7 wt%). The coatings were porous with an anatase phase with improved charge separation and visible light absorption. The photocatalytic activity of the materials was investigated for the degradation of rhodamine b (RhB) and pharmaceutical compounds, namely carbamazepine (CBZ), venlafaxine (VLX) and bezafibrate (BZF), by using a solar simulator. Increasing Ag content was correlated with decreasing the TiO<sub>2</sub> crystal size. The optimal photodegradation activity was observed for a silver content of 0.4% in the composite coatings.

## 6.1. Introduction

Pharmaceuticals are emerging environmental organic wastewater contaminants (OWCs) due to their potential impact on humans, animals and microorganisms at threshold concentrations [1]. Industrial development coupled with acceleration in population growth rate has led to the occurrence of these chemicals in wastewater effluents and drinking water supplies. Exposure to OWCs is linked to serious concerns such as environmental damage and human diseases [2]. The occurrence of

pharmaceutical chemicals in municipal wastewaters is due to effluents arising from pharmaceutical manufacturing facilities and human excretions into sewers [3-5]. Conventional municipal biological wastewater treatment facilities are ineffective in removing several pharmaceutical chemicals [6-8]. In addition, operational costs and the generation of secondary toxic pollutants are major problems associated with municipal biological treatments [9, 10]. Advanced oxidation processes such as ozone ( $O_3$ ),  $O_3/H_2O_2$ , Fenton and photo-Fenton are promising technologies for the degradation of pharmaceutical chemicals [11]. However, the major disadvantages of these processes include incomplete degradation and the production of toxic byproducts. Photocatalysis based on  $TiO_2$  is an emerging technology which can overcome these problems [6, 7, 11-15].

The semiconductor  $TiO_2$  has widespread applications as a photocatalyst to degrade organic pollutants in water [6, 7, 13] and for dye-sensitized solar cells [16-21]. The valance band of  $TiO_2$  is more positive than the  $O_2/H_2O$  redox potential and the conductive band is more negative than the  $H_2/H_2O$  redox potential [9]. These characteristic properties allow  $TiO_2$  to be an excellent candidate for many electrochemical applications including water splitting [8, 10]. However, the application of  $TiO_2$  is limited to UV activation due to its wide band gap (3.2 eV). This limits the use of  $TiO_2$  as solar or room-light activated catalysts, because the majority of the sunlight consists of visible light with only a 3-5% UV light content [15]. Developing visible light induced  $TiO_2$  photo-catalysts with high efficiency is essential for enhancing the process practicality, feasibility and economics [14]. Another factor restricting the photocatalytic activity of  $TiO_2$  is the low quantum yield of excitons due to the fast electron-hole ( $e^-/h^+$ )

recombination [8]. In competition, these electrons and holes can undergo reduction and oxidation before the recombination reaction. However, the small lifetime of  $e^-/h^+$  and absence of suitable scavengers causes dissipation of stored energy within a few nanoseconds by recombination [15].

Many studies have demonstrated that improving the PCA can be accomplished by narrowing the absorption band gap to the visible portion of the spectra, and by reducing the recombination reaction. Incorporating  $TiO_2$  with metals has been reported to improve the photocatalytic activities based on improvement in the two factors previously discussed [2, 8, 14, 15, 22, 23]. Silver is a common element employed to incorporate  $TiO_2$ . Incorporating  $TiO_2$  with Ag is advantageous because of its low cost, inherent antibacterial activity, and facile preparation [2, 24-30]. In addition, incorporating Ag leads to excellent corrosion resistance and improved hardness [31].

The photocatalytic efficiency of  $TiO_2$  thin films is strongly dependent on the preparation methods. In general, the photocatalytic preparatory method can influence the structural and chemical properties such as structure, porosity, stoichiometry, density of defects and recombination rates between the photo-generated carriers [32]. In the case of thin film photocatalysts and other similar photocatalysts, one consideration in developing innovative preparation processes is to maximize the catalytic activity while another is economics by increasing the deposition rate.  $TiO_2$  thin films can be prepared using methods such as deposition assisted by plasma [33].  $TiO_2$  coatings deposited by plasma are characterized with excellent physicochemical properties which adhere strongly to different substrates, but with relatively low deposition rates when deposited at low and even at atmospheric pressure [33]. A non-equilibrium atmospheric pressure plasma jet

(APPJ), characterized by a relatively high gas temperature (1000-1500 K), has been reported to be effective for surface treatments [34-37] and for coating thin films with high deposition rates [38, 39]. However, the physicochemical properties of the coatings are dependent on the operational parameters. In previous studies, Fakhouri *et al.* [40] reported depositing TiO<sub>2</sub> coatings by APPJ and These researchers reported the photocatalytic activity of the TiO<sub>2</sub> thin films prepared by APPJ was significantly improved when compared to optimum N-doped TiO<sub>2</sub> thin films which was prepared by reactive radio frequency (RF) magnetron sputtering [41]. The APPJ offers the possibility to deposit coatings on 3D substrates as well without the need to use vacuum which is the drawback in magnetron sputtering [41].

In this study, the first part of sixth objective is to use the APPJ system reportedly used by Fakhouri *et al.* [40] to deposit Ag nanoparticles (NPs) and create a Ag-TiO<sub>2</sub> composite coating by means of a PECVD process. The second part of sixth objective is to investigate the impact of the Ag concentration, air gas flow rate and the discharge pulse frequency on the coating phase structure, crystal size and photocatalytic activity. The third part of sixth objective is to investigate the photocatalytic activity of the APPJ Ag-TiO<sub>2</sub> coating for degrading RhB and three pharmaceutical compounds, namely carbamazepine (CBZ), venlafaxine (VLX) and bezafibrate (BZF), in water by using a solar simulator light irradiation.

## 6.2. Experimental Methods

The thin film photocatalytic activity tests are included in Chapter 2 (Section 2.3.12). Ag-TiO<sub>2</sub> coating were prepared by introducing TTIP detailed in Chapter 2 (Section 2.4.3).

### *6.2.1. Optical emission spectroscopy of atmospheric pressure plasma jet (APPJ) plasma*

Plasma emission was sampled using optical emission spectroscopy described in Chapter 2 (Section 2.3.11). Briefly, plasma emission was sampled using an optical fiber located downstream, at 10 mm from the nozzle exit of the torch, and connected to an optical emission spectrometer (OES) (Ocean Optics USB2000+, FL, USA) which was configured with a grating of  $300 \text{ gmm}^{-1}$  in the UV-visible spectrum range and a  $25 \text{ }\mu\text{m}$  slit. The OES spectra were recorded in the range of 200 nm to 1100 nm to identify the excited chemical species in the plasma with and without the presence of the TTIP precursor including Ag NPs.

### *6.2.2. Thin film characterization*

The thin films crystal structure was characterized by X-ray diffraction (XRD) (X'Pert Pro PW3040-Pro, Panalytical Inc., Nottingham, UK) using a Cu  $K\alpha 1$  ( $\lambda = 1.5418 \text{ }\text{\AA}$ ) X-ray radiation source in the Bragg-Brentano configuration. X'Pert High Score pattern processing was used to collect and process the data. Surface morphology and film thicknesses were determined using field emission scanning electron microscopy (FESEM) (JEOL, Japan).

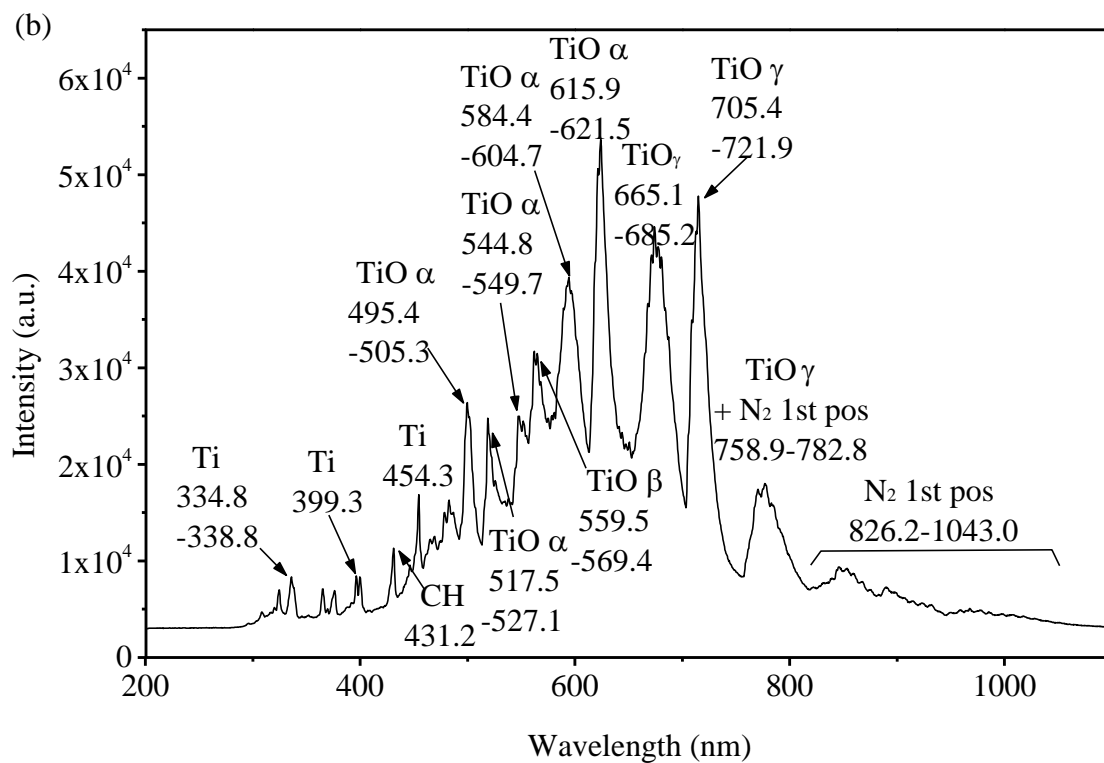
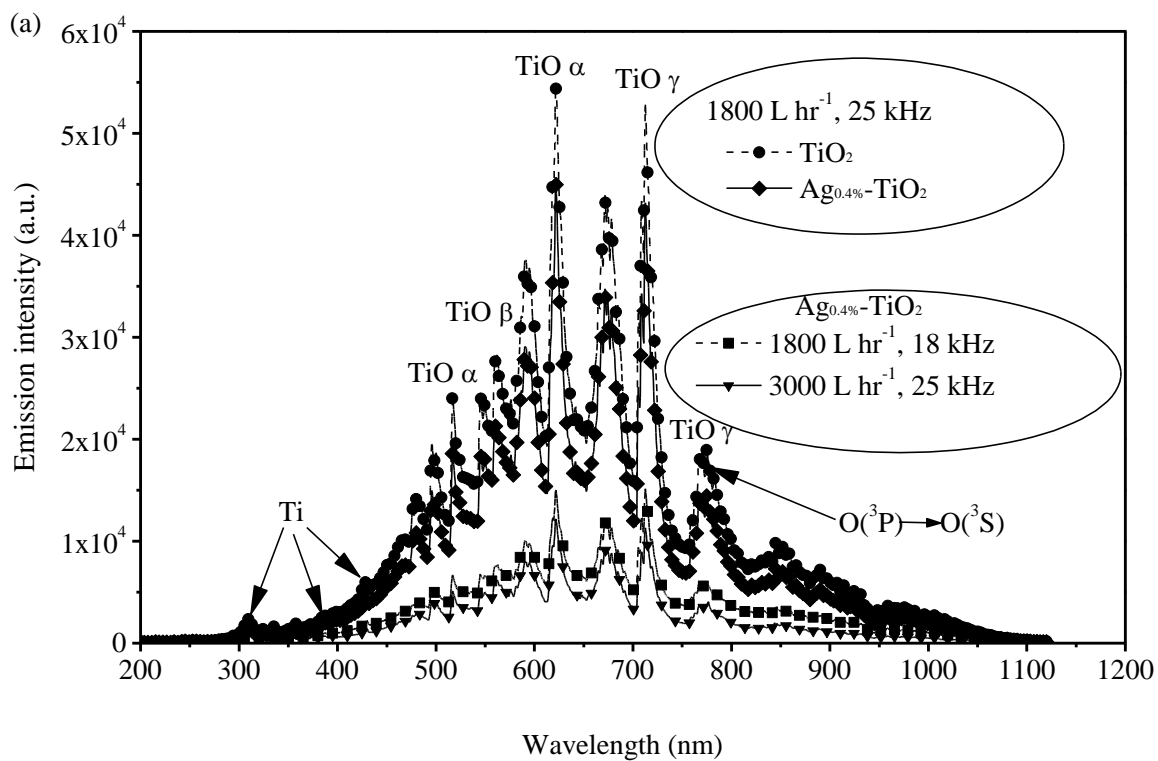
## **6.3. Results and discussion**

### *6.3.1. Plasma jet characterization*

The plasma optical emission spectra for samples with and without the TTIP precursor and with Ag NPs were recorded to understand the formation of the Ag-TiO<sub>2</sub> coatings. During metal deposition, the plasma luminosity was strongly enhanced, and the spectra



were dominated by the emission of the  $\text{TiO}_2$  molecules. No Ag emission peak was observed based on the data shown in Figure 6.1. The data in Figure 6.1 also illustrate the role of the pulse frequency and air flow rate on the plasma emission lines for the 0.4% Ag TTIP precursor micro-droplets. The emission spectra are shown for the case where the spray of the  $\text{TiO}_2$  precursor is introduced in the air plasma with an air flow of  $1800 \text{ L h}^{-1}$  and a pulse frequency of 25 kHz without Ag NPs and with 0.4% Ag NPs. The intensity of the optical emission spectra of the TTIP precursor decreases drastically when either the pulse frequency was decreased from 25kHz to 18kHz, or the air flow rate is increased from  $1800 \text{ L}\cdot\text{h}^{-1}$  to  $3000 \text{ L}\cdot\text{h}^{-1}$ . In both cases, the decrease of the intensity of the emission lines at lower pulse frequency and higher air flow rate are related to the decrease of the energy injected in the discharge, and the lower residence time of the species in the discharge, respectively. In Figure 6.1b, other emitting species besides TiO and atomic oxygen can be observed in more detail. Ti atoms and CH radicals have been identified and are caused by the fragmentation of the TTIP precursor.



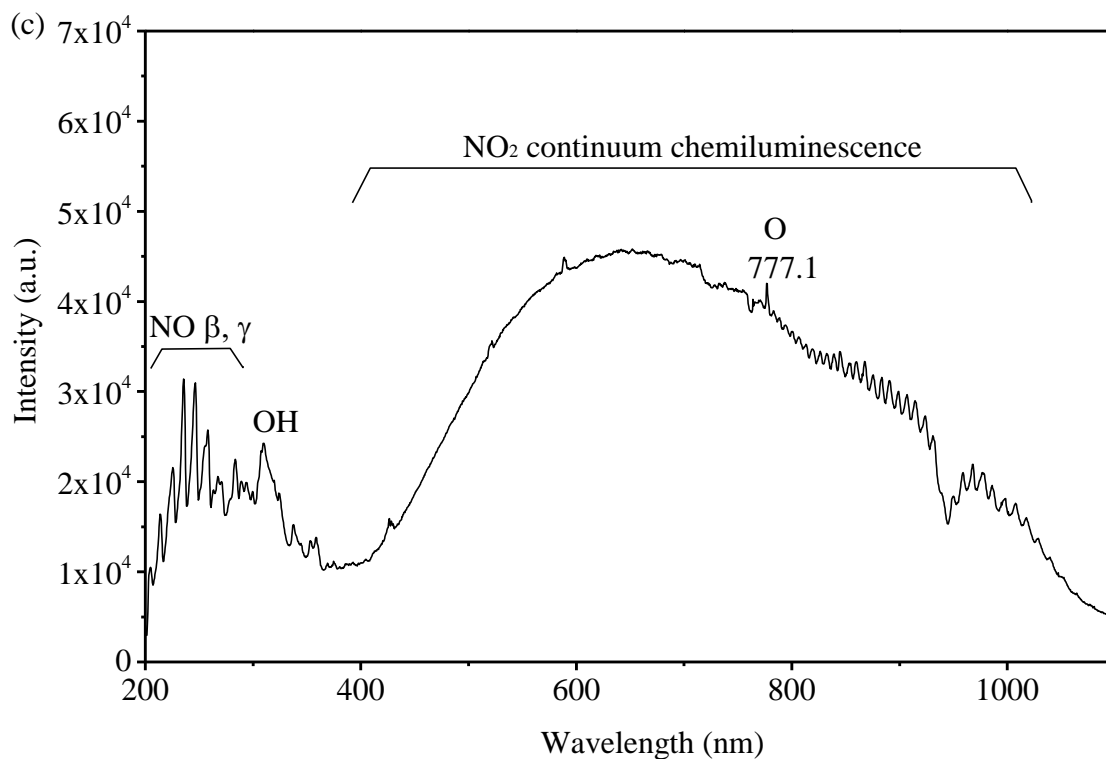


Figure 6.1: (a) optical emission spectra with TTIP spray injection under two different pulse frequencies and air flow rates, (b) optical emission spectra with TTIP spray using an air flow of  $1800 \text{ L h}^{-1}$  and a pulse frequency of 25 kHz without Ag NPs, and (c) optical emission spectra without TTIP spray injection using an air flow of  $1800 \text{ L h}^{-1}$  and a pulse frequency of 25 kHz.

Notes: <sup>a</sup>The plasma cycle time is 100%, and <sup>b</sup>the optical fiber located downstream at 10 mm from the nozzle exit of the torch.

The highly reactive species (radicals, metastables, vibrationally excited molecules, photons) in the plasma jet is able to enable a very rich chemistry for surface treatment. The technique used in this study is a blown arc system which is affiliated with high temperatures at the nozzle exit (i.e.  $T_g \sim 1000\text{-}1500 \text{ K}$ ) and a sharp temperature decrease gradient. These characteristics leads to an interesting heat transfer phenomenon which allows tailoring the physicochemical properties of the coatings as well as the dispersion of Ag in the host material. Rapid quenching of the high temperature further away from the nozzle exit provides the possibility of temperature sensitive materials thermal

treatment. More interestingly, controlling the heat transfer predominantly impacted the position of the Ag entrapped sites in the host material (TiO<sub>2</sub>) [40].

### 6.3.2. Morphology and Ag diffusion in composite Ag-TiO<sub>2</sub> thin films

The effect of deposition power (pulse frequency) and air flow rate on the photocatalyst morphology was examined under 3 conditions (18 kHz and 1800 L·h<sup>-1</sup>, 25 kHz and 1800 L·h<sup>-1</sup>, 18 kHz and 3000 L·h<sup>-1</sup>). The surface morphology under the different conditions are shown in Figure 6.2. At low deposition frequencies (low power) and low air flow rates, the preferred composite formation produced core-shell Ag encircled by TiO<sub>2</sub> (Figure 6.2a) spheres with diameters ranging between 800 nm and 3000 nm. Ag was partially oxidized between the Ag core and the TiO<sub>2</sub> shell as shown in Figure 6.2d. At a high frequency of 25 kHz, Ag was present as isolated and small NPs in the coating (Figure 6.2b). The coatings deposited by APPJ were composed of nanoclusters with a uniform grain size of approximately 30-40 nm and the pore size of approximately 0.3 to 1 μm as shown in Figure 6.2b. Small grain size is closely related to high surface area. Ag NPs were homogeneously dispersed in the host material to form Ag cores encircled by the TiO<sub>2</sub> NPs [42]. This morphology could be attributed to the fast fragmentation rate of TTIP in the plasma under high pulse frequencies. Increasing the air flow rate during deposition caused a decrease in the residence time of the precursor chemical molecules condensing on the surface. Lowering the residence time leads to reducing reactions within the plasma and results in diminishing the specific surface area (Figure 6.2c).

In the case of the APPJ-spray process, the deposition rate is estimated at  $10\text{-}20\ \mu\text{m}\cdot\text{s}^{-1}$ . Whereas, in the case of RF reactive sputtering, the deposition rate is typically between  $1\text{-}10\ \text{nm}\cdot\text{min}^{-1}$  for  $\text{TiO}_2$  in the oxide mode and the films are characterized by a 1D columnar structure [41]. The difference in the porosity between the films deposited by sputtering and APPJ can be explained by the higher deposition rate of the APPJ technique of approximately nine to ten orders of magnitude. Also, the APPJ technique is characterized by a lower kinetic energy of the reactive species in the plasma reaching the surface. This lowering of the kinetic energy which eventually causes reduced mobility of the substrate surface species explains the higher porosity of the coatings.

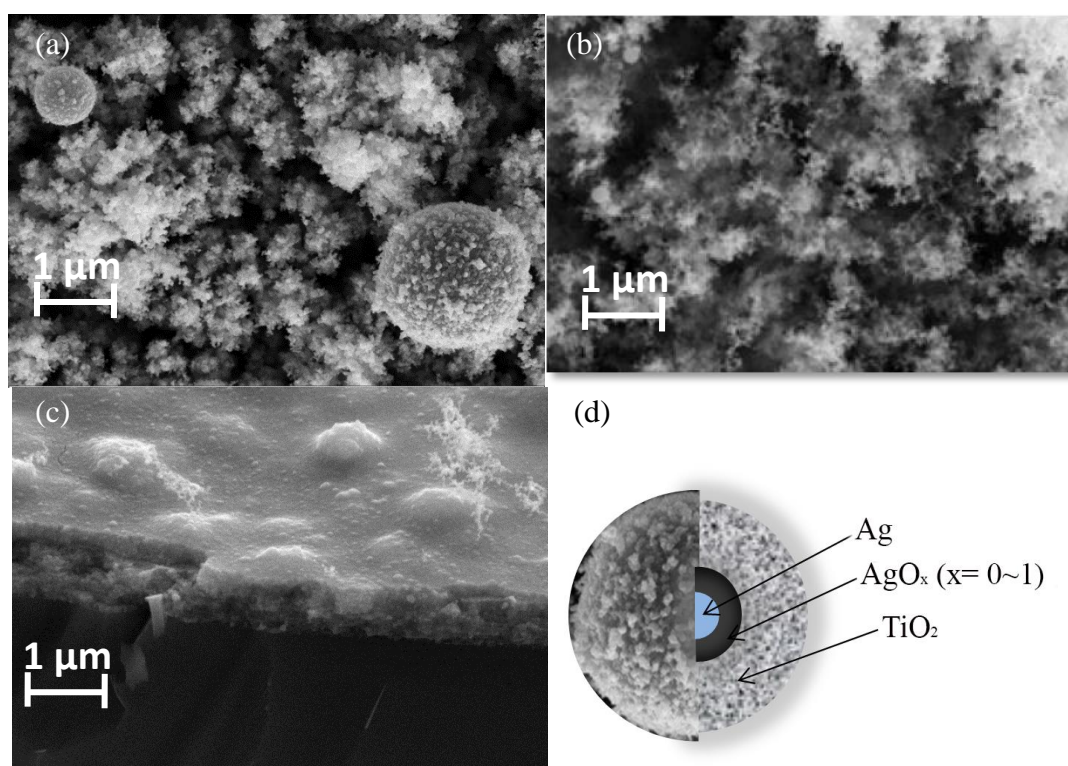


Figure 6.2: Field emission scanning electron microscopy (FESEM) images for Ag- $\text{TiO}_2$  thin films deposited by atmospheric pressure plasma jet (APPJ) under three conditions (a) 18 kHz and  $1800\ \text{Lh}^{-1}$ , (b) 25 kHz and  $1800\ \text{Lh}^{-1}$ , (c) 18 kHz and  $3000\ \text{Lh}^{-1}$ , and (d) The proposed Ag- $\text{TiO}_2$  core-shell structure.

### 6.3.3. *Effect of Ag incorporating on the crystal structure*

The XRD patterns for the Ag-TiO<sub>2</sub> thin films deposited by APPJ with different Ag concentrations at 21 kHz and an air flow rate of 1800 L·h<sup>-1</sup> are depicted in Figure 6.3a. The coatings post annealing conditions at 450°C for 1 h in ambient air produced primarily the anatase phase regardless of the Ag concentration. The peaks located at  $2\theta = 25.4^\circ$ ,  $37.9^\circ$ ,  $38.7^\circ$ ,  $48.1^\circ$ ,  $54.1^\circ$ ,  $55.2^\circ$  and  $66.8^\circ$  correspond to the (101), (004), (112), (200), (105), (211) and (204) orientation of the anatase TiO<sub>2</sub> phase, respectively, with (101) as the preferential orientation. The peaks located at  $2\theta = 38.2^\circ$ ,  $44.0^\circ$  and  $64.6^\circ$  correspond to the (111), (200) and (220) surfaces of Ag, respectively.

The effect of air flow rate and impulse frequency for samples produced using 0.4% Ag is shown in Figure 6.3b. The data indicate, at 18 kHz, that a low air flow rate (1800 L·h<sup>-1</sup>) was favorable for producing a more crystalline surface when compared to the surface characteristics observed at a higher air flow rate (3000 L·h<sup>-1</sup>). The TiO<sub>2</sub> anatase phase coatings were crystalline regardless of the pulse frequency. However, the degree of crystallinity varied with the pulse frequency. The coatings became more crystalline when increasing the power from 18 kHz to 25 kHz. This was coupled with decreasing Ag(111) and Ag(200) peak intensities and changing the morphology from a layer to a ‘coral’ like structure (see Figure 6.2). In the case of a high air flow rate condition, less crystallinity was detected in the anatase and crystalline Ag phases.

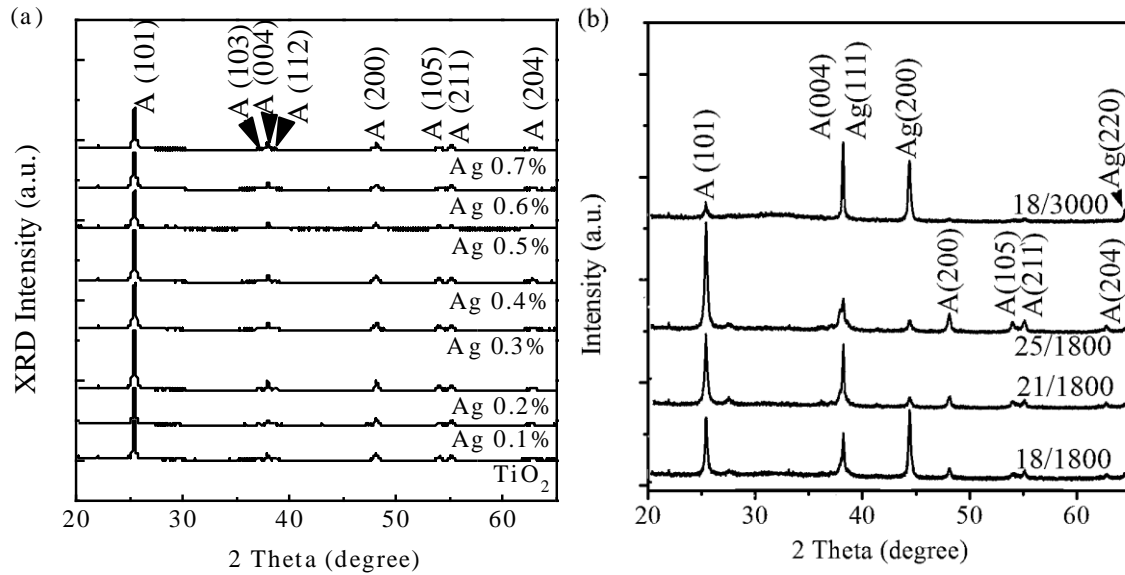


Figure 6.3: XRD patterns for Ag-TiO<sub>2</sub> thin films deposited by APPJ using Ag-TTIP liquid solution sprayed and annealed at 450°C for 1 h in ambient air, (a) with different Ag concentrations at 21 kHz and air flow rate of 1800 L·h<sup>-1</sup>, and (b) with 0.4% Ag at different pulse frequencies/ different air flow rates.

The crystal size of anatase crystals was calculated using the Scherer formula (Eq. 6.1) for the different samples [43-45].

$$d = \frac{K\lambda}{\beta \cos(\theta)} \quad (6.1)$$

Where  $d$  is the crystal size (nm),  $K$  is a constant called shape factor (typically equal to 0.9),  $\lambda$  is the wavelength of XRD radiation ( $\lambda = 0.154$  nm),  $\beta$  is the full width at half maximum (FWHM) and  $\theta$  is the diffraction angle. According to the calculations using equation (Eq. 6.1), higher pulse frequencies are associated with lower crystal sizes. The variation of the anatase crystal size as a function of the Ag concentration is shown in Figure 6.4a. The decrease in anatase crystal size is closely correlated with increasing the Ag concentration. This demonstrates the role of Ag in decreasing TiO<sub>2</sub> crystal size. This

is in agreement with previous studies which report that the presence of Ag particles on the titanium oxide surface is known to inhibit growth of TiO<sub>2</sub> crystals [46-48].

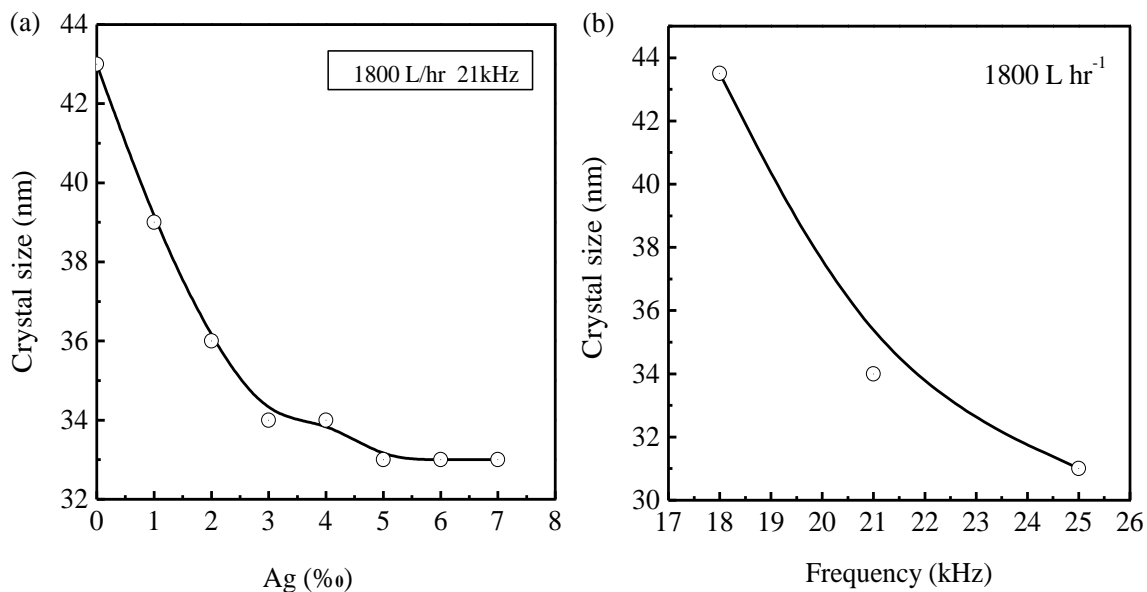


Figure 6.4: Anatase crystal size as a function of (a) Ag concentration, (b) and pulse frequency.

Higher deposition power significantly affected the anatase crystal size. For the low air flow rate condition set at 1800 L·h<sup>-1</sup>, the crystal sizes were 41 nm, 34 nm and 31 nm for pulse frequencies (Figure 6.4b) of 18 kHz, 21 kHz and 25 kHz, respectively. Achieving enhanced crystallinity using higher pulse frequencies in the jet was likely due to higher energy input into the plasma.

#### 6.3.4. Photocatalytic activity

The photocatalytic activity degradation work was performed by assessing the photodegradation of RhB using the Ag-TiO<sub>2</sub> photocatalyst under white solar light conditions. The RhB degradation kinetics in the presence of the Ag-TiO<sub>2</sub> samples (with different Ag concentrations at a fixed pulse power of 21 kHz) coated on glass substrates,



under white light irradiation is shown in Figure 6.5. The initial concentration of RhB in distilled water was adjusted to  $5 \text{ mg}\cdot\text{L}^{-1}$  before each experiment. Large photocatalytic activities were observed for samples containing 0.3% and 0.4% Ag. The decreasing photocatalytic activity caused by Ag concentrations larger than 0.4% was due to the negative effect of excessive Ag acting as recombination centers between the photo-generated electron-hole pairs.

RhB degradation kinetics was assessed using samples prepared by employing a fixed 0.4% Ag concentration but with different pulse powers and air flow rates (Figure 6.6). The pseudo first order [49] rate constant was much larger in the case of the Ag-TiO<sub>2</sub> coatings when compared to the non-incorporated coatings. Using an optimized pulse frequency at 21 kHz resulted producing a coating which is able to accomplish faster kinetics. Also, the Ag-TiO<sub>2</sub> half-life ( $t_{1/2}$ ) was less than the  $t_{1/2}$  for the TiO<sub>2</sub> coatings. Note that the best  $t_{1/2}$  of 42 min was observed for a sample prepared using a pulse frequency of 18 or 21 kHz and air flow rate equal to  $1800 \text{ L}\cdot\text{h}^{-1}$ . The data indicate that the major parameters of the deposition parameters affecting the photocatalytic activity of the coatings were the pulse frequency and the air flow rate.

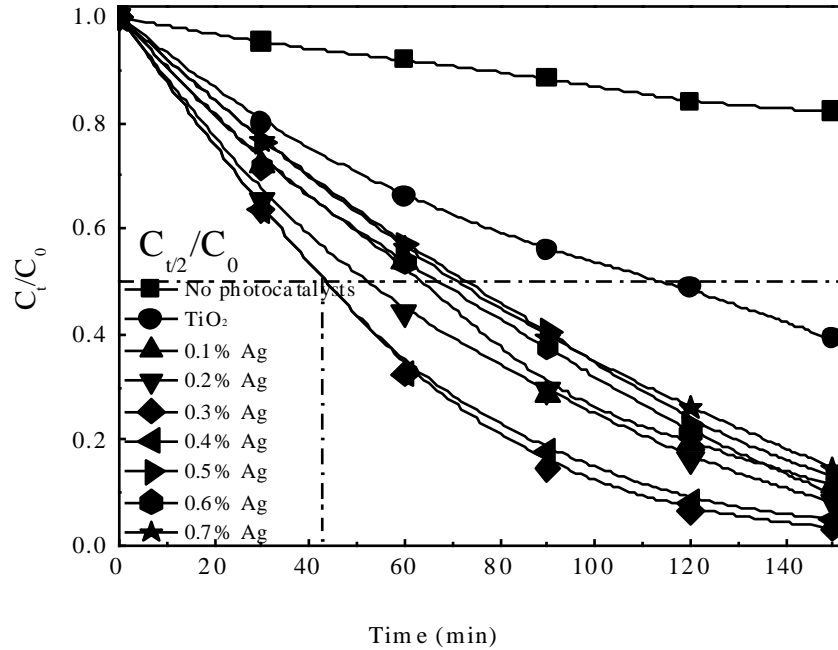


Figure 6.5: RhB photocatalytic degradation (initial concentration  $5.0 \text{ mg}\cdot\text{L}^{-1}$ ) with the Ag-TiO<sub>2</sub> coatings deposited by atmospheric pressure plasma jet (APPJ) for different Ag concentrations.

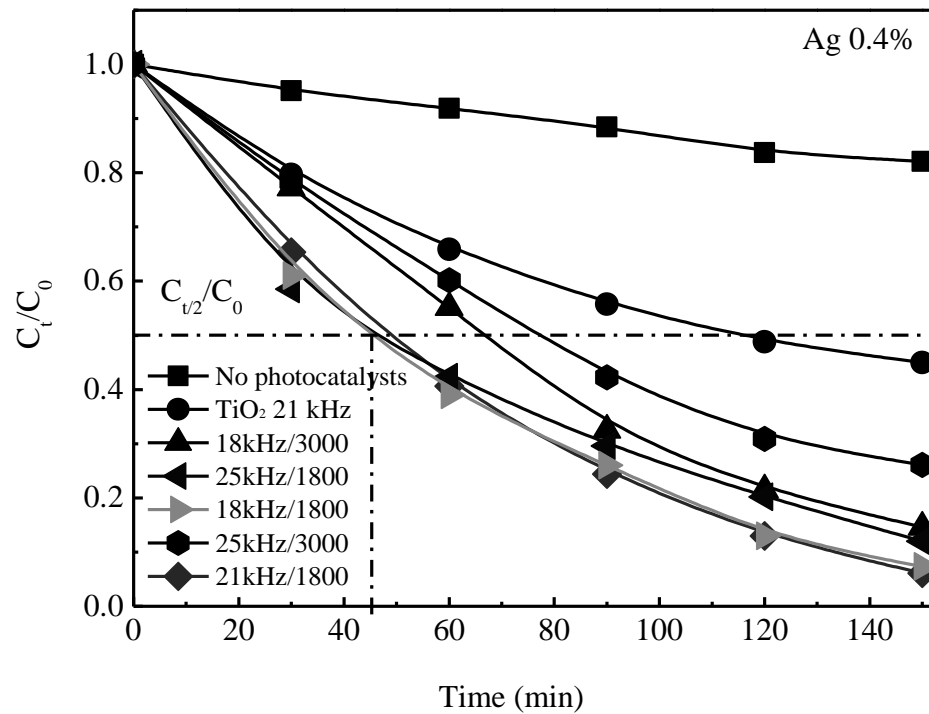


Figure 6.6: RhB degradation kinetic for samples prepared at fixed concentration of Ag (0.4%) and under different pulse frequencies and air flow rates.

Following the preliminary screening test to establish a preforming photocatalytic thin film using RhB as a target contaminant, the photocatalytic activity for 0.4% Ag-TiO<sub>2</sub> sample was further examined using CBZ, VLX and BZF. CBZ degradation profiles of photolysis and photo-catalysis using TiO<sub>2</sub> and 0.4% Ag-TiO<sub>2</sub> composites are shown in Figure 6.7. CBZ is an antiepileptic drug, and one of the most frequently detected compounds in the aquatic environment due to its resistance to biological degradation [50]. At all exposure times, CBZ was consistently not susceptible to photolysis by solar irradiation; however, degradation was observed by employing TiO<sub>2</sub>-based photocatalysis. Photocatalysis using the Ag-TiO<sub>2</sub> composite sample caused approximately 75% removal of CBZ within 60 mins (Figure 6.7).

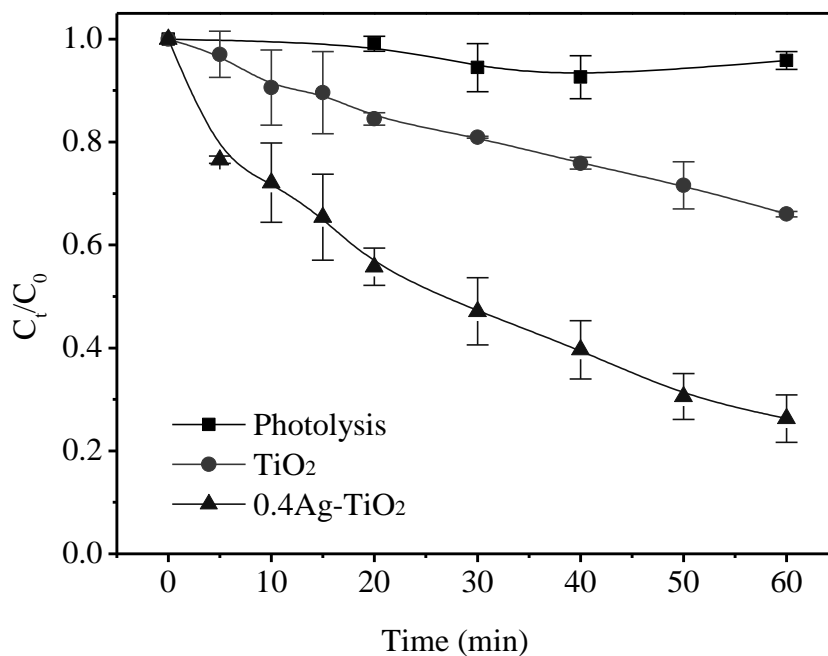


Figure 6.7: Degradation of 100  $\mu\text{g}\cdot\text{L}^{-1}$  (pH=7) CBZ by photolysis and photocatalysis using TiO<sub>2</sub> and 0.4% Ag- TiO<sub>2</sub> produced at 21 kHz and an air flow rate of 1800  $\text{L}\cdot\text{h}^{-1}$  under solar simulated irradiation.

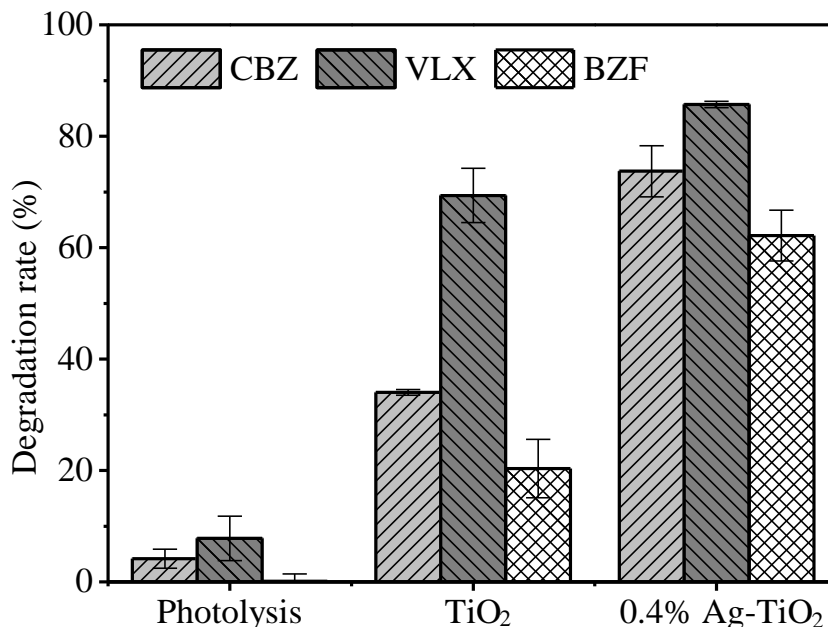


Figure 6.8: Pharmaceutical compounds degradation percentage ( $C_0$ , CBZ/VLX/BZF =  $100 \mu\text{g}\cdot\text{L}^{-1}$ , pH=7) using photolysis (irradiation only), photocatalytic oxidation using  $\text{TiO}_2$  and 0.4% Ag- $\text{TiO}_2$  (deposited at 21 kHz and air flow rate of  $1800 \text{ L h}^{-1}$ ) after 60 min irradiation under solar simulated irradiation

The degradation of CBZ, VLX and BZF each at an initial concentration of  $100 \mu\text{g}\cdot\text{L}^{-1}$  and pH=7 was examined using photolysis (irradiation only),  $\text{TiO}_2$  and 0.4% Ag- $\text{TiO}_2$  under solar light irradiation for 60 min (Figure 6.8). The results show that all tested pharmaceutical compounds are not susceptible to photolysis; however, substantial degradation by  $\text{TiO}_2$  and 0.4% Ag- $\text{TiO}_2$  photocatalysis was observed in the following order: VLX > CBZ > BZF. Significantly higher degradation rates of the tested chemicals were observed for the Ag- $\text{TiO}_2$  composite catalyst when compared to the unmodified  $\text{TiO}_2$  samples. The highest removal rates observed for VLX by employing  $\text{TiO}_2$  and Ag- $\text{TiO}_2$  photocatalysts were  $69.4\pm 4\%$  and  $85.7\pm 1\%$ , respectively. These large removal rates can be explained based on the electrostatic interactions between VLX and the photocatalyst surface. A negatively-charged  $\text{TiO}_2$  surface under the experimental conditions

examined [51] can aid in the selective adsorption of VLX, a hydrophilic and the only positively-charged tested compound ( $pK_a=8.9$ ;  $\log D=0.84$ , Table 6.1) in this study.

No decrease in CBZ, VLX and BZF concentration in the solution was observed after 60 min of exposure to the  $TiO_2/Ag-TiO_2$  catalyst under dark conditions. This indicates the adsorption for each pollutant onto the  $Ag-TiO_2$  coating is negligible. For photodegradation using solar irradiation, BZF showed only  $20.3\pm 5.2\%$  degradation by  $TiO_2$ ; however, the degradation improved significantly to  $62.2\pm 4.6\%$  when using 0.4%  $Ag-TiO_2$ . CBZ has also showed a higher degradation by 0.4%  $Ag-TiO_2$  with  $73.7\pm 4.6\%$  as opposed to  $34.0\pm 0.5\%$  degradation by  $TiO_2$ . BZF is negatively charged and relatively hydrophilic at the experimental pH ( $pK_a=3.8$ ;  $\log D=0.97$ , Table 6.1), while CBZ is neutrally charged and hydrophobic ( $pK_a=13.9$ ;  $\log D=2.77$ , Table 6.1). The similar behavior of both compounds, possessing different chemical properties, suggests that although a favorable interaction between the target compound and the catalyst is an advantage, it is not prerequisite for photocatalytic oxidation. To summarize, Ag incorporation in the  $TiO_2$  clearly provided superior photocatalytic efficiency owing to the improved charge transfer and separation [8, 14, 15, 52] and the porous structure facilitating higher active surface area.

Table 6.1: Physicochemical properties of the examined compounds

Compound	Class	Molecular formula	$pK_a^1$	Charge (pH=7)	$\log D^a$ (pH=7)
RhB <sup>b</sup>	Dye	$C_{28}H_{31}ClN_2O_3$	4.3	negative	2.34
CBZ	Antiepileptic	$C_{15}H_{12}N_2O$	13.9	neutral	2.77
VLX	Antidepressant	$C_{17}H_{27}NO_2$	8.9	positive	0.84
BZF	Lipid regulator	$C_{19}H_{20}ClNO_4$	3.8	negative	0.97

Notes: <sup>a</sup> Source: [www.chemicalize.com](http://www.chemicalize.com) (last accessed May 1, 2018), and <sup>b</sup> RhB, CBZ, VLX, and BZF represent rhodamine b, carbamazepine, venlafaxine and bezafibrate, respectively.

### 6.3.5. Mechanism of photocatalytic oxidation by Ag-TiO<sub>2</sub>

Ag NPs at the metal-TiO<sub>2</sub> interface region functions as electron traps to facilitate electron-hole separation and eventually promoting the interfacial electron transfer process to enhance the photocatalytic efficiency [53]. In comparison, incorporating Ag into TiO<sub>2</sub> host materials is associated with a decrease of the bandgap [14, 52]. TiO<sub>2</sub> has a bandgap of 3.2 eV and shifting the absorbance towards longer wavelengths by incorporating Ag reduces the band gap to 2.9 eV for Ag-TiO<sub>2</sub> [14, 52]. The decrease in the band gap extends the light absorption in the visible range and enhanced the photocatalytic activity [15]. However, with extensive concentrations of Ag in the host material, Ag nanoparticles which are able to behave as recombination centers between the photo-generated electron hole pairs within TiO<sub>2</sub> drastically reduces the photocatalytic activity of the composite photocatalyst. Hence, 0.4% Ag is the optimum condition for photodegrading organic pollutants. The 0.4% Ag-TiO<sub>2</sub> core-shell structure enhanced the photoactivity of TiO<sub>2</sub> by increasing the interfacial charge transfer efficiency of the TiO<sub>2</sub> thin films. Furthermore, decreasing the anatase grain size caused an increase of the specific surface area, inhibition of bulk recombination between the e<sup>-</sup>/h<sup>+</sup> pairs and enhancement of the charge separation.

## 6.4. Conclusions

An arc blown atmospheric pressure plasma jet (APPJ) was used as a simple and effective technique to produce a unique composite Ag-TiO<sub>2</sub> coating with controlled porosity and crystal size. The one-step process significantly improved the photocatalytic activity of TiO<sub>2</sub> towards the removal of RhB and pharmaceutical compounds (CBZ, VLX

and BZF). The coating process was employed to control the Ag NPs distribution and the crystallinity (crystal size) by varying the deposition parameters such as the plasma energy and carrier gas flow rate. The APPJ process produced Ag-TiO<sub>2</sub> composite photocatalysts with significant improvement in the homogeneous dispersion of Ag and the photocatalytic activity under solar irradiation conditions when compared to the pure TiO<sub>2</sub> coatings deposited by APPJ. The photocatalytic activity of the combined Ag-TiO<sub>2</sub> coating was more improved when compared to N-doped TiO<sub>2</sub> thin films which were prepared by reactive RF magnetron sputtering. This improvement is due to the Ag incorporation along with the enhanced specific surface area of the APPJ coatings. Finally, the concentration of Ag ions in water exposed to 0.4% Ag-TiO<sub>2</sub> slides was below the detection limit. Hence, use of the Ag-TiO<sub>2</sub> film synthesized using APPJ can be considered as a potential photocatalyst for drinking water treatment. This novel and simple method to deposit porous TiO<sub>2</sub> films at a high deposition rate can be utilized in many applications such as photocatalysis and dye sensitized solar cells.

## 6.5. References

- [1] D.W. Kolpin, E.T. Furlong, M.T. Meyer, E.M. Thurman, S.D. Zaugg, L.B. Barber, H.T. Buxton, Pharmaceuticals, Hormones, and Other Organic Wastewater Contaminants in U.S. Streams, 1999–2000: A National Reconnaissance, *Environ. Sci. Technol.* 36 (2002) 1202-1211.
- [2] Y. Ling, G. Liao, Y. Xie, J. Yin, J. Huang, W. Feng, L. Li, Coupling photocatalysis with ozonation for enhanced degradation of atenolol by Ag-TiO<sub>2</sub> micro-tube, *J. Photochem. Photobiol. A: Photochem. Rev.* 329 (2016) 280-286.

- [3] M.S. Kostich, A.L. Batt, J.M. Lazorchak, Concentrations of prioritized pharmaceuticals in effluents from 50 large wastewater treatment plants in the US and implications for risk estimation, *Environ. Pollut.* 184 (2014) 354-359.
- [4] A. Causanilles, C. Ruepert, M. Ibanez, E. Emke, F. Hernadez, P. de Voogt, Occurrence and fate of illicit drugs and pharmaceuticals in wastewater from two wastewater treatment plants in Costa Rica., *Sci. Total Environ.* 599-600 (2017) 98-107.
- [5] Y. Yang, Y.S. Ok, K.-H. Kim, E.E. Kwon, Y.F. Tsang, Occurrences and removal of pharmaceuticals and personal care products (PPCPs) in drinking water and water/sewage treatment plants: A review, *Sci. Total Environ.* 596 IS - (2017) 303-320.
- [6] J. Sun, L. Qiao, S. Sun, G. Wang, Photocatalytic degradation of orange g on nitrogen-doped TiO<sub>2</sub> catalysts under visible light and sunlight irradiation., *J. Hazard. Mater.* 155 (2008) 312-319.
- [7] I.M. Arabatzis, T. Stergiopoulos, M.C. Bernard, D. Labou, S.G. Neophytides, P. Falaras, Silver-modified titanium dioxide thin films for efficient photodegradation of methyl orange, *Appl. Catal., B Environ.* 42 (2003) 187-201.
- [8] Z. Xiong, J. Ma, W.J. Ng, T.D. Waite, X.S. Zhao, Silver-modified mesoporous TiO<sub>2</sub> photocatalyst for water purification, *Water Res.* 45 (2011) 2095-2103.
- [9] O. Carp, C.L. Huisman, A. Reller, Photoinduced reactivity of titanium dioxide, *Prog. Solid State Chem.* 32 (2004) 33-177.
- [10] U.I. Gaya, A.H. Abdullah, Heterogeneous photocatalytic degradation of organic contaminants over titanium dioxide: A review of fundamentals, progress and problems, *J. Photochem. Photobiol. C: Photochem. Rev.* 9 (2008) 1-12.



- [11] R. Andreozzi, V. Caprio, A. Insola, R. Marotta, Advanced oxidation processes (AOP) for water purification and recovery, *Catal. Today* 53 (1999) 51-59.
- [12] M.F.A. Messih, M.A. Ahmed, A. Soltan, S.S. Anis, Facile approach for homogeneous dispersion of metallic silver nanoparticles on the surface of mesoporous titania for photocatalytic degradation of methylene blue and indigo carmine dyes, *J. Photochem. Photobiol. A: Photochem. Rev.* 335 (2017) 40-51.
- [13] M. Sui, Y. Dong, Z. Wang, F. Wang, H. You, A biocathode-driven photocatalytic fuel cell using an Ag-doped TiO<sub>2</sub>/Ti mesh photoanode for electricity generation and pollutant degradation, *J. Photochem. Photobiol. A: Photochem. Rev.* 348 (2017) 238-245.
- [14] S.S. Boxi, S. Paria, Visible light induced enhanced photocatalytic degradation of organic pollutants in aqueous media using Ag doped hollow TiO<sub>2</sub> nanospheres, *RSC Adv.* 5 (2015) 37657-37668.
- [15] M.K. Seery, R. George, P. Floris, S.C. Pillai, Silver doped titanium dioxide nanomaterials for enhanced visible light photocatalysis, *J. Photochem. Photobiol. A: Photochem. Rev.* 189 (2007) 258-263.
- [16] M. Gratzel, Solar energy conversion by dye-sensitized photovoltaic cells, *Inorg. Chem.* 44 (2005) 6841-6851.
- [17] S.Y. Huang, G. Schlichthorl, A.J. Nozik, M. Gratzel, A.J. Frank, Charge recombination in dye-sensitized nanocrystalline TiO<sub>2</sub> solar cells, *J. Phys. Chem. B* 101 (1997) 2576-2582.
- [18] B. O'Regan, M. Gratzel, A low-cost, high-efficiency solar cell based on dye-sensitized colloidal TiO<sub>2</sub> films, *Nature* 353 (1991) 737-740.

- [19] C.-P. Lee, L.-Y. Lin, K.-W. Tsai, R. Vittal, K.-C. Ho, Enhanced performance of dye-sensitized solar cell with thermally-treated TiN in its TiO<sub>2</sub> film prepared at low temperature, *J. Power Sources* 196 (2011) 1632-1638.
- [20] C.L. Bianchi, E. Colombo, S. Gatto, M. Stucchi, G. Cerrato, S. Morandi, V. Capucci, Photocatalytic degradation of dyes in water with micro-sized TiO<sub>2</sub> as powder or coated on porcelain-gres tiles, *J. Photochem. Photobiol. A: Photochem. Rev.* 280 (2014) 27-31.
- [21] S. Salaeh, M. Kovacic, D. Kosir, H. Kusic, U.L. Stangar, D.D. Dionysiou, A.L. Bozic, Reuse of TiO<sub>2</sub>-based catalyst for solar driven water treatment; thermal and chemical reactivation, *J. Photochem. Photobiol. A: Photochem. Rev.* 333 (2017) 117-129.
- [22] P. Van Viet, B.T. Phan, D. Mott, S. Maenosono, T.T. Sang, C.M. Thi, L.V. Hieu, Silver nanoparticle loaded TiO<sub>2</sub> nanotubes with high photocatalytic and antibacterial activity synthesized by photoreduction method, *J. Photochem. Photobiol. A: Photochem. Rev.* 352 (2018) 106-112.
- [23] M.F. Brugnera, M. Miyata, C.Q.F. Leite, M.V.B. Zanoni, Silver ion release from electrodes of nanotubes of TiO<sub>2</sub> impregnated with Ag nanoparticles applied in photoelectrocatalytic disinfection, *J. Photochem. Photobiol. A: Photochem. Rev.* 278 (2014) 1-8.
- [24] D.J.R. Gutiérrez, N.R. Mathews, S.S. Martínez, Photocatalytic activity enhancement of TiO<sub>2</sub> thin films with silver doping under visible light, *J. Photochem. Photobiol. A: Photochem. Rev.* 262 (2013) 57-63.

- [25] D. Yang, Y. Sun, Z. Tong, Y. Tian, Y. Li, Synthesis of Ag/TiO<sub>2</sub> nanotube heterojunction with improved visible-light photocatalytic performance inspired by bioadhesion, *J. Phys. Chem. C* 119 (2015) 5827-5835.
- [26] J.H. Hsieh, R.B. Yu, Y.K. Chang, C. Li, Structural analysis of TiO<sub>2</sub> and TiO<sub>2</sub>-Ag thin films and their antibacterial behaviors, *J. Phys. Conf. Ser.* 339 (2012) 012012.
- [27] D. Guin, S.V. Manorama, J.N.L. Latha, S. Singh, Photoreduction of silver on bare and colloidal TiO<sub>2</sub> nanoparticles/nanotubes: synthesis, characterization, and tested for antibacterial outcome, *J. Phys. Chem. C* 111 (2007) 13393-13397.
- [28] J. Yi, S. Zhang, H. Wang, H. Yu, F. Peng, Fabrication of uniformly dispersed Ag nanoparticles loaded TiO<sub>2</sub> nanotube arrays for enhancing photoelectrochemical and photocatalytic performances under visible light irradiation, *Mater. Res. Bull.* 60 (2014) 130-136.
- [29] W. Smith, S. Mao, G. Lu, A. Catlett, J. Chen, Y. Zhao, The effect of Ag nanoparticle loading on the photocatalytic activity of TiO<sub>2</sub> nanorod arrays, *Chem. Phys. Lett.* 485 (2010) 171-175.
- [30] C. He, Y. Yu, X. Hu, A. Larbot, Influence of silver doping on the photocatalytic activity of titania films, *Appl. Surf. Sci.* 200 (2002) 239-247.
- [31] X. Zhang, M. Li, X. He, X. Huang, R. Hang, Effects of silver concentrations on microstructure and properties of nanostructured titania films, *Mater. Des.* 65 (2015) 600-605.
- [32] X. Chen, S.S. Mao, Titanium dioxide nanomaterials: Synthesis, properties, modifications, and applications, *Chem. Rev.* 107 (2007) 2891-2959.

- [33] L.-B. Di, X.-S. Li, C. Shi, Y. Xu, D.-Z. Zhao, A.-M. Zhu, Atmospheric-pressure plasma CVD of TiO<sub>2</sub> photocatalytic films using surface dielectric barrier discharge, *J. Phys. D: Appl. Phys.* 42 (2008) 032001.
- [34] K. Gotoh, S. Yoshitaka, Improvement of soil release from polyester fabric with atmospheric pressure plasma jet, *Text. Res. J.* 83 (2013) 1606-1614.
- [35] R.B. Tyata, D.P. Subedi, A. Shrestha, D. Baral, Development of atmospheric pressure plasma jet in air, *Kathmandu University Journal of Science, Engineering and Technology* 8 (2012).
- [36] O. Carton, D. Ben Salem, S. Bhatt, J. Pulpytel, F. Arefi-Khonsari, Plasma polymerization of acrylic acid by atmospheric pressure nitrogen plasma jet for biomedical applications, *Plasma Processes Polym.* 9 (2012) 984-993.
- [37] D. Ben Salem, O. Carton, H. Fakhouri, J. Pulpytel, F. Arefi-Khonsari, Deposition of water stable plasma polymerized acrylic acid/MBA organic coatings by atmospheric pressure air plasma jet, *Plasma Processes Polym.* 11 (2014) 269-278.
- [38] A. Schutze, J.Y. Jeong, S.E. Babayan, P. Jaeyoung, G.S. Selwyn, R.F. Hicks, The atmospheric-pressure plasma jet: a review and comparison to other plasma sources, *IEEE Trans. Plasma Sci.* 26 (1998) 1-10.
- [39] C. Huang, C.-H. Liu, S.-Y. Wu, Surface characterization of the SiO<sub>x</sub> films prepared by a remote atmospheric pressure plasma jet, *Surf. Interface Anal.* 41 (2009) 44-48.
- [40] H. Fakhouri, D.B. Salem, O. Carton, J. Pulpytel, F. Arefi-Khonsari, Highly efficient photocatalytic TiO<sub>2</sub> coatings deposited by open air atmospheric pressure plasma jet with aerosolized TTIP precursor, *J. Phys. D: Appl. Phys.* 47 (2014) 265301-265311.

- [41] H. Fakhouri, J. Pulpytel, W. Smith, A. Zolfaghari, H.R. Mortaheb, F. Meshkini, R. Jafari, E. Sutter, F. Arefi-Khonsari, Control of the visible and UV light water splitting and photocatalysis of nitrogen doped TiO<sub>2</sub> thin films deposited by reactive magnetron sputtering, *Appl. Catal., B Environ.* 144 (2014) 12-21.
- [42] J. Kulczyk-Malecka, P.J. Kelly, G. West, G.C.B. Clarke, J.A. Ridealgh, K.P. Almqvist, A.L. Greer, Z.H. Barber, Investigation of silver diffusion in TiO<sub>2</sub>/Ag/TiO<sub>2</sub> coatings, *Acta Mater.* 66 (2014) 396-404.
- [43] Y. Wen, H. Ding, Y. Shan, Preparation and visible light photocatalytic activity of Ag/TiO<sub>2</sub>/graphene nanocomposite, *Nanoscale* 3 (2011) 4411-4417.
- [44] K. Awazu, M. Fujimaki, C. Rockstuhl, J. Tominaga, H. Murakami, Y. Ohki, a. Naoya Yoshida, T. Watanabe, A plasmonic photocatalyst consisting of silver nanoparticles embedded in titanium dioxide, *J. Am. Chem. Soc.* 130 (2008) 1676-1680.
- [45] Y. Ohko, T. Tatsuma, T. Fujii, K. Naoi, C. Niwa, Y. Kubota, A. Fujishima, Multicolour photochromism of TiO<sub>2</sub> films loaded with silver nanoparticles, *Nat. Mater.* 2 (2002) 29-31.
- [46] A. Ramchiary, S.K. Samdarshi, Ag deposited mixed phase titania visible light photocatalyst – Superiority of Ag-titania and mixed phase titania co-junction, *Appl. Surf. Sci.* 305 (2014) 33-39.
- [47] T.-D. Pham, B.-K. Lee, Feasibility of silver doped TiO<sub>2</sub>/glass fiber photocatalyst under visible irradiation as an indoor air germicide, *Int. J. Environ. Res. Public Health* 11 (2014) 3271-3288.
- [48] P. Navabpour, S. Ostovarpour, C. Tattershall, K. Cooke, P. Kelly, J. Verran, K. Whitehead, C. Hill, M. Raulio, O. Priha, Photocatalytic TiO<sub>2</sub> and doped TiO<sub>2</sub> coatings to

improve the hygiene of surfaces used in food and beverage processing—a study of the physical and chemical resistance of the coatings, *Coatings* 4 (2014) 433-449.

[49] F. Zhang, J. Zhao, T. Shen, H. Hidaka, E. Pelizzetti, N. Serpone, TiO<sub>2</sub>-assisted photodegradation of dye pollutants II. Adsorption and degradation kinetics of eosin in TiO<sub>2</sub> dispersions under visible light irradiation, *Appl. Catal., B Environ.* 15 (1998) 147-156.

[50] C. Chen, W. Cai, M. Long, B. Zhou, Y. Wu, D. Wu, Y. Feng, Synthesis of visible-light responsive graphene oxide/TiO<sub>2</sub> composites with p/n heterojunction, *ACS Nano* 4 (2010) 6425-6432.

[51] L.G. Harris, S. Tosatti, M. Wieland, M. Textor, R.G. Richards, Staphylococcus aureus adhesion to titanium oxide surfaces coated with non-functionalized and peptide-functionalized poly(L-lysine)-grafted-poly (ethylene glycol) copolymers, *Biomaterials* 25 (2004) 4135-4148.

[52] I. Tunc, M. Bruns, H. Gliemann, M. Grunze, P. Koelsch, Bandgap determination and charge separation in Ag@TiO<sub>2</sub> core shell nanoparticle films, *Surf. Interface Anal.* 42 (2010) 835-841.

[53] S.I. Mogal, V.G. Gandhi, M. Mishra, S. Tripathi, T. Shripathi, P.A. Joshi, D.O. Shah, Single-step synthesis of silver-doped titanium dioxide: influence of silver on structural, textural, and photocatalytic properties, *Ind. Eng. Chem. Res.* 53 (2014) 5749-5758.

## GENERAL CONCLUSIONS AND RECOMMENDATIONS

The work outlined in this thesis describes the significance of using quasi-one-dimension (Q1D) TiO<sub>2</sub> as photocatalysts for the photodegrading aqueous hazardous pollutants. In Chapter 3, the effects of three hydrothermal synthesis factors on Q1D TiO<sub>2</sub> bandgap were examined using a 3-factor 3-level Box Behnken design (BBD) statistical model. The hydrothermal synthesis factors significantly affected Q1D TiO<sub>2</sub> phase structure, crystal size [1] and SSA, bandgap and photocatalytic activities in terms of photodegrading aqueous hazardous pollutants [2] and producing H<sub>2</sub> [3]. The factors investigated included temperature, NaOH concentration and TiO<sub>2</sub> concentration. The temperature and NaOH concentration significantly affected the crystal phase and Q1D TiO<sub>2</sub> bandgap. Pure anatase synthesized at middle level of temperature ( $\geq 120^{\circ}\text{C}$  and  $< 190^{\circ}\text{C}$ ) and NaOH concentration was associated with a higher bandgap ( $3.258 \pm 0.003$ - $3.305 \pm 0.004$ ). A maximum bandgap of  $3.305 \pm 0.004$  eV was obtained when the conditions were set at  $150^{\circ}\text{C}$ , 12 M NaOH and  $14 \text{ g}\cdot\text{L}^{-1}$  TiO<sub>2</sub>. The biphasic anatase-TiO<sub>2</sub>-B phase synthesized at higher temperature and NaOH concentration was linked with the middle level of bandgap between  $3.203 \pm 0.006$ - $3.229 \pm 0.009$  eV. The biphasic anatase-rutile phase synthesized at lower temperature and NaOH concentration was closely correlated to a lower bandgap. A minimum bandgap of  $3.044 \pm 0.002$  eV was obtained at  $120^{\circ}\text{C}$ , 5 M NaOH and  $63 \text{ g}\cdot\text{L}^{-1}$  TiO<sub>2</sub>. In addition, the lower temperature and NaOH concentration were associated with the decrease of the crystal size and increase of SSA. Decreasing the crystal size (increasing the SSA) was correlated with increasing the bandgap which was caused by the size quantization effect [4].

The work presented in Chapter 4 was focused on evaluating the effect of the hydrothermal synthesis factors on the photocatalytic activity in terms of: photodegrading aqueous organic pollutants (Part 1) and photocatalytic H<sub>2</sub> production using Q1D TiO<sub>2</sub> (Part 2) based on the research presented in Chapter 3. The first model (Fourth objective part 1) was developed for photocatalytic degradation of rhodamine b (RhB). The BBD model demonstrated that lower temperature (120°C) and lower NaOH concentration (5 M) were linked to Q1D TiO<sub>2</sub> containing biphasic anatase-rutile phase with smaller mean crystal size (9.5±0.1 nm) and maximum photodegradation rate of aqueous organic pollutants. The RhB photodegradation rate for Q1D TiO<sub>2</sub> synthesized using the optimized conditions was approximately 46% greater when compared to anatase-TiO<sub>2</sub>-B prepared using a surfactant molecular self-assembly process reported by Zhang et al [5]. This result was validated by photodegrading phenol, methyl orange (MO) and methylene blue (MB). The second model (Fourth objective part 2) was developed for photocatalytic H<sub>2</sub> production using 20 v/v% ethanol solutions as feedstock. The model demonstrated that lower temperature and higher NaOH concentration were correlated to Q1D TiO<sub>2</sub> containing pure anatase phase with a mean crystal size of 20.1±0.2 nm and an enhanced H<sub>2</sub> production rate. The optimum conditions for synthesizing Q1D anatase TiO<sub>2</sub> with the maximum H<sub>2</sub> production rate of 475±12 μmol·h<sup>-1</sup> (quantum efficiency (ε) = 20.2±0.5%) was observed at 126°C, 15 M NaOH and 49 g·L<sup>-1</sup> TiO<sub>2</sub>. The maximum H<sub>2</sub> production rate was significantly improved when compared to a biphasic anatase-TiO<sub>2</sub>-B photocatalyst reported by Kuo et al [3]. The model demonstrated that higher temperature (190°C) and higher NaOH concentration (≥10 M) were linked to Q1D TiO<sub>2</sub> containing TiO<sub>2</sub>-B phase with larger crystal size (≥ 46.4±0.3 nm) and low photocatalytic activities.



Table 7.1: The apparent photocatalysis rate constant ( $\text{min}^{-1}$ ) for selected photocatalysts using UV irradiation.

Experiment	Apparent photocatalysis rate constant $k$ ( $\text{min}^{-1}$ ) for:			
	MO	RhB	MB	Phenol
No catalysts	$0.0003 \pm 0.0001^D$	$0.003 \pm 0.0008^D$	$0.0046 \pm 0.0004^D$	$0.0014 \pm 0.0001^D$
Commercial				
P25	$0.2202 \pm 0.0038^C$	$0.3483 \pm 0.0051^C$	$0.4674 \pm 0.0071^C$	$0.0371 \pm 0.0007^C$
Optimized				
Q1D TiO <sub>2</sub> <sup>b</sup>	$0.2361 \pm 0.0021^B$	$0.4470 \pm 0.0041^B$	$0.5891 \pm 0.0108^B$	$0.0431 \pm 0.0008^B$
GT-95 <sup>1h</sup>	$0.3118 \pm 0.0012^A$	$1.1345 \pm 0.0052^A$	$1.5758 \pm 0.0110^A$	$0.0548 \pm 0.0005^A$

Notes: <sup>a</sup> A, B, C, D: Means the terms that do not share a letter in superscript are significantly different in each column according to Tukey's test [9], and  $A > B > C > D$ , <sup>b</sup> GT-95<sup>1h</sup> shows RGO atomic O/C ratio of approximately  $0.130 \pm 0.003$ , and <sup>c</sup> optimized Q1D TiO<sub>2</sub> data is from Chapter 4, and GT-95<sup>1h</sup> data is from Chapter 5.

The work described in Chapter 5 was focused on enhancing Q1D TiO<sub>2</sub> (nanorods) with partially RGO (Fifth objective part 1) and partially RGO plus Ag nanoparticles (NPs) (Fifth objective part 2) for photodegrading aqueous hazardous pollutants. In part 1, enhanced TiO<sub>2</sub> nanorods (TNRs) with partially reduced graphene oxide (RGO) (designated as GT) were prepared. The degree of RGO oxidation (atomic O/C ratio) played an important role in affecting the photocatalytic activities in terms of photoelectrochemical current and photodegrading rhodamine b (RhB), methyl orange (MO), methylene blue (MB) and phenol by using ultraviolet (UV) light. The RGO atomic O/C ratio for GT photocatalyst under consideration ranged from  $0.09 \pm 0.0021$  to  $0.85 \pm 0.0075$ . The results of the photocurrent and photodegradation study showed that the RGO atomic O/C ratio of approximately  $0.130 \pm 0.003$  was optimum for maximizing the photocatalytic activities. The photocatalytic degradation rate was significantly enhanced when compared to the optimized Q1D TiO<sub>2</sub> photocatalyst in Chapter 4 (Table 7.1). The highest photocurrent increase for GT with optimum RGO atomic O/C ratio was approximately 6-fold when compared to the UV-assisted TiO<sub>2</sub>-RGO reported by

Williams et al. [6]. The MB photodegradation rate increase of approximately 8-fold with the optimum GT photocatalyst when compared to Degussa TiO<sub>2</sub> P25-RGO is corroborated by Zhang et al. [7] and Du et al. [8].

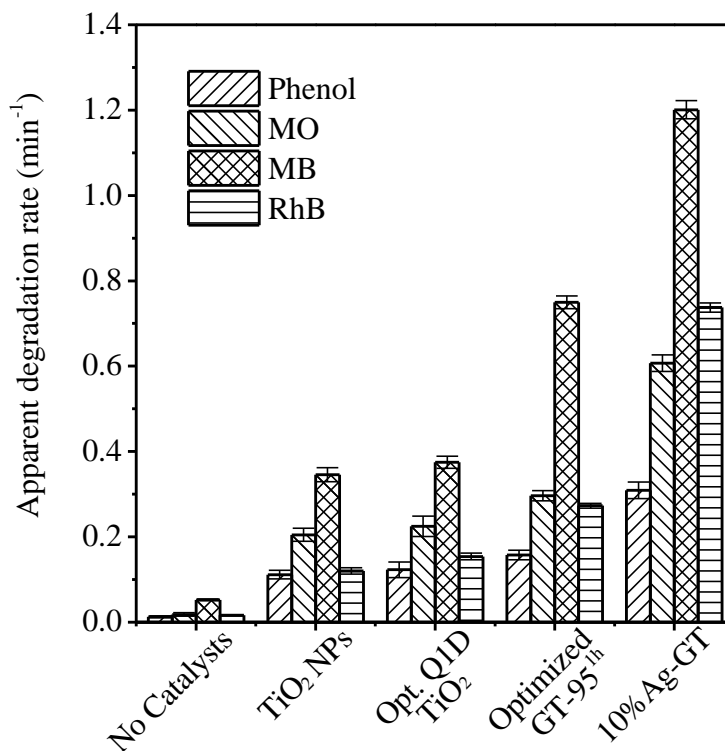


Figure 7.1: Photocatalytic degradation rate constant ( $k$ ) for phenol, methyl orange (MO), methylene blue (MB) and rhodamine B (RhB) under visible light conditions. Note: Optimized Q1D TiO<sub>2</sub> and GT-95<sup>lh</sup> data are from Chapter 4 and Chapter 5, respectively.

In Chapter 5, part 2 of the fifth objective, a hierarchical three-dimensional (3D) Ag nanoparticle-RGO-TiO<sub>2</sub> nanorods (designated as Ag-GT) films was synthesized for degrading aqueous organic pollutants using visible irradiation. The synthesis of Ag-GT with an optimum RGO atomic O/C ratio was based on Part 1. The Ag-GT photocatalyst was characterized with a larger SSA of approximately  $181 \pm 5 \text{ m}^2 \cdot \text{g}^{-1}$  when compared to TiO<sub>2</sub> NPs with a SSA of  $50 \pm 5 \text{ m}^2 \cdot \text{g}^{-1}$ . The 3D Ag-GT photocatalysts with an enhanced

visible light absorption between 400 to 700 nm and decreasing bandgap to approximately 2.55 eV was due to the localized surface plasmon resonance (SPR) absorption of Ag NPs [10, 11]. In addition, the impact of Ag content (5-15wt%) on the photocatalytic activities was investigated. A maximum photocurrent and photodegradation rate were observed for a photocatalyst film containing 10% silver. The photocatalytic degradation rate was significantly enhanced when compared to the optimized Q1D TiO<sub>2</sub> photocatalyst in Chapter 4 and optimized GT-95<sup>th</sup> (Figure 7.1). This largest photodegradation rate observed with the optimum Ag-GT catalyst was approximately a 2.6-fold increase when compared to a Ag doped TiO<sub>2</sub> film reported by Bensouici et al [12].

In Chapter 6, micrometer thick Ag nanoparticles (NPs) modified TiO<sub>2</sub> (designated as Ag-TiO<sub>2</sub>) coatings were deposited in a single and facile step by spraying the precursor solution in a non-equilibrium atmospheric pressure plasma jet (APPJ). The arc blown APPJ is a simple and effective technique for depositing the Ag-TiO<sub>2</sub> coating (deposition rate of 10-20  $\mu\text{m}\cdot\text{s}^{-1}$ ) when compared to the deposition rate of RF reactive sputtering (1~10  $\text{nm}\cdot\text{min}^{-1}$ ) [13]. The distribution of Ag, the crystallinity of TiO<sub>2</sub> and the TiO<sub>2</sub> particle size during the coating process was controlled by varying the deposition parameters such as the plasma energy and carrier gas flow rate. The coating was characterized as a porous anatase phase and Ag-TiO<sub>2</sub> core-shell structure with improved charge separation/transfer and visible light absorption. The photocatalytic activity using solar irradiation of the materials was investigated for the degradation of rhodamine b (RhB) and pharmaceutical organic wastewater contaminants (OWCs), namely carbamazepine (CBZ), venlafaxine (VLX) and bezafibrate (BZF). The effect of the Ag content (0-0.7 wt%) on the photocatalytic activity was examined. The enhanced

photodegradation rate was observed for a silver content of 0.4wt% in the composite coating. The photocatalytic activity of the optimum Ag-TiO<sub>2</sub> thin films prepared by APPJ was significantly improved when compared to the pure TiO<sub>2</sub> coating obtained by APPJ as well as the low pressure sputtering technique[13, 14].

The study in this dissertation demonstrated the possibility of using Q1D TiO<sub>2</sub> synthesized by the alkaline hydrothermal process as a photocatalyst for wastewater treatment and renewable energy production. Enhancing Q1D TiO<sub>2</sub> with partial RGO and Ag nanoparticle improved the photocatalytic efficiency. Immobilizing Ag-GT and Ag-TiO<sub>2</sub> simplified the wastewater treatment process when compared to using photocatalyst powder. However, a few obstacles need to be addressed for future application. Redesigning the existing photocatalytic reactor used to degrade aqueous hazardous pollutants will offer the possibility to transform from batch degradation to a continuous degradation process for practical implementation and scale-up.

Work to reduce the multi-step Ag-GT thin-film synthesis is required to reduce the processing cost. Increasing the H<sub>2</sub> production rate using strategies such as coupling with a narrow bandgap semiconductor, doping with ions, co-catalyst loading, surface dye-sensitization or noble metal deposition are required to improve the Q1D TiO<sub>2</sub> photocatalytic activity [15]. Modifying the Q1D TiO<sub>2</sub> catalyst could allow using solar light and significantly enhance the solar energy conversion efficiency [15]. Note, the maximum energy conversion of UV-activated photocatalyst is 2% of the solar energy [15].

Studies on smaller bandgap semiconductors such as CdS are required to enhance visible-light photocatalytic activities. CdS is an alternative solar light photocatalyst. CdS

quantum dots (<10 nm) shows a relatively narrow bandgap of 2.42 eV corresponding to a response when using visible light below 510 nm [16]. However, CdS suffers anodic photocorrosion since  $S^{2-}$  is susceptible to chemical corrosion [17-19]. Further, modifying CdS with RGO, noble metal (e.g. Pt, Au and Ag), metal-organic framework and other semiconductors will likely improve its photocatalytic activities and chemical stability [17-20]. Finally, the APPJ used to deposit Ag-TiO<sub>2</sub> thin film photocatalyst coatings with improved photocatalytic properties can present a great potential to make other TiO<sub>2</sub> modified coatings. Indeed, a wide range of other composites such as functionalized graphene or Fe<sub>2</sub>O<sub>3</sub> (Photo-Fenton system) can be incorporated in TiO<sub>2</sub> coating to improve the photocatalytic activity under solar irradiation conditions.

## References

- [1] D.V. Bavykin, V.N. Parmon, A.A. Lapkin, F.C. Walsh, The effect of hydrothermal conditions on the mesoporous structure of TiO<sub>2</sub> nanotubes, *J. Mater. Chem.* 14 (2004) 3370-3378.
- [2] S.D. Perera, R.G. Mariano, K. Vu, N. Nour, O. Seitz, Y. Chabal, K.J. Balkus Jr., Hydrothermal synthesis of graphene-TiO<sub>2</sub> nanotube composites with enhanced photocatalytic activity, *ACS Catal.* 2 (2012) 949-956.
- [3] H.-L. Kuo, C.-Y. Kuo, C.-H. Liu, J.-H. Chao, C.-H. Lin, A highly active bi-crystalline photocatalyst consisting of TiO<sub>2</sub> (B) nanotube and anatase particle for producing H<sub>2</sub> gas from neat ethanol, *Catal. Lett.* 113 (2007) 7.
- [4] I. Okura, M. Kaneko, *Photocatalysis science and technology*, Springer and Kodansha, Japan, 2002.

- [5] L. Zhang, W. Zheng, H. Jiu, W. Zhu, G. Qi, Preparation of the anatase/TiO<sub>2</sub>(B) TiO<sub>2</sub> by self-assembly process and the high photodegradable performance on RhB, *Ceram. Int.* 42 (2016) 12726-12734.
- [6] G. Williams, B. Seger, P.V. Kamat, TiO<sub>2</sub>-graphene nanocomposites. UV-assisted photocatalytic reduction of graphene oxide, *ACS Nano* 2 (2008) 1487-1491.
- [7] H. Zhang, X. Lv, Y. Li, Y. Wang, J. Li, P25-graphene composite as a high performance photocatalyst, *ACS Nano* 4 (2010) 380-386.
- [8] J. Du, X. Lai, N. Yang, J. Zhai, D. Kisailus, F. Su, D. Wang, L. Jiang, Hierarchically ordered macro-mesoporous TiO<sub>2</sub>-graphene composite films: improved mass transfer, reduced charge recombination, and their enhanced photocatalytic activities, *ACS Nano* 5 (2011) 590-596.
- [9] M.N.G.D. Sharma, Power of Tukey's test for non-additivity, (2017) 1-7.
- [10] Y. Wen, H. Ding, Y. Shan, Preparation and visible light photocatalytic activity of Ag/TiO<sub>2</sub>/graphene nanocomposite, *Nanoscale* 3 (2011) 4411-4417.
- [11] K. Awazu, M. Fujimaki, C. Rockstuhl, J. Tominaga, H. Murakami, Y. Ohki, a. Naoya Yoshida, T. Watanabe, A plasmonic photocatalyst consisting of silver nanoparticles embedded in titanium dioxide, *J. Am. Chem. Soc.* 130 (2008) 1676-1680.
- [12] F. Bensouici, T. Souier, A.A. Dakhel, A. Iratni, R. Tala-Ighil, M. Bououdina, Synthesis, characterization and photocatalytic behavior of Ag doped TiO<sub>2</sub> thin film, *Superlattices Microstruct.* 85 (2015) 255-265.
- [13] H. Fakhouri, D.B. Salem, O. Carton, J. Pulpytel, F. Arefi-Khonsari, Highly efficient photocatalytic TiO<sub>2</sub> coatings deposited by open air atmospheric pressure plasma jet with aerosolized TTIP precursor, *J. Phys. D: Appl. Phys.* 47 (2014) 265301-265311.

- [14] H. Fakhouri, J. Pulpytel, W. Smith, A. Zolfaghari, H.R. Mortaheb, F. Meshkini, R. Jafari, E. Sutter, F. Arefi-Khonsari, Control of the visible and UV light water splitting and photocatalysis of nitrogen doped TiO<sub>2</sub> thin films deposited by reactive magnetron sputtering, *Appl. Catal., B Environ.* 144 (2014) 12-21.
- [15] A.A. Ismail, D.W. Bahnemann, Photochemical splitting of water for hydrogen production by photocatalysis: A review, *Sol. Energy Mater. Sol. Cells* 128 (2014) 85-101.
- [16] Q. Zhou, M.-L. Fu, B.-L. Yuan, H.-J. Cui, J.-W. Shi, Assembly, characterization, and photocatalytic activities of TiO<sub>2</sub> nanotubes/CdS quantum dots nanocomposites, *J. Nanopart. Res.* 13 (2011) 6661-6672.
- [17] S. Saha, G. Das, J. Thote, R. Banerjee, Photocatalytic metal–organic framework from CdS quantum dot incubated luminescent metallohydrogel, *J. Am. Chem. Soc.* 136 (2014) 14845-14851.
- [18] A. Cao, Z. Liu, S. Chu, M. Wu, Z. Ye, Z. Cai, Y. Chang, S. Wang, Q. Gong, Y. Liu, A facile one - step method to produce graphene - CdS quantum dot nanocomposites as promising optoelectronic materials, *Adv. Mater.* 22 (2010) 103-106.
- [19] C.Y. Park, U. Kefayat, N. Vikram, T. Ghosh, W.C. Oh, K.Y. Cho, Preparation of novel CdS-graphene/TiO<sub>2</sub> composites with high photocatalytic activity for methylene blue dye under visible light, *Bull. Mater. Sci.* 36 (2013) 869-876.
- [20] C. Zhai, M. Zhu, F. Pang, D. Bin, C. Lu, M.C. Goh, P. Yang, Y. Du, High efficiency photoelectrocatalytic methanol oxidation on CdS quantum dots sensitized Pt electrode, *ACS Appl. Mater. Interfaces* 8 (2016) 5972-5980.

## RESUME DE LA THESE

Le dioxyde de titane ( $\text{TiO}_2$ ) est largement considéré comme une solution potentielle pour la photodégradation de polluant dangereux et la production d'énergie propre. Les principales applications de photocatalyse incluent les deux catégories suivantes : 1. photocatalyse d'eau en  $\text{O}_2$  et  $\text{H}_2$  et 2. photodégradation de polluants organiques aqueux [1, 2]. Cependant, l'activités photocatalytique de  $\text{TiO}_2$  pur peut atteindre un niveau faible d'efficacité en raison de la recombinaison rapide de paires  $e^-h^+$  photogénérés [2] d'une part et à la valeur élevée de la largeur de la bande optique qui est de 3.2 eV d'autre part conduisant donc uniquement à l'absorption du rayonnement UV ( 2 à 3% du spectre solaire) [2, 3].

Dans cette thèse nous avons modifié la morphologie, la taille et la phase cristalline de  $\text{TiO}_2$  par le dépôt des nanoparticules métalliques [2, 4] et par l'incorporation des matériaux à base du carbone [5, 6]. Le  $\text{TiO}_2$  nanostructuré quasi-unidimensionnel (Q1D) est particulièrement intéressant pour sa très grande surface spécifique (SSA), sa taille cristalline nanométrique, sa phase cristalline contrôlable, ainsi qu'à la conductivité plus importante de ses porteurs de charge, à une amélioration de séparation des paires  $e^-h^+$  photogénérés et à son excellente propriété mécanique [1].

Le travail présenté dans cette thèse décrit la modification et la caractérisation des nanoparticules photocatalytique de  $\text{TiO}_2$  (Q1D) pour le traitement des eaux usées dangereux et la production hydrogène. Dans le Chapitre 1, les processus photocatalytiques fondamentaux et l'état de l'art seront décrits pour la synthèse et la



modification de TiO<sub>2</sub>. Dans le Chapitre 2, la méthodologie sera décrite pour la synthèse et la caractérisation du photocatalyseur TiO<sub>2</sub> Q1D.

Dans le Chapitre 3, les effets de trois facteurs de synthèse hydrothermale (la température de réaction, la concentration de NaOH et la concentration de TiO<sub>2</sub>) sur la structure de la phase, la taille de cristaux, la SSA, le gap optique de TiO<sub>2</sub> Q1D, seront examinés en utilisant le modèle à 3 facteurs-3 niveaux du modèle statique de Box Behnken design (BBD). La température et la concentration NaOH ont une influence significative sur la phase cristalline et la largeur de gap du TiO<sub>2</sub> Q1D. Anatase pur synthétisé à une valeur moyenne de la température ( $\geq 120^{\circ}\text{C}$  et  $< 190^{\circ}\text{C}$ ) et de la concentration NaOH a été associé à une plus grande valeur de l'énergie du gap ( $3.258 \pm 0.003$ - $3.305 \pm 0.004$ ). Une valeur maximale d'énergie du gap de  $3.305 \pm 0.004$  eV a été obtenue quand les conditions ont été mises à  $150^{\circ}\text{C}$ , 12 M NaOH and  $14 \text{ g}\cdot\text{L}^{-1}$  TiO<sub>2</sub>.

Le matériau anatase-TiO<sub>2</sub>-B biphasique synthétisée à la température et concentration plus élevée de NaOH a permis d'avoir un niveau moyen d'énergie de bandgap entre  $3.203 \pm 0.006$ - $3.229 \pm 0.009$  eV. Le matériau anatase-rutile biphasique synthétisée à la température et concentration de NaOH plus faible, était étroitement corrélée à une valeur de la largeur du gap plus faible. Un minimum de la largeur du gap de  $3.044 \pm 0.002$  eV a été obtenu à  $120^{\circ}\text{C}$ , 5 M NaOH and  $63 \text{ g}\cdot\text{L}^{-1}$  TiO<sub>2</sub>. De plus, ces conditions ont été associées à la diminution de la taille du cristal et de SSA.

Le chapitre 4 a été concentré sur l'évaluation de l'effet des paramètres de synthèse hydrothermale sur des activités photocatalytiques en termes de : la photodégradation de polluants organiques dans une solution aqueuse (la Partie 1) et la production H<sub>2</sub> photocatalytique utilisant TiO<sub>2</sub> Q1D (la Partie 2) basé sur le résultats présentés dans le

Chapitre 3. Le premier modèle (la Partie 1) a été développé pour la dégradation photocatalytique de rhodamine b (RhB). Le modèle de BBD démontrait que la température inférieure (120°C) et la concentration plus faible de NaOH (5 M) a été liée avec la structure TiO<sub>2</sub> Q1D contenant la structure cristalline biphasique anatase-rutile avec une taille moyenne plus petite de cristal (9.5±0.1 nm) et le taux de photodégradation maximal de polluants organiques aqueux. Le taux de photodégradation RhB pour TiO<sub>2</sub> Q1D synthétisé sous les conditions optimales était approximativement 46 % supérieur à anatase-TiO<sub>2</sub>-B préparé en utilisant un processus d'auto assemblage moléculaire de tensio-actif rapporté par Zhang et al[7]. Ce résultat a été validé pour la photodégradation de phénol, l'orange de méthyle (MO) et le bleu de méthylène (le MO). Le deuxième modèle (la Partie 2) a été développé pour la production H<sub>2</sub> photocatalytique en utilisant une solution de 20 v/v% d'éthanol.

Le modèle démontrait que les températures inférieures et concentrations plus importantes de NaOH étaient corrélées à la structure TiO<sub>2</sub> Q1D contenant l'anatase pur avec une taille cristalline moyenne de 20.1±0.2 nm et avec une production d'hydrogène importante. Les conditions optimales pour synthétiser TiO<sub>2</sub> Q1D anatase avec le taux de production H<sub>2</sub> maximal de 475±12 μ Mol H<sup>-1</sup> (l'efficacité quantique (ε) = 20.2±0.5 %) ont été observés à une température de 126°C, une concentration molaire 15M de NaOH et 49 g·L<sup>-1</sup> TiO<sub>2</sub>. Le taux maximal de production d'H<sub>2</sub> a été amélioré significativement en comparaison avec un photocatalyseur anatase-TiO<sub>2</sub>-B biphasique rapporté par Kuo et al [8]. Les deux modèles démontraient que la température plus haute (190°C) et la concentration NaOH plus importante (=10 M) permettaient d'obtenir de TiO<sub>2</sub> Q1D

contenant la phase TiO<sub>2</sub>-B avec une taille du cristal plus importante (= 46.4±0.3 nm) et donc des activités photocatalytiques plus faible.

Le chapitre 5 porte sur l'amélioration TiO<sub>2</sub> Q1D (nanorods) soit avec RGO (Oxyde de Graphène Réduit) (la Partie 1) soit par RGO plus des nanoparticules d'Ag (NPs) (la Partie 2) pour photodégrader des polluants dangereux aqueux. Dans la partie 1, TiO<sub>2</sub> nanorods améliorée (TNRs) avec l'oxyde de graphène partiellement réduit (RGO) (désigné comme GT) ont été préparé. Le degré d'oxydation RGO (le ratio atomique de O/C obtenu par XPS) a joué un rôle important dans l'affectation des activités photocatalytiques en termes de courant photoélectrochimique et la photodégradation du rhodamine b (RhB), le méthyle d'orange (MO), le bleu de méthylène (le MO) et le phénol en utilisant la lumière (UV) ultra-violette. Le ratio atomique de O/C de RGO pour le photocatalyseur GT s'étendait de 0.09±0.0021 à 0.85±0.0075. Les résultats du photocourant et l'étude de la photodégradation ont montré que le rapport O/C de RGO égal à 0.130±0.003 était optimal pour maximiser les activités photocatalytiques. Le taux de dégradation photocatalytique a été significativement amélioré comparé au photocatalyseur TiO<sub>2</sub> Q1D optimisé dans le Chapitre 4. L'augmentation la plus importante du photocourant, pour GT avec l'optimum du rapport atomique O/C était approximativement 6 fois plus important en comparaison avec TiO<sub>2</sub>-RGO assisté par UV rapporté par Williams et al [9]. L'augmentation de 8 fois du taux de photodégradation de MO pour le photocatalyseur GT optimal en comparaison avec P25-RGO est corroborée par Zhang et al. [10] et Du et al. [11].

Dans le Chapitre 5, la Partie 2, une structure tridimensionnelle hiérarchique des nanorods composés de nanoparticules d'Ag -RGO-TiO<sub>2</sub> (désigné comme Ag-GT) ont été

synthétisés pour dégrader des polluants organiques aqueux utilisant l'irradiation visible. La synthèse d'Ag-GT avec un rapport atomique optimal de O/C de RGO a été basée sur la Partie 1. Le photocatalyseur d'Ag-GT a été caractérisé avec une surface spécifique (SSA) d'environ  $181 \pm 5 \text{ m}^2 \text{ g}^{-1}$  comparé aux NP  $\text{TiO}_2$  qui possède SSA de  $50 \pm 5 \text{ m}^2 \cdot \text{g}^{-1}$ . Les photocatalyseurs 3D Ag-GT avec une absorption améliorée dans le visible dans la gamme de longueur d'onde comprise entre 400 à 700 nm et une diminution de l'énergie du gap à une valeur de 2.55 eV sont dus à l'absorption localisée de résonance plasmon de surface (SPR) des NP d'argent. De plus, l'influence de la teneur d'Ag (le % 5-15wt) sur les activités photocatalytiques a été examinée. Il a été observé que le photocourant optimal ainsi qu'un taux de photodégradation maximal ont été obtenus pour un film de photocatalyseur contenant 10 % de l'argent. Le taux de dégradation photocatalytique a été significativement augmenté en comparaison avec le photocatalyseur  $\text{TiO}_2$  Q1D optimisé dans le Chapitre 4. Ce taux maximal de photodégradation obtenu pour le catalyseur Ag-GT est 2.6 fois plus grand par rapport  $\text{TiO}_2$  dopé Ag rapporté par Bensouici et al [12].

Dans le Chapitre 6, les couches minces micrométriques de  $\text{TiO}_2$  modifié par des nanoparticules d'Ag (désigné comme Ag- $\text{TiO}_2$ ) ont été déposées en une seule étape simple et rapide en vaporisant la solution de précurseur dans un jet de plasma hors équilibre à la pression atmosphérique (APPJ). L'arc soufflé APPJ est une technique simple et efficace pour déposer la couche Ag- $\text{TiO}_2$  avec une vitesse de dépôt compris entre 10 à 20  $\mu \text{ m} \cdot \text{s}^{-1}$  en comparaison avec des couches de  $\text{TiO}_2$  obtenues par pulvérisation cathodique magnétron réactive ( $1 \sim 10 \text{ nm} \cdot \text{min}^{-1}$ ) [13]. La distribution d'Ag, la cristallinité de  $\text{TiO}_2$  et la taille des particules  $\text{TiO}_2$  constituant la couche mince ont été contrôlées en variant les paramètres de dépôt comme la puissance plasma et le débit de gaz vecteur. Les couches déposées sont poreuses et de phase anatase avec une structure cœur-coquille d'Ag dans la matrice de  $\text{TiO}_2$  qui permettent une amélioration de la séparation/transfert de charge et une absorption dans le visible. L'activité

photocatalytique utilisant l'irradiation d'un simulateur solaire a été examinée pour la dégradation de rhodamine b (RhB) et des traces des polluants pharmaceutiques, à savoir le carbamazepine (CBZ), le venlafaxine (VLX) et le bezafibrate (BZF). L'effet de la teneur d'Ag (de 0 à 0.7 % en poids) sur l'activité photocatalytique a été examiné. Le taux de photodégradation maximale a été obtenu pour un contenu d'argent de % 0.4 en poids dans les couches composites. Les chapitres 7 et 8 représentent la conclusion générale et les perspectives, respectivement.

Le travail de recherche dans ce manuscrit de thèse a démontré la possibilité de préparer le  $\text{TiO}_2$  Q1D synthétisé par le processus hydrothermal alcalin comme un photocatalyseur pour la production d'énergie renouvelable et le traitement des eaux usées. La modification de  $\text{TiO}_2$  Q1D avec l'ajout des nanoparticules de RGO et Ag a amélioré l'efficacité photocatalytique. La préparation des nanorods de  $\text{TiO}_2$  avec les nanoparticules d'Ag et RGO (Ag-GT et Ag- $\text{TiO}_2$ ) a simplifié le processus de traitement des eaux usées en comparaison avec l'utilisation de la poudre commerciale de P25. Cependant, quelques obstacles doivent être adressés pour les applications de future. Il faut mettre à l'échelle le réacteur batch de la dégradation des polluants dangereux aqueux à un processus de dégradation en continu.

Comme perspectives de cette thèse il serait intéressant de réduire la synthèse multi-étape des matériaux 3D de Ag-GT pour réduire le coût du traitement. Le taux de production  $\text{H}_2$  peut-être augmenté en utilisant des stratégies comme couplage avec un semi-conducteur à largeur de bande étroite, un dopage avec des ions, l'utilisation de co-catalyseur, l'utilisation des colorants de surface ou le dépôt des métaux nobles sont nécessaires pour améliorer l'activité photocatalytique de  $\text{TiO}_2$  Q1D [14]. Modifier le catalyseur  $\text{TiO}_2$  Q1D pourrait permettre d'utiliser la lumière solaire et améliorer significativement l'efficacité de conversion d'énergie solaire [14]. Note, la conversion

d'énergie maximale de photocatalyseur activé par l'UV est 2 % [14]. Finalement l'utilisation des procédés plasma (APPJ) pour déposer de photocatalyseur Ag-TiO<sub>2</sub> pour leurs propriétés photocatalytiques peut présenter un procédé attirant pour synthétiser d'autres couches TiO<sub>2</sub> modifiés. En effet une large gamme d'autres matériaux composites tels que le graphène fonctionalisé ou Fe<sub>2</sub>O<sub>3</sub> (Photo-Fenton) peuvent être incorporés dans la couche de TiO<sub>2</sub> pour améliorer l'activité photocatalytique sous rayonnement solaire.

### Références

- [1] P. Roy, S. Berger, P. Schmuki, TiO<sub>2</sub> nanotubes: synthesis and applications, *Angew. Chem. Int. Ed.* 50 (2011) 2904-2939.
- [2] F. Han, V.S.R. Kambala, M. Srinivasan, D. Rajarathnam, R. Naidu, Tailored titanium dioxide photocatalysts for the degradation of organic dyes in wastewater treatment: a review, *Appl. Catal., A Applied* 359 (2009) 25-40.
- [3] X. Chen, S.S. Mao, Titanium dioxide nanomaterials: Synthesis, properties, modifications, and applications, *Chem. Rev.* 107 (2007) 2891-2959.
- [4] S. Linic, P. Christopher, D.B. Ingram, Plasmonic-metal nanostructures for efficient conversion of solar to chemical energy, *Nat. Mater.* 10 (2011) 911-921.
- [5] X. Li, J. Yu, S. Wageh, A.A. Al Ghamdi, J. Xie, Graphene in photocatalysis: a review, *Small* 12 (2016) 6640-6696.
- [6] C. Chen, W. Cai, M. Long, B. Zhou, Y. Wu, D. Wu, Y. Feng, Synthesis of visible-light responsive graphene oxide/TiO<sub>2</sub> composites with p/n heterojunction, *ACS Nano* 4 (2010) 6425-6432.

- [7] L. Zhang, W. Zheng, H. Jiu, W. Zhu, G. Qi, Preparation of the anatase/TiO<sub>2</sub>(B) TiO<sub>2</sub> by self-assembly process and the high photodegradable performance on RhB, *Ceram. Int.* 42 (2016) 12726-12734.
- [8] H.-L. Kuo, C.-Y. Kuo, C.-H. Liu, J.-H. Chao, C.-H. Lin, A highly active bi-crystalline photocatalyst consisting of TiO<sub>2</sub> (B) nanotube and anatase particle for producing H<sub>2</sub> gas from neat ethanol, *Catal. Lett.* 113 (2007) 7.
- [9] G. Williams, B. Seger, P.V. Kamat, TiO<sub>2</sub>-graphene nanocomposites. UV-assisted photocatalytic reduction of graphene oxide, *ACS Nano* 2 (2008) 1487-1491.
- [10] H. Zhang, X. Lv, Y. Li, Y. Wang, J. Li, P25-graphene composite as a high performance photocatalyst, *ACS Nano* 4 (2010) 380-386.
- [11] J. Du, X. Lai, N. Yang, J. Zhai, D. Kisailus, F. Su, D. Wang, L. Jiang, Hierarchically ordered macro-mesoporous TiO<sub>2</sub>-graphene composite films: improved mass transfer, reduced charge recombination, and their enhanced photocatalytic activities, *ACS Nano* 5 (2011) 590-596.
- [12] F. Bensouici, T. Souier, A.A. Dakhel, A. Iratni, R. Tala-Ighil, M. Bououdina, Synthesis, characterization and photocatalytic behavior of Ag doped TiO<sub>2</sub> thin film, *Superlattices Microstruct.* 85 (2015) 255-265.
- [13] H. Fakhouri, D.B. Salem, O. Carton, J. Pulpytel, F. Arefi-Khonsari, Highly efficient photocatalytic TiO<sub>2</sub> coatings deposited by open air atmospheric pressure plasma jet with aerosolized TTIP precursor, *J. Phys. D: Appl. Phys.* 47 (2014) 265301-265311.
- [14] A.A. Ismail, D.W. Bahnemann, Photochemical splitting of water for hydrogen production by photocatalysis: A review, *Sol. Energy Mater. Sol. Cells* 128 (2014) 85-101.

## ENGINEERING SIGNIFICANCE

Titanium dioxide ( $\text{TiO}_2$ ) is a widely studied semiconductor. The development of highly active  $\text{TiO}_2$  photocatalyst is a challenge for using solar energy to remediate polluted water and produce green energy such as hydrogen ( $\text{H}_2$ ). However, the  $\text{TiO}_2$  photocatalyst shows a low quantum efficiency, optical response, utilization rate of visible light and fast charge recombination. The top-priority goal of this dissertation is to enhance  $\text{TiO}_2$  photocatalytic activities for degrading aqueous hazardous pollutants and producing  $\text{H}_2$  energy.

Alkaline hydrothermal process was used to convert  $\text{TiO}_2$  NPs Q1D  $\text{TiO}_2$  with controllable phases structure and crystal size which showed enhanced photocatalytic activities. Hydrothermal synthesis factors (temperature, NaOH concentration and  $\text{TiO}_2$  concentration) significantly affected the Q1D  $\text{TiO}_2$  phase structure, crystal size, SSA as well as the bandgap which is known to affect the photocatalytic activities. The lack of research data describing the influence of the different hydrothermal synthesis process parameters on the Q1D  $\text{TiO}_2$  phase structure, crystal size, specific surface area (SSA), bandgap and photocatalytic activities was the motivation for the work reported in Chapter 3 and Chapter 4. The Box-Behnken design (BBD) model was used to statistically evaluate the influence of the hydrothermal synthesis factors on the Q1D  $\text{TiO}_2$  bandgap, photodegradation rate of aqueous hazardous pollutants and photocatalytic  $\text{H}_2$  production efficiency. The BBD models derived for the various studies were able to predict the optimum hydrothermal conditions employed to synthesize Q1D  $\text{TiO}_2$  with maximum and



minimum bandgap and maximum photocatalytic activities for photodegradation and H<sub>2</sub> production, respectively.

Another significant outcome from Chapter 3 and 4 is the identification of the optimum phase structure, crystal size (SSA) and bandgap for maximizing pollutants photodegradation rate and H<sub>2</sub> production rate. These models are significant because they can aid in engineering Q1D TiO<sub>2</sub> based compounds with controllable crystal phase, crystal size, SSA and bandgap and thereby, has been promising to enhance the photocatalytic activities of the existing photocatalytic applications.

In part 1 of the fifth objective (Chapter 5), Q1D TiO<sub>2</sub> was modified with partially reduced graphene oxide (RGO) (designated as GT photocatalyst) for photodegrading aqueous organic pollutants. RGO played an important role in enhancing charge transfer/separation and photocatalytic activities under UV light. The study examined the influence of the RGO atomic oxygen-to-carbon (O/C) ratio on GT photocatalytic activities. This research suggests the importance of partial oxygen functionalization of graphene as a means to enhance photocatalytic activities. Extreme cases of high and low RGO O/C ratio correlating to low electron conductivities and a loss of interaction between RGO and TiO<sub>2</sub>, respectively, should be avoided. The work reported in this study on optimizing the RGO-TiO<sub>2</sub> photocatalyst could serve as a promising process for preparing and optimizing other types of functionalized carbon based photocatalysts such as “graphene based CdS”.

In part 2 of the fifth objective (Chapter 5), the use of TiO<sub>2</sub> powder as slurry was associated with many disadvantages such as the need for separation or filtration steps, the problematic use in continuous flow systems. Immobilizing TiO<sub>2</sub> on solid substrate is a

promising approach. GT photocatalysts was enhanced with Ag NPs and subsequently deposited on glass substrate (designated as Ag-GT thin film). Ag-GT thin film photocatalysts were characterized with enhanced visible-light activities, charge separation/transfer, SSA and visible photocatalytic activities for degrading aqueous organic pollutants.

In Chapter 6, atmospheric pressure plasma jet (APPJ) was used to produce Ag-TiO<sub>2</sub> coating with controlled porosity and crystal size in a one-step process. The APPJ Ag-TiO<sub>2</sub> coating had shown significantly enhanced photocatalytic activities towards the degrading RhB and trace pharmaceutical compounds (TrPCs) from treated water. The APPJ was able to give significantly control of the distribution of Ag NPs and the TiO<sub>2</sub> crystallinity by varying deposition parameters such as Ag content (0-0.7 wt%), the plasma energy and carrier gas flow rate. This facile method to deposit porous Ag-TiO<sub>2</sub> films at a high deposition rate is promising for preparing other photocatalyst coatings (i.e. Pt-TiO<sub>2</sub> and Ag-ZnO<sub>2</sub>) and many applications such as photocatalysis and dye sensitized solar cells, among others.

# APPENDICES

## Chapter 3: copyright

6/18/2018

Rightslink® by Copyright Clearance Center



# RightsLink®

Home

Account Info

Help



**Title:** The role of hydrothermal conditions in determining 1D TiO<sub>2</sub> nanomaterials bandgap energies and crystal phases

**Author:** Tao Peng, Srimanta Ray, Sathyanarayanan Sevilimedu Veeravalli, Jerald A. Lalman, Farzaneh Arefi-Khonsari

Logged in as:

Tao Peng

LOGOUT

**Publication:** Materials Research Bulletin

**Publisher:** Elsevier

**Date:** September 2018

© 2018 Elsevier Ltd. All rights reserved.

Please note that, as the author of this Elsevier article, you retain the right to include it in a thesis or dissertation, provided it is not published commercially. Permission is not required, but please ensure that you reference the journal as the original source. For more information on this and on your other retained rights, please visit: <https://www.elsevier.com/about/our-business/policies/copyright#Author-rights>

BACK

CLOSE WINDOW

Copyright © 2018 Copyright Clearance Center, Inc. All Rights Reserved. [Privacy statement](#). [Terms and Conditions](#). Comments? We would like to hear from you. E-mail us at [customercare@copyright.com](mailto:customercare@copyright.com)

## Chapter 5: copyright

### SPRINGER NATURE LICENSE TERMS AND CONDITIONS

Jun 18, 2018

---

This Agreement between 436 Randolph Ave. ("You") and Springer Nature ("Springer Nature") consists of your license details and the terms and conditions provided by Springer Nature and Copyright Clearance Center.

License Number	4371970432312
License date	Jun 18, 2018
Licensed Content Publisher	Springer Nature
Licensed Content Publication	Environmental Science and Pollution Research
Licensed Content Title	Enhanced TiO <sub>2</sub> nanorods photocatalysts with partially reduced graphene oxide for degrading aqueous hazardous pollutants
Licensed Content Author	Tao Peng, Jian Zhang, Srimanta Ray et al
Licensed Content Date	Jan 1, 2018
Type of Use	Thesis/Dissertation
Requestor type	academic/university or research institute
Format	print and electronic
Portion	full article/chapter
Will you be translating?	no
Circulation/distribution	>50,000
Author of this Springer Nature content	yes
Title	Synthesizing Efficient Quasi-one-dimension Titanium Dioxide Nanocatalyst for Enhanced Photocatalytic Degradation of Aqueous Organic Pollutants and Hydrogen Production
Instructor name	Jerald A. Lalman
Institution name	University of Windsor
Expected presentation date	Jul 2018
Requestor Location	436 Randolph Ave. 436 Randolph Ave.  Windsor, ON N9b 2T6 Canada Attn: 436 Randolph Ave.
Billing Type	Invoice
Billing Address	436 Randolph Ave. 436 Randolph Ave.  Windsor, ON N9b 2T6 Canada Attn: 436 Randolph Ave.
Total	0.00 CAD
Terms and Conditions	

**Springer Nature Terms and Conditions for RightsLink Permissions**  
**Springer Customer Service Centre GmbH (the Licensor)** hereby grants you a non-exclusive, world-wide licence to reproduce the material and for the purpose and requirements specified in the attached copy of your order form, and for no other use, subject to the conditions below:

1. The Licensor warrants that it has, to the best of its knowledge, the rights to license reuse of this material. However, you should ensure that the material you are requesting is original to the Licensor and does not carry the copyright of another entity (as credited in the published version).  
  
If the credit line on any part of the material you have requested indicates that it was reprinted or adapted with permission from another source, then you should also seek permission from that source to reuse the material.
2. Where **print only** permission has been granted for a fee, separate permission must be obtained for any additional electronic re-use.
3. Permission granted **free of charge** for material in print is also usually granted for any electronic version of that work, provided that the material is incidental to your work as a whole and that the electronic version is essentially equivalent to, or substitutes for, the print version.
4. A licence for 'post on a website' is valid for 12 months from the licence date. This licence does not cover use of full text articles on websites.
5. Where '**reuse in a dissertation/thesis**' has been selected the following terms apply: Print rights for up to 100 copies, electronic rights for use only on a personal website or institutional repository as defined by the Sherpa guideline ([www.sherpa.ac.uk/romeo/](http://www.sherpa.ac.uk/romeo/)).
6. Permission granted for books and journals is granted for the lifetime of the first edition and does not apply to second and subsequent editions (except where the first edition permission was granted free of charge or for signatories to the STM Permissions Guidelines <http://www.stm-assoc.org/copyright-legal-affairs/permissions/permissions-guidelines/>), and does not apply for editions in other languages unless additional translation rights have been granted separately in the licence.
7. Rights for additional components such as custom editions and derivatives require additional permission and may be subject to an additional fee. Please apply to [Journalpermissions@springernature.com](mailto:Journalpermissions@springernature.com)/[bookpermissions@springernature.com](mailto:bookpermissions@springernature.com) for these rights.
8. The Licensor's permission must be acknowledged next to the licensed material in print. In electronic form, this acknowledgement must be visible at the same time as the figures/tables/illustrations or abstract, and must be hyperlinked to the journal/book's homepage. Our required acknowledgement format is in the Appendix below.
9. Use of the material for incidental promotional use, minor editing privileges (this does not include cropping, adapting, omitting material or any other changes that affect the meaning, intention or moral rights of the author) and copies for the disabled are permitted under this licence.
10. Minor adaptations of single figures (changes of format, colour and style) do not require the Licensor's approval. However, the adaptation should be credited as shown in Appendix below.

#### **Appendix — Acknowledgements:**

##### **For Journal Content:**

Reprinted by permission from [the Licensor]: [Journal Publisher (e.g.

Nature/Springer/Palgrave)] [JOURNAL NAME] [REFERENCE CITATION (Article name, Author(s) Name), [COPYRIGHT] (year of publication)

**For Advance Online Publication papers:**

Reprinted by permission from [the Licensor]: [Journal Publisher (e.g. Nature/Springer/Palgrave)] [JOURNAL NAME] [REFERENCE CITATION (Article name, Author(s) Name), [COPYRIGHT] (year of publication), advance online publication, day month year (doi: 10.1038/sj.[JOURNAL ACRONYM].)

**For Adaptations/Translations:**

Adapted/Translated by permission from [the Licensor]: [Journal Publisher (e.g. Nature/Springer/Palgrave)] [JOURNAL NAME] [REFERENCE CITATION (Article name, Author(s) Name), [COPYRIGHT] (year of publication)

**Note: For any republication from the British Journal of Cancer, the following credit line style applies:**

Reprinted/adapted/translated by permission from [the Licensor]: on behalf of Cancer Research UK: : [Journal Publisher (e.g. Nature/Springer/Palgrave)] [JOURNAL NAME] [REFERENCE CITATION (Article name, Author(s) Name), [COPYRIGHT] (year of publication)

**For Advance Online Publication papers:**

Reprinted by permission from The [the Licensor]: on behalf of Cancer Research UK: [Journal Publisher (e.g. Nature/Springer/Palgrave)] [JOURNAL NAME] [REFERENCE CITATION (Article name, Author(s) Name), [COPYRIGHT] (year of publication), advance online publication, day month year (doi: 10.1038/sj.[JOURNAL ACRONYM])

**For Book content:**

Reprinted/adapted by permission from [the Licensor]: [Book Publisher (e.g. Palgrave Macmillan, Springer etc) [Book Title] by [Book author(s)] [COPYRIGHT] (year of publication)

**Other Conditions:**

Version 1.0

Questions? [customercare@copyright.com](mailto:customercare@copyright.com) or +1-855-239-3415 (toll free in the US) or +1-978-646-2777.

## LIST OF PUBLICATIONS AND CONFERENCES

### *Publications*

- [1] **T. Peng**, S. Ray, S.S. Veeravalli, J.A. Lalman, F. Arefi-Khonsari, The role of hydrothermal conditions in determining 1D TiO<sub>2</sub> nanomaterials bandgap energies and crystal phases, *Materials Research Bulletin*, 105 (2018) 104-113.
- [2] **T. Peng**, J. Zhang, S. Ray, H. Fakhouri, X. Xu, F. Arefi-Khonsari, J.A. Lalman, Enhanced TiO<sub>2</sub> nanorods photocatalysts with partially reduced graphene oxide for degrading aqueous hazardous pollutants, *Environmental Science and Pollution Research*, (2018).
- [3]. **T. Peng**, J. Zhang, S. Ray, H. Fakhouri, S. S. Veeravalli, F. Arefi-Khonsari, J. A. Lalman. Optimization of hydrothermal synthesis of TiO<sub>2</sub> nanotubes for photocatalysis of organic chemicals, *Desalination and Water Treatment* (2018) (Accepted)
- [4] M. Bao, I.S. Amiin, **T. Peng**, W. Li, S. Liu, Z. Wang, Z. Pu, D. He, Y. Xiong, S. Mu, Surface Evolution of PtCu Alloy Shell over Pd Nanocrystals Leads to Superior Hydrogen Evolution and Oxygen Reduction Reactions, *ACS Energy Lett.* 3 (2018) 940-945.
- [5] J. Zhang, H. Zhou, J. Zhu, P. Hu, C. Hang, J. Yang, **T. Peng**, S. Mu, Y. Huang, Facile synthesis of defect-rich and S/N co-doped graphene-like carbon nanosheets as an efficient electrocatalyst for primary and all-solid-state Zn–air batteries, *ACS Appl. Mater. Interfaces* 9 (2017) 24545–24554.

- [6] J. Zhang, H. Zhou, X. Liu, J. Zhang, **T. Peng**, J. Yang, Y. Huang, S. Mu, Keratin-derived S/N co-doped graphene-like nanobubble and nanosheet hybrids for highly efficient oxygen reduction, *J. Mater. Chem. A* 4 (2016) 15870-15879.
- [7]. H. Fakhouri, **T. Peng**, A. Anagri, J. Pulpytel, E. Sutter, F. S. G. Bagh, J. A. Lalman, F. Arefi-Khonsari. Designing a three-dimensional Ag-reduced graphene oxide-TiO<sub>2</sub> nanorods photocatalyst thin-film for degrading organic pollutants under visible light conditions. (In preparation)
- [8]. **T. Peng**, J. Pulpytel, I. Horovitz, A. K. Jaiswal, D. Avisar, H. Mamane, J. A. Lalman, F. Arefi-Khonsari, One-step deposition of nano-Ag-TiO<sub>2</sub> coatings by APPJ for water treatment: Application to trace pharmaceutical removal by solar photocatalysis, *Journal of Photochemistry and Photobiology A: Chemistry* (2017) (Under review)
- [9]. **T. Peng**, J. Zhang, S. Ray, H. Fakhouri, F. Arefi-Khonsari, and J. Lalman. Optimizing photocatalytic hydrogen production from a water-ethanol mixture using 1D TiO<sub>2</sub>, *Journal of Renewable and Sustainable Energy*, Manuscript (2018) (Under review)

### ***International Conferences***

- [1]. **T. Peng**, J. A. Lalman, F. Arefi-Khonsari. Ag-reduced graphene oxide-TiO<sub>2</sub> nanorods thin-film photocatalyst for degrading organic hazardous pollutants under visible light conditions. *Proceedings of 2018 Energy & Sustainability Symposium*, Windsor, Ontario, Canada (2018).
- [2]. **T. Peng**, S. Ray, J. A. Lalman, F. Arefi-Khonsari. Accessing the impact of hydrothermal synthesis parameters of the bandgap and crystal phases of titanium dioxide (TiO<sub>2</sub>). *The ACS 48th Central Regional Meeting (CREM)* (2017).



[3]. **T. Peng**, J. Zhang, J. A. Lalman and F. Arefi-Khonsari. Synthesis of an enhanced visible-Light activated hierarchical three-dimensional Ag/TiO<sub>2</sub> nanowires/graphene sandwich photocatalyst. *International Conference on Material Science (ICMS) 2017*.

[4]. **T. Peng**, J. A. Lalman and F. Arefi-Khonsari. Partially reduced graphene oxide-TiO<sub>2</sub> nanorods photocatalyst for degrading aqueous hazardous pollutants. ACS National Meeting & Expo. Boston, MA (2018) (Accepted).

## VITA AUCTORIS

NAME: Tao Peng

PLACE OF BIRTH: Sichuan, China

YEAR OF BIRTH: 1987

EDUCATION: Longchang 2<sup>nd</sup> High School, Neijiang, Sichuan, China  
2005

Chengdu University of Technology, B.Eng., Chengdu,  
Sichuan, China 2010

Wuhan University of Technology, M.Eng., Wuhan,  
Hubei, China 2013